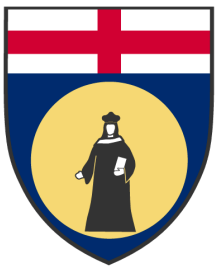

UNIVERSITÀ DEGLI STUDI DI GENOVA
DOTTORATO DI RICERCA IN FISICA

ANOMALOUS EFFECTS IN QUANTUM SPIN HALL-BASED JOSEPHSON JUNCTIONS

DOCTORAL THESIS

Author
Lucia Vigliotti

Tutor (s)
Prof. Maura Sassetti
Dr. Niccolò Traverso Ziani

Reviewer (s)
Prof. Roberta Citro (Università degli Studi di Salerno)
Dr. Fernando Dominguez (TU Braunschweig)

The Coordinator of the PhD Program
Prof. Riccardo Ferrando

Genova, March 2024

XXXVI Cycle

To all, still with me or no longer,
who have filled these years with the deepest affection

... and you are so many.

"Quale mondo giaccia di là di questo mare non so,
ma ogni mare ha l'altra riva, e arriverò."
C. Pavese, *Il mestiere di vivere*

Contents

List of publications

This Thesis is based on the following papers co-authored by myself:

- **L. Vigliotti**, F. Cavaliere, G. Passetti, M. Sassetti and N. Traverso Ziani, *Reconstruction-induced φ_0 Josephson effect in Quantum Spin Hall constrictions*, Nanomaterials **13**, 1497 (2023).
- **L. Vigliotti**, A. Calzona, N. Traverso Ziani, F. S. Bergeret, M. Sassetti and B. Trauzettel, *Effects of the spatial extension of the edge channels on the interference pattern of a helical Josephson junction*, Nanomaterials **13**, 569 (2023).
- **L. Vigliotti**, *4π-periodic AC Josephson current through a reconstructed Quantum Spin Hall constriction*, Il nuovo cimento C **45**, 1-11 (2022).
- **L. Vigliotti**, A. Calzona, B. Trauzettel, M. Sassetti and N. Traverso Ziani, *Anomalous flux periodicity in proximitised Quantum Spin Hall constrictions*, New Journal of Physics **24**, 053017 (2022).

Other publications not included in this Thesis are:

- **L. Vigliotti**, F. Cavaliere, M. Carrega and N. Traverso Ziani, *Assessing bound states in a one-dimensional topological superconductor: Majorana versus Tamm*, Symmetry **13**, 1100 (2021).
- N. Traverso Ziani, C. Fleckenstein, **L. Vigliotti**, B. Trauzettel and M. Sassetti, *From fractional solitons to Majorana fermions in a paradigmatic model of topological superconductivity*, Physical Review B **101**, 195303 (2020).

Introduction

The discovery of the integer Quantum Hall Effect in 1980 [107, 195] is nowadays recognized as a watershed moment in condensed matter physics, as it introduced into the field topological concepts belonging to mathematics. In Quantum Hall systems, one-dimensional gapless channels emerge along the edges of a two-dimensional Hall bar subjected to a strong perpendicular magnetic field. Whereas the bulk of the material is insulating, these edge states behave as perfect conductors, allowing for ballistic and coherent electron transport, just like waveguides used in quantum optics for the coherent transport of photons. Their unique conduction properties were understood to take roots in their topological protection against backscattering.

However, it took some time for researchers to really grasp the potential of the interplay between topology and solid state physics. However, eventually, in the years thereafter there has been a remarkable surge in both the theoretical prediction and the experimental realization of new topological materials. The relevance of the subject was conclusively acknowledged by the award of the 2016 Nobel Prize in Physics to D. J. Thouless, F. D. M. Haldane, and J. M. Kosterlitz for their pioneering theoretical discoveries in the realms of topological phase transitions and phases of matter [80, 102].

One of the most intriguing aspects of topological materials is, as we mentioned, the existence of edge states. These states arise at the physical boundaries of the system and exhibit exceptional properties due to the so-called bulk-boundary correspondence, which relates the non-trivial topology of the bulk to the topologically-protected properties of the edge states. Importantly, such properties are robust against perturbations, making these states appealing and exploitable in experiments, and expected to enable a new generation of electronics, sensors, and optical components for a range of technological applications.

Over the past fifteen years, an innovative field has emerged: that of two-dimensional topological insulators, and in particular of the Quantum Spin Hall Effect [20, 95]. These materials are particularly intriguing due to the helical nature of their one-dimensional edge channels: along them, the electron spin and the direction of propagation are locked, resulting in two counter-propagating channels having opposite spin polarization. This property opens the way to spintronics advancements [121, 131, 145], as the manipulation of electron spins is directly achievable through the control of the helical

edge states.

After the first experimental evidencies of the helical edge states in HgTe-CdTe heterostructures [103], as theoretically predicted by B. A. Bernevig, T. L. Hughes and S.-C. Zhang [21], research has predominantly moved in two directions:

- finding the Quantum Spin Hall Effect in new materials, with the main task of making the effect observable at room temperature;
- creating functional nanostructures that leverage the properties of edge states in view of applications in spintronics, superconducting spintronics, and topological quantum computation.

Among other possibilities, two powerful tools are the proximity effect to induce superconductivity, which has been largely investigated in the last years [104, 133, 149, 165], and the realization of constrictions between the edges [49, 110, 113, 152, 176], whose first – and only – experimental signature was provided in an experiment conducted in 2020 [168].

- The combination of topological insulators and superconductivity has attracted from the beginning a lot of attention, with the primary task of developing topological superconductivity to realize protected Majorana bound states [63, 96], but also in view of superconducting spintronics [25, 112, 175].

  On the one hand, a Quantum Spin Hall Insulator in close proximity to superconductors inherits superconducting correlations [118], thanks to a leakage of Cooper pairs – couple of correlated electrons that realize the ground state of the superconductor – extending over the superconducting coherence length ξ, which measures how far correlations between paired electrons penetrate into the normal region, and represents effectively the "size" of Cooper pairs.

  As a byproduct of proximity effect, there have been also theoretical and experimental studies of topological Josephson junctions, namely hybrid structures where not only one, but two superconducting leads proximitize a topological insulator on opposite sides [45,50,63]. At energies lower than the superconducting gap[1], transport across the junction is mediated by Cooper pairs traveling from one lead to the other through the helical edge states, forming a dissipationless current named Josephson current [93]. Importantly, if the junction's width is comparable to ξ, the two electrons of a Cooper pair can not only be injected into a same edge, but also split and propagate over opposite edges [78, 148]. Topological Josephson junctions are often studied in the presence of magnetic fields, to benefit of magnetic interference phenomena that provide a deeper insight into the transport properties of the junction [54].

- On the other hand, constrictions consist in bringing the opposite edges of a topological insulator closer to each other, such that they can hybridize or interact. Of special significance are single-electron inter-edge scattering events [49, 110, 113, 152, 176], which broaden the potential applications of Quantum Spin Hall-based systems. Indeed, they effectively make the two edges similar – in terms of spectral properties – to a spin-orbit coupled quantum wire, which is regarded as the main

[1] Let's assume for simplicity that the two superconductors are characterized by a same gap.

platform to realize Majorana fermions and parafermions. However, the Quantum Spin Hall Effect has the advantages over quantum wires that cleaner samples can be fabricated and that multiterminal experiments are more easily designed. Moreover, most proposals for the realization of topologically confined Majoranas on Quantum Spin Hall platforms require the coexistence of superconductive and ferromagnetic ordering [2, 39, 175], which turns out to be difficult to achieve in the laboratory, and the constriction potentials are able to make ferromagnetic barriers unessential. The full versatility of Quantum Spin Hall constrictions is not only restricted to the formation of the renowned non-Abelian anyons, but ranges over several related topics, such as odd-frequency superconductivity [22, 38, 60, 171, 174] or Floquet topology.

In this Thesis, the system under consideration is a long Quantum Spin Hall constriction, employed as the non-superconducting element of a Josephson junction, with a magnetic field and bias possibly included. This configuration combines the two nanostructures we have previously introduced. Despite the continuous interest in finding new schemes to access and manipulate the Quantum Spin Hall states, this one was largely uncharted in the realm of theoretical investigation. Although the implementation of a proximitized constriction in experimental settings is not attested in literature to date, both the constriction itself and the proximization of topological insulators have been achieved. Therefore, the assembly of the entire structure appears as a feasible goal, and its theoretical analysis holds significant relevance. This represents the starting motivation of this Thesis.

Through our investigations, two additional facts emerge and make this system worthy of attention:

1. We have mentioned that a reference lengthscale in proximitized systems is the coherence length ξ of the induced superconducting pairing, which represents effectively the Cooper pair size and, in turn, the distance over which the two bounded electrons can split. The presence of the constriction places the system in a regime where additional effects involving single electrons become relevant: each of the two electrons can independently undergo inter-edge tunneling, and if the edge channels have spatial extent comparable to ξ, they can propagate over different trajectories pertaining to a same edge. From a fundamental point of view, this system represents therefore a good platform to study the role of single-electron physics within the superconducting context, which as we will demonstrate originates clear-cut signatures.

2. It turns out that this experimentally conceivable system is also naturally entitled to interesting functionalities in the realm Josephson junctions, as it can host the anomalous Josephson effect, that can be used to design phase batteries and to drive superconducting circuits and superconducting memories, and the superconducting diode effect, which inspires great perspectives as well, without the need of external bias or magnetic fields.

This Thesis is organized as follows:

In **Chapter 1**, we revise the roadmap that led to the realization of the Quantum Spin Hall Effect.

We start from the integer Quantum Hall Effect (1980) and the lattice model proposed by F. D. M. Haldane (1988) to reproduce the same physics in the absence of a net magnetic field, identifying time-reversal symmetry breaking as the essential ingredient. We then discuss the proposal by C. L. Kane and E. J. Mele (2005), who discovered that one sheet of graphene, with spin-orbit interaction, realizes a time-reversal invariant extension of the Haldane model: more specifically, the system is equivalent to two copies of the Haldane model, and represents the first appearance of the Quantum Spin Hall Effect. Next we describe A. Bernevig, T. L. Hughes and S.-C. Zhang's alternative (2006), based on HgTe-CdTe heterostructures, which was the first experimentally feasible proposal, and is still nowadays one of the most popular platforms. Some of the first experimental evidencies of the effect are reviewed, as well as the main ways of nanostructuring the edge states and their major technological applications.

In **Chapter 2**, we provide an overview of the Josephson effect.
We start from the description of superconductivity through the Ginzburg-Landau theory, and derive the DC and AC Josephson effect. We subsequently discuss the consequences of a magnetic field applied to the junction on the Josephson effect. Within this framework, we introduce the so-called interference pattern, a measurable quantity strongly related to the transport properties of the non-superconducting part of the junction. We first discuss the simpler scenario where Cooper pairs do no split, with a focus on the case of topological Josephson junctions, including the first experiment on this subject. We then include the splitting of Cooper pairs over opposite edges of the topological insulator, showing that this is associated to a specific feature arising in the interference pattern. We revise a tunneling model [78] for topological Josephson junctions which captures the coexistence and competition between these two transport arrangements. This work is the starting point for the results of the Thesis.

Chapter 3 contains our original results published in [187, 188].
We incorporate in the Josephson junction of [78] the presence of a long constriction between the Quantum Spin Hall edge states. We perturbatively compute the Josephson current analytically both in the absence and in the presence of a bias, and discuss the new Cooper pair transport processes allowed by the presence of the constriction. We show that these processes reflect into a novel and well recognizable feature of the interference pattern – a peculiar periodicity in the magnetic flux piercing the junction – that is absent in previous models where the two edges are not tunnel-coupled to each other. The result represents a possible experimental signature of the coupling between the helical edges, and is discussed in a range of parameters. We interpret the result in the light of the single-electron physics dominating the constriction. At the end of the Chapter we further comment on two points. First, the robustness of the results against edge reconstruction [187], which is a spatial separation of the two counter-propagating channels. This may arise if the potential confining the edge states is not infinitely sharp, but smooth, which is an experimentally more realistic assumption. Second, the generalization to the case of uniform inter-edge tunneling, namely the constriction corresponds to the whole system and not only a subregion of it.

Chapter 4 is based on the results published in [191].
We revise the requirements for the so-called anomalous Josephson effect: whereas in general a Josephson current can flow only if the phases characterizing the superconductors differ with each other, under appropriate symmetry breakings an "anomalous" cur-

rent can arise even in the absence of any phase difference. We also introduce a closely related phenomenon, the superconducting diode effect, which shares similarities with the celebrated semiconducting diode, and mention some of the suitable experimental platforms. Lastly, we show that among them is also the proximitized Quantum Spin Hall constriction with reconstructed edge channels introduced in Chapter 3. Notably, in this system the two effects do not need the presence of a magnetic field.

In **Chapter 5**, we present our results published in [189].
Here, we inspect the role of the spatial extent of the edge states on the transport properties and the interference pattern of the junction. This aspect is usually neglected, and the edge states are often modeled in theoretical works as strongly localized. In some cases of the literature, where the edge shape is considered, the lengthscales involved are such that the two electrons can be assumed not to split. However, apart from the splitting into opposite edges that we mentioned above, if the edge channels themselves have spatial extent comparable to ξ, the electrons can also split over different trajectories within a same edge. The number of paths they can follow remarkably increases, leaving an imprint on the interference pattern. We suggest an intuitive way of describing this setup for arbitrary edge shapes, and discuss the interference pattern with a particular focus on the case of prevailing non-local transport, namely highly broadened edge states and a large occurrence of Cooper pair splittings.

Appendices A and **B** illustrate technical parts of the calculations and discuss details in support of the comments presented in the main text.

CHAPTER 1

Two-dimensional topological insulators

1.1 Early topology: the Quantum Hall Effect

This Section is devoted to the Quantum Hall Effect, which can be considered as the precursor of topological condensed matter physics. In Subsec. 1.1.1 we will describe the effect, which works as follows: a clean two-dimensional electron gas, at very low temperature, subjected to a strong perpendicular magnetic field, is insulating in the bulk but hosts chiral metallic channels at the physical boundaries of the sample. Moreover, such channels are ballistic even in the presence of impurities. In Subsec. 1.1.2 we will formally derive that the conductance of the system is quantized to the values ne^2/h, with n an integer number (corresponding to the number of chiral edge channels). In Subsec. 1.1.3 we will discuss a lattice model of spinless electrons in the presence of a periodic magnetic flux, suggested by F. D. M. Haldane in 1988 to reproduce the Quantum Hall Effect physics.

1.1.1 From Classical to Quantum Hall Effect

Reminder of the Classical Hall Effect

The first observation of the Classical Hall Effect dates back to 1879, due to E. H. Hall. He analyzed a thin metallic plaquette subjected to a perpendicular magnetic field, $\mathbf{B} = B\mathbf{e}_3$[1]. He injected a current along $\mathbf{e}_1$ and observed a longitudinal resistance independent of the magnetic field and a transverse resistance, called Hall resistance, proportional to B. The system is conveniently described by the Drude model for diffusive transport in a metal [52, 97].

Let us suppose that N free electrons are moving on a xy planar system of dimensions

[1] From now on, $\mathbf{e}_i$, $i = 1, 2, 3$ will denote the unit vectors along the x, y, z axis.

L_x and L_y, pierced by a perpendicular magnetic field B and subjected to an in-plane electric field. The electron density is

$$n_e = \frac{N}{L_x L_y}. \tag{1.1}$$

Between two successive scattering events – due to impurities in the sample or electron-electron and electron-phonon interactions – electrons are accelerated by the Lorentz force

$$\mathbf{F} = -e\left[\mathbf{E} + \mathbf{v}_D \times \mathbf{B}\right], \tag{1.2}$$

where $\mathbf{v}_D$ is the drift velocity of the electrons in the metal and $-e$ ($e > 0$) is the electron charge. In Eq. (1.2), the first contribution is due to the electric field and the second one to the magnetic field. The equation of motion for each electron reads as

$$\frac{d\mathbf{p}}{dt} = -\frac{\mathbf{p}}{\tau} + \mathbf{F} = -\frac{\mathbf{p}}{\tau} - e\left[\mathbf{E} + \mathbf{v}_D \times \mathbf{B}\right], \tag{1.3}$$

with $\mathbf{p} = m_e \mathbf{v}_D$ its momentum. Here, m_e is the electron mass and τ the relaxation time, which is the time interval between a scattering event and the next one. The macroscopic properties we are interested in refer to the stationary regime, namely $\frac{d\mathbf{p}}{dt} = 0$. In this case, we have

$$0 = -eE_x - \omega_c p_y - \frac{p_x}{\tau}, \tag{1.4a}$$

$$0 = -eE_y + \omega_c p_x - \frac{p_y}{\tau}, \tag{1.4b}$$

where we have defined the cyclotron frequency $\omega_c = \frac{eB}{m_e}$. We now introduce the current density

$$\mathbf{J} = -en_e \mathbf{v}_D = -\frac{en_e}{m_e}\mathbf{p}, \tag{1.5}$$

which combined with Eq. (1.4) returns

$$\sigma_0 E_x = \omega_c \tau J_y + J_x, \tag{1.6a}$$

$$\sigma_0 E_y = -\omega_c \tau J_x + J_y. \tag{1.6b}$$

Here we have introduced $\sigma_0 = \frac{n_e \tau e^2}{m_e}$, which is the Drude conductivity in the absence of magnetic field. Recalling that $E_i = \rho_{ik} J_k$, $i = x, y$, from the previous equations we can easily read the resistivity tensor:

$$\rho = \begin{pmatrix} \rho_{xx} & \rho_{xy} \\ \rho_{yx} & \rho_{xx} \end{pmatrix} = \begin{pmatrix} \frac{1}{\sigma_0} & \frac{\omega_c \tau}{\sigma_0} \\ -\frac{\omega_c \tau}{\sigma_0} & \frac{1}{\sigma_0} \end{pmatrix}. \tag{1.7}$$

Notice that, in the absence of magnetic field, the tensor is diagonal and $\mathbf{E}$ and $\mathbf{J}$ are directly proportional. Its inverse tensor is the conductivity tensor

$$\sigma = \begin{pmatrix} \frac{\rho_{xx}}{\rho_{xx}^2 + \rho_{xy}^2} & -\frac{\rho_{xy}}{\rho_{xx}^2 + \rho_{xy}^2} \\ \frac{\rho_{xy}}{\rho_{xx}^2 + \rho_{xy}^2} & \frac{\rho_{xx}}{\rho_{xx}^2 + \rho_{xy}^2} \end{pmatrix}. \tag{1.8}$$

We can now assess the dynamics of the system. In the initial state, there is only the J_x component of the current density. Due to the magnetic contribution to the Lorentz

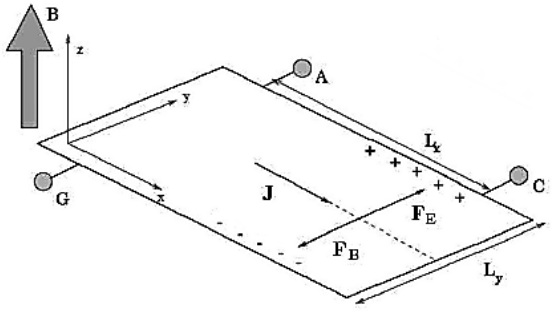

Figure 1.1: *The Hall bar. The magnetic field B is directed along the z direction, and an in-plane electric field* $\mathbf{E}$ *pushes electrons to move creating a current density* $\mathbf{J}$*. Due to the magnetic contribution to the Lorenz force, denoted by* $\mathbf{F}_B$ *electrons accumulate on the upper edge of the bar. Due to the imbalance of charge between the two edges of the bar, an electric component of the Lorenz force* $\mathbf{F}_E$ *arises. When they compensate, the only surviving component of the current density is along the* x *direction.*

force, electrons accumulate on the lower edge of the bar (see Fig. 1.1), creating a non-zero J_y component. This out-of-equilibrium situation is compensated by the occurrence of an electric field along $-\mathbf{e}_2$ and, consequently, an electric force term. The stationary regime is reached as soon as the two forces compensate. At that stage, there is no electron flow along $\mathbf{e}_2$ and only J_x survives. In that case, we have

$$E_x = \frac{1}{\sigma_0} J_x, \qquad E_y = -\frac{\omega_c \tau}{\sigma_0} J_x. \tag{1.9}$$

where E_y is the most relevant component of the electric field (the Hall electric field). For a uniform electric field, the associated voltage drops are

$$V_L = E_x L_x = \frac{1}{\sigma_0} J_x L_x, \qquad V_H = E_y L_y = -\frac{\omega_c \tau}{\sigma_0} J_x L_y, \tag{1.10}$$

and since the current flowing through the sample is $I = J_x L_y$, we have

$$V_L = \frac{1}{\sigma_0} \frac{L_x}{L_y} I, \qquad V_H = -\frac{\omega_c \tau}{\sigma_0} I. \tag{1.11}$$

Finally, the longitudinal and Hall resistances are

$$R_L = \frac{|V_L|}{I} = \frac{1}{\sigma_0} \frac{L_x}{L_y} = \rho_{xx} \frac{L_x}{L_y}, \qquad R_H = \frac{|V_H|}{I} = \frac{\omega_c \tau}{\sigma_0} = \rho_{xy}. \tag{1.12}$$

Notably, R_L strongly depends on the dimension of the Hall bar, whereas R_H is universal and independent of the geometry of the system. This stems from the two-dimensionality of the sample. As anticipated R_L (ρ_{xx}) in independent of the magnetic field, while R_H (ρ_{xy}) depends linearly on that.

We mention in passing that, since a same discussion holds for holes provided that $-e \to e$ and $n_e \to n_h$, measurements of Classical Hall Effect can be employed to extract information about the charge carriers and their densities in the analyzed material.

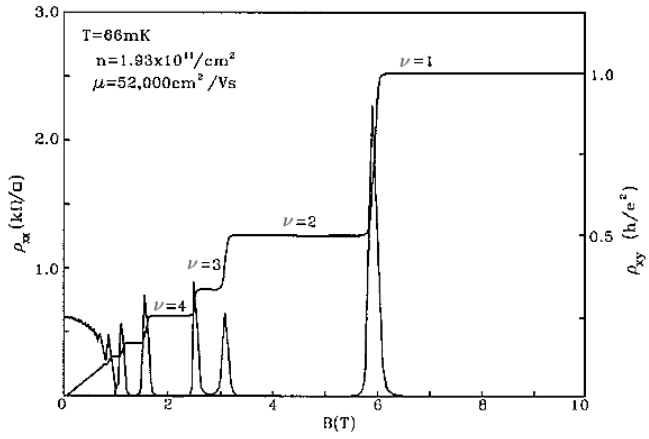

Figure 1.2: *Longitudinal resistivity (ρ_{xx}) and Hall resistivity (ρ_{xy}) as a function of the magnetic field for the states of the Integer Quantum Hall Effect. The former drops to zero where the latter shows extremely precise quantized plateaux. Adapted with permission from [183]. Copyright 2024 by the American Physical Society.*

The Quantum Hall Effect

In 1980, more than a hundred years later than the experiments performed by E. H. Hall, K. von Klitzing and his collaborators studied the Hall effect in Silicon MOSFET samples at high magnetic fields (up to 10 T) and very low temperature ($\sim$ 1.5 K) [195]. In this regime, which is known as Integer Quantum Hall regime, they found very different results from those of the Classical Hall Effect. Indeed, in such condition, the Hall resistivity ρ_{xy} is no longer linear in the magnetic field, but quantized with the plateau structure in Fig. 1.2. In correspondence with the plateaux, the longitudinal resistivity vanishes. Since plateaux appear at

$$R_H = \rho_{xy} = \frac{1}{\nu}\frac{h}{e^2}, \tag{1.13}$$

with ν an integer, this phenomenology has been called Integer Quantum Hall Effect [69]. Within a single-particle picture in terms of Landau levels, it has been shown that each plateau corresponds to the first ν levels being occupied [107]. The quantization is extremely precise (order of one part in 10^9). For $\nu = 1$, one obtains the quantum of resistance

$$R_K = \frac{h}{e^2}, \tag{1.14}$$

named Klitzing resistance. The measured value of R_K in 1990, $R_K = 25812.807\,\Omega$, has become the standard of maintenance for the International System Ohm[2]. For his astonishing discover, von Klitzing was awarded the Nobel Prize in 1985.

In terms of conductivity, when $\rho_{xx} = 0$ (namely, where a plateau occurs),

$$\sigma_{xx} = 0, \qquad \sigma_{xy} = \nu\frac{e^2}{h}. \tag{1.15}$$

[2]The Klitzing resistance is also related to the fine-structure constant α, $\alpha = c\mu_0/2R_K = 1/137$, with $\mu_0 = 4\pi \cdot 10^{-7}$ H/m the vacuum permittivity.

Then, the bulk of the system becomes insulating and transport occurs only along one-dimensional channels at the boundary of the sample. In particular, in Eq. (1.15), ν corresponds to the number of chiral channels on each edge, see Fig. 1.3. Semiclassically, this can be understood by thinking about the different orbits performed by the electrons. Due to magnetic field, electrons in the bulk are localized in closed cyclotron orbits with a fixed center of motion, and therefore cannot travel from one end of the sample to the other. On the other hand, orbits near the edges are interrupted, such that electrons bounce forward with the so-called skipping orbits. Moreover, all the electrons on one edge propagate in the same direction, and electrons close to the other edge propagate in the opposite direction. This results in the creation of chiral one-dimensional conducting channels. Owing to chirality, these channels are protected against backscattering. They exist as long as ρ_{xy} lies on a plateau, and are thus insensitive to small variations of the magnetic field, as well as robust with respect to disorder and impurities.

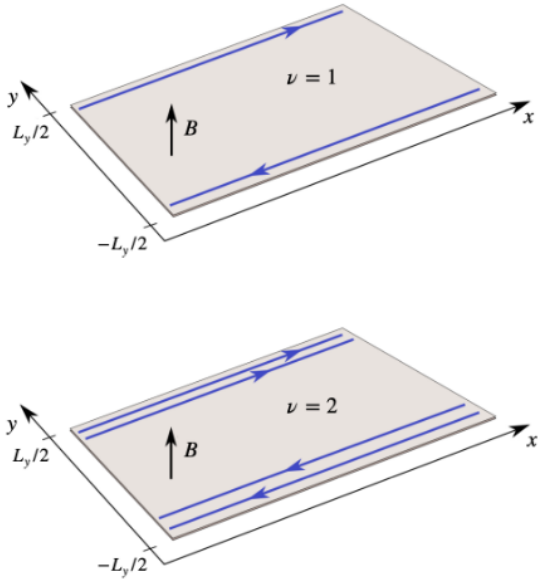

Figure 1.3: *Hall system corresponding to the first and second plateaux, with a couple and two couples of chiral channels, respectively. Figure from [140].*

Our goal will now be to highlight the topological origin of the Quantum Hall Effect. To this aim, in what follows, we give a formal demonstration of the quantization of the Hall conductance by relating it to a global topological invariant quantity.

1.1.2 Conductance quantization

In this Subsection, we will prove that the transverse conductance of an insulator is quantized in units of the conductance quantum e^2/h. We will first introduce the concepts of Berry phase and Berry curvature. Then we will demonstrate that the system's conductance is given by the integral of the Berry curvature over the Brillouin zone or, in other words, by the sum of the Chern numbers of all the filled bands. Lastly, we will show that the Chern number of a fully filled band is an integer.

Berry phase and Berry curvature

Let us now introduce a crucial definition for topology in condensed matter physics, which is the Berry phase [20].

Let us consider a system described by a time-dependent Hamiltonian $H(\mathbf{R})$, with $\mathbf{R} = \mathbf{R}(t)$ a set of parameters on which H depends. We are interested in the adiabatic evolution of the system: this means that the parameters $\mathbf{R}(t)$ have a slow variation if compared to the energy scales at play (such as the energy gap for an insulator). In particular, we assume that the parameter evolution follows a curve $\mathcal{C}$, which for now can be either open or closed.

We define the instantaneous orthonormal basis of eigenstates of $H(\mathbf{R}(t))$, $|n(\mathbf{R}(t))\rangle$, satisfying

$$H(\mathbf{R}(t))\,|n(\mathbf{R}(t))\rangle = E_n(\mathbf{R}(t))\,|n(\mathbf{R}(t))\rangle\,. \tag{1.16}$$

We notice that, as any wavefunction, each $|n(\mathbf{R}(t))\rangle$ is defined by Eq. (1.16) up to a phase factor, which may depend on $\mathbf{R}$. As $\mathbf{R}$ evolves with time, the Hamiltonian is diagonalized by a new instantaneous basis and, in principle, the phase of each $|n(\mathbf{R})\rangle$ can change independently from the others. Keeping this warning in mind, let's then try to understand how a state evolves as $\mathbf{R}$ moves along $\mathcal{C}$.

Let us assume that the system has been prepared in an instantaneous eigenstate $|n(\mathbf{R}(t_0))\rangle$ (we set $t_0 = 0$ for simplicity), and let $|n(\mathbf{R}(t))\rangle$ be nondegenerate for every $\mathbf{R}(t) \in \mathcal{C}$. We want to identify the evoluted state of the system, which we denote as $|\psi(t)\rangle$, at the generic time t. The adiabatic theorem comes to our aid [120]: indeed, if the variation of $\mathbf{R}$ is adiabatic and the Hamiltonian changes continuously from $H(\mathbf{R}(0))$ to $H(\mathbf{R}(t))$, then $|\psi(t)\rangle$ corresponds at every time to an instantaneous eigenstate of $H(\mathbf{R}(t))$. In particular, to an eigenstate continuously connected to $|n(\mathbf{R}(0))\rangle$. This means

$$|\psi(t)\rangle = e^{-i\theta(t)}\,|n(\mathbf{R}(t))\rangle\,. \tag{1.17}$$

In order to specify the phase $\theta(t)$, we plug $|\psi(t)\rangle$ in the time-dependent Schrödinger equation

$$\begin{aligned} H(\mathbf{R}(\mathbf{t}))\,|\psi(t)\rangle &= i\hbar\frac{d}{dt}\,|\psi(t)\rangle \\ \Rightarrow E_n(\mathbf{R}(t))\,|\psi(t)\rangle &= \hbar\dot{\theta}(t)\,|\psi(t)\rangle + i\hbar\frac{d}{dt}\,|\psi(t)\rangle\,, \end{aligned} \tag{1.18}$$

and project the equation onto $|n(\mathbf{R}(t))\rangle$, obtaining

$$E_n(\mathbf{R}(t)) = \hbar\dot{\theta}(t) + i\hbar\,\langle n(\mathbf{R}(t))|\,\frac{d}{dt}\,|n(\mathbf{R}(t))\rangle\,. \tag{1.19}$$

Solving for $\theta(t)$ and recalling that $\theta(0) = 0$, we get

$$\theta(t) = \frac{1}{\hbar}\int_0^t E_n(\mathbf{R}(t'))dt' - i\int_0^t \langle n(\mathbf{R}(t'))|\,\frac{d}{dt'}\,|n(\mathbf{R}(t'))\rangle\,dt'. \tag{1.20}$$

The evoluted state is hence given by

$$|\psi(t)\rangle = e^{-\frac{i}{\hbar}\int_0^t E_n(\mathbf{R}(t'))dt'}e^{i\gamma_n}\,|n(\mathbf{R}(t))\rangle\,, \tag{1.21}$$

where, apart from the dynamic phase factor, a second phase is present: we define it as the Berry phase γ_n.

Definition 1.1.1. *Berry phase:* $\gamma_n = i \int_0^t \langle n(\mathbf{R}(t'))| \frac{d}{dt'} |n(\mathbf{R}(t'))\rangle \, dt'$.

We can rewrite the Berry phase as follows

$$\gamma_n = i \int_0^t \langle n(\mathbf{R}(t'))| \nabla_{\mathbf{R}} |n(\mathbf{R}(t'))\rangle \cdot \frac{d\mathbf{R}(t')}{dt'} dt' = i \int_{\mathcal{C}} \langle n(\mathbf{R})| \nabla_{\mathbf{R}} |n(\mathbf{R})\rangle \cdot d\mathbf{R}, \quad (1.22)$$

making clear that it only depends on the path $\mathcal{C}$ in the parameter space. The Berry phase has thus a purely geometric nature. By analogy with the magnetic vector potential, we can define the Berry vector potential (or Berry connection) $\mathbf{A}_n(\mathbf{R})$, such that $\gamma_n = \int_{\mathcal{C}} d\mathbf{R} \cdot \mathbf{A}_n(\mathbf{R})$.

Definition 1.1.2. *Berry connection:* $\mathbf{A}_n(\mathbf{R}) = i \langle n(\mathbf{R})| \nabla_{\mathbf{R}} |n(\mathbf{R})\rangle$.

This leads us to two comments:

1. γ_n is real by construction, hence is it proper to call it a phase. Indeed, it is straightforward to show that the quantity $\langle n(\mathbf{R})| \nabla_{\mathbf{R}} |n(\mathbf{R})\rangle = - \langle n(\mathbf{R})| \nabla_{\mathbf{R}} |n(\mathbf{R})\rangle^*$ is purely imaginary. The Berry connection is thus real and so is the Berry phase.

2. The Berry connection is gauge-dependent. A gauge transformation of the instantaneous eigenstates corresponds to $|n(\mathbf{R})\rangle \to e^{i\xi(\mathbf{R})} |n(\mathbf{R})\rangle$, with $\xi(\mathbf{R})$ smooth and single-valued. As a consequence, $\mathbf{A}_n(\mathbf{R}) \to \mathbf{A}_n(\mathbf{R}) - \nabla_{\mathbf{R}} \xi(\mathbf{R})$ and, lastly, $\gamma_n \to \gamma_n - \int_{\mathcal{C}} d\mathbf{R} \cdot \nabla_{\mathbf{R}} \xi(\mathbf{R}) = \gamma_n - (\xi(\mathbf{R}_f) - \xi(\mathbf{R}_i))$.

However, if $\mathcal{C}$ is a closed curve and if we require the instantaneous eigenstates to be single-valued, it is easy to show that $\xi(\mathbf{R}_f) = \xi(\mathbf{R}_i) + 2m\pi$, $m \in \mathbb{Z}$, and the Berry phase is no longer gauge-dependent (and defined less than multiples of 2π). Keeping $\mathcal{C}$ as a closed path, and leveraging Stokes' theorem, we can rewrite

$$\begin{aligned}
\gamma_n &= -\mathrm{Im} \int_{\mathcal{C}} \langle n(\mathbf{R})| \nabla_{\mathbf{R}} |n(\mathbf{R})\rangle \cdot d\mathbf{R} = -\mathrm{Im} \int_{\partial S = \mathcal{C}} \nabla \times \langle n(\mathbf{R})| \nabla_{\mathbf{R}} |n(\mathbf{R})\rangle \, d\mathbf{S} \\
&= -\mathrm{Im} \int \epsilon_{ijk} \partial_j \langle n(\mathbf{R})| \partial_k |n(\mathbf{R})\rangle \, dS_i = -\mathrm{Im} \int \epsilon_{ijk} \langle \partial_j n(\mathbf{R}) | \partial_k n(\mathbf{R})\rangle \, dS_i \\
&= -\frac{1}{2} \mathrm{Im} \int \epsilon_{ijk} \left(\langle \partial_j n(\mathbf{R}) | \partial_k n(\mathbf{R})\rangle - \langle \partial_k n(\mathbf{R}) | \partial_j n(\mathbf{R})\rangle \right) dS_i. \qquad (1.23)
\end{aligned}$$

From the last expression, we can infer the definition of the Berry curvature.

Definition 1.1.3. *Berry curvature:* $\Omega_{jk} = i \left(\langle \partial_j n(\mathbf{R}) | \partial_k n(\mathbf{R})\rangle - \langle \partial_k n(\mathbf{R}) | \partial_j n(\mathbf{R})\rangle \right)$.

In conclusion

$$\gamma_n = -\frac{1}{2} \mathrm{Im} \int \epsilon_{ijk} \Omega_{jk} dS_i. \qquad (1.24)$$

We notice that the Berry curvature is evidently gauge-invariant. It will play a crucial role in the computation of the quantized conductance. In that case, the parameter space will be nothing but the Brillouin zone.

Computation of the Hall conductance

Now that we have introduced all the needed quantities, we can move on towards the demonstration of the quantized conductance [147]. This derivation is closely related to the Thouless adiabatic pump (1983). The interested reader can find more details in Ref. [177].

Suppose we have an insulating system in a magnetic field $\mathbf{B}$ arising from a vector potential $\mathbf{A}$. Under the hypothesis of independent electrons, the single-particle Hamiltonian reads as

$$H = \frac{1}{2m}\left(\mathbf{p} + e\mathbf{A}\right)^2 + V(\mathbf{r}), \tag{1.25}$$

where $V(\mathbf{r})$ is the periodic lattice potential. Due to the vector potential, the system is not translationally invariant anymore. However, it can be shown that it is possible to build a new kind of translation operators, called magnetic translation operators, and a new (reduced) Brillouin zone [106]. We do not delve into the details, and just tell that this allows to invoke an analogous of Bloch theorem and define a set of magnetic Bloch eigenfunctions with the same structure as the original ones:

$$\psi_{\mathbf{k}}(\mathbf{r}) = e^{i\mathbf{k}\cdot\mathbf{r}} u_{\mathbf{k}}(\mathbf{r}). \tag{1.26}$$

In order to compute the conductivity, we have to introduce an electric field. Let's then assume to apply a small and uniform electric field $\mathbf{E}$. As we don't want to spoil the magnetic Bloch eigenfunctions just introduced, we can refer it to a time-dependent vector potential

$$\mathbf{E} = -\partial_t \mathbf{A}_E(t) \Rightarrow \mathbf{A}_E(t) = -\mathbf{E}t. \tag{1.27}$$

For a continuous system, at the Hamiltonian level, the introduction of $\mathbf{A}_E(t)$ corresponds to the substitution

$$\mathbf{p} + e\mathbf{A} \to \mathbf{p} + e\left(\mathbf{A} + \mathbf{A}_E(t)\right) = \mathbf{p} + e\mathbf{A} + \mathbf{R}(t), \tag{1.28}$$

where $\mathbf{R}(t) \equiv \hbar\boldsymbol{k}(t) = -et\mathbf{E}$. It can be shown that, given the (magnetic) Bloch solution in Eq. (1.26) for $\boldsymbol{k} = 0$, $\psi_{\mathbf{k}}(\mathbf{r}) = e^{i\mathbf{k}\cdot\mathbf{r}} u_{\mathbf{k}+\boldsymbol{k}(t)}(\mathbf{r})$ is a solution for any $\boldsymbol{k}$. To recap,in order to maintain the translational invariance, it has been necessary to introduce a time-dependence in the Hamiltonian, $H \to H(\mathbf{R}(t))$.

If $|\mathbf{E}|$ is small, then $\dot{\mathbf{R}}$, which represents the electric force experienced by each electron, is also small. Recalling that the ground state is separated from the excited states by a gap (as we are considering an insulating system), the linear response to the electric field can be regarded as an adiabatic perturbation to the Hamiltonian. We don't draw here the derivation of the first correction to the adiabatic theorem, and just state the result [147, 177]. Let's suppose that, at the initial time, the system is in the instantaneous ground state $|\phi_0(t=0)\rangle$. The adiabatically evoluted state at time t is given by

$$|\Psi(t)\rangle = e^{i\gamma_0(t)} e^{-\frac{i}{\hbar}\int_0^t dt' E_0(t')} \left[|\phi_0(t)\rangle + i\hbar \sum_{n\neq 0} |\phi_n(t)\rangle \frac{\langle\phi_n(t)|\partial_t\phi_0(t)\rangle}{E_n(t) - E_0(t)} \right], \tag{1.29}$$

with $|\phi_n(t)\rangle$ the instantaneous eigenstates of $H(t)$, $E_n(t)$ their eigenenergies and

$$\gamma_n = i\int_0^t \langle\phi_0(\mathbf{R}(t'))|\, \nabla_{\mathbf{R}}\, |\phi_0(\mathbf{R}(t'))\rangle \cdot \frac{d\mathbf{R}(t')}{dt'} dt' \tag{1.30}$$

the Berry phase written in the form of Eq. (1.22).

The first quantity we need is the current operator associated to the problem. By using the Kohn approach, it can be proven that it reads as

$$\mathbf{J} = \frac{1}{\hbar}\frac{\partial H}{\partial \boldsymbol{k}} = \nabla_{\mathbf{R}} H(\mathbf{R}). \tag{1.31}$$

We now compute the average current on the state $|\Psi(t)\rangle$, at the first-order correction to the adiabatic theorem:

$$\begin{aligned}\langle\Psi(t)|\mathbf{J}|\Psi(t)\rangle &= \langle\phi_0(t)|\nabla_{\mathbf{R}} H(\mathbf{R}(t))|\phi_0(t)\rangle \\ &+ i\hbar\sum_{n\neq 0}\left[\frac{\langle\phi_0(t)|\nabla_{\mathbf{R}} H(\mathbf{R}(t))|\phi_n(t)\rangle\,\langle\phi_n(t)|\partial_t\phi_0(t)\rangle}{E_n(t)-E_0(t)} - c.c.\right].\end{aligned} \tag{1.32}$$

Some manipulations allow us to rewrite both addends conveniently:

1. The first term can be rewritten by using the Feynman-Hellmann theorem as $\langle\phi_0(t)|\nabla_{\mathbf{R}} H(\mathbf{R}(t))|\phi_0(t)\rangle = \nabla_{\mathbf{R}}\langle\phi_0(t)|H(\mathbf{R}(t))|\phi_0(t)\rangle = \nabla_{\mathbf{R}} E_0(\mathbf{R}(t))$.
2. In the second term, $\frac{\langle\phi_0(t)|\nabla_{\mathbf{R}} H(\mathbf{R}(t))|\phi_n(t)\rangle}{E_n(t)-E_0(t)} = -\langle\nabla_{\mathbf{R}}\phi_0(t)|\phi_n(t)\rangle$.

Substituting into Eq. (1.32), we get

$$\langle\Psi(t)|\mathbf{J}|\Psi(t)\rangle = \nabla_{\mathbf{R}} E_0(\mathbf{R}(t)) - i\hbar\sum_{n\neq 0}\left(\langle\nabla_{\mathbf{R}}\phi_0(t)|\phi_n(t)\rangle\,\langle\phi_n(t)|\partial_t\phi_0(t)\rangle - c.c.\right). \tag{1.33}$$

We notice that, for an insulating system, the first term is zero. Indeed, since all bands are either completely filled or completely empty, and $\mathbf{R}(t)$ simply boosts all the momenta, we have that the ground state energy is independent of that. Concerning the second term, we can safely include $n = 0$ into the sum, as

$$\langle\nabla_{\mathbf{R}}\phi_0(t)|\phi_0(t)\rangle\,\langle\phi_0(t)|\partial_t\phi_0(t)\rangle - c.c. = 0.$$

We obtain

$$\langle\Psi(t)|\mathbf{J}|\Psi(t)\rangle = -i\hbar\sum_{n}\left(\langle\nabla_{\mathbf{R}}\phi_0(t)|\phi_n(t)\rangle\,\langle\phi_n(t)|\partial_t\phi_0(t)\rangle - c.c.\right), \tag{1.34}$$

and lastly, rewriting $|\partial_t\phi_0\rangle = \frac{d\mathbf{R}}{dt}\cdot|\nabla_{\mathbf{R}}\phi_0\rangle = -e\mathbf{E}\cdot|\nabla_{\mathbf{R}}\phi_0\rangle$, we have

$$\langle\Psi(t)|J_\alpha|\Psi(t)\rangle = ie\hbar\sum_{\beta}\left[\langle\partial_\alpha\phi_0|\partial_\beta\phi_0\rangle - \langle\partial_\beta\phi_0|\partial_\alpha\phi_0\rangle\right]E_\beta. \tag{1.35}$$

Denoting by V the sample volume, the average current density is finally

$$J^e_\alpha = \frac{-e}{V}\langle\Psi(t)|J_\alpha|\Psi(t)\rangle = \sigma_{\alpha\beta}E_\beta, \tag{1.36}$$

from which

$$\sigma_{\alpha\beta} = \frac{-ie^2\hbar}{V}\left[\langle\partial_\alpha\phi_0|\partial_\beta\phi_0\rangle - \langle\partial_\beta\phi_0|\partial_\alpha\phi_0\rangle\right]\big|_{\mathbf{R}=0}. \tag{1.37}$$

As expected, $\sigma_{\alpha\alpha} = 0$: as we are dealing with an insulating system, there is no longitudinal current flow.

To conclude, we need to rewrite $\sigma_{\alpha\beta}$ in terms of the magnetic Bloch eigenfunctions. Since we are assuming the electrons to be independent from each other, the ground state at the initial time $t = 0$, in second quantization, is

$$|\phi_0(0)\rangle = \prod_n \prod_{\mathbf{k}} c^\dagger_{n,\mathbf{k}} |0\rangle , \tag{1.38}$$

where $c^\dagger_{n,\mathbf{k}}$ is the fermionic operator creating an electron with wavevector $\mathbf{k}$ in the n^{th} band, and $|0\rangle$ is the vacuum of the Fock space. Moreover, $\psi_{n,\mathbf{k}}(\mathbf{r}) = \langle \mathbf{r}|c^\dagger_{n,\mathbf{k}}|0\rangle$. The instantaneous ground state at time t is

$$|\phi_0(t)\rangle = \prod_n \prod_{\mathbf{k}} c^\dagger_{n,\mathbf{k}}(t) |0\rangle , \tag{1.39}$$

where, as we formerly discussed, $|\phi_0(t)\rangle = e^{i\mathbf{k}\cdot\mathbf{r}} u_{n,\mathbf{k}+\boldsymbol{k}(t)} = \langle \mathbf{r}|c^\dagger_{n,\mathbf{k}}(t)|0\rangle$. The instantaneous ground state has energy

$$E_0(t) = \sum_n \sum_{\mathbf{k}} \epsilon_{n,\mathbf{k}+\boldsymbol{k}(t)}. \tag{1.40}$$

As stated below Eq. (1.33), in the thermodynamic limit it doesn't depend on $\boldsymbol{k}$. Plugging Eq. (1.39) into the expression for the conductivity, we find

$$\sigma_{\alpha\beta} = \frac{-e^2\hbar}{V} \sum_n \sum_{\mathbf{k}} i \left[\langle \partial_{R_\alpha} \psi_{n,\mathbf{k}} | \partial_{R_\beta} \psi_{n,\mathbf{k}} \rangle - \langle \partial_{R_\beta} \psi_{n,\mathbf{k}} | \partial_{R_\alpha} \psi_{n,\mathbf{k}} \rangle \right] \Big|_{\mathbf{R}=0} . \tag{1.41}$$

The derivatives are given by

$$\partial_{R_\alpha} \psi_{n,\mathbf{k}} = \partial_{R_\alpha} e^{i\mathbf{k}\cdot\mathbf{r}} u_{n,\mathbf{k}+\mathbf{R}/\hbar} = \frac{1}{\hbar} e^{i\mathbf{k}\cdot\mathbf{r}} \partial_{k_\alpha} u_{n,\mathbf{k}+\mathbf{R}/\hbar}. \tag{1.42}$$

The term in parenthesis, evaluated at $\boldsymbol{k} = 0$ ($\mathbf{R} = 0$), becomes

$$\frac{1}{\hbar^2} \left[\langle \partial_{k_\alpha} u_{n,\mathbf{k}} | \partial_{k_\beta} u_{n,\mathbf{k}} \rangle - \langle \partial_{k_\beta} u_{n,\mathbf{k}} | \partial_{k_\alpha} u_{n,\mathbf{k}} \rangle \right] . \tag{1.43}$$

At this stage, the conductivity reads as

$$\sigma_{\alpha\beta} = \frac{-e^2}{\hbar} \frac{1}{V} \sum_n \sum_{\mathbf{k}} i \left[\langle \partial_{k_\alpha} u_{n,\mathbf{k}} | \partial_{k_\beta} u_{n,\mathbf{k}} \rangle - \langle \partial_{k_\beta} u_{n,\mathbf{k}} | \partial_{k_\alpha} u_{n,\mathbf{k}} \rangle \right] . \tag{1.44}$$

In the thermodynamic limit, the sum is replaced by an integral over the first Brillouin zone. For a two-dimensional $\mathbf{k}$-space (on which we will focus in the following),

$$\begin{aligned} \sigma_{\alpha\beta} =& \frac{-e^2}{\hbar} \frac{1}{(2\pi)^2} \sum_n \int d\mathbf{k}^2 i \left[\langle \partial_{k_\alpha} u_{n,\mathbf{k}} | \partial_{k_\beta} u_{n,\mathbf{k}} \rangle - \langle \partial_{k_\beta} u_{n,\mathbf{k}} | \partial_{k_\alpha} u_{n,\mathbf{k}} \rangle \right] \\ =& \frac{-e^2}{h} \sum_n c_n, \end{aligned} \tag{1.45}$$

with c_n the Chern number associated to the n^{th} band.

Definition 1.1.4. *Chern number:* $c_n = \frac{1}{2\pi} \int d\mathbf{k}^2 i \left[\langle \partial_{k_\alpha} u_{n,\mathbf{k}} | \partial_{k_\beta} u_{n,\mathbf{k}} \rangle - \langle \partial_{k_\beta} u_{n,\mathbf{k}} | \partial_{k_\alpha} u_{n,\mathbf{k}} \rangle \right]$.

Quantization of the Chern number

The last part of this discussion aims at proving that the Chern number can only take integer values. This will finally imply the quantization of the conductance.

The Chern number is given by the integration of the Berry curvature, which is gauge-independent, over the Brillouin zone. The latter, due to periodic boundary conditions, is a thorus. We will denote it as T^2_{BZ}. We have previously derived the Berry curvature as the rotor of the Berry connection. If it were possible to have $\mathbf{A}$ smoothly defined over all the Brillouin zone, by switching to its line integral over the Brillouin zone contour, we would obtain a zero Chern number. The point is that, for topologically non-trivial systems, a gauge such that the Berry connection is well defined over the entire Brillouin zone doesn't exist. A non-zero Chern number is precisely a sign of hurdle in the application of Stokes' theorem.

We have seen that the Berry connection is modified by a gauge-transformation as

$$\mathbf{A}_n(\mathbf{k}) \to \mathbf{A}_n(\mathbf{k}) - \nabla_{\mathbf{k}}\xi(\mathbf{k}), \tag{1.46}$$

where n labels the instantaneous eigenstates basis $|u_{n,\mathbf{k}}\rangle$. Let us suppose that we couldn't find a gauge such that $|u_{n,\mathbf{k}}\rangle$ is smooth and well defined over all the Brillouin zone. On the contrary, let us assume that $|u_{n,\mathbf{k}}\rangle$ has a singularity at $\mathbf{k} = \tilde{\mathbf{k}}$. We consider a small region $R^{\epsilon}_{\tilde{\mathbf{k}}}$ sorrounding such point, $R^{\epsilon}_{\tilde{\mathbf{k}}} = \{\mathbf{k} \in T^2_{BZ} : |\mathbf{k}-\tilde{\mathbf{k}}| < \epsilon\}$, and choose a second gauge such that the wavefunction is there well defined. In particular

$$\mathbf{k} \in R^{\epsilon}_{\tilde{\mathbf{k}}}: \quad |u_{n,\mathbf{k}}\rangle' = e^{i\xi(\mathbf{k})}\,|u_{n,\mathbf{k}}\rangle\,. \tag{1.47}$$

On the boundary of R^{ϵ}, ∂R^{ϵ}, both gauges are well defined, and the corresponding Berry connections $\mathbf{A}_n(\mathbf{k})$ and $\mathbf{A}'_n(\mathbf{k})$ differ by the quantity $\nabla_{\mathbf{k}}\xi(\mathbf{k})$. While computing the Chern number, we have to split the integration:

$$\begin{aligned} c_n &= \frac{1}{2\pi}\left(\int_{T^2_{BZ}-R^{\epsilon}_{\tilde{\mathbf{k}}}} \nabla\times\mathbf{A}_n(\mathbf{k})d^2\mathbf{k} + \int_{R^{\epsilon}_{\tilde{\mathbf{k}}}} \nabla\times\mathbf{A}'_n(\mathbf{k})d^2\mathbf{k}\right) \\ &= \frac{1}{2\pi}\oint_{\partial R^{\epsilon}_{\tilde{\mathbf{k}}}} (\mathbf{A}'_n(\mathbf{k}) - \mathbf{A}_n(\mathbf{k}))\cdot d\mathbf{k} = -\frac{1}{2\pi}\oint_{\partial R^{\epsilon}_{\tilde{\mathbf{k}}}} \nabla_{\mathbf{k}}\xi(\mathbf{k})\cdot d\mathbf{k} \\ &= \frac{1}{2\pi}\left(\xi(0) - \xi(2\pi)\right), \end{aligned} \tag{1.48}$$

where in the last step we have parametrized $\partial R^{\epsilon}_{\tilde{\mathbf{k}}}$ with $\mathbf{k}(\theta) = \tilde{\mathbf{k}} + \epsilon(\cos(\theta), \sin\theta)$. For any gauge choice, the wavefunction has to be single-valued, whence

$$|u_{n,\mathbf{k}(\theta=2\pi)}\rangle' = |u_{n,\mathbf{k}(\theta=0)}\rangle'\,, \qquad |u_{n,\mathbf{k}(\theta=2\pi)}\rangle = |u_{n,\mathbf{k}(\theta=0)}\rangle\,. \tag{1.49}$$

This allows to conclude

$$\xi(\mathbf{k}(0)) - \xi(\mathbf{k}(2\pi)) = 2m\pi,\ m \in \mathbb{Z}, \tag{1.50}$$

and that the Chern number in Eq. (1.48) is quantized to integer numbers.

To summarize, throughout this Subsection we have demonstrated that the Hall conductance is quantized to integer multiples of e^2/h, which is the conductance quantum. Being quantized, it is not spoiled by small perturbations of the system. As long as our

assumptions hold, the Chern number cannot change. On the other hand, if our hypotheses are violated and the sysyem is drastically perturbed (for instance, the gap closes and reopens), the Chern number is not robust anymore. In the next Subsection, in the context of the Haldane model, we will see that a non-zero Chern number, for a finite-size system, is associated to metallic edge states having energies within the energy gap.

1.1.3 Haldane lattice model

So far, we have introduced the Quantum Hall Effect and its stunning properties. The dissipationless current flow and the robustness of the boundary states with respect to disorder and perturbations are highly promising in view of technological applications. However, such appeal is somehow weakened by the need for strong magnetic fields. The quest for more convenient experimental platforms started soon.

In this Subsection, we will show that it is possible to reproduce the physics of the Quantum Hall Effect even in the absence of a net magnetic field. At least for spinless systems, in order to have a non-zero Chern number (and hence protected boundary states), it is sufficient to break time-reversal symmetry. Such symmetry breaking, in the original setup, was guaranteed by the magnetic field.

To this regard, in 1988, F. D. M. Haldane proposed a two-dimensional, honeycomb lattice model with nearest- and next-to nearest-neighbor hopping amplitudes [80]. Moreover, a magnetic field with the lattice periodicity and symmetry (and thus with no net magnetic flux through the unitary cell) was included. Such model represents a precursor of the so-called Quantum Anomalous Hall Effect, and attracted renewed interest starting from 2004, when it was realized that graphene could accommodate its experimental realization. In what follows, we analyze the Haldane model. Some of graphene properties will be discussed in the next Section.

Time-reversal symmetry for spinless systems

First of all, we prove that a system of spinless particles requires time-reversal symmetry breaking to have a non-zero Chern number. For a spinless particle, it can be derived that the time-reversal operator $\mathcal{T}$ simply acts on the states as the complex conjugation operator $\mathcal{K}$. More generally, in presence of other degrees of freedom such as spin, $\mathcal{T} = U\mathcal{K}$ with U a unitary operator. Hence $\mathcal{T}^2 = \pm 1$ (for spinless systems, $\mathcal{T}^2 = 1$). Let us consider a spinless lattice system, and let c_i be the fermionic operator which destroys a particle on the i-th site. Since we have discrete translational invariance, by imposing periodic boundary conditions we can define the Fourier-transformed operator

$$c_i = \frac{1}{\sqrt{N}} \sum_{\mathbf{k}} e^{i\mathbf{k}\cdot\mathbf{R}_i} c_{\mathbf{k}}, \tag{1.51}$$

with N the number of cells and the sum running over the first Brillouin zone. It is straightforward to check

$$\mathcal{T} c_i \mathcal{T}^{-1} = c_i, \tag{1.52}$$

namely the creation and annihilation operators on each site are invariant under time-reversal. Moreover, for the Fourier-transformed operators

$$\mathcal{T} c_{\mathbf{k}} \mathcal{T}^{-1} = c_{-\mathbf{k}}. \tag{1.53}$$

Let $H = \sum_{\mathbf{k}} c^\dagger_{\mathbf{k}} h(\mathbf{k}) c_{\mathbf{k}}$ be a time-reversal invariant Hamiltonian, such that

$$[H, \mathcal{T}] = 0 \Rightarrow \mathcal{T} H \mathcal{T}^{-1} = H. \tag{1.54}$$

Making use of Eq. (1.53), it is easy to show that

$$\mathcal{T} h(\mathbf{k}) \mathcal{T}^{-1} = h(-\mathbf{k}). \tag{1.55}$$

Then, if $\psi(\mathbf{k})$ is an eigenstate of $h(\mathbf{k})$ with energy $\epsilon(\mathbf{k})$, we find

$$h(\mathbf{k})\psi(\mathbf{k}) = h(\mathbf{k})\mathcal{T}^{-1}\mathcal{T}\psi(\mathbf{k}) = \epsilon(\mathbf{k})\psi(\mathbf{k}) \Rightarrow h(-\mathbf{k})\mathcal{T}\psi(\mathbf{k}) = \epsilon(\mathbf{k})\mathcal{T}\psi(\mathbf{k}), \tag{1.56}$$

which means that $\mathcal{T}\psi(\mathbf{k}) = \psi^*(\mathbf{k})$ is an eigenstate of $h(-\mathbf{k})$ with energy $\epsilon(\mathbf{k})$ as well.

Let us now compute the Berry curvature for a spinless, time-reversal invariant system. For simplicity, we consider a single filled band with Bloch states $|u(\mathbf{k})\rangle$:

$$\Omega_{ij}(-\mathbf{k}) = i \left(\langle \partial_i u(-\mathbf{k}) | \partial_j u(-\mathbf{k}) \rangle - \langle \partial_j u(-\mathbf{k}) | \partial_i u(-\mathbf{k}) \rangle \right), \tag{1.57}$$

and by expanding on a basis $|u_n(\mathbf{k})\rangle$, we get

$$\begin{aligned} \Omega_{ij}(-\mathbf{k}) =& i \sum_n \left(\langle \partial_i u_n(-\mathbf{k}) | \partial_j u_n(-\mathbf{k}) \rangle - \langle \partial_j u_n(-\mathbf{k}) | \partial_i u_n(-\mathbf{k}) \rangle \right) \\ =& - i \sum_n \left(\langle \partial_i u_n(\mathbf{k}) | \partial_j u_n(\mathbf{k}) \rangle - \langle \partial_j u_n(\mathbf{k}) | \partial_i u_n(\mathbf{k}) \rangle \right) \\ =& - \Omega_{ij}(\mathbf{k}). \end{aligned} \tag{1.58}$$

The integration of the Berry curvature over the Brillouin zone returns 0. In order to see effects related to the Berry phase, time-reversal symmetry breaking is hence necessary. Given this premise, we are now ready to introduce and discuss the Haldane model.

Nearest neighbor hopping

Let us consider a two-dimensional system with honeycomb lattice of lattice constant a. It is described by a rhombic Bravais lattice and a basis with two atoms per cell. We can identify two sublattices A and B, marked in Fig. 1.4 by empty and filled dots. Two primitive vectors can be chosen among

$$\mathbf{v}_1 = \sqrt{3} a \mathbf{e}_1, \quad \mathbf{v}_2 = \frac{\sqrt{3}}{2} a \mathbf{e}_1 + \frac{3}{2} a \mathbf{e}_2, \quad \mathbf{v}_3 = -\frac{\sqrt{3}}{2} a \mathbf{e}_1 + \frac{3}{2} a \mathbf{e}_2. \tag{1.59}$$

We will use $\mathbf{v}_2$ and $\mathbf{v}_3$. Notice that nearest neighbors, separated by the distance a, belong to different sublattices, and that $\mathbf{v}_2 - \mathbf{v}_3 = \mathbf{v}_1$. We also introduce the vectors which link a site of sublattice A to its nearest neighbors belonging to sublattice B:

$$\mathbf{d}_1 = \frac{\sqrt{3}}{2} a \mathbf{e}_1 + \frac{1}{2} a \mathbf{e}_2, \quad \mathbf{d}_2 = -\frac{\sqrt{3}}{2} a \mathbf{e}_1 + \frac{1}{2} a \mathbf{e}_2, \quad \mathbf{d}_3 = -a \mathbf{e}_2. \tag{1.60}$$

The first term we include in the Hamiltonian is a hopping term between nearest neighbor sites:

$$H_{nn} = -t \sum_i \left(a^\dagger_i b_{i+\mathbf{d}_1} + a^\dagger_i b_{i+\mathbf{d}_2} + a^\dagger_i b_{i+\mathbf{d}_3} \right) + h.c. \tag{1.61}$$

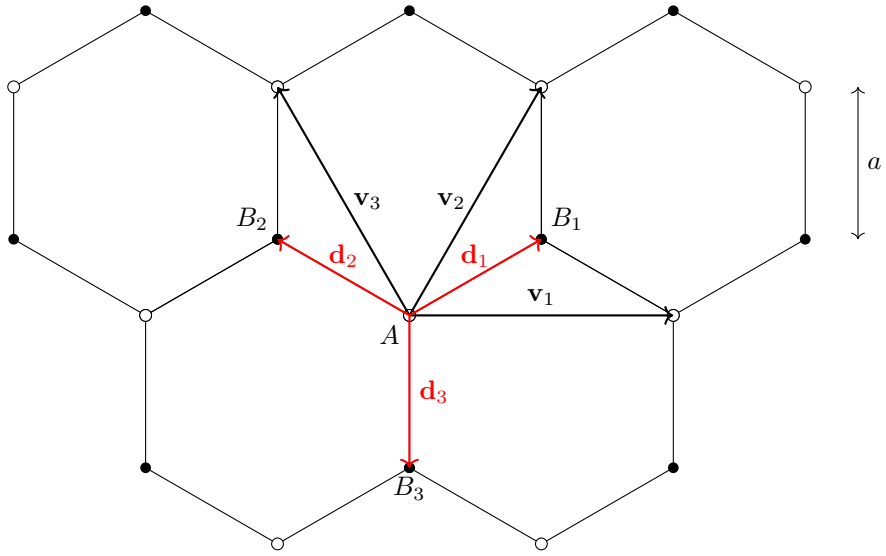

Figure 1.4: *Honeycomb lattice of the Haldane model. The two sublattices, denoted by A and B, are identified with empty and filled dots, respectively. The vectors $\mathbf{v}_i$, $i = 1, 2, 3$ are also shown. Any couple of them identifies the primitive cell, whose origin is set on a site of sublattice A. $\mathbf{d}_i$, $i = 1, 2, 3$ are the vectors linking a A site to its three nearest neighbor B sites.*

Here, i labels the cell identified by the vector $\mathbf{R_i} = m\mathbf{v}_2 + n\mathbf{v}_3$, $m, n \in \mathbb{Z}$. For our choice of coordinates, $\mathbf{R_i}$ points to a site of sublattice A. We denote by $a_i^\dagger (b_{i\mathbf{d}_j}^\dagger,\ j \in \{1, 2, 3\}$) the creation operator of a spinless fermion at position $\mathbf{R_i}$ ($\mathbf{R_i} + \mathbf{d}_j$) of sublattice $A(B)$. We choose to characterize the position of sublattice B sites as, for instance, $\mathbf{R_i}^B = \mathbf{R_i} + \mathbf{d}_3$.

We are ultimately interested in solving the problem, namely in diagonalizing the Hamiltonian. To do so, we have to move to $\mathbf{k}$-space. As done before, we impose periodic boundary conditions and Fourier-transform the fermionic operators. We choose the following convention

$$\begin{aligned} a(\mathbf{k}) &= \sum_j e^{i\mathbf{k}\cdot\mathbf{R}_j} a_j, & b(\mathbf{k}) &= \sum_j e^{i\mathbf{k}\cdot\mathbf{R}_j} b_j \\ a_j &= \int_{\mathbf{k}\in BZ} e^{-i\mathbf{k}\cdot\mathbf{R}_j} a(\mathbf{k}), & b_j &= \int_{\mathbf{k}\in BZ} e^{-i\mathbf{k}\cdot\mathbf{R}_j} b(\mathbf{k}), \end{aligned} \tag{1.62}$$

where the integral has to be intended as a two-dimensional integration over the Brillouin zone. Moreover, we notice that for the b operators we center the Fourier-transform on the origin of the primitive cell $\mathbf{R}_j$ and not on the site as in the original paper. For our purposes, this is a legitimate choice. To summarize, the three nearest neighbor B sites of the A_j site belong to three different cells, with origins in $\mathbf{R}_j$, $\mathbf{R}_j + \mathbf{v}_2$, $\mathbf{R}_j + \mathbf{v}_3$.

By substitution of Eq. (1.62) into Eq. (1.61), we get

$$\begin{aligned} H_{nn} = -t \int\int \sum_j \big[& e^{i\mathbf{k}\cdot\mathbf{R}_j} e^{-i\mathbf{k}'\cdot\mathbf{R}_j} + e^{i\mathbf{k}\cdot\mathbf{R}_j} e^{-i\mathbf{k}'\cdot(\mathbf{R}_j+\mathbf{v}_2)} \\ & + e^{i\mathbf{k}\cdot\mathbf{R}_j} e^{-i\mathbf{k}'\cdot(\mathbf{R}_j+\mathbf{v}_3)} \big] a^\dagger(\mathbf{k}) b(\mathbf{k}') + h.c. \end{aligned} \tag{1.63}$$

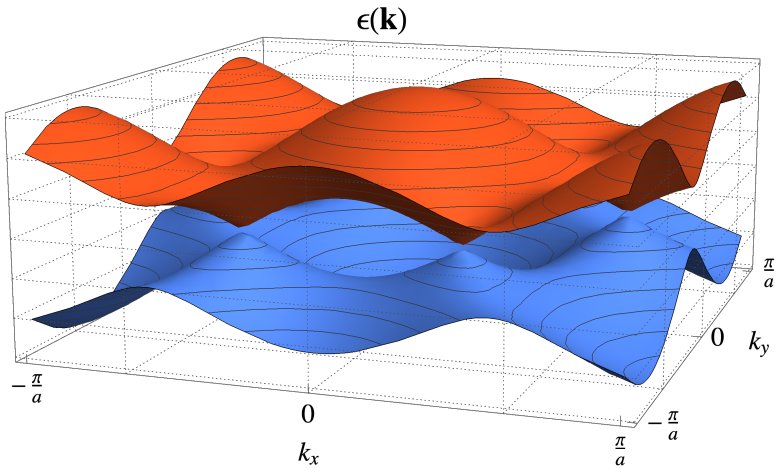

Figure 1.5: *Dispersion relation in Eq. (1.67) over the first Brillouin zone. The gap closes at the Dirac points, and has a linear dispersion around them.*

Recalling that $\sum_j e^{i(\mathbf{k}-\mathbf{k}')\cdot\mathbf{R}_j} = \delta_{\mathbf{k},\mathbf{k}'}$, we can simplify the previous equation as

$$H_{nn} = -t\int_{\mathbf{k}\in BZ}\left[1+e^{-i\mathbf{k}\cdot\mathbf{v}_2}+e^{-i\mathbf{k}\cdot\mathbf{v}_3}\right]a^\dagger(\mathbf{k})b(\mathbf{k})+h.c. = \int_{\mathbf{k}\in BZ} H^{\mathbf{k}}_{nn}, \tag{1.64}$$

with

$$H^{\mathbf{k}}_{nn} = -t\left[f(\mathbf{k})a^\dagger(\mathbf{k})b(\mathbf{k})+f^*(\mathbf{k})b^\dagger(\mathbf{k})a(\mathbf{k})\right], \tag{1.65}$$

being $f(\mathbf{k}) = 1+e^{-i\mathbf{k}\cdot\mathbf{v}_2}+e^{-i\mathbf{k}\cdot\mathbf{v}_3}$. Choosing the basis $(a_\mathbf{k}, b_\mathbf{k})^T$, we can rewrite

$$H^{\mathbf{k}}_{nn} = -t(a^\dagger_\mathbf{k}, b^\dagger_\mathbf{k})\begin{pmatrix}0 & f(\mathbf{k})\\ f^*(\mathbf{k}) & 0\end{pmatrix}\begin{pmatrix}a_\mathbf{k}\\ b_\mathbf{k}\end{pmatrix}. \tag{1.66}$$

We started from an $N\times N$ matrix and end up with a 2×2 matrix to be diagonalized. The diagonalization returns

$$\epsilon(\mathbf{k}) = \pm t|f(\mathbf{k})| = \pm t\sqrt{3+2\sum_{i=1}^{3}\cos\left(\mathbf{k}\cdot\mathbf{v}_i\right)}. \tag{1.67}$$

This dispersion relation for the first Brillouin zone is depicted in Fig. 1.5. It is clearly visible that around the zero-energy points it has a linear behavior, originating the famous Dirac cones. Such zero-energy points are given by

$$|f(\mathbf{k})| = 0 \Leftrightarrow \begin{cases}\mathrm{Re}\{f(\mathbf{k})\} = 0 = 1+\cos\left(\mathbf{k}\cdot\mathbf{v}_2\right)+\cos\left(\mathbf{k}\cdot\mathbf{v}_3\right)\\ \mathrm{Im}\{f(\mathbf{k})\} = 0 = -\sin\left(\mathbf{k}\cdot\mathbf{v}_2\right)+\sin\left(\mathbf{k}\cdot\mathbf{v}_3\right)\end{cases} \tag{1.68}$$

We observe that the reciprocal lattice basis vectors, which we denote by $\tilde{\mathbf{v}}_2$ and $\tilde{\mathbf{v}}_3$, and satisfy $\tilde{\mathbf{v}}_i\cdot\mathbf{v}_j = 2\pi\delta_{ij},\ i,j\in\{1,2,3\}$, help us to construct the solutions. It can indeed be verified they are[3]

[3]More precisely, this is just one of three possible choices, shown in Fig. 1.6 Indeed, $\mathbf{k}^{\pm 1}$ are located at two of the six vertices of the Brillouin zone. Each of them is equivalent to two of the others, since they differ by an integer multiples of the primitive reciprocal lattice vectors.

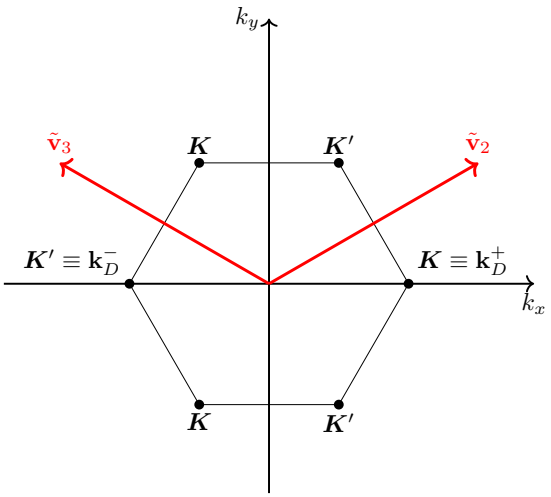

Figure 1.6: *First Brillouin zone, with the reciprocal lattice basis vectors. The chosen Dirac points* $\mathbf{k}_D^\xi$ *are also shown.*

$$\mathbf{k}^\xi = \xi \frac{\tilde{\mathbf{v}}_2 - \tilde{\mathbf{v}}_3}{3}, \; \xi = \pm 1. \tag{1.69}$$

Moreover, $\sum_{i=1}^{3} \cos\left(\mathbf{k}^\xi \cdot \mathbf{v}_i\right) = -3/2$, which in fact cancels the squareroot in Eq. (1.67). The special points just found are named Dirac points, and often denoted by $\mathbf{k}_D^\xi$. The index ξ is called valley isospin.

Next-nearest neighbor hopping

The second term to be included in the Hamiltonian is the next-nearest neighbor hopping, which we will denote as H_{nnn}. This term is made of a real term of next-nearest neighbor hopping and a local magnetic field $\mathbf{B}(\mathbf{r})$ directed perpendicularly to the two-dimensional lattice. As we anticipated, $\mathbf{B}(\mathbf{r})$ has the lattice periodicity and symmetry, and thus a zero net magnetic flux through the unitary cell. The latter property allows to choose a periodic vector potential $\mathbf{A}(\mathbf{r})$. It can be shown [20] that the presence of $\mathbf{A}(\mathbf{r})$ modifies the hopping amplitude as $t \to te^{i(e/\hbar)\int \mathbf{A}\cdot d\mathbf{r}} \equiv te^{i\phi}$. Such replacement is the so-called Peierls substitution. The integration has to be performed along the hopping path. Any closed path made of nearest neighbor hoppings encloses the unitary cell, hence H_{nn} is unchanged by the Peierls substitution. On the other hand, the hopping amplitude t' of H_{nnn} acquires a complex phase. Let us analyze its consequences.

We have

$$\begin{aligned} H_{nnn} = &- t' e^{i\phi} \sum_i \left(a_i^\dagger a_{i+\mathbf{v}_1} + a_{i+\mathbf{v}_1}^\dagger a_{i+\mathbf{v}_2} + a_{i+\mathbf{v}_2}^\dagger a_i \right) \\ &- t' e^{-i\phi} \sum_i \left(b_i^\dagger b_{i+\mathbf{v}_1} + b_{i+\mathbf{v}_1}^\dagger b_{i+\mathbf{v}_2} + b_{i+\mathbf{v}_2}^\dagger b_i \right) + h.c. \end{aligned} \tag{1.70}$$

The next-nearest neighbor hopping occurs within sites of a same sublattice, A or B. Each line of Eq. (1.70) describes the hopping of an electron across sites of one sublattice, with an associated phase $e^{\pm i\phi}$ having opposite sign for the two sublattices. This

complex phase and its sign are crucial, since they chiralize the problem provoking time-reversal symmetry breaking.

In order to diagonalize $H = H_{nn} + H_{nnn}$, we have to rewrite H_{nnn} in **k**-space. Differently from H_{nn}, we skip the full calculation. We find

$$H^{\mathbf{k}}_{nnn} = -2t'(a^\dagger_{\mathbf{k}}, b^\dagger_{\mathbf{k}}) \begin{pmatrix} \cos\phi C(\mathbf{k}) + \sin\phi S(\mathbf{k}) & 0 \\ 0 & \cos\phi C(\mathbf{k}) - \sin\phi S(\mathbf{k}) \end{pmatrix} \begin{pmatrix} a_{\mathbf{k}} \\ b_{\mathbf{k}} \end{pmatrix} \tag{1.71}$$

where

$$C(\mathbf{k}) = \cos(\mathbf{k}\cdot\mathbf{v}_1) + \cos(\mathbf{k}\cdot\mathbf{v}_2) + \cos(\mathbf{k}\cdot\mathbf{v}_3), \tag{1.72}$$
$$S(\mathbf{k}) = \sin(\mathbf{k}\cdot\mathbf{v}_1) - \sin(\mathbf{k}\cdot\mathbf{v}_2) + \sin(\mathbf{k}\cdot\mathbf{v}_3). \tag{1.73}$$

The full Hamiltonian $H = H_{nn} + H_{nnn}$ can be recast as

$$H = (a^\dagger_{\mathbf{k}}, b^\dagger_{\mathbf{k}})[H_0\sigma_0 + \boldsymbol{H}(\mathbf{k})\cdot\boldsymbol{\sigma}] \left(a_{\mathbf{k}}, b_{\mathbf{k}}\right)^T, \tag{1.74}$$

with

$$H_0(\mathbf{k}) = -2t'\cos\phi C(\mathbf{k}), \tag{1.75a}$$
$$H_x(\mathbf{k}) = -t[1 + \cos(\mathbf{k}\cdot\mathbf{v}_2) + \cos(\mathbf{k}\cdot\mathbf{v}_3)], \tag{1.75b}$$
$$H_y(\mathbf{k}) = -t[\sin(\mathbf{k}\cdot\mathbf{v}_2) + \sin(\mathbf{k}\cdot\mathbf{v}_3)], \tag{1.75c}$$
$$H_z(\mathbf{k}) = -2t'\sin\phi S(\mathbf{k}). \tag{1.75d}$$

Here σ_0 is the 2×2 identity matrix and σ_i are the Pauli matrices. Being proportional to the identity, the first term in Eq. (1.74) can be neglected for the calculation of eigenvalues and eigenvectors[4].

Being written in terms of the Pauli matrices, the Hamiltonian in Eq. (1.74) is the one of a two-level system. The diagonalization for a generic such Hamiltonian goes as follows. We have

$$\boldsymbol{H}(\mathbf{k})\cdot\boldsymbol{\sigma} = \begin{pmatrix} H_z & H_x - iH_y \\ H_x + iH_y & -H_z \end{pmatrix}, \tag{1.76}$$

with the associated eigenvalue equation

$$(\epsilon - H_z)(\epsilon + H_z) - (H_x - iH_y)(H_x + iH_y) = 0 \Rightarrow \epsilon = \pm\sqrt{H_x^2 + H_y^2 + H_z^2}. \tag{1.77}$$

Restoring the contribution we previously neglected:

$$\epsilon(\mathbf{k}) = H_0(\mathbf{k}) \pm \sqrt{H_x^2(\mathbf{k}) + H_y^2(\mathbf{k}) + H_z^2(\mathbf{k})}. \tag{1.78}$$

Given the expressions in Eq. (1.75), we have hence access to the energy spectrum. In the last equation, the sum $H_x^2(\mathbf{k}) + H_y^2(\mathbf{k})$ represents the contribution of H_{nn}, explicitly

$$H_x^2(\mathbf{k}) + H_y^2(\mathbf{k}) = t^2|f(\mathbf{k})|^2 = t^2\left[3 + 2\sum_{i=1}^{3}\cos(\mathbf{k}\cdot\mathbf{v}_i)\right], \tag{1.79}$$

[4]To do so, we have to assume that such term does not introduce any degeneracies. This holds as true for $|t'/t| < 3$.

where we used Eq. (1.67). The gap-closing points are given by

$$H_x^2(\mathbf{k}) + H_y^2(\mathbf{k}) + H_z^2(\mathbf{k}) = 0. \tag{1.80}$$

This requires, for sure, $H_x^2(\mathbf{k}) + H_y^2(\mathbf{k}) = 0$, which is satisfied by $\mathbf{k}_D^\xi$, $\xi = \pm 1$ as shown before ($f(\mathbf{k}_D^\xi) = 0$). Maintaining our former choice $\mathbf{k}_D^\xi = \xi(\tilde{\mathbf{v}}_2 - \tilde{\mathbf{v}}_3)/3$, we have

$$C(\mathbf{k}_D^\xi) = \cos(\xi\frac{4\pi}{3}) + \cos(\xi\frac{2\pi}{3}) + \cos(-\xi\frac{2\pi}{3}) = -\frac{3}{2}, \tag{1.81}$$

$$S(\mathbf{k}_D^\xi) = \sin(\xi\frac{4\pi}{3}) - \sin(\xi\frac{2\pi}{3}) + \sin(-\xi\frac{2\pi}{3}) = -3\xi\frac{\sqrt{3}}{2}. \tag{1.82}$$

Finally,

$$\epsilon^\lambda(\mathbf{k}_D^\xi) = 3t'\cos\phi + \lambda 3\sqrt{3}t'\sin\phi, \tag{1.83}$$

where $\lambda = \pm 1$ labels the two bands, and $\phi \in [0, \pi]$. The two bands are separated by a gap $\epsilon^{+1}(\mathbf{k}_D^\xi) - \epsilon^{-1}(\mathbf{k}_D^\xi) = 6\sqrt{3}t'\sin\phi$. A gap-closing is only allowed by $\phi = \{0, \pi\}$, namely if the next-nearest neighbor hopping amplitude is purely real. Any other value of ϕ is responsible for a gap-opening, maximized by a purely imaginary hopping amplitude ($\phi = \pi/2$). By looking at Eq. (1.75), we can hence conclude that the term responsible for the transition from a semimetal to an insulating dispersion relation is $H_z \propto \sigma_z$.

At zero temperature, only the lower band is filled. Concerning the Bloch eigenstates of the generic two-level system of Eq. (1.74) it can be verified that for the lower band they read as

$$u = \begin{pmatrix} H_z - |\boldsymbol{H}| \\ H_x + iH_y \end{pmatrix}, \tag{1.84}$$

with eigenvalues $-|\boldsymbol{H}|$. Moreover, their modulus squared is

$$|u|^2 = 2|\boldsymbol{H}|(|\boldsymbol{H}| - H_z), \tag{1.85}$$

which equals zero for $|\boldsymbol{H}| = H_z$. For the Haldane model, this corresponds to

$$\begin{aligned} &H_x^2(\mathbf{k}) + H_y^2(\mathbf{k}) + H_z^2(\mathbf{k}) = H_z^2(\mathbf{k}),\ H_z > 0 \\ &\Rightarrow \begin{cases} H_x^2(\mathbf{k}) + H_y^2(\mathbf{k}) = 0 \\ H_z > 0 \Rightarrow -2t'\sin\phi S(\mathbf{k}) = \xi 3\sqrt{3}t'\sin\phi > 0 \end{cases} \\ &\Leftrightarrow \mathbf{k} = \mathbf{k}_D^{+1}. \end{aligned} \tag{1.86}$$

To summarize, within the first Brillouin zone, the Bloch eigenstate $u(\mathbf{k})$ of the lower band of the Haldane model has zero norm at the Dirac point $\mathbf{k}_D^{+1}$.

As formerly discussed when presenting the Berry phase, we can always multiply u by a phase factor:

$$u' = e^{-i\varphi}u. \tag{1.87}$$

By choosing

$$e^{-i\varphi} = \frac{H_z + |\boldsymbol{H}|}{H_x + iH_y}\left|\frac{H_z + |\boldsymbol{H}|}{H_x + iH_y}\right|^{-1}, \tag{1.88}$$

we obtain

$$|u'|^2 = 2|\boldsymbol{H}|(H_z + |\boldsymbol{H}|). \tag{1.89}$$

It can be easily checked that in this case the norm equals zero at $\mathbf{k}_D^{-1}$. This suggests that there might be not a well defined gauge over all the Brillouin zone. If this were true, from the Chern number quantization discussion, we know that the Chern number would be different from 0.

Competing masses in the Haldane model

Now that we have understood that the Hamiltonian term responsible for the gap opening is the one proportional to σ_z, it is clear that any other added term $\propto \sigma_z$ would play the same game. Let's add an (on site) chemical potential term to the Hamiltonian,

$$H_\mu = \mu \sum_i \left(a_i^\dagger a_i - b_i^\dagger b_i \right), \tag{1.90}$$

which distinguishes the two sublattices and hence breaks inversion symmetry. In $\mathbf{k}$-space,

$$H_\mu^{\mathbf{k}} = (a_{\mathbf{k}}^\dagger, b_{\mathbf{k}}^\dagger) \begin{pmatrix} \mu & 0 \\ 0 & -\mu \end{pmatrix} \begin{pmatrix} a_{\mathbf{k}} \\ b_{\mathbf{k}} \end{pmatrix} = (a_{\mathbf{k}}^\dagger, b_{\mathbf{k}}^\dagger) \mu \sigma_z \left(a_{\mathbf{k}}, b_{\mathbf{k}} \right)^T, \tag{1.91}$$

proportional to σ_z as could be expected by the fact that it doesn't couple the two sublattices. In the complete Hamiltonian, this term will compete with $H_{nnn}^{\mathbf{k}}$ in opening the gap. Eq. (1.74) is unchanged except its z component, reading now as

$$H_z(\mathbf{k}) = -2t' \sin\phi S(\mathbf{k}) + \mu. \tag{1.92}$$

The energy spectrum is only modified by such replacement of $H_z(\mathbf{k})$. At the Dirac point, where we found the gap opening,

$$H_z(\mathbf{k}_\mathbf{D}^\xi) = -2t' \sin\phi S(\mathbf{k}_D^\xi) + \mu = \xi 3\sqrt{3} t' \sin\phi + \mu. \tag{1.93}$$

If $\mu = -\xi 3\sqrt{3} t' \sin\phi$, the gap at $\mathbf{k}_D^\xi$ is closed, while the other at $\mathbf{k}_D^{-\xi}$ remains open. As we anticipated and will be soon re-discussed, the competition of μ and t', by closing and reopening the gap, allows to switch from a zero to a non-zero Chern number.

Chern number in the Haldane model

We have now all we need to discuss the Chern number and the different topological phases in the Haldane model. In Eq. (1.84) we have introduced the Bloch eigenstate for the lower band of the Haldane model, normalized as

$$u = \frac{1}{\sqrt{2|\boldsymbol{H}|(|\boldsymbol{H}| - H_z)}} \begin{pmatrix} H_z - |\boldsymbol{H}| \\ H_x + iH_y \end{pmatrix}, \tag{1.94}$$

which has a singularity for $|\boldsymbol{H}| = H_z$ (recall that now H_z includes also the term $\propto \mu$). This condition might be satisfied only at $\mathbf{k} = \mathbf{k}_D^\xi$, provided that $H_z(\mathbf{k}_\mathbf{D}^\xi) = |H_z(\mathbf{k}_\mathbf{D}^\xi)|$, namely

$$\xi 3\sqrt{3} t' \sin\phi + \mu = |\xi 3\sqrt{3} t' \sin\phi + \mu|. \tag{1.95}$$

- For $\mu > 3\sqrt{3}t' \sin\phi > 0$, it is satisfied by both $\mathbf{k_D^{+1}}$ and $\mathbf{k_D^{-1}}$, which are hence both singularities for u.
- For $\mu < -3\sqrt{3}t' \sin\phi < 0$, it is satisfied by neither $\mathbf{k_D^{+1}}$ nor $\mathbf{k_D^{-1}}$. u is thus well defined over all the Brillouin zone. In this case, from previous discussions, we know that the Chern number is 0.

By operating a gauge transformation, we also introduced (again, after normalization)

$$u' = e^{-i\phi}u = \frac{1}{\sqrt{2|\boldsymbol{H}|(|\boldsymbol{H}| + H_z)}} \begin{pmatrix} -H_x + iH_y \\ H_z + |\boldsymbol{H}| \end{pmatrix}, \tag{1.96}$$

which has a singularity for $-|\boldsymbol{H}| = H_z$. In this case, for $\mu > 3\sqrt{3}t' \sin\phi$, u' has no singularities and we can conclude that the Chern number is again 0.

The last and most intriguing range to be inspected is $|\mu| < 3\sqrt{3}t' \sin\phi$. We could already expect $|\mu| > 3\sqrt{3}t' \sin\phi$ to be a trivial regime, since it is adiabatically connected to the atomic limit $|\mu| \to \infty$. In such limit, the hopping is suppressed and electrons are all localized, belonging either to atoms of type A or to atoms of type B (depending on which configuration corresponds to lower-energy), and no Hall conductance - and non-zero Chern number - is possible. If $|\mu| < 3\sqrt{3}t' \sin\phi$, the valley isospin ξ plays a crucial role. It is easy to check that, in particular, u is singular at $\mathbf{k} = \mathbf{k}_D^{+1}$ and u' is singular at $\mathbf{k} = \mathbf{k}_D^{-1}$.

We can follow the procedure described when we discussed the quantization of the Chern number: we consider a small region $R^{\epsilon}_{\mathbf{k}_D^{+1}}$ surrounding $\mathbf{k}_D^{+1}$ (and not containing $\mathbf{k}_D^{-1}$), within which we choose the gauge $\mathbf{A}' = \mathbf{A} - \nabla_{\mathbf{k}}\varphi$. We have

$$c = \frac{1}{2\pi} \oint_{\partial R^{\epsilon}_{\mathbf{k}_D^{+1}}} (\mathbf{A}'(\mathbf{k}) - \mathbf{A}(\mathbf{k})) \cdot d\mathbf{k} = ... = 1. \tag{1.97}$$

We do not report here the calculation of the two Berry curvatures $\mathbf{A}$ and $\mathbf{A}'$ and just focus on the result. As long as $|\mu| < 3\sqrt{3}t' \sin\phi$, we have $c = 1$ and $\sigma_{xy} = e^2/\hbar$ from Eq. (1.45). We expect to have topologically protected boundary states, lying within the energy gap.

If $\phi \Rightarrow -\phi$, we essentially exchange the two Dirac points and the gauges chosen inside and outside $R^{\epsilon}_{\mathbf{k}_D^{+1}}$. As a consequence, c and σ_{xy} gain an extra sign as well. In Fig. 1.7 we finally draw the phase diagram of the Haldane model.

To conclude, it can be shown that via diagonalization of the full Haldane Hamiltonian for a finite-size system in the topological phase $c \neq 0$, one finds that there exist eigenenergies closing the gap, associated to c (metallic) chiral eigenstates located at the physical boundary of the system. This reproduces the physics we discussed for the Quantum Hall Effect. The gap closing and reopening marks a so-called topological phase transition, and the correspondence between bulk properties (a finite Chern number) and protected metallic states at the boundary is the bulk-boundary correspondence, a key-concept in topological phases of matter.

1.2 The Quantum Spin Hall Effect

The Quantum Hall state represented the first example of a topologically non-trivial state of matter, where the quantization of the Hall conductance is protected by a topo-

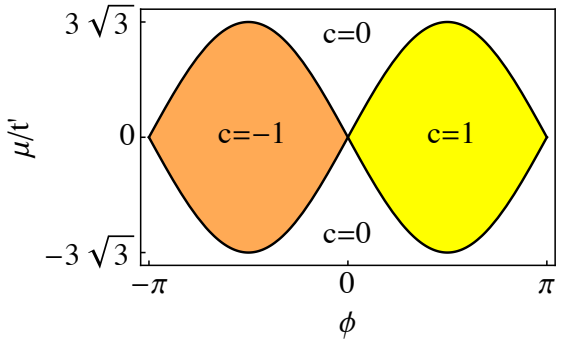

Figure 1.7: *Phase diagram of the Haldane model: the orange and yellow regions correspond to the topological phases with Chern number* $c = \pm 1$.

logical invariant. In this Section, we can now address the Quantum Spin Hall Effect, characterized by non-trivial topological properties similar to, but distinct from the Quantum Hall state. In this case not the Chern number, but a $\mathbb{Z}_2$ topological invariant marks it from a mathematical point of view. Physically, this new phase features couples of robust[5] counter-propagating helical channels at the boundary of a bulk-insulating sample. In Subsec. 1.2.1 we will present the (unfortunately, never implemented) Kane-Mele model, which devises a graphene-based platform to realize the Quantum Spin Hall Effect. Many concepts and results of the Haldane model will come in handy. In Subsec. 1.2.2 we will discuss a later Quantum Spin Hall model, by B. A. Bernevig, T. L. Hughes, and S.-C. Zhang, exploiting the peculiar band structure arising in CdTe/HgTe/CdTe quantum wells. In Subsec. 1.2.3 we will briefly review the first experimental evidencies of the effect and mention more recent achievements on the helical edge states. Subsec. 1.2.4 will revise how to engineer interesting properties in the Quantum Spin Hall Effect via the appropriate nanostructuring. Lastly, in Subsec. 1.2.4 we will mention some of its potential applications, with a focus on the realization of Majorana bound states.

1.2.1 Kane-Mele model

In this Subsection, we discuss the generalization of the Haldane model to a graphene sheet with spin-orbit coupling suggested by Kane and Mele in 2005 [95], which provided the theoretical basis for two-dimensional topological insulators. Spin-orbit coupling acts as two effective and opposite magnetic fields for opposite spins. Such model is hence, effectively, as two copies of Haldane model. In the present case, two metallic edge states appear in the bulk energy gap. Indeed, due to time-reversal symmetry (which is respected by spin-orbit coupling) and to Kramers' theorem, eigenstates come in doublets, and the two edge states are exactly Kramers' partners of each other. As we will discuss, thanks to Kramers' theorem they are protected from backscattering as long as time-reversal symmetry is preserved, giving rise to a symmetry protected topological phase. Lastly, electrons with opposite spin turn out to propagate in opposite directions: this property is often referred to as spin-momentum locking. These edge states originate the so-called Quantum Spin Hall Effect, namely a longitudinal charge current produces a quantized transverse spin bias, with a quantized spin Hall conductance.

[5] As we will discuss in a while, the robustness is guaranteed only for an odd number of couples of channels.

Graphene

Before discussing the model, we recall that graphene is a two-dimensional system, consisting of a layer of carbon atoms bound in a hexagonal honeycomb lattice. It has been the first two-dimensional crystal to be identified and has been isolated for the first time in 2004 at the University of Manchester, by A. Geim and K. Novoselov [125] who were awarded the Nobel Prize in 2010. A honeycomb lattice of identical atoms has been introduced in the former Section, within the description of Haldane model. In Eq. (1.59) we have introduced the primitive vectors

$$\mathbf{v}_1 = \sqrt{3}a\mathbf{e}_1, \quad \mathbf{v}_2 = \frac{\sqrt{3}}{2}a\mathbf{e}_1 + \frac{3}{2}a\mathbf{e}_2, \quad \mathbf{v}_3 = -\frac{\sqrt{3}}{2}a\mathbf{e}_1 + \frac{3}{2}a\mathbf{e}_2, \tag{1.98}$$

with a the lattice constant, $a \approx 0.142$ nm for graphene. Any couple of vectors can be chosen to define the primitive unit cell.

With a tight-binding approach, which we do not explicitly recover here, it is possible to obtain the dispersion relation of graphene, which reads as

$$\epsilon^{\lambda}_{\mathbf{k}} = 2(t_{nnn} - st_{nn}) \sum_{i=1}^{3} \cos(\mathbf{k} \cdot \mathbf{v_i}) + \lambda t_{nn} \sqrt{3 + 2\sum_{i=1}^{3} \cos(\mathbf{k} \cdot \mathbf{v_i})}, \tag{1.99}$$

where $\lambda = \pm 1$, t_{nnn} is the next-nearest neighbor hopping amplitude, t_{nn} is the nearest neighbor hopping amplitude (also known as transfer integral) and s gives a measure of the overlap of the orbital wavefunctions on nearest neighbor sites. This is exactly what we obtained as a dispersion relation for the Haldane model in Eq. (1.78), provided that the phase ϕ is set to zero, that we substitute $t_{nn} \to -t$, and that we identify $t_{nnn} - st_{nn} = -t'$ as an effective hopping amplitude. The overlap correction brought by s gives a renormalization of the next-nearest neighbor hopping. That comment aside, all the results obtained for the Haldane model (in the specific case $\phi = 0$) hold true.

The presence of next-nearest neighbor hopping breaks particle-hole symmetry. As a consequence, the energy dispersion is no longer symmetric for positive and negative energies. Moreover, being the next-nearest neighbor hopping real, no gap is opened at the Dirac point.

The experimental synthesis of single-layer graphene, together with its physical and chemical stability, marked a breakthrough in condensed matter and renewed the interest in the Haldane model: after almost twenty years, a suitable platform was finally found.

Formulation of the model

The Kane-Mele model appeared as the first possible experimental realization of Haldane model on a graphene-based platform. As a mass term, spin-orbit interaction is exploited. Unfortunately, spin-orbit coupling in graphene turned out to be too weak, making it impossible to observe the Quantum Spin Hall Effect. Indeed, the gap opened by spin-orbit interaction is only $24\,\mu$eV [68]. However, it shed light on the $\mathbb{Z}_2$ classification of topological insulators in the presence of time-reversal symmetry.

The starting point is to derive a low-energy Hamiltonian for graphene, expanding it around the first Brillouin zone's vertices $\mathbf{K}$, $\mathbf{K}'$, which coincide with the Dirac points

(Eq. (1.69)). It can be shown that such expansion reads as

$$H(\mathbf{q}^{\xi}) = \frac{3}{2}ta(\xi q_x\sigma_x + q_y\sigma_y) \equiv \hbar v_F(\xi q_x\sigma_x + q_y\sigma_y), \tag{1.100}$$

where $\mathbf{q}^{\xi} = \mathbf{k} - \mathbf{k}_D^{\xi}$ is the expansion variable and, for graphene, $v_F \approx 3 \cdot 10^{-3}c$. Such Hamiltonian can be recast into a new form in real space, which will be denoted as $\mathcal{H}_0$. To do so, we substitute $q_j \to -i\partial_j$ and we consider a larger spinor with four components

$$\Psi(\mathbf{r}) = \begin{pmatrix} u_A(\mathbf{K},\mathbf{r}) \\ u_B(\mathbf{K},\mathbf{r}) \\ u_A(\mathbf{K}',\mathbf{r}) \\ u_B(\mathbf{K}',\mathbf{r}) \end{pmatrix} \psi(\mathbf{r}), \tag{1.101}$$

where the components describe basis states at momentum $\mathbf{K}$, $\mathbf{K}'$ centered on atoms the A, B sublattice, $\mathbf{K}$, $\mathbf{K}'$ are the first Brillouin zone vertices, and $\psi(\mathbf{r})$ is the envelope function. This leads to

$$\mathcal{H}_0 = -i\hbar v_F\psi^{\dagger}(\sigma_x\tau_z\partial_x + \sigma_y\tau_0\partial_y)\psi, \tag{1.102}$$

where τ_i is a Pauli matrix acting in the $\mathbf{K}$, $\mathbf{K}'$ space, and τ_0 the identity matrix in the same space. In a matricial form,

$$\mathcal{H}_0 = -i\hbar v_F\psi^{\dagger}\begin{pmatrix} \sigma_x\partial_x + \sigma_y\partial_y & 0 \\ 0 & -\sigma_x\partial_x + \sigma_y\partial_y \end{pmatrix}\psi. \tag{1.103}$$

From our discussion of the Haldane model, we know that an interesting gap opening may arise from a term proportional to $\sigma_z\tau_z$. Notice that this is odd under time-reversal, and that so far we have not included the spin degree of freedom. We do it now.

It is known from the theory of special relativity that an electron with momentum $\mathbf{p}$ and in the presence of an electric field $\mathbf{E}$, perceives in its rest frame a magnetic field $\mathbf{B} = \mathbf{p} \times \mathbf{E}/mc^2$, with c the speed of light. Such field interacts with the magnetic moment of the electron proportionally to its spin. The corresponding Hamiltonian contribution is

$$H_{SO} = \frac{e\hbar}{4m^2c^2}\mathbf{s} \cdot \mathbf{p} \times \mathbf{E}. \tag{1.104}$$

Here, $\mathbf{s}$ is the electron spin expressed in units of $\hbar/2$. The spin-orbit term enters the low-energy Hamiltonian via

$$\mathcal{H}_{SO} = \Delta_{SO}\psi^{\dagger}\sigma_z\tau_z s_z\psi, \tag{1.105}$$

which respects time-reversal symmetry. Δ_{SO} can be related to the parameters in Eq. (1.104) [95], but it is not important for what follows.

Thanks to spin-orbit interaction, a gap opens around $\mathbf{K}$, $\mathbf{K}'$. Indeed, the energy dispersion is now

$$\epsilon(\mathbf{q}) = \pm\sqrt{(\hbar v_F|\mathbf{q}|)^2 + \Delta_{SO}^2}, \tag{1.106}$$

with a gap of $2\Delta_{SO}$ around $\mathbf{q} = \mathbf{0}$. If $s_z = \pm 1$ is selected in $\mathcal{H}_{SO}$, two Hamiltonians are obtained: they both violate time-reversal symmetry and correspond to two Haldane

models for spinless electrons, having opposite Chern numbers. To see it more explicitly, let's look back at the low-energy Hamiltonian for graphene in k-space, incorporating the spin-orbit interaction as well:

$$H(\mathbf{q}^{\xi})^{K-M} = \hbar v_F(\xi q_x \sigma_x + q_y \sigma_y) + \Delta_{SO}\xi\sigma_z s_z. \tag{1.107}$$

The derivation of a low-energy Hamiltonian for the Haldane model, having set the chemical potential to zero, returns

$$H(\mathbf{q}^{\xi})^{H} = \hbar v_F(\xi q_x \sigma_x + q_y \sigma_y) + \xi 3\sqrt{3}t' \sin\phi\sigma_z. \tag{1.108}$$

Identifying $\Delta_{SO} = 3\sqrt{3}t'\sin\phi$, we see that $s_z = +1$ corresponds to a Haldane model having Chern number +1, whereas $s_z = -1$ (which realizes $\phi \to -\phi$) corresponds to a Haldane model having Chern number -1.

We can finally discuss the physics revealed by the Kane-Mele model. A Quantum Spin Hall Effect arises with Hall conductance e^2/h for spin up electrons, and with Hall conductance $-e^2/h$ for spin down electrons: an electric field induces opposite currents for opposite spins. The Hall conductance is zero, but a spin Hall conductance emerges as a consequence of the spin current. If s_z is a good quantum number, such conductance is quantized. To identify the spin Hall conductance quantum, we start from a spin current density

$$\mathbf{J}^s = \frac{\hbar}{2e}(\mathbf{J}^{\uparrow} - \mathbf{J}^{\downarrow}), \tag{1.109}$$

where $\mathbf{J}^{\uparrow}(\mathbf{J}^{\downarrow})$ represents the current density associated to spin up(down) electrons. From the comments above, and choosing a y-oriented electric field, we get

$$J_x^{\uparrow} = \frac{e^2}{h}E_y, \quad J_x^{\downarrow} = -\frac{e^2}{h}E_y. \tag{1.110}$$

From Eq. (1.109),

$$J_x^s = \frac{e}{2\pi}E_y, \tag{1.111}$$

which allows to identify the spin Hall conductance quantum as $\sigma_{xy}^s = e/2\pi$.

Boundary states and topological protection

Having highlighted the analogy to the Haldane model, solving the Kane-Mele model for a finite-size sample should lead to two boundary states. The Hamiltonian under consideration is that of two Haldane tight-binding models corresponding to opposite spins and having opposite phases (set to $\phi = \pm\pi/2$ for simplicity) and $\mu = 0$:

$$H = -t\sum_{\langle ij\rangle}\sum_{\alpha} c_{i\alpha}^{\dagger}c_{j\alpha} - it'\sum_{\langle\langle ij\rangle\rangle}\sum_{\alpha\beta}\nu_{ij}s_{\alpha\beta}^{z}c_{i\alpha}^{\dagger}c_{j\beta}. \tag{1.112}$$

Here, $\nu_{ij} = -\nu_{ji}$ acts as inverter of the Haldane phase depending on the hopping direction and $t' = \Delta_{SO}/3\sqrt{3}$.

In their paper [95], Kane and Mele solved the model for a strip with zig-zag edges and a finite y-size. As shown in Fig. 1.8, two bands cross the gap, linking the one-dimensional projections of $\mathbf{K}$ and $\mathbf{K}'$, and correspond to edge states located at the

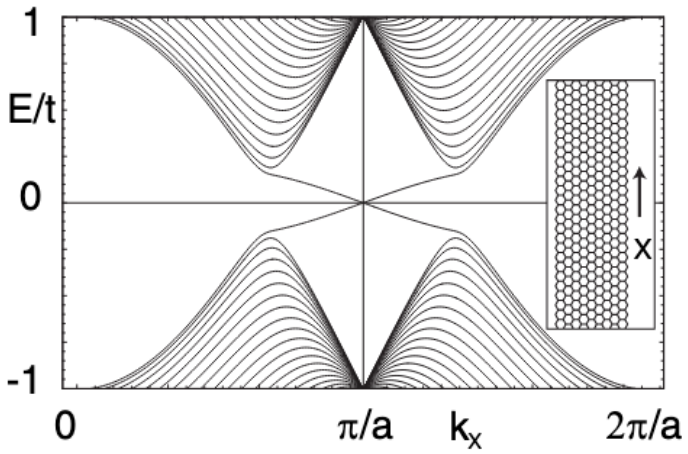

Figure 1.8: *Result of the Kane-Mele diagonalization with periodic boundary conditions on the x direction and zig-zag edges, with the boundary states emerging inside the energy gap. Reprinted with permission from [95]. Copyright 2024 by the American Physical Society.*

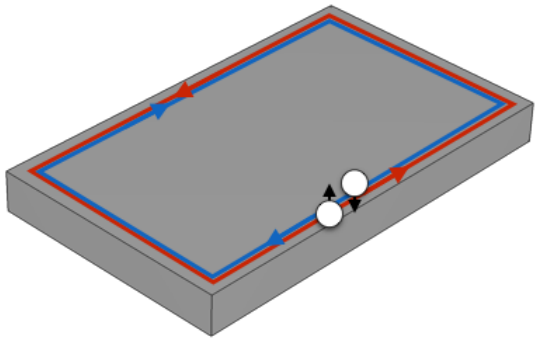

Figure 1.9: *The helical edge states of the Quantum Spin Hall Effect: on each side of the sample, electrons having opposite spins are counter-propagating.*

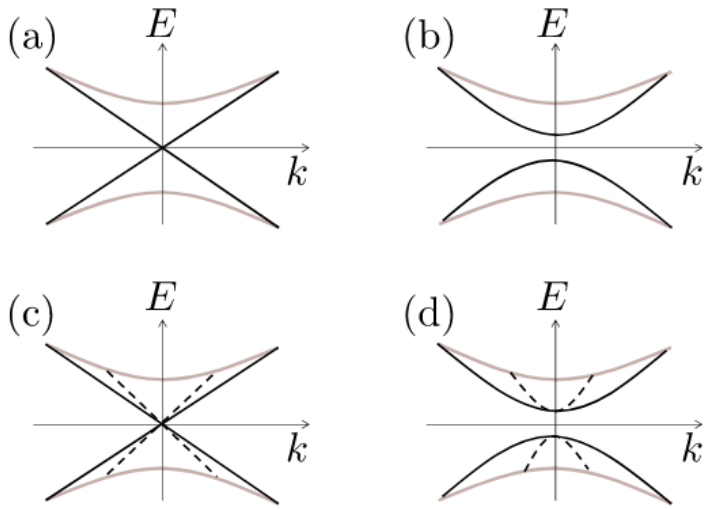

Figure 1.10: *Whenever an odd number of Kramers doublets is present on the edge, as in panel (a), a gap in the edge state spectrum cannot be opened without a violation of Kramers theorem (b). However, if an even number of Kramers doublets is present, as in panel (c), the edge states can be fully gapped out even in the presence of time-reversal symmetry as shown in panel (d). Figure from [48], reproduced with permission from Springer Nature.*

boundary of the graphene strip. Each band has two degenerate states, one per edge. On each edge, the two states with opposite spins are counter-propagating: they are hence said to be helical (Fig. 1.9).

The band crossing is protected via Kramers theorem, which states that, in the presence of time-reversal symmetry, for each energy of a 1/2-spin system there are at least two degenerate eigenstates (Kramers doublets) [20]. On each edge of the strip, the two opposite-spin states form a Kramers doublets. Also at their crossing point, $k_x = \pi/a$, the Kramers partners must be degenerate. Such degeneration cannot be lifted. If an odd number of Kramers doublets is present, as in the Kane-Mele solution, it is not possible to gap them out without violating the Kramers theorem: the Quantum Spin Hall phase is not adiabatically connected to a trivial insulator and represents a completely new topological phase. On the other hand, if an even number of Kramers doublets is present, one can gap out all of them without violating Kramers theorem (see Fig. 1.10), obtaining a state which is topologically equivalent to a trivial insulator. For this distinction based on the number of Kramers pairs, the topological order of the Quantum Spin Hall Effect is $\mathbb{Z}_2$: it is 0 for trivial insulators and 1 for topological insulators.

We emphasize that Kramers theorem ensures that the helical edge states are protected from elastic and non-magnetic backscattering (which are perturbations respecting time-reversal symmetry). It doesn't say anything about inelastic backscattering or scattering off magnetic impurities, which can in principle occurr.

Unfortunately, it was soon realised that the bulk gap is too tiny ($\sim 10^{-3}$ meV) to experimentally observe the Quantum Spin Hall Effect in graphene. The search for the Quantum Spin Hall state then turned to new platforms, in particular to semiconducting systems.

1.2.2 Bernevig-Hughes-Zhang (BHZ) model

Soon after the Kane-Mele model, in 2006, B. A. Bernevig, T. L. Hughes, and S.-C. Zhang found a more suitable system to realize the Quantum Spin Hall Effect, namely CdTe/HgTe/CdTe quantum wells. They predicted that such a heterostructure can behave as a two-dimensional topological insulator, provided that the HgTe layer is thicker than a critical thickness d_c. This prediction was confirmed only a year later, in 2007, by the experimentalists in the group of L. W. Molenkamp in Würzburg [103].

The modified Dirac equation and the emergence of edge states

Already in the discussion of the Haldane model, we found that a competition of mass terms, leading to a closing and reopening of the energy gap, allows to switch from a zero to a non-zero Chern number, with the emergence of states having energies within the band gap and located at the boundaries of the system. We here stop and revise this fact explicitly, in one- and two-dimensional systems [159]. This will allow for a simpler understanding of the BHZ model.

Let us start from the Dirac equation, which describes a relativistic particle with spin $1/2$,

$$\mathcal{H} = cp_i\alpha_i + mc^2\beta, \tag{1.113}$$

where c is the speed of light, m the particle's rest mass, and α_i, $i = 1, 2, 3$ and β are related to the Dirac γ matrices and satisfy the Clifford algebra. We first consider the $d = 1 + 1$-dimensional case. The Hamiltonian density reads as ($\hbar = 1$)[6]

$$\mathcal{H} = -iv\partial_x\sigma_x + M\sigma_z, \tag{1.114}$$

where we substituted $p_x = -i\partial_x$, $M = mv^2$, v is the Fermi velocity and σ_i are the Pauli matrices. Solving the eigenvalue problem, eigenstates with positive and negative energies turn out to be separated by a gap large $|2M|$. We observe that the Dirac Hamiltonian above is invariant under the transformation $M \to -M$, $\sigma_{y,z} \to -\sigma_{y,z}$, $\sigma_x \to \sigma_x$. In order to better analyze this fact, we can complicate a bit the picture by introducing a change of sign in the mass term:

$$M(x) = \begin{cases} m_1 > 0 & \text{for} \quad x \ll 0 \\ m_2 < 0 & \text{for} \quad x \gg 0. \end{cases} \tag{1.115}$$

If we assume $M(x)$ to have a continuous profile, the gap vanishes at some point near the domain wall $x = 0$, having opposite signs before and after that point. Where the gap closes, a state having energy inside the gap exists. In particular, it is easy to show that intra-gap bound states cannot exist for $\text{sgn}(m_1 m_2) = +1$, while, for $\text{sgn}(m_1 m_2) = -1$, a zero-energy bound state emerges, having wavefunction

$$\psi(x) = \begin{pmatrix} 1 \\ i \end{pmatrix} \sqrt{\frac{1}{v}\left|\frac{m_1 m_2}{m_1 - m_2}\right|} e^{-|M(x)x|/v}. \tag{1.116}$$

Such state is hence embedded in the energy gap and is exponentially localized in the vicinity of the domain wall, spreading over a distance $v/|m_{1/2}|$ on the two sides. To

[6] In one dimension, the two Dirac matrices α_1 and β are any two of the three Pauli matrices, for example $\alpha_1 = \sigma_x$, $\beta = \sigma_z$ [159].

summarize, the Dirac Hamiltonian accommodates the presence of intra-gap states localized around the physical point where the mass changes sign. We can think of the vacuum as a region with a large and positive energy gap: therefore, at the ends of a finite-size system with negative mass, intra-gap bound states are expected.

Looking back at the indistinguishability of Hamiltonians with $\pm M$, we can introduce a term to break such symmetry:

$$h^{1D} = vp_x\sigma_x + (M - Bp_x^2)\sigma_z, \tag{1.117}$$

obtaining a so-called modified Dirac Hamiltonian. We want to study the existence of zero-energy bound states at the boundaries of the system. To this end, let us assume to deal with a semi-infinite one-dimensional system, extending from $x = 0$ to $+\infty$. From the zero-energy condition,

$$\begin{aligned}
&\left[vp_x\sigma_x + (M - Bp_x^2)\sigma_z\right]\psi(x) = 0 \\
&\Rightarrow -i\partial_x\sigma_x\psi(x) = -\frac{1}{v}(M + B\partial_x^2)\sigma_z\psi(x) \\
&\Rightarrow \partial_x\psi(x) = -\frac{1}{v}(M + B\partial_x^2)\sigma_y\psi(x),
\end{aligned} \tag{1.118}$$

where in the last row we have multiplied by σ_x from the left. The wavefunction will hence be written in terms of $\psi^\eta(x) = \chi_\eta\phi(x)$, where $\sigma_y\chi_\eta = \eta\chi_\eta$ (hence $\chi_\eta = 1/\sqrt{2}(\eta, i)^T$), and $\phi(x = 0) = 0$. The function $\phi(x)$ is a solution of

$$\partial_x\phi(x) = -\frac{\eta}{v}(M + B\partial_x^2)\phi(x). \tag{1.119}$$

Assuming a trial function $\phi(x) \propto e^{-\lambda x}$,

$$-\lambda = -\frac{\eta}{v}(M + B\lambda^2) \Rightarrow B\lambda^2 - \frac{v}{\eta}\lambda + M = 0 \Rightarrow B\lambda^2 - v\eta\lambda + M = 0. \tag{1.120}$$

Hence, we obtain two solutions $\lambda_\pm$,

$$\lambda_\pm = \frac{v\eta \pm \sqrt{v^2 - 4MB}}{2B}. \tag{1.121}$$

Their sum and product are $\lambda_+ + \lambda_- = v\eta/B$ and $\lambda_+\lambda_- = M/B$. So far, we have

$$\psi^\eta(x) \propto \frac{1}{\sqrt{2}}\begin{pmatrix}\eta\\ i\end{pmatrix}(ae^{-\lambda_+ x} + be^{-\lambda_- x}). \tag{1.122}$$

Since we want the wavefunction to vanish at $x = 0$, $b = -a$. To obtain a well defined solution at $x = +\infty$, we need $\lambda_\pm > 0$. From their sum and product, this implies that:

- $\eta = \text{sgn}(B)$, hence only one of the χ_η is suitable to have a bound state and we have to plug this information also in the λ factors, $\lambda_\pm \to \lambda_\pm|_{\eta=\text{sgn}(B)}$;
- $\text{sgn}(MB) = 1$.

We can thus conclude that, under the condition $\text{sgn}(MB) = 1$, there exist a solution of a bound state with zero-energy,

$$\psi(x) \propto \frac{1}{\sqrt{2}}\begin{pmatrix}\text{sgn}(B)\\ i\end{pmatrix}(e^{-x/\xi_+} - e^{-x/\xi_-}), \tag{1.123}$$

with $\xi_{\pm}^{-1} = v(1 \pm \sqrt{1 - 4MB/v^2})/2|B|$. $\xi_{\pm}$ determine the spatial distribution of the wavefunction, which is sharply localized at the boundary for large MB. A crucial result of this discussion is that the existence of the edge state is only related to the global quantity sgn(MB), which has to amount to +1. The specific values of M and B are not relevant.

We can now easily generalize the discussion for the case of two spatial dimensions, which will be needed for what follows. The modified Dirac Hamiltonian, written in momentum space, is

$$h_{\pm}^{2D}(\mathbf{k}) = \mathbf{d}(\mathbf{k}) \cdot \boldsymbol{\sigma}, \tag{1.124}$$

where $\boldsymbol{\sigma} = (\sigma_x, \sigma_y, \sigma_z)$ is the vector of the Pauli matrices, $\mathbf{k} = (k_x, k_y)$ and $\mathbf{d}(\mathbf{k}) = (vk_x, \pm vk_y, M(k))$, with $M(k) = M - B(k_x^2 + k_y^2)$. As an example, we will analyze the "+" case. We consider a semi-infinite plane $x > 0$ and require that the wavefunction vanishes at the boundary $x = 0$. k_y is a good quantum number, because the system is translationally invariant along the y direction. Moreover, at $k_y = 0$, the two-dimensional equation recovers the one-dimensional equation, hence the x-dependent part of the solution has the identical (known) form as Eq. (1.123) for sgn$(MB) = 1$. The solution for non-zero k_y is simply given by the bound state along x multiplied by a plane wave along y

$$\psi_{k_y}(x, y) \propto \frac{1}{\sqrt{2}} \begin{pmatrix} \text{sgn}(B) \\ i \end{pmatrix} (e^{-x/\xi_+} - e^{-x/\xi_-}) e^{ik_y y} \tag{1.125}$$

with a slight abuse of notation, because $\xi_{\pm}$ now also depend on k_y,

$$\xi_{\pm}^{-1} = v \left(1 \pm \sqrt{1 - 4MB/v^2 + 4B^2 k_y^2/v^2}\right) /2|B|. \tag{1.126}$$

We can look at the y-dependent part of h_+^{2D} as a perturbation to the one-dimensional Hamiltonian. We denote it by $h_+^{2D}(k_y)$ and project it onto the edge state solution, $\langle \psi_{k_y} | h_+^{2D}(k_y) | \psi_{k_y} \rangle$ to obtain a one-dimensional effective model for the edge state. To leading order in k_y, its energy dispersion results in

$$E_{edge\,state}(k_y) = vk_y \text{sgn}(B) \Rightarrow v_{edge\,state} = \frac{\partial E_{edge\,state}(k_y)}{dk_y} = v\text{sgn}(B). \tag{1.127}$$

Recalling that sgn$(B) = \eta$, which is the eigenvalue of σ_y associated to $\psi_{k_y}(x, y)$, we deduce that for $B > 0 (B < 0)$ it corresponds to a state propagating with positive(negative) velocity and with positive(negative) spin-polarization along y. This reflects the property we already encountered in the Kane-Mele model, the spin-momentum locking: electrons with opposite spin counter-propagate.

Before moving to the realization of helical edge states in realistic systems, we emphasize once more the role of sgn(MB). At small momenta, the sign of the momentum-dependent mass term $M(k)$ is the same as sgn(M), while at large momenta it is the same as $-$sgn(B). If sgn$(MB) = -1$, the sign of the mass term $M(k)$ at small and large momenta (for instance, sweeping across the Brillouin zone) remains the same. If sgn$(MB) = +1$, $M(k)$ changes sign. We recover what we discussed at the beginning of the Subsection, namely the emergence of bound states when the mass term changes sign.

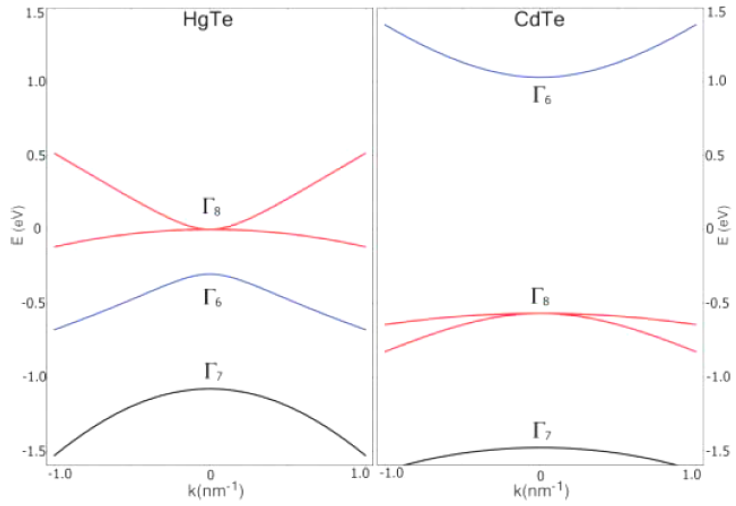

Figure 1.11: *Bulk energy bands of HgTe and CdTe near the* Γ*-point. The* Γ_8 *band is indicated in red and the* Γ_6 *band is indicated in blue. Figure from [21], reprinted with permission from AAAS.*

Without computing it explicitly, we lastly mention that the Chern number is found to be

$$c = -\frac{1}{2}[\mathrm{sgn}(M) + \mathrm{sgn}(B)]. \tag{1.128}$$

In the trivial regime, $\mathrm{sgn}(MB) = -1$ and the Chern number $c = 0$, while $c = \pm 1$ in the topological regime ($\mathrm{sgn}(MB) = +1$).

Band structures of HgTe and CdTe

A crucial point of the BHZ model is represented by the different band structures of the materials involved, HgTe and CdTe, which we briefly describe here. CdTe has a normal semiconductor band structure, with the valence band Γ_8 separated by an energy gap from the conduction band Γ_6. On the other hand, HgTe has an inverted semimetallic band structure [123], with the Γ_8 band above the Γ_6 valence band, as shown in Fig. 1.11. Intuitively, thin and thick quantum wells will exhibit different band structures: when the central layer of HgTe is thin, the energy bands align in a normal ordering, similarly to CdTe. On the contrary, when the width of HgTe is (sufficiently) thick, the energy bands will be in the inverted regime, similarly to HgTe. The closing and reopening of the gap, necessarily separating the two regimes (normal and inverted), marks a topological phase transition and the emergence, as we shall see, of the helical edge states, see Fig. 1.12.

BHZ model

As in the original paper by Bernevig, Hughes and Zhang [21], it is possible to introduce an effective band model to describe the system around the Γ-point (the center of the first Brillouin zone), where the essential physics takes place.[7] We will follow Refs. [21], [99] and [48].

[7] For both materials the gap is minimum at Γ-point, see Fig. 1.11.

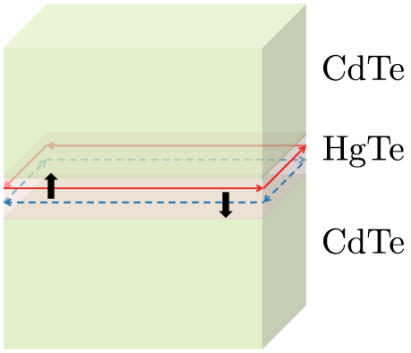

Figure 1.12: *Scheme of the CdTe/HgTe/CdTe quantum well in the topological regime, featuring the helical edge states. Figure from [48], reproduced with permission from Springer Nature.*

For both HgTe and CdTe, the important bands around the typical Fermi level are close to the Γ-point and are the s-type band, Γ_6, and the p-type band which is split by spin-orbit coupling into the Γ_7 band (with $J = 1/2$) and the Γ_8 band (with $J = 3/2$). The Γ_7 band has negligible effects on the band structure, therefore the starting point can be a six-band model taking into account the Γ_6 and Γ_8 bands only. In particular, the following six-component spinor, including the six essential atomic states per unit cell, can be considered:

$$\Psi = \left(|\Gamma_6, 1/2\rangle, |\Gamma_6, -1/2\rangle, |\Gamma_8, 3/2\rangle, |\Gamma_8, 1/2\rangle, |\Gamma_8, -1/2\rangle, |\Gamma_8, -3/2\rangle\right)^T. \quad (1.129)$$

These six bands combine with each other and originate the spin up and spin down states ($\pm$) of three types of subbands: electron-like ($|E_{n=1}, \pm\rangle$), heavy-hole-like ($|H_{n=1}, \pm\rangle$), and light-hole-like ($|L_{n=1}, \pm\rangle$), where this distinction is related to properties of the respective wavefunctions, and the subscript n labels states with an increasing number of nodes along the growth-direction z ($n = 1$ identifies the lowest subbands). Since the L_1 subband is well separated in energy from the others, it will be neglected. We can thus deal with an effective four-band model for the subbands that participate in the mentioned inversion crossing: $|E_1, m_J = \pm 1/2\rangle$ and $|H_1, m_J = \pm 3/2\rangle$, which we order as

$$\{|E_1, +\rangle, |H_1, +\rangle, |E_1, -\rangle, |H_1, -\rangle\}. \quad (1.130)$$

At the Γ-point with in-plane momentum $\mathbf{k} = 0$, m_J is still a good quantum number. In particular, at this point the H_1 subband comes from the $|\Gamma_8, m_J = \pm 3/2\rangle$ states while the E_1 subband comes from a linear combination of the $|\Gamma_6, m_J = \pm 1/2\rangle$ and $|\Gamma_8, m_J = \pm 1/2\rangle$ states. In the presence of time-reversal symmetry, Kramers theorem states that each state, as E_1 and H_1, must be doubly degenerate: $|E_1, \pm\rangle$ and $|H_1, \pm\rangle$ are indeed Kramers partners.

An effective low-energy Hamiltonian, to describe the quantum well near the Γ-point, can be built on this basis by making some symmetry considerations.

- Due to Kramers theorem, terms connecting Kramers partners, namely $(|E_1, +\rangle, |E_1, -\rangle)$ and $(|H_1, +\rangle, |H_1, -\rangle)$, must vanish.
- $|E_1, \pm\rangle$ and $|H_1, \pm\rangle$ have opposite transformations under two-dimensional spatial reflections. Hence, a Hamiltonian matrix element connecting them must be an

odd function of the in-plane momentum $\mathbf{k} = (k_x, k_y)$ (remember that we consider a quantum well built along the z direction), since we assume that the Hamiltonian preserves inversion symmetry. To lowest order in k, $(|E_1, +\rangle, |H_1, +\rangle)$ and $(|E_1, -\rangle, |H_1, -\rangle)$ will be coupled via a term linear in k.

- To preserve rotational symmetry around the growth-axis (z-axis), it can be shown that these matrix elements must by proportional to $k_\pm = k_x \pm ik_y$.
- Again for parity constraints, diagonal terms can only contain even powers of momentum k, including k-independent terms.
- Terms coupling $(|E_1, +\rangle, |H_1, -\rangle)$ and $(|E_1, -\rangle, |H_1, +\rangle)$ are not admitted, because they would split the Kramers degeneracy via second order perturbation processes.

Altogether, these considerations lead to

$$H(k_x, k_y) = \begin{pmatrix} h(\mathbf{k}) & 0 \\ 0 & h^*(-\mathbf{k}), \end{pmatrix} \tag{1.131}$$

with

$$h(\mathbf{k}) = \epsilon(k)\sigma_0 + \mathbf{d}(\mathbf{k}) \cdot \boldsymbol{\sigma}. \tag{1.132}$$

Here, $\epsilon(k) = C - D(k_x^2 + k_y^2)$, $\mathbf{d}(\mathbf{k}) = (Ak_x, Ak_y, M(k))$, $M(k) = M - B(k_x^2 + k_y^2)$, and A, B, C, D, M are material parameters depending on the geometrical structure of the quantum well[8], and the zero of the energy is set by the overall constant C at the top of the valence band of HgTe, as in Fig. 1.11. As we anticipated, $d_3(k)$ is an even function of k, while $d_1(k)$, $d_2(k)$ are odd. Moreover, $d_1(k) \pm d_2(k) = A(k_x \pm k_y) = Ak_\pm$ as needed.

The main parameter is M, which is the energy difference between the E_1 and H_1 levels at the Γ-point. The band inversion in HgTe makes it unavoidable to have a level crossing at some critical thickness of the HgTe layer, d_c. Indeed, for thin HgTe layers, with thickness $d < d_c$, the quantum well is in the "normal" (not inverted) regime, where CdTe is dominant and for the overall band structure, at the Γ-point, $E(\Gamma_6) > E(\Gamma_8)$. On the other hand, for $d > d_c$, the quantum well is in the inverted regime, with $E(\Gamma_6) < E(\Gamma_8)$. By varying the thickness of the well, E_1 and H_1 necessarily cross at some d_c, leading to a change of sign for M (see Fig. 1.13).

We can now connect to our previous discussion about the modified Dirac equation and the emergence of edge states. If we neglect $\epsilon(k)$ and identify $A \equiv v$, we are dealing with the modified Dirac Hamiltonian $h(\mathbf{k})$ in two-spatial dimensions as $h_+^{2D}(\mathbf{k})$ in Eq. (1.124). As that Hamiltonian, $h(\mathbf{k})$ breaks time-reversal symmetry, although the symmetry is recovered as soon as the complete four-band model is considered: the quantum well corresponds to two modified Dirac Hamiltonian $h(\mathbf{k})$ and $h^*(-\mathbf{k})$ related with each other by time-reversal symmetry. Therefore, under the appropriate condition $\text{sgn}(MB) = 1$, two helical states appear at the boundary of the sample. They are Kramers partners, having opposite direction of propagation and spin polarization. In a CdTe/HgTe/CdTe quantum well, the parameter B is always negative. Hence

[8] This connection to the material parameters is done in [21] by deriving the Hamiltonian in Eq. (1.131) rigorously through the $\mathbf{k} \cdot \mathbf{p}$ theory.

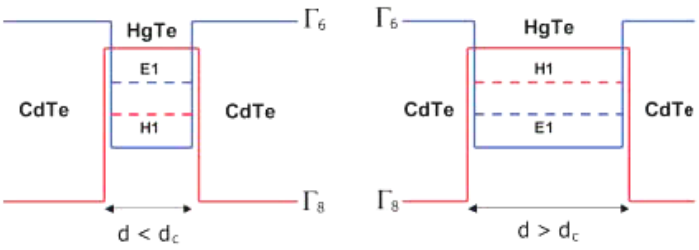

Figure 1.13: *Quantum-well geometry and lowest subbands for the two different regimes $d < d_c$ and $d > d_c$. Figure from [21], reprinted with permission from AAAS.*

$\text{sgn}(MB) = -\text{sgn}(M)$, and it is -1 in the normal regime ($M > 0$), which is hence trivial, and $+1$ in the inverted regime ($M < 0$), which is hence topological. In the topological regime, the Chern numbers c_+ and c_- associated to the two Hamiltonians $h(\mathbf{k})$ and $h^*(-\mathbf{k})$ are opposite, $c_+ = +1$ and $c_- = -1$. Although the total Chern number is zero, a new Chern number can be defined

$$c = \frac{c_+ - c_-}{2}, \tag{1.133}$$

which is zero in the trivial phase and ± 1 in the topological one. The band structure of the quantum well in the two regimes is shown in Fig. 1.14.

To summarize: from the form of the effective Dirac Hamiltonian and the gap sign change for the CdTe/HgTe/CdTe quantum well, together with general considerations about the modified Dirac equations and the emergence of edge states, we straightforwardly concluded the existence of the Quantum Spin Hall state in the system proposed by Bernevig, Hughes and Zhang.

1.2.3 Experimental evidencies

Already in the original paper [21], it was suggested that signatures of the Quantum Spin Hall Effect could be detected via a series of electrical measurements. The first experimental evidence of the one-dimensional edge states in topological insulators dates back to 2007, thanks to the work of L. W. Molenkamp and collaborators [103]. Through conductance measurements, it was shown that if the Fermi energy lies within the bulk energy gap, the system is equivalent to a trivial insulator for $d < d_C$ while, in the topological regime $d > d_C$, a current flow is present. Measures on different devices in the topological regime and shorter than the mean inelastic free path[9] ($\sim 1\mu$m at the measurement temperature) led to a four-terminal resistance $R_{14,23} = h/2e^2$, independent of the sample and corresponding to a conductance of $2e^2/h$. This confirmed the physical picture of two counter-propagating and one-dimensional channels where backscattering is forbidden. This scenario has been validated also in other multi-terminal transport experiments [145]. These measurements are widely acknowledged as representing a definitive experimental evidence for the existence of edge states in the Quantum Spin Hall regime [33]. Before discussing the experimental results, we here derive the expected resistance value relying on the Landauer Büttiker formalism [32], a quantum

[9] We remind that the helical edge states are robust against single-particle elastic backscattering, but inelastic mechanisms can cause backscattering.

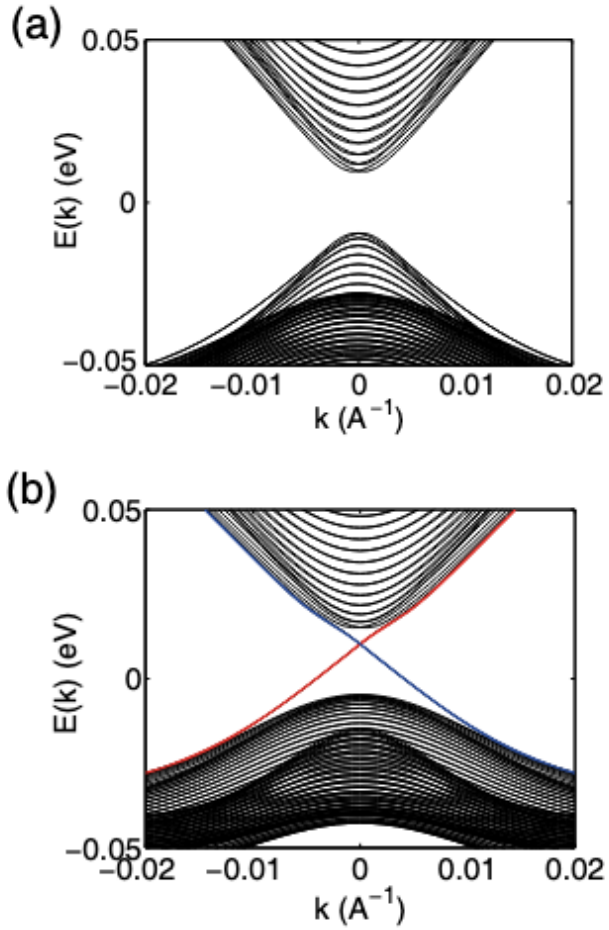

Figure 1.14: *Energy spectrum of the CdTe/HgTe/CdTe quantum well (a) in the normal ($d < d_c$) and (b) inverted ($d > d_c$) regime. Reprinted with permission from [137]. Copyright 2024 by the American Physical Society.*

transport theory which well describes non-local transport and which is also suitable for the Quantum Hall Effect. We here follow Ref. [137].

Hints on the Landauer-Büttiker description

Within the Landauer-Büttiker formalism, the relationship between current and voltage is [31]

$$I_i = \frac{e^2}{h} \sum_{j \neq i} (T_{ji} V_i - T_{ij} V_j), \tag{1.134}$$

where I_i is the current flowing out of the i-th electrode into the sample, V_i is the voltage on the i-th electrode, and T_{ji} is the transmission probability from the i-th to the j-th electrode. The current conservation implies that the total current flow is $\sum_i I_i = 0$. A voltage lead j is defined as a lead drawing a zero net current, $I_j = 0$. In the equilibrium condition, all the probes have equal voltage and zero current flow, whence $\sum_{j \neq i} T_{ij} =$

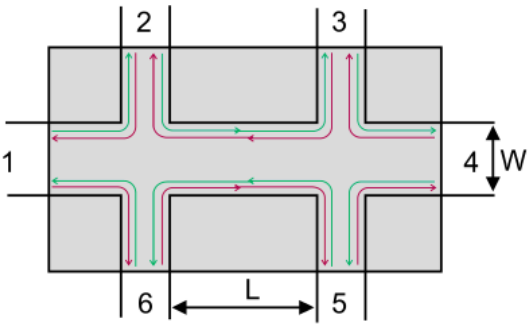

Figure 1.15: *Six-terminal Quantum Spin Hall setup employed for the transport measurement we discussed. Current flows through contacts 1 and 4, I_{14}, while the voltage drop is measured at contacts 2 and 3, V_{23}. Figure from [103], reprinted with permission from AAAS.*

$\sum_{j\neq i} T_{ji}$. This enables to rewrite the Landauer-Büttiker formula as

$$I_i = \frac{e^2}{h}\left[\sum_{j\neq i} T_{ji}V_i - \sum_{j\neq i} T_{ij}V_j\right] = \frac{e^2}{h}\left[\sum_{j\neq i} T_{ij}V_i - \sum_{j\neq i} T_{ij}V_j\right]$$
$$= \frac{e^2}{h}\sum_{j\neq i} T_{ij}(V_i - V_j). \tag{1.135}$$

Moreover, in a time-reversal invariant system, $T_{ij} = T_{ji}$. In general, for a two-dimensional device, T_{ij} has a complicated and sample-dependent form. If transport takes place only on edge states, however, it greatly simplifies.

To this regard, let us start by the Quantum Hall Effect with $\nu = 1$, where transport is realized through one couple of chiral edge states. In this case, for N current and voltage leads, the transmission matrix has entries $T^{QHE}_{i+1,i} = 1$, $i = 1, ..., N$ and $T^{QHE}_{ij} = 0$ otherwise (we periodically identify the $(N+1)$-th electrode with the 1-st electrode). This originates from the fact that chiral edge states are protected against backscattering, and hence the i-th electrode transmits with unit probability to the neighboring $(i+1)$-th electrode only on one side (owing to chirality). Let us consider now a Quantum Hall setup with the same labeling as the one in Fig. 1.15, assuming 1 and 4 to be current leads and 2, 3, 5, 6 to be voltage leads. Then $I_1 = -I_4 \equiv I_{14}$, $V_2 - V_3 = 0$ and $V_1 - V_4 = (h/e^2)I_{14}$. The four-terminal and two-terminal resistances are then

$$R_{14,23} = \frac{V_2 - V_3}{I_{14}} = 0, \qquad R_{14,14} = \frac{V_1 - V_4}{I_{14}} = h/e^2. \tag{1.136}$$

Let us move to the Quantum Spin Hall Effect, featuring counter-propagating helical edge states. As we have already commented in this Thesis, they can be regarded as two copies of chiral edge states linked one to another by time-reversal symmetry. Therefore, the T matrix satisfies $T^{QSHE} = T^{QHE} + (T^{QHE})^\dagger$. Recalling the form of T^{QHE}_{ij}, we find $T^{QSHE}_{i+1,i} = T^{QSHE}_{i,i+1} = 1$, and $T^{QSHE}_{ij} = 0$ otherwise. If we now look back to the sample in Fig. 1.15 with current leads on 1 and 4, we find again $I_1 = -I_4 \equiv I_{14}$, but $V_2 - V_3 = (h/2e^2)I_{14}$ and $V_1 - V_4 = (3h/e^2)I_{14}$. This yields

$$R_{14,23} = h/2e^2, \qquad R_{14,14} = 3h/2e^2. \tag{1.137}$$

At first sight, it might seem absurd to get a non-vanishing four-terminal longitudinal resistance, given the dissipationless character of the Quantum Spin Hall edge states and the fact that it is zero for the Quantum Hall case. How can the leads cause any dissipation of the helical edge states, that are protected from backscattering? The point is that, as the counter-propagating channels enter the voltage leads, they interact with a reservoir containing a large number of low-energy degrees of freedom, and time-reversal symmetry is effectively broken by the macroscopic irreversibility. As a result, the channels equilibrate at the same chemical potential, determined by the voltage of the lead, and dissipation occurs due to the equilibration process. A more rigorous and microscopic analysis on the different role played by a metallic lead on the Quantum Hall and on the Quantum Spin Hall state (see the Supporting Material of [145]) is consistent with our simple discussion.

The four-terminal resistance is, in particular, what is measured in the following experiment [99, 103].

Experimental results

A prototype the experimental setup is shown in Fig. 1.16. The heterostructure is realized with techniques such as molecular-beam epitaxy, and the peculiar multi-layer structure allows to enhance the carriers' mobility in the HgTe layer. Moreover, a metallic gate (V_g) allows to tune the Fermi energy within the quantum well's band structure. The experimental results for the four-terminal resistance discussed above are shown in Fig. 1.17. Different curves are associated to different devices. In particular, curve I corresponds to a quantum well with $d = 5.5$ nm (normal regime), and curves II, III, IV to quantum wells with $d = 7.3$ nm (inverted regime). In the main panel, $B = 0$ T and $T = 30$ mK. The inset shows measures performed on two samples of the same wafer, with same device size but at different temperature, 30 mK (green) and 1.8 K (black).

When the Fermi energy lies within the bulk energy gap, the red and green curves show data in good agreement with the theoretical prediction $R_{14,23} = h/2e^2$ associated to the presence of protected edge states. If the distance between the contacts is greater than the inelastic mean free path, as we anticipated, some sort of scattering mechanism can take place. The form of the scattering matrix becomes non-universal, and deviations from the predicted plateau arise (as for the blue curve). Lastly, as expected, for a quantum well in the trivial regime (black curve) the edge states disappear: the well behaves as a trivial insulator, whose resistance saturates inside the bulk energy gap. The inset further shows that the quantum plateau is only weakly sensitive to temperature variations.

Since this first experiment, many more have been performed to better understand the properties of the Quantum Spin Hall phase, and not only on HgTe/CdTe platforms. Here we just mention the main idea of two, still in the earlier stages of topological insulators.

The first identifies a transport signature of the spin polarization of the Quantum Spin Hall State [27]. Via split-gate technique, two T-shaped bars are combined, one in the Quantum Spin Hall regime and the other in the non-topological Spin Hall regime, to fabricate a hybrid H-shaped bar (see Fig. 1.18). With reference to panel (a), a current is injected in the metallic region through contacts 3 and 4. Due to Spin Hall Effect, a spin imbalance accumulates at opposite edges of the T-bar; here, if the helical edge states

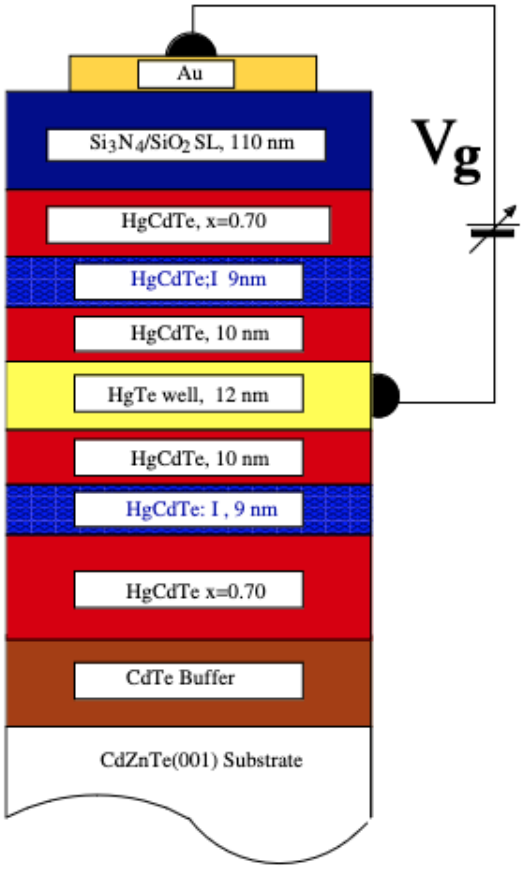

Figure 1.16: *Scheme of the typical structure of the samples. The top metallic gate allows to tune the Fermi energy. Figure from [17], © 2007 WILEY-VCH Verlag GmbH & Co. KGaA, Weinheim.*

of the Quantum Spin Hall part are spin-polarized, the spin imbalance is transferred to contacts 1 and 2, where a finite potential difference is measured. In panel (b), the injecting and detecting contacts are simply interchanged. Both configurations provided multi-terminal resistances in agreement with the presence of spin-polarized edge states.

In the second experiment [126], the idea is to image the magnetic fields produced by current flowing in Hall bars made from HgTe quantum wells with a scanning superconducting quantum interference device (SQUID) (Fig. 1.19). Then, for a two-dimensional current density there is a one-to-one correspondence through the Biot Savart law between the current density and the z component of the magnetic field produced by the current, allowing to infer the former. When transport is supposedly dominated by bulk conduction, the measured magnetic profile crosses smoothly through zero in the Hall bar, as expected for a homogeneous current flow through the Hall bar. On the other hand, when transport is supposedly dominated by edge channels, the magnetic profile shows two steep crossings through zero at the top and bottom edge of the Hall bar, indeed consistently with a dominant current flow at the edge of the bar. Such current images confirmed once more the existence of edge channels in the Quantum Spin Hall regime, see Fig. 1.20.

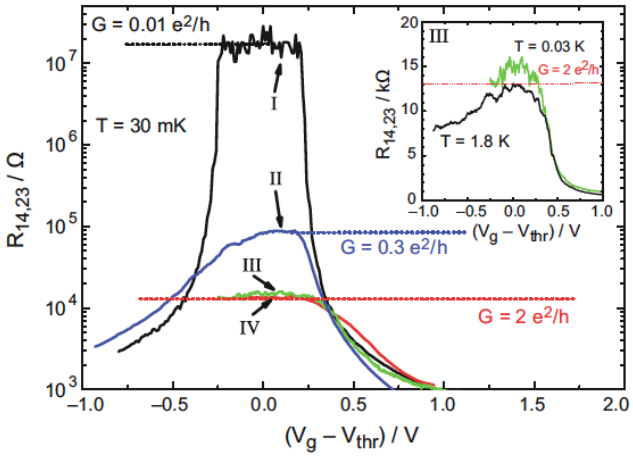

Figure 1.17: *Measures of the four-terminal resistance $R_{14,23}$ as a function of the gate voltage V_g (used to tune the Fermi energy) for different devices. Only the black curve corresponds to a device in the normal regime, $d = 5.5$ nm. For all the others, $d = 7.3$ nm. The inset shows the same quantity measured at different temperature (30 mK and 1.8 K). Figure from [103], reprinted with permission from AAAS.*

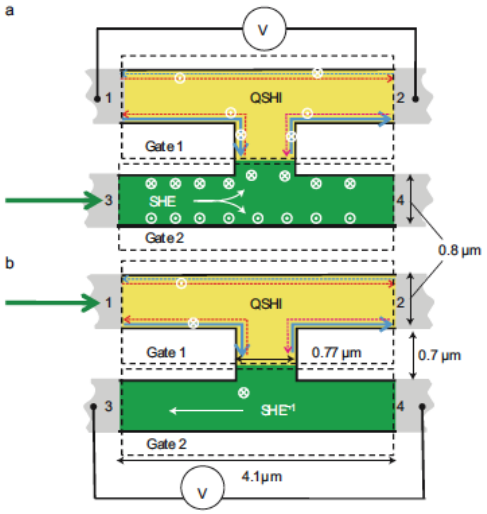

Figure 1.18: *Schematic of the setup for spin polarization measurements in [27] (whence the Figure is taken, reproduced with permission from Springer Nature) with two T-shaped bars, a Quantum Spin Hall one (in yellow) and a metallic one which shows the Spin Hall Effect (in green), combined to form a hybrid H-shaped bar.*

Many experimental progresses have been achieved thereafter, that both improved the cleanliness and stability of the edge states, and that revealed new physics. On the one hand, we mention [18], where a new generation of high quality (Cd,Hg)Te/HgTe-structures, based on a new chemical etching method, was analyzed. Significant improvements in the transport properties were obtained: in particular, the mean free path turned out to be comparable to the sample dimensions (over 10 μm) and the stability of the Quantum Spin Hall conductance persisted until high temperature. On the other hand, it was surprisingly found that the edge states can be robust even in the

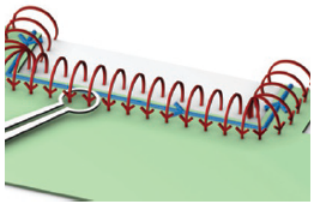

Figure 1.19: *Outline of the measurement. The magnetic field (in red) generated by the current (in blue) is measured by detecting the flux through the SQUID's pickup loop. Figure from [126], reproduced with permission from Springer Nature.*

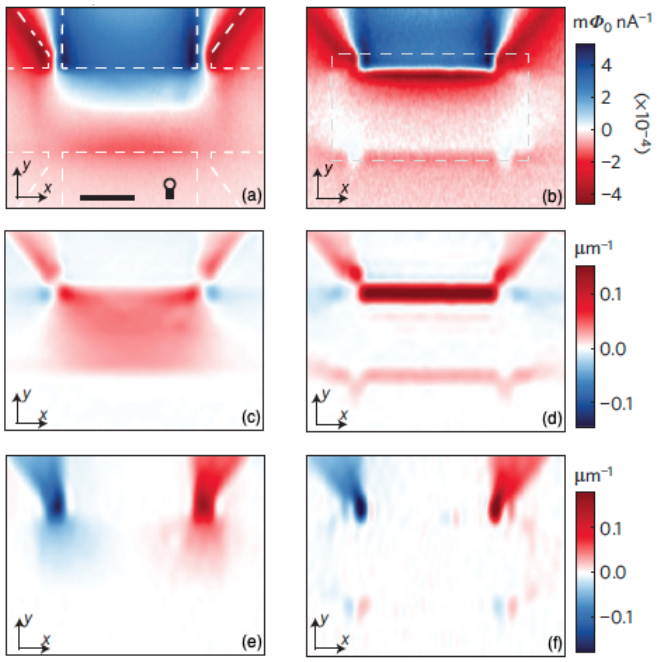

Figure 1.20: *(a)-(b) Magnetic images at two different gate voltages corresponding to bulk and edge transport. In (a), the white dashed line sketches the Hall bar, while the SQUID's pickup loop is shown in black. In (b), the top gate's outline is indicated by the grey dashed line. The current flows along the edges of the gated part of the Hall bar, whereas it spreads out in the ungated parts and the contacts. (c)-(d) x component of the two-dimensional current density obtained from the current inversion of the magnetic images (a)-(b). (e)-(f) Same for the y component. The magnetic images and the current densities are normalized to the applied current. Figure adapted from [126], reproduced with permission from Springer Nature.*

presence of strong magnetic fields and, hence, under time-reversal symmetry breaking [53, 116, 205].

1.2.4 Nanostructuring the helical edge states

After the experimental realization of topological insulators, two main challenges have been faced:

- The first is the quest for new experimental platforms hosting the Quantum Spin Hall Effect. Indeed, in HgTe-CdTe quantum wells, the topological phase transition

depends on the thickness and cannot be manipulated. Other structures, such as type-II inverted semiconductors, allow to electrostatically tune the system either in the inverted or in the normal regime [114].

- The second is the creation of nanostructures to access and manipulate the edge states in view of technological applications, in particular for spintronics, superconducting spintronics and topological quantum computation.

In the following, we will focus on nanostructuring. In particular, we will recap the main available tools to act on the edges' dispersion relation (in terms of band splittings and gap-opening mechanisms) and their potential for applications. For those experimentally achieved, mentions will be made.

Bare edge Hamiltonian

As discussed, a single edge of a two-dimensional topological insulator hosts two counter-propagating modes with opposite spin, as schematized in Fig. 1.21. The corresponding effective Hamiltonian $H_{kin.}$ is given by

$$H_{kin.} = \sum_{\sigma=\pm} \int_0^L dx\, \psi_\sigma^\dagger(x)(-i\hbar\sigma v_F \partial_x)\psi_\sigma(x). \tag{1.138}$$

Here the sample extends from $x = 0$ to $x = L$, v_F is the Fermi velocity, $\sigma = \pm$ is the spin projection and $\psi_\sigma(x)$ is the Fermi annihilation operator of an electron with spin projection σ at position x. The crossing point of the two edges, in thin quantum wells, can be accessed by gating. We also notice that, due to the helical nature of the edge states, the single edge has half the degrees of freedom with respect to usual one-dimensional spinful systems. Hence, in some sense, the helical edge represents half of a Dirac fermion in one dimension.

Figure 1.21: *Single edge of a two-dimensional topological insulator, hosting two counter-propagating modes with opposite spin.*

In the limit of infinitely long sample, the energy spectrum associated to both the edges is shown in Fig. 1.22, and compared to that of the Quantum Hall Effect.

Magnetic barriers

A first possible additional term is represented by magnetic barriers. This term shows analogies with the mass in the Dirac equation we previously discussed, with the extra degree of freedom given by the direction of the magnetization. If the magnetization is parallel to the quantization axis, no gap opens. Let us assume that σ is defined along the z axis. Then the Hamiltonian describing magnetic barriers is [136]

$$H_B = \sum_{\sigma,\sigma'=\pm} \int_0^L dx\, \psi_\sigma^\dagger(x) \left(M_x(x)[\sigma_x]_{\sigma,\sigma'} + M_y(x)[\sigma_y]_{\sigma,\sigma'}\right) \psi_{\sigma'}(x). \tag{1.139}$$

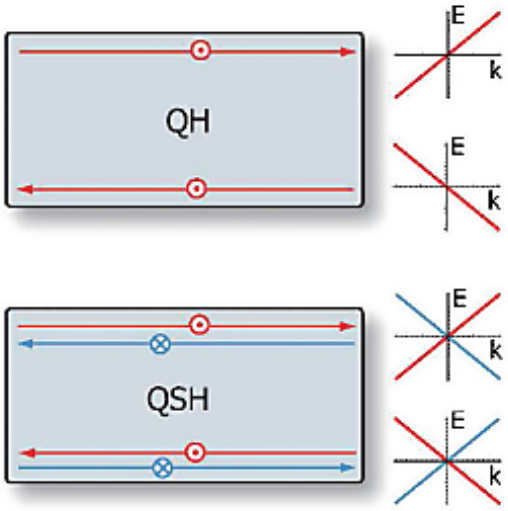

Figure 1.22: *A schematic comparison between the energy dispersion of the Quantum Hall Effect and the Quantum Spin Hall Effect. For the latter, each edge hosts two channels with opposite chirality, and same-chirality channels on opposite edges have opposite spin polarization.*

Here, $M_{x/y}(x)$ are the magnetization components in the x and y directions and $\sigma_{x/y}$ are the Pauli matrices. By changing the mass to mimick the Jackiw-Rebbi model [91] (or more precisely the Goldstone-Wilczek model [71]), fractional charges appear [182, 190]. We however emphasize that, so far, magnetic barriers have not been successfully implanted on the Quantum Spin Hall Effect.

Proximity effect

By covering a Quantum Spin Hall sample with a superconductor, a leakage of Cooper pairs occurs over a typical lengthscale ξ, which is called the coherence length. As a consequence, a superconducting pairing (and a superconducting gap Δ) is induced in the material [98, 101, 118, 194]. In particular, $\xi \sim \hbar v_F/\Delta$, where v_F is its Fermi velocity. Interestingly, the induced Cooper pairs do not have in general the same properties and symmetries as in the proximitizing superconductor, because the induced superconductivity is deeply influenced by the peculiar transport properties of the hosting material. As an implication, despite most known superconductors feature zero-momentum spin-singlet Cooper pairs (s-wave superconductors), very exotic superconducting states can be implemented in proximitized materials [196]. The derivation of the proximity effect starts from the two Hamiltonians of the superconducting and non-superconducting system, connected via a single-electron tunneling Hamiltonian:

$$H_T = \int d\mathbf{r}\, dx \Psi_s^\dagger(\mathbf{r}) \mathcal{T}(\mathbf{r}, x) \psi_\sigma(x) + h.c., \tag{1.140}$$

where the integration is over the entire volume of the two materials. $\Psi_s(\mathbf{r})$ is the fermionic annihilation operator of an electron at position $\mathbf{r}$ with spin polarization s within the superconductor, and $\mathcal{T}(\mathbf{r}, x)$ is the tunneling matrix. The form of $\mathcal{T}(\mathbf{r}, x)$ is responsible for the type of induced pairing in the normal material and for the region

over which it is induced. Let us assume that the single-electron tunneling between the two subsystems is characterized by an amplitude Γ. In the large gap limit $\Gamma k_{F,S} \ll \Delta_S$, with Δ_S the superconductor's gap and $k_{F,S}$ the superconductor's Fermi wavevector, H_T can be treated perturbatively. Indeed, single-electron tunneling is strongly suppressed due to the parent superconductor's gap. At second order, an effective Cooper-pair hopping term arises.

In the simplest case [3], the inherited superconducting term is also of s-wave type and, in practise, it is described by the low-energy Hamiltonian

$$H_\Delta = \int_0^L dx \psi_+^\dagger(x) \Delta \psi_-^\dagger(x) + h.c., \tag{1.141}$$

where Δ is the induced superconducting pairing (different from Δ_S) and L is the length of the proximitized region (see the sketch in Fig. 1.23).

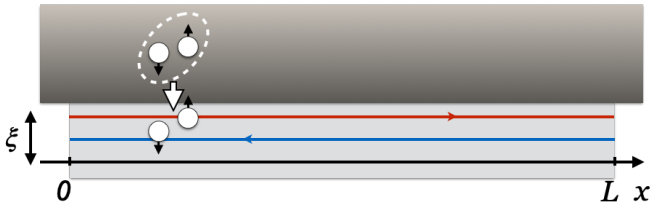

Figure 1.23: *Sketch of the helical edge proximitized by a s-wave superconductor. A leakage of Cooper pairs occurs over a lengthscale $\xi \sim \hbar v_F/\Delta$ (see the main text). This results in an induced superconducting pairing in the topological insulator.*

Interesting effects, such as odd-frequency pairing [22, 38, 60, 171, 174] and missing Shapiro steps [198], arise in the proximitized Quantum Spin Hall Effect. Further intriguing phenomena, in combination with magnetic barriers, include the emergence of Majorana bound states and 4π-periodic Josephson currents [63].

Given the proximity effect, it is possible to realize a topological Josephson junction. Two standard possibilities are putting a superconductor on top of the outer edge of a quantum spin-Hall Corbino disk pierced by a magnetic flux [63] (see Fig. 1.24), or covering a two-dimensional topological insulators with two superconductors [45, 50] (see Fig. 1.25). Such setup will be discussed in the next Chapter.

We underline here that a more rigorous analysis of the proximity effect is in order to obtain a deeper quantitative understanding of the induced pairing [78, 104, 133, 149, 165]. One possibility is to construct the action corresponding to the proximitized system, and then to integrate out the parent superconductor's degrees of freedom. A calculation with this method will be addresses in the following Chapter and the associated Appendix A (Sec. A.2).

Quantum spin Hall constriction and edge reconstruction

A further mass term is present when two edges (indexed by $\tau = \pm 1$) are brought close to each other. In this case, the kinetic energy $H_{kin.}$ becomes $H'_{kin.} = \sum_\tau H^\tau_{kin.}$, with $H^\tau_{kin.} = \sum_{\sigma=\pm} \int_0^L dx\, \psi^\dagger_{\sigma,\tau}(x)(-i\tau\sigma v_F \partial_x)\psi_{\sigma,\tau}(x)$, $\psi_{\sigma,\tau}(x)$ being the Fermi operator on the τ edge. In the presence of time-reversal symmetry, two scattering terms arise

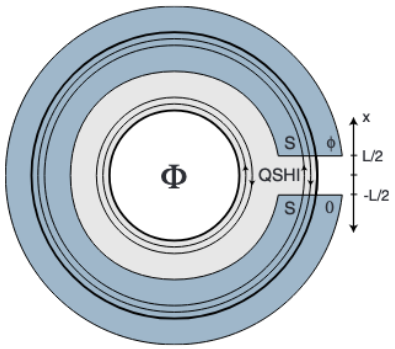

Figure 1.24: *A topological Josephson junction realized with a Quantum Spin Hall insulator in a Corbino disk geometry proximitized by a superconductor and pierced by a magnetic flux Φ. Reprinted with permission from [63]. Copyright 2024 by the American Physical Society.*

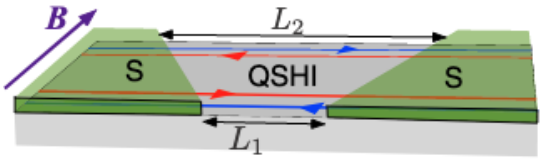

Figure 1.25: *A topological Josephson junction realized with a Quantum Spin Hall insulator proximitized by two superconducting leads. Reprinted with permission from [50]. Copyright 2024 by the American Physical Society.*

[49, 110, 113, 152, 176]. The first is a mass term

$$H_{b.s.} = \sum_{\sigma,\tau} \int_0^L dx\, b(x) \psi^\dagger_{\sigma,\tau}(x) \psi_{\sigma,-\tau}(x), \tag{1.142}$$

with $b(x)$ parametrizing the scattering amplitude. In this case, the direction of motion of the scattered electron is reversed and its spin polarization is unchanged. We notice that $H_{b.s.}$ preserves both time-reversal symmetry and axial spin symmetry. The second term which is always included, and which describes forward scattering events, reads as

$$H_{f.s.} = \sum_{\sigma,\tau} \int_0^L dx\, f(x) \psi^\dagger_{\sigma,\tau}(x) \psi_{-\sigma,-\tau}(x). \tag{1.143}$$

Again, $f(x)$ is a parameter determining the term amplitude. As the backward scattering contribution, the forward scattering one $H_{f.s.}$ is also time-reversal invariant. It however breaks axial spin symmetry: in order to maintain the direction of motion, a spin-flip occurs. As we shall explain, the combination of $H_{b.s.}$ and $H_{f.s.}$ is extremely promising for designing heterostructures. The processes just described are shown in Fig. 1.26.

For a point-like quantum point contact located at $x = \overline{x}$ in the sample, $f(x)$, $b(x) \propto \delta(x - \overline{x})$. We are here interested in the opposite regime: let us assume $f(x)$ and $b(x)$ to be uniform, $f(x) = f$, $b(x) = b$[10]. In this case, $H_{f.s.}$ acts effectively as a spin-orbit coupling [200], splitting in energy same-chirality states by a quantity $\pm f$. On

[10]We will maintain this assumption also in the next Chapters, where we will deal with long Quantum Spin Hall constrictions (having length $\gg k_F^{-1}$).

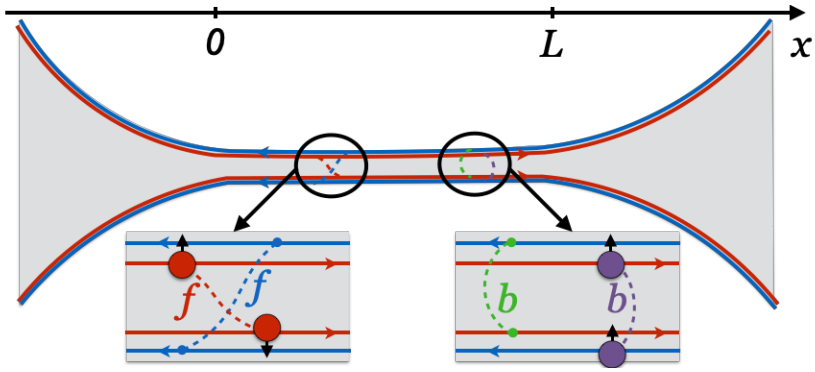

Figure 1.26: *Quantum Spin Hall constriction of length L, with the two possible inter-edge scattering mechanisms: the forward one denoted by f, and the backward one denoted by b.*

the other hand, $H_{b.s.}$ opens a gap large $2b$ at the Dirac point. The resulting energy spectrum for an infinite sample is shown in Fig. 1.27. Notably, in terms of spectral

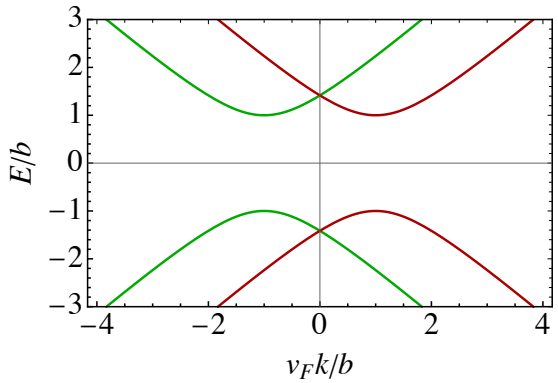

Figure 1.27: *Spectrum of the infinitely long Quantum Spin Hall constriction taking into account the forward and backward scattering processes. Different colors represent states having orthogonal spin. We have set $f/b = 1$.*

properties, either $E > 0$, $E < 0$ are equivalent to a spin-orbit coupled quantum wire, which is regarded as the main platform to realize Majorana fermions and parafermions. However, the Quantum Spin Hall Effect allows for cleaner samples and more easily conceivable multiterminal experiments. Moreover, it allows to overcome two issues concerning quantum wires: first, true quantum wires are not purely one-dimensional systems, and higher sub-bands can in principle contribute to the low-energy physics; second, detection schemes are limited by the absence of symmetries in the wire and in the leads. On the contrary, although the Quantum Spin Hall system is described by the same number of fermionic fields as a quantum wire, it naturally possesses a charge-conjugation symmetry and benefits from the helical nature of its channels. This enables to envision novel spin-selective detection schemes. Lastly, the constriction is able to make ferromagnetic barriers unessential in superconducting spintronics and topological quantum computation applications, which is extremely relevant since, to date, they were never successfully implanted on these systems. To summarize, the Quantum Spin Hall constriction appears as a symmetry enriched, spin-orbit coupled, quantum wire.

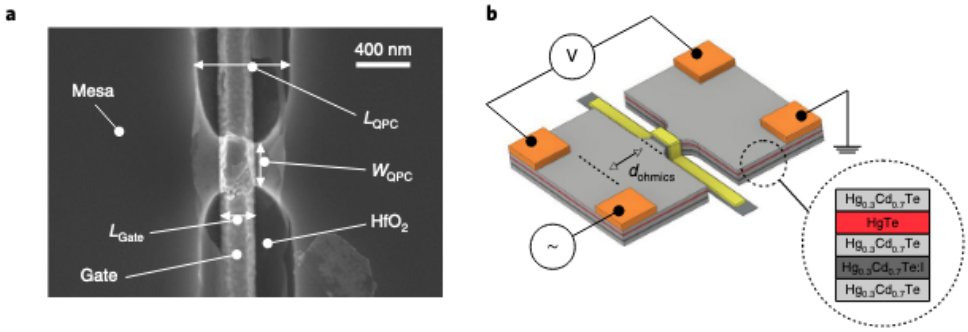

Figure 1.28: *(a) SEM image of the device, with the well visible narrow channel defined in the HgTe mesa. (b) A schematic of the constriction design and measurement setup. The yellow part is the gate electrode and the orange parts are the ohmic contacts for measurements. The central part is the one sketched in Fig. 1.26. Figures from [168], reproduced with permission from Springer Nature.*

A (long) Quantum Spin Hall constriction has been experimentally realized in 2020 [168], formed by wet chemical etching of the HgTe heterostructure and using a top gate electrode to tune the chemical potential. In that paper, the only experimental result reported in literature to date, the constriction was pinpointed by an interaction induced reduction of the conductance. A scanning electron microscope (SEM) image and a skecth of the experimental setup are shown in Fig. 1.28.

To conclude this Subsection, we anticipate here that it can happen that each scattering amplitude assumes two different values for different couples of channels involved. Namely, the dashed lines in Fig. 1.26 may correspond to $f_1 \neq f_2$ and $b_1 \neq b_2$. This phenomenon is known as edge reconstruction [197], and we will come back on that in Chapter 4. Its origin resides in spontaneous time-reversal symmetry breaking possibly arising due to a smooth confinement potential for the edge states. The basic idea is the following. Let us assume that the density of electrons is controlled by an external gate. In order to minimize the Coulomb energy, it is electrostatically convenient for the electron density to mimic the positive-charge distribution on the gate. If such distribution goes smoothly to zero near the edge of the system, the electron density can try to accommodate it by separation of the edge modes. The smoother the confining potential, the larger can be the separation between the edge modes. Then, for differently distanced couples of channels, the scattering amplitudes will change accordingly.

1.2.5 Potential applications of the helical edge

We have seen that the metallic edges of two-dimensional topological insulators represent a new and intriguing gapless electronic system. Their most promising feature in view of technological applications is spin-momentum locking, which allows for a purely electric manipulation of the spin degree of freedom, and might hence have a relevant impact in spintronics [121, 131, 145]. When proximitized with s-wave superconductors and eventually ferromagnetic barriers, systems featuring spin-momentum locking can furtherly exhibit topological superconductivity [62, 63] and odd-frequency superconductivity [22, 38, 60, 171, 174], with potential applications in superconducting spintronics [25, 112, 175]. Concerning topological quantum computation [124], Majorana bound states [63] (and, with strong electron–electron interactions, parafermions

[127, 192, 203]), may arise in topological heterostructures. Regarding Majorana bound states, these systems could in principle represent an alternative to spin–orbit coupled quantum wires in the presence of magnetic fields and induced superconductivity, which are nowadays regarded as the main platform.

In this Subsection, we will discuss in more details how to engineer, in principle, Majorana bound states with a two-dimensional topological insulator as a playground. This goal was already investigated by Fu and Kane both in two-dimensional [63] and in three-dimensional [62] topological insulators.

In the following discussion, the essential ingredient will be a single helical edge. We will make use of the building blocks introduced in Subsec. 1.2.4 and find under which conditions they can reproduce the physics of the renowned Kitaev model [96]. We start from the Hamiltonian introduced in Eq. (1.138)

$$H_{kin.} = \int dx\, \psi^\dagger(x)(-i\hbar\sigma_z v_F \partial_x - \mu)\psi(x), \tag{1.144}$$

where now $\psi(x) = (\psi_+(x), \psi_-(x))^T$, μ is the chemical potential, and we are assuming the ring-geometry in Fig. 1.29(a) with periodic boundary conditions. The edge states' dispersion corresponds to the blue and red lines in Fig. 1.29(b). To achieve topological (spinless) superconductivity, a term such as that H_Δ in Eq. (1.141) is enough. Indeed, as we already pointed out, the energy spectrum supports a single pair of Fermi points (as long as the Fermi level doesn't touch the bulk bands), and hence in some sense the system appears as effectively spinless. The presence of a superconductor superimposed on the helical edge (see Fig. 1.29(c)) gaps out the spectrum, which results in the (physical) quasiparticle energies

$$E_{1,2}(k) = \sqrt{(\pm\hbar v_F k - \mu)^2 + \Delta^2}, \tag{1.145}$$

describing a topological superconductor, as the weak-pairing phase of the Kitaev chain [96], with time-reversal symmetry.

However, in order to make clear the emergence of a p-wave type superconductivity, it is useful to introduce a time-reversal symmetry breaking term, similar to the one in Eq. (1.139) but with uniform magnetization:

$$H_B = -M_x \int dx \psi^\dagger(x)\sigma_x\psi(x), \tag{1.146}$$

where $M_x \geq 0$ corresponds to the Zeeman energy. For our purpose, differently from Eq. (1.139), it is sufficient to consider a Zeeman field only along the x axis. The effect of the Zeeman term alone is two-fold: it tilts the spin polarization of the edge states away from the z axis and opens a gap at their intersections. These effects are shown in Fig. 1.29(b) by the solid black lines and the arrows. For $\Delta = 0$, the spectrum is given by

$$\epsilon_{1,2}(k) = \mu \pm \sqrt{(v_F k^2) + M_x^2}, \tag{1.147}$$

and the gap at $k = 0$ is allowed by time-reversal symmetry breaking. The best way to understand the effect of H_Δ is to rewrite the total Hamiltonian $H = H_{kin.} + H_B + H_\Delta$ in terms of the operators $\psi_{1,2}(k)$ that diagonalize $H_{kin.} + H_B$ (thus corresponding to

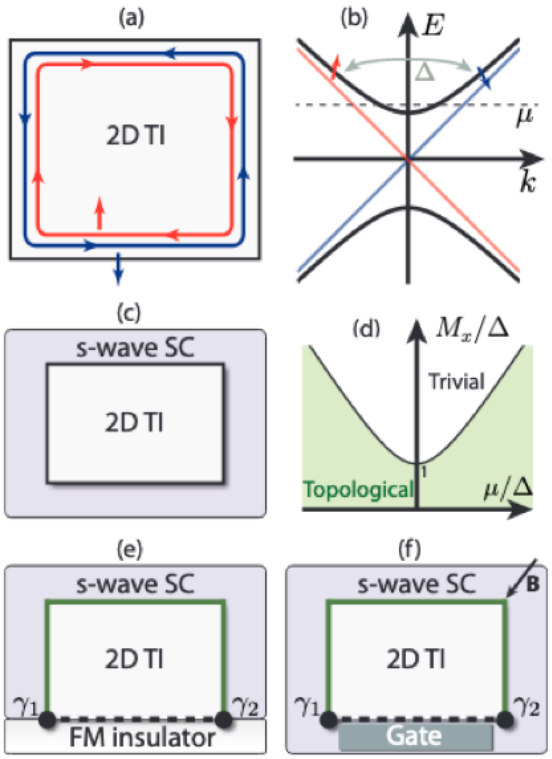

Figure 1.29: *(a) Schematic of the system, consisting in the two counter-propagating, helical edge states of a Quantum Spin Hall Insulator in a ring geometry. (b) The bare edge states' dispersion (red and blue lines) and the modified spectrum in the presence of a Zeeman term (black solid lines). (c) The system is proximitized by a s-wave superconductor, which pushes the edge into a topological superconducting phase such as the weak-pairing phase in Kitaev model. (d) Phase diagram of the system, elucidating the trivial and topological regimes as a function of M_x and μ. (e)-(f) Domain walls between topological (green lines) and trivial regions (dashed lines) localize Majorana zero-modes (denoted by $\gamma_{1,2}$). This can be done either with a ferromagnetic insulator (e) or with a Zeeman field with a proper tuning of μ by gating (f). Figure adapted with permission of IOP Publishing, Ltd, from [3]; permission conveyed through Copyright Clearance Center, Inc.*

electrons with energies $\epsilon_{1,2}$). Then H reads as

$$\begin{aligned} H = \int \frac{dk}{2\pi} [&\epsilon_1(k)\psi_1^\dagger(k)\psi_1(k) + \epsilon_2(k)\psi_2^\dagger(k)\psi_2(k) \\ &+\Delta_s(k)(\psi_2(-k)\psi_1(k) + h.c.) \\ &+\frac{\Delta_p(k)}{2}(\psi_1(-k)\psi_1(k) + \psi_2(-k)\psi_2(k) + h.c.)], \end{aligned} \tag{1.148}$$

where

$$\Delta_p(k) = \frac{v_F k \Delta}{\sqrt{(v_F k)^2 + M_x^2)}}, \quad \Delta_s(k) = \frac{M_x \Delta}{\sqrt{(v_F k)^2 + M_x^2)}}. \tag{1.149}$$

The first line of Eq. (1.148) describes the band energies of $H_{kin.} + H_B$, while the others represent the effect of superconductivity. In particular, the second line is the *inter*-band s-wave pairing, while the third is an *intra*-band p-wave pairing. The latter is shown in Fig. 1.29(b). Notice that $\Delta_p(k)$ must have odd parity since it couples electrons from a same band, but overall the Fermi statistics has to be respected. We have explicitly shown a fact we mentioned in the previous Subsection: the induced superconductivity is influenced by the properties of the hosting material. In this case, thanks to spin-orbit coupling, a p-wave pairing is effectively generated from an s-wave pairing.

If $M_x \gg \Delta$ and μ is tuned close to the bottom of the upper band, as in Fig. 1.29(b), it is straightforward to make a connection with the Kitaev model. The lower band is uninfluential, so that we can take $\psi_2 \to 0$. Also, the relevant momenta are those around $k = 0$, from which we can expand $\epsilon_1(k) \approx -(\mu - M_x) + v_F^2 k^2 / 2M_x \equiv -\mu' + k^2/2m'$. Moreover, $\Delta_p(k) \approx v_F \Delta k / M_x \equiv \Delta' k$. All in all, the effective Hamiltonian is

$$H' = \int dx \left[\psi_1^\dagger(x) \left(-\mu' - \frac{\partial_x^2}{2m'} \psi_1(x) \right) + \frac{\Delta'}{2}(-\psi_1(x) i\partial_x \psi_1(x) + h.c.) \right], \tag{1.150}$$

which is indeed the Hamiltonian for the continuum version of a p-wave superconductor in one dimension. This confirms that, for $M_x \gg \Delta$ and $|\mu| \gtrsim M_x$, the edge described by H corresponds to the topological weak-pairing phase of the Kitaev chain.

The (physical) quasiparticle energy spectrum of the full Hamiltonian in Eq. (1.148) is

$$E'_{1,2}(k) = \sqrt{\Delta^2 + \frac{\epsilon_1^2 + \epsilon_2^2}{2} \pm (\epsilon_1 - \epsilon_2)\sqrt{\Delta_s^2 + \mu^2}}, \tag{1.151}$$

with a gap closing for $M_x^2 = \Delta^2 + \mu^2$. Since we already found that the topological phase corresponds to $M_x \gg \Delta$ and $|\mu| \gtrsim M_x$, we can conclude that in the most general case the topological superconductivity regime is given by

$$M_x < \sqrt{\Delta^2 + \mu^2}, \tag{1.152}$$

which is the one with a superconductivity-dominated gap. Notice that this includes also the case $M_x = 0$, as we briefly mentioned before introducing H_B. The resultant phase diagram is depicted in Fig. 1.29(d).

For now, we have obtained a one-dimensional topological superconductor from a ring-shaped helical edge. In order to isolate Majorana zero-modes, we have to introduce domain walls separating differently gapped (topological/trivial) regions. Two

possibilities to do that are shown in Figs. 1.29(e)-(f). In panel (e), the upper and lateral sides of the system are gapped by superconductivity (green regions), while the lower side is gapped by the Zeeman term (dashed region). This is in principle achievable via proximization to a ferromagnet [59, 150] (and, importantly, the chemical potential has to be set within the gap). A second option, shown in panel (f), is to introduce both superconductivity and the magnetic term everywhere in the system, with $M_x > \Delta$, and to tune the chemical potential through gates such that $M_x > \sqrt{\Delta^2 + \mu^2}$ only on the lower arm.

As a final remark, we underline that $M_x > \Delta$ doesn't forbid to be far below the superconductor's critical field (the Zeeman energy in the topological insulator can prevail the one in the superconductor thanks to the spin-orbit enhancement of the g-factor, see [199]).

CHAPTER 2

Josephson junctions and interference effects

In the previous Chapter we have introduced the Quantum Spin Hall edge states and the main possibilities to create functional nanostructures exploiting their properties. When discussing the proximity effect, we mentioned that so-called topological Josephson junctions can be realized, namely structures made of two superconducting leads connected by a Quantum Spin Hall sample.

The first part of this Chapter is devoted to general aspects of Josephson junctions. In Sec. 2.1 we describe the Josephson effect, which consists in a non-dissipative current flowing through such junctions even without the need for external electromagnetic fields. In Sec. 2.2 we introduce a magnetic field piercing the junction and describe the interference effects which arise, with a particular focus on the interference pattern. At the end of the Section we specialize to the case of Quantum Spin Hall-based Josephson junctions. Lastly, in Sec. 2.3, we discuss under which circumstances and in what way transport can become non-local, with Cooper pairs splitting through the junction.

2.1 The Josephson effect

In this Section, we provide an overview of the Josephson effect. It is possible to give a complete description of the phenomenon in terms of a microscopic theory, based on a tunneling Hamiltonian formalism. This can be found for instance in [5, 12], but also in [41, 94]. In Sec. 2.3 we will deal with a microscopic tunneling model applied to a topological Josephson junction in a similar spirit. However, in the present Section we propose a simpler handling of the topic, mainly focusing on the phenomenological aspects. Some of the first experimental evidencies of the phenomenon are also mentioned.

In Subsec. 2.1.1 we discuss how a superconductor can be described as a quantum

state described by a macroscopic complex quantity, the Ginzburg-Landau order parameter, which is related to the local number of Cooper pairs. Relying on the Ginzburg-Landau description, in Subsec. 2.1.2 we will easily derive the DC Josephson effect, which consists in a supercurrent flow across a Josephson junction in the absence of applied voltage bias, as far as the phases of the superconducting order parameters are different. In Subsec. 2.1.3 we will present Feynman's model [56], based on a "two-level system" picture, which allows to understand how the effect is modified by the presence of a constant bias (AC Josephson effect). Lastly, we will mention the consequences of an AC voltage and the physics of the so-called Shapiro steps.

We will mainly follow [12, 76, 179], but the interested reader can also refer to [178].

2.1.1 The order parameter for a superconductor

The aim of this Subsection is to introduce the order parameter associated to a superconductor. To do so, we have to give some hints about the Ginzburg-Landau description of superconductivity.

In 1950, Ginzburg and Landau [105] provided a phenomenological description of superconductivity as a second-order phase transition. In particular, they introduced a macroscopic and complex quantity $\psi(\mathbf{r})$, the order parameter, which gives a measure of the order in the superconducting phase (that is, below the critical temperature T_c). At any given temperature, such order parameter is related to the local density of Cooper pairs as

$$\rho = |\psi(\mathbf{r})|^2. \tag{2.1}$$

The theory is developed with a variational method applied to a supposed expansion of the free-energy in powers of $|\psi(\mathbf{r})|^2$ and $|\boldsymbol{\nabla}\psi(\mathbf{r})|^2$. This leads to two coupled differential equations for $\psi(\mathbf{r})$ and the vector potential $\mathbf{A}(\mathbf{r})$, the Ginzburg-Landau equations.

Given its phenomenological origin, Ginzburg-Landau theory initially received little consideration. However, in 1959 [73], Gor'kov showed that the theory could be obtained as a limiting case of the microscopic theory of BCS [11] near T_c, generalized to include spatially varying situations. In this reassessment of the theory, $\psi(\mathbf{r})$ turned out to be proportional to the BCS gap parameter $\Delta(\mathbf{r})$. A strongpoint of Ginzburg-Landau theory is that, by focusing on the overall free energy instead of on the detailed spectrum of excitations, a macroscopic discussion of superconductivity is possible. We will not revise Gor'kov derivation, and rather move directly to the phenomenological treatment by Ginzburg and Landau.

The basic assumption of Ginzburg-Landau theory is that the superconductor free energy density, around T_c, can be written as a functional of the order parameter of the form

$$f_S(T, \psi(\mathbf{r})) = f_N(T) + \alpha(T)|\psi(\mathbf{r})|^2 + \frac{1}{2}\beta(T)|\psi(\mathbf{r})|^4 + \frac{1}{2m^*}\left|\left(\mathbf{p} - \frac{e^*}{c}\mathbf{A}\right)\psi(\mathbf{r})\right|^2, \tag{2.2}$$

where $f_N(T)$ is the free energy density in the normal phase ($\psi = 0$) and α and β are phenomenological quantities. For now m^*, e^* are just parameters, but they will turn out to be the effective mass and charge of superconducting particles (*i.e.* Cooper pairs). The free energy cannot depend on the global phase of $\psi(\mathbf{r})$, but just on its modulus, because the global phase of quantum states is not observable. Moreover, odd powers

are excluded since they are not differentiable at $\psi = 0$. For a deeper insight into Eq. (2.2), let us consider the simpler case $\mathbf{A}(\mathbf{r}) = 0$ and $\psi(\mathbf{r}) =$ constant. Then

$$f_S(T,\psi) - f_N(T) = \alpha(T)|\psi|^2 + \frac{1}{2}\beta(T)|\psi|^4, \tag{2.3}$$

namely the change in free energy from the normal ($\psi = 0$) to the superconducting ($\psi \neq 0$) phase is nothing but an expansion in $|\psi|^2$ up to second order. Higher order terms can be reasonably neglected as long as $|\psi|^2$ is small, which holds true near the transition point. β has to be positive, otherwise the lowest free energy would correspond to arbitrarily large values of $|\psi|^2$, where the expansion is certainly non valid. Moreover, we know that T_c is, by definition, the highest temperature at which $|\psi|^2 \neq 0$ gives a lower free energy than $|\psi|^2 = 0$. The parameter α has thus to change sign at T_c, such that the free energy change has a negative minimum for a finite $|\psi|^2$, see Fig. 2.1.

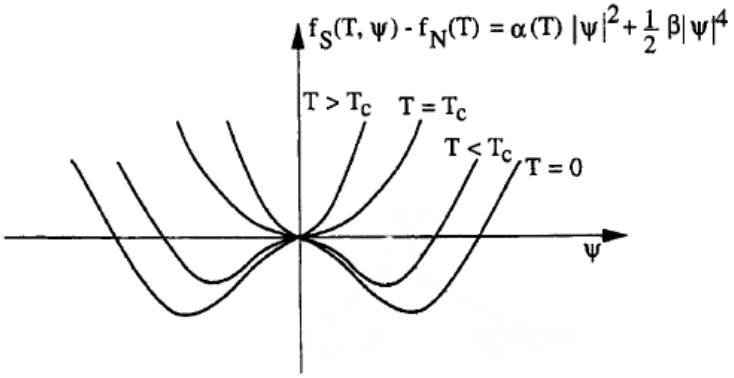

Figure 2.1: *Schematic behavior of the Ginzburg-Landau free-energy change, $f_S(T,\psi) - f_N(T)$, as a function of the order parameter ψ, in the absence of fields and gradients. Figure adapted from [76], copyright © 2000 ACADEMIC PRESS. Published by Elsevier Ltd All rights reserved.*

By minimizing the overall free energy – the volume integral $F_S = \int d\mathbf{r} f_S(T,\psi)$ – with respect to variations of ψ (or ψ^*) and of $\mathbf{A}$, one obtains the two following Ginzburg-Landau equations[1]

$$\frac{1}{2m^*}\left(\mathbf{p} - \frac{e^*}{c}\mathbf{A}\right)^2 \psi(\mathbf{r}) + \beta|\psi(\mathbf{r})|^2\psi(\mathbf{r}) = -\alpha(T)\psi(\mathbf{r}), \tag{2.4a}$$

$$\mathbf{J}_S = \frac{-i\hbar e^*}{2m^*}[\psi^*(\mathbf{r})\boldsymbol{\nabla}\psi(\mathbf{r}) - \psi(\mathbf{r})\boldsymbol{\nabla}\psi^*(\mathbf{r})] - \frac{e^{*2}}{m^*c}|\psi(\mathbf{r})|^2\mathbf{A}(\mathbf{r}). \tag{2.4b}$$

The first is analogous to the Schrödinger equation for a free particle with energy eigenvalue $-\alpha$, with an additional nonlinear term. The second has the usual form of a

[1] Explicitely, we start from the extremum principle $\delta F_S = 0$. We define

$$\psi(\mathbf{r}) = \psi_0(\mathbf{r}) + \eta(\mathbf{r}),$$

where $\psi_0(\mathbf{r})$ is the solution that we are looking for, and $\eta(\mathbf{r})$ is a small deviation from it. We can write down $F_S[\psi_0 + \eta]$ up to the linear order in η, η^*, and require that such linear terms vanish for any $\eta(\mathbf{r}), \eta^*(\mathbf{r})$ (since $\psi_0(\mathbf{r})$ minimizes F_S). This is equivalent to demand that their prefactors vanish for all $\mathbf{r}$, obtaining Eq. (2.4a) after dropping the subscript "0". A similar approach, starting from

$$A(\mathbf{r}) = A_0(\mathbf{r}) + a(\mathbf{r}),$$

leads to Eq. (2.4b). See [178] for more details.

quantum current density for particles having mass m^*, charge e^* and wavefunction $\psi(\mathbf{r})$. Without delving into the details, but relying on flux-quantization experiments [46, 51, 178], it is natural to set $e^* = 2e$, with e the electron charge. Concerning m^*, one could then choose twice the effective electron mass in the metal. Since $m^*_{\text{metal}} \approx m$, with m the bare electron mass, it is common to simply set $m^* = 2m$.

We have found that the order parameter can be regarded as a wavefunction for "superconducting electrons" (namely, for Cooper pairs). A single wavefunction captures a macroscopic number of electrons which are assumed to "condense" in a same quantum state. In this sense, the superconducting state is macroscopic, and "particles" with charge $2e$ and mass $2m$ are described by a whole wavefunction

$$\psi(\mathbf{r}) = |\psi(\mathbf{r})|e^{i\theta(\mathbf{r})}. \tag{2.5}$$

Eq. (2.4b) becomes

$$\mathbf{J}_S = |\psi(\mathbf{r})|^2 \left[\frac{e\hbar}{m}\boldsymbol{\nabla}\theta(\mathbf{r}) - \frac{2e^2}{mc}\mathbf{A}(\mathbf{r})\right] = \frac{\rho e}{m}\left[\hbar\boldsymbol{\nabla}\theta(\mathbf{r}) - \frac{2e}{c}\mathbf{A}(\mathbf{r})\right]. \tag{2.6}$$

Having summarized what is the order parameter describing a superconductor, a last comment is in order. Eq. (2.6) states that the supercurrent, which is an observable physical quantity, depends on the phase of the macroscopic wavefunction and on the vector potential, which cannot be accessed in experiments and are only defined up to gauge transformations. We have to require the gauge-invariancy of $\mathbf{J}_S$. This is ensured if, under a transformation of the vector potential $\mathbf{A} \to \mathbf{A} + \boldsymbol{\nabla}\chi$, the phase varies accordingly as $\theta \to \theta + \frac{2e}{\hbar c}\chi$. The quantity

$$\boldsymbol{\gamma} = \boldsymbol{\nabla}\theta(\mathbf{r}) - \frac{2e}{\hbar c}\mathbf{A}(\mathbf{r}) \tag{2.7}$$

is called the gauge-invariant phase gradient.

We can now move to the description of the Josephson effect. Let us suppose to make a so-called superconducting S-I-S junction, made of two superconducting films of the same material, having superconducting gap Δ, separated by an insulating layer. If the intermediate layer is thin enough, quasiparticles ("normal electrons") can flow from one superconductor to the other by means of tunneling. In particular, at $T = 0$ we expect no tunneling as long as the applied voltage to the junction is smaller than $2\Delta/e$, which gives a measure of the energy gap voltage[2]. On the other hand, if $eV \geq 2\Delta$, a Cooper pair can be broken into two normal electrons which can then tunnel across the barrier [76]. It is natural to ask whether a sufficiently thin barrier would allow an entire Cooper pair to tunnel. Around 1962, this possibility was considered as highly implausible to be measured: being the tunneling probability for a single electron very small (typically, $\lesssim 10^{-4}$), that same probability squared for a Cooper pair would be even smaller. However, B. D. Josephson showed that the probability for a Cooper pair to tunnel through the barrier is the same as for a single electron. The process does not correspond to the leakage of two incoherent electron waves; much differently, it is the macroscopic wavefunction describing the entire ensemble of superconducting electrons

[2]For different superconductors, the threshold would be $(\Delta_1 + \Delta_2)/e$.

that tunnels through the barrier. The electron pair correlations and the superconducting long-range order extend through the barrier. In some sense, the system behaves as a single superconductor, and paired electrons flow without dissipation [93]. Only one year after Josephson's prediction, P. W. Anderson and J. M. Rowell gave the first experimental confirmation of the effect [7].

2.1.2 The DC Josephson effect

Let us consider an S-I-S junction made now of two different superconductors, separated by a barrier of thickness a, as in Fig. 2.2. For a very thick barrier, the two superconductors are characterized by the order parameters $\psi_l = |\psi_l|e^{i\theta_l}$ and $\psi_r = |\psi_r|e^{i\theta_r}$. Each of them is assumed to be uniform within the entire volume of the corresponding superconductor. However, if the insulating barrier is thin, we expect the two superconducting order parameters to decay within such region. A reasonable ansatz for the order parameter in the barrier region is the linear combination

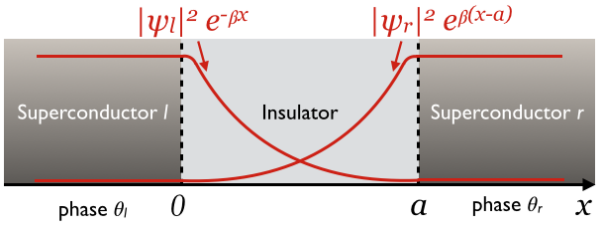

Figure 2.2: *Junction between two superconductors separated by an insulating barrier of thickness a. In red it is shown the behavior of the order parameter wavefunctions, decaying within the barrier.*

$$\psi(x) = \psi_l e^{-\beta x} + \psi_r e^{\beta(x-a)}, \tag{2.8}$$

where β represents the damping within the barrier. Plugging Eq. (2.8) into Eq. (2.4b) in the absence of magnetic fields, we obtain the Josephson supercurrent density

$$\begin{aligned} J_S &= \frac{-i\hbar e}{2m}\left[\psi^*(x)\frac{d}{dx}\psi(x) - \psi(x)\frac{d}{dx}\psi^*(x)\right] = \frac{-i\hbar e}{m}\beta e^{-\beta a}(\psi_l^*\psi_r - \psi_l\psi_r^*) \\ &= \frac{-i\hbar e}{m}\beta e^{-\beta a}|\psi_r||\psi_l|(e^{i(\theta_r-\theta_l)} - e^{-i(\theta_r-\theta_l)}) = \frac{2\hbar e}{m}\beta e^{-\beta a}|\psi_r||\psi_l|\sin(\theta_r-\theta_l) \\ &\equiv J_c \sin(\theta_r - \theta_l). \end{aligned} \tag{2.9}$$

The Josephson supercurrent flowing between two superconductors separated by a thin insulating barrier is thus of the form[3]

$$I = I_c \sin(\theta_r - \theta_l), \tag{2.10}$$

where I_c is the critical or maximum Josephson supercurrent and depends on the (geometrical and physical) properties of the junction. The expression above is the so-called current-phase relation of the junction.

[3] With a more general approach, I can be written as a Fourier series of both sine and cosine terms. However, due to symmetry constraints, in most cases all the coefficients of the cosine terms must vanish. An example is time-reversal symmetry, which requires $I(\theta_r - \theta_l) = -I(\theta_l - \theta_r)$, excluding any cosine term from a Fourier series. In the next Chapters we will discuss the physical consequences of time-reversal symmetry breaking in Josephson junctions.

We have here followed a heuristic approach and in the simplified case without applied bias and magnetic field. We now discuss a different derivation due to R. Feynman [56]. Though very simple, it allows to understand all the essential physics even in the presence of a voltage bias. Later on, we will extensively discuss the effects of a magnetic field.

2.1.3 The AC Josephson effect and Shapiro steps

Let us consider, as before, a superconductor-barrier-superconductor junction as in Fig. 2.2, with superconducting wavefunctions $\psi_{r/l}$. It has been said that such wavefunctions describe a macroscopic state, $|\psi|^2$ corresponding to the Cooper pair density ρ. From now on in this Subsection, $|r\rangle$ and $|l\rangle$ will denote the base state for the right and left superconductor, respectively. Then, we have

$$\langle l|\psi_l^*\psi_l|l\rangle = |\psi_l|^2 = \rho_l, \qquad \langle r|\psi_r^*\psi_r|r\rangle = |\psi_r|^2 = \rho_r. \tag{2.11}$$

Taking into account the weak coupling between the superconductors, some kind of transition between $|r\rangle$ and $|l\rangle$ states can occur owing to the finite overlap of ψ_l and ψ_r, as mentioned in the previous Subsection. A state vector will then be of the form

$$|\psi\rangle = \psi_r\,|r\rangle + \psi_l\,|l\rangle\,, \tag{2.12}$$

namely a particle can be either in a left or in a right state with associated amplitude $\psi_{r/l}$. The system evolves according to

$$i\hbar\frac{\partial\,|\psi\rangle}{\partial t} = H\,|\psi\rangle\,, \tag{2.13}$$

where the Hamiltonian is made of three terms,

$$H = H_l + H_r + H_T. \tag{2.14}$$

Here $H_l = E_l\,|l\rangle\,\langle l|$ and $H_r = E_r\,|r\rangle\,\langle r|$ are the unperturbed left and right Hamiltonians, with $E_{r/l}$ the superconductors' ground state energies, and

$$H_T = K(|l\rangle\,\langle r| + |r\rangle\,\langle l|) \tag{2.15}$$

is the interaction (tunneling) term. K is the coupling amplitude of the two state system and depends on the junction's properties. With no vector potential, K can be assumed to be real[4] [12]. By projecting the Schrödinger equation, Eq. (2.13), on the two basis states, we obtain

$$i\hbar\frac{\partial\psi_r}{\partial t} = E_r\psi_r + K\psi_l, \tag{2.18a}$$

$$i\hbar\frac{\partial\psi_l}{\partial t} = E_l\psi_l + K\psi_r. \tag{2.18b}$$

[4] In order to take into account a vector potential $\mathbf{A}$, the coupling amplitude K should be modified by a phase factor as [44]

$$K_{\mathbf{A}} \equiv \langle l|\,H_T\,|r\rangle_{\mathbf{A}} = \langle l|\,H_T\,|r\rangle_{\mathbf{A}=0}\,e^{i\frac{2e}{\hbar c}\int_r^l \mathbf{A}\cdot d\mathbf{l}}. \tag{2.16}$$

In this case, moving on with the calculations, we would obtain

$$J_S(t) = J_c\sin\left[(\theta_l-\theta_r) - \frac{2e}{\hbar c}\int_r^l \mathbf{A}\cdot d\mathbf{l}\right], \qquad \frac{\partial}{\partial t}\left[(\theta_l-\theta_r) - \frac{2e}{\hbar c}\int_r^l \mathbf{A}\cdot d\mathbf{l}\right] = \frac{2eV}{\hbar}. \tag{2.17}$$

If a constant bias difference V is included, the two chemical potentials $\mu_{r/l}$ of the superconductors are shifted by a quantity eV. Hence[5] $E_l - E_r = 2eV$. We set the zero of the energy halfway, such that

$$i\hbar\frac{\partial\psi_r}{\partial t} = -eV\psi_r + K\psi_l, \tag{2.19a}$$

$$i\hbar\frac{\partial\psi_l}{\partial t} = eV\psi_l + K\psi_r. \tag{2.19b}$$

Substituting $\psi_{r/l} = \sqrt{\rho_{r/l}}e^{i\theta_{r/l}}$ and separating the real and imaginary terms, we get

$$\begin{cases} \frac{\partial\rho_l}{\partial t} = \frac{2}{\hbar}K\sqrt{\rho_l\rho_r}\sin(\theta_l - \theta_r) \\ \frac{\partial\rho_r}{\partial t} = -\frac{2}{\hbar}K\sqrt{\rho_l\rho_r}\sin(\theta_l - \theta_r) \end{cases}, \qquad \begin{cases} \frac{\partial\theta_l}{\partial t} = \frac{K}{\hbar}\sqrt{\frac{\rho_l}{\rho_r}}\cos(\theta_l - \theta_r) + \frac{eV}{\hbar} \\ \frac{\partial\theta_r}{\partial t} = \frac{K}{\hbar}\sqrt{\frac{\rho_l}{\rho_r}}\cos(\theta_l - \theta_r) - \frac{eV}{\hbar} \end{cases}. \tag{2.20}$$

The tunneling supercurrent density is given by $J_S \equiv e^*\frac{\partial\rho_l}{\partial t} = -e^*\frac{\partial\rho_r}{\partial t}$, whence

$$J_S(t) = \frac{2e^*K}{\hbar}\sqrt{\rho_l\rho_r}\sin(\theta_l - \theta_r). \tag{2.21}$$

If $e^* = 2e$ and if we assume two identical superconductors $\rho_l = \rho_r = \rho$,

$$J_S(t) = J_c\sin(\theta_l - \theta_r), \tag{2.22}$$

with $J_c = 4eK\rho/\hbar$ the critical supercurrent density[6]. Notice that we recover the structure of Eq. (2.9), but now with a time dependence owing to

$$\frac{\partial(\theta_l - \theta_r)}{\partial t} = \frac{2eV}{\hbar}. \tag{2.23}$$

The last two equations are the Josephson equations. If the potential across the junction is zero, $V = 0$, we get that the phase difference is constant and any finite supercurrent density with intensity ranging from $-J_c$ to $+J_c$ can flow through the junction. This is the DC Josephson effect we already found. The first observation dates back to 1963 by P. W. Anderson and J. M. Rowell [7]. Later, in 1965, T. I. Smith measured the voltage developed across the junction in the DC regime [164]. In particular, he measured the persistent current in superconducting loops with an inserted junction, getting an upper bound of 4×10^{-16} V. A typical voltage-current behavior is shown in Fig. 2.3, with the well visible zero-resistance (dissipationless) spike at $V = 0$. When the current exceeds the value $I_c = J_c\mathcal{V}$, where $\mathcal{V}$ is the volume of each superconductor, a finite voltage appears across the junction. In the Figure, this appears as a switching from a zero-voltage state to a quasiparticle branch of the $I - V$ characteristic curve. So, whereas from Eq. (2.6) the supercurrent within each superconductor is due to the phase gradient, in a Josephson junction it originates from the phase difference between the two weakly coupled superconductors. Let us suppose now that a non-zero constant voltage is applied. Then, from Eq. (2.23) we have

$$\theta_l - \theta_r = (\theta_l - \theta_r)_0 + \frac{2eV}{\hbar}t, \tag{2.24}$$

[5] $E_{r/l} = 2\mu_{r/l}$ for an isolated superconductor, see [12].

[6] The supercurrent is obtained by multiplying by the superconductors' volume.
Note that in order to keep the particle densities in the superconducting electrodes constant, the junction has to be attached to a current source. The current source adds and removes charges from the two superconductors keeping ρ constant. Such feeding currents are not included in the equations above, since they would not change the expressions of the tunnel pair current density.

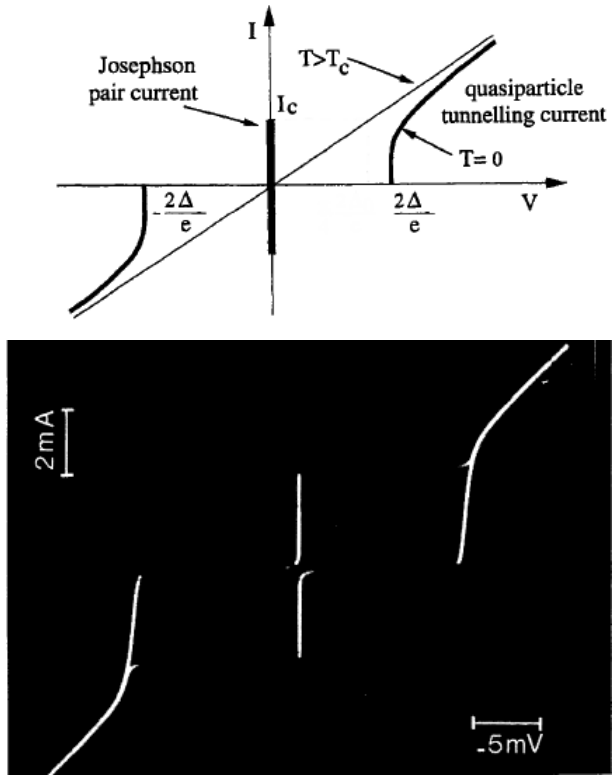

Figure 2.3: *Upper panel: scheme of the (direct) $I-V$ characteristic curve (at $T=0$) of an S-I-S junction displaying the Josephson current. When $V=0$, a direct supercurrent can flow (DC Josephson effect, up to a maximum value I_c). For $|V|>2\Delta/e$ the quasiparticle tunneling current is shown. Figure adapted from [76], copyright © 2000 ACADEMIC PRESS. Published by Elsevier Ltd All rights reserved. Lower panel: same characteristic curve for a $Sn-Sn_xO_y-Sn_x$ junction at a temperature $T=1.52\,K$. Figure from [12], copyright © 1982 by John Wiley & Sons, Inc.*

where $(\theta_l-\theta_r)_0$ is the superconducting phase difference with no bias, and the resulting supercurrent density is an AC one,

$$J_S(t)=J_c\sin\left[(\theta_l-\theta_r)_0+\frac{2eV}{\hbar}t\right]. \tag{2.25}$$

Accordingly, the Josephson supercurrent is

$$I(t)=I_c\sin\left[(\theta_l-\theta_r)_0+\frac{2eV}{\hbar}t\right]. \tag{2.26}$$

This is the AC Josephson effect, and the angular frequency is given by $\omega_J=2eV/\hbar$, with

$$\frac{\omega_J}{2\pi V}=483.597898(19)\frac{\text{MHz}}{\mu\text{V}}. \tag{2.27}$$

As Josephson himself suggested, a convenient way to observe the AC supercurrent is to apply to the junction a constant voltage V and a radiofrequency or microwave voltage, such as $V_r\cos(\omega_r t)$. In this case, Eq. (2.23) becomes

$$\frac{\partial(\theta_l-\theta_r)}{\partial t}=\frac{2eV}{\hbar}+\frac{2eV_r}{\hbar}\cos(\omega_r t). \tag{2.28}$$

After integration, we get

$$\theta_l - \theta_r = (\theta_l - \theta_r)_0 + \frac{2eV}{\hbar}t + \frac{2eV_r}{\hbar\omega_r}\sin(\omega_r t). \tag{2.29}$$

Finally, the supercurrent is

$$I(t) = I_c \sin\left[(\theta_l - \theta_r)_0 + \frac{2eV}{\hbar}t + \frac{2eV_r}{\hbar\omega_r}\sin(\omega_r t)\right], \tag{2.30}$$

which is frequency modulated. Leveraging

$$\cos(a\sin x) = \sum_{n=-\infty}^{+\infty} J_n(a)\cos(nx), \qquad \sin(a\sin x) = \sum_{n=-\infty}^{+\infty} J_n(a)\sin(nx), \tag{2.31}$$

where $J_n(x)$ are Bessel functions of first kind of order n, we have

$$\sin(b + a\sin x) = \sum_{n=-\infty}^{+\infty} J_n(a)\sin(b + nx). \tag{2.32}$$

Substituting into Eq. (2.30), one obtains

$$I(t) = I_c \sum_{n=-\infty}^{+\infty} J_n\left(\frac{2eV_r}{\hbar\omega_r}\right)\sin\left[(\theta_l - \theta_r)_0 + \left(\frac{2eV}{\hbar} + n\omega_r\right)t\right]. \tag{2.33}$$

Since Josephson junctions are often considered in circuit configurations in parallel with a resistance R, which therefore acts as a shunt, an additional shunt current V/R has to be included in the total current,

$$I(t) = \frac{V}{R} + I_c \sum_{n=-\infty}^{+\infty} J_n\left(\frac{2eV_r}{\hbar\omega_r}\right)\sin\left[(\theta_l - \theta_r)_0 + \left(\frac{2eV}{\hbar} + n\omega_r\right)t\right]. \tag{2.34}$$

The DC part of the current is therefore V/R unless

$$2eV = -n\hbar\omega_r. \tag{2.35}$$

For such values of voltage, an additional zero-frequency contribution arises, given by

$$I_c J_n\left(\frac{2eV_r}{\hbar\omega_r}\right)\sin(\theta_l - \theta_r)_0. \tag{2.36}$$

The resulting DC current increases linearly as V/R with the bias, except when the latter satisfies Eq. (2.35), where it suddenly jumps, and reads as

$$\begin{aligned}\langle I(t)\rangle &= \frac{V}{R} + I_c J_n\left(\frac{2eV_r}{\hbar\omega_r}\right)\sin(\theta_l - \theta_r)_0 \\ &\in \left[\frac{V}{R} - I_c J_n\left(\frac{2eV_r}{\hbar\omega_r}\right), \frac{V}{R} + I_c J_n\left(\frac{2eV_r}{\hbar\omega_r}\right)\right].\end{aligned} \tag{2.37}$$

These jumps are called Shapiro spikes and are shown in Fig. 2.4. In reality, circuits

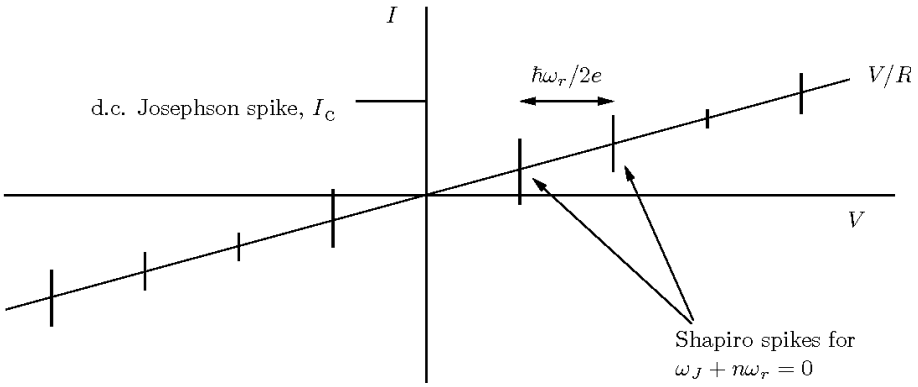

Figure 2.4: *DC current of a Josephson junction driven by an AC voltage, with the well visible Shapiro spikes of width $\hbar\omega_r/2e$. Figure adapted from [135].*

are usually driven by a current instead of a voltage. The plot of the DC current versus the average voltage exhibits a simple ladder behavior, shown in Fig. 2.5. The corresponding steps are known as Shapiro steps after S. Shapiro, who first observed this phenomenon in 1963 [157]. Their appearance follows naturally from the discussion above, occurring precisely when the average voltage matches $\langle V \rangle = n\hbar\omega_r/2e$, as described for the Shapiro spikes.

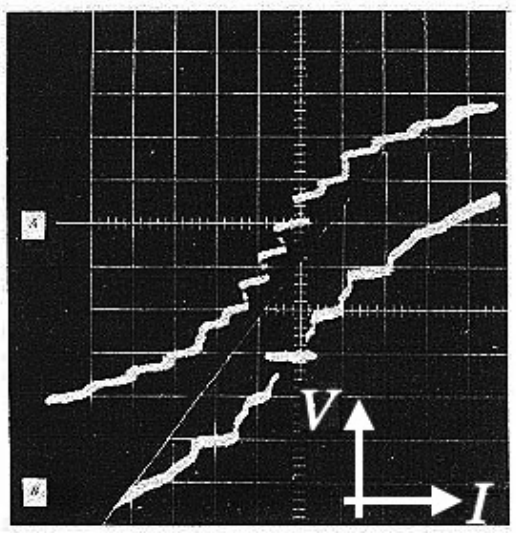

Figure 2.5: *Microwave power at 9300 MHz (A) and 24850 MHz (B) giving rise to many zero-slope regions spaced at V or $2V$. For A, $2V = 38.5\,\mu V$ and for B $2V = 103\,\mu V$. The vertical scale is $58.8\,\mu V/cm$ for A and $50\,\mu V/cm$ for B. The horizontal scale is $67\,nA/cm$ for A and $50\,\mu A/cm$ for B. Adapted with permission from [157]. Copyright 2024 by the American Physical Society.*

To conclude this discussion, we emphasize that the Josephson effect does not only occur in the presence of a very thin insulating barrier, as in its original formulation. Indeed, the superconductors can be linked via a Quantum Hall or a Quantum Spin Hall insulator – as we mentioned in the previous Chapter – or via a ferromagnet, and the link is not necessarily as thin as in the pioneering works by Josephson (tens of Å), as we will see.

2.2 Quantum interference in the Josephson effect

In this Section, we want to analyze the consequences on the Josephson effect of a magnetic field applied to the junction. In Subsec. 2.2.1 we will first discuss how the gauge-invariant phase difference and the current-phase relation are modified. We will emphasize the important role played by the supercurrent density distribution, and show how the latter can be related to the so-called interference pattern within the Dynes-Fulton description. To this regard, we will take into account both uniform and non-uniform supercurrent density distributions, and will revise some relevant examples. In Subsec. 2.2.2 we will present an experiment which applies the introduced concepts on measurements in topological Josephson junctions. We will conclude by commenting on a similar experiment which importantly sheds light on the fragility of Dynes-Fulton's hypothesis of local nature of the supercurrent, an issue we will investigate in Sec. 2.3.

2.2.1 Dynes and Fulton approach and the interference pattern

Gauge-invariant phase difference with a magnetic field

Let us consider the junction depicted in Fig. 2.6, pierced by a magnetic field along the z direction, $\mathbf{B} = B\mathbf{e}_3$. We draw our attention to the effects of the magnetic field on the phase difference from the left to the right side of the barrier defined in a gauge-invariant way. We are interested in understanding how this quantity changes as a function of the y position. To this aim, we can consider a section of the junction in the xy plane. We will see that the external magnetic field generates spatial changes of the gauge-invariant phase difference, giving rise to spatial interference phenomena in Josephson supercurrents. The resulting interference effect will be conceptually analogous to the diffraction at a slit in optics.

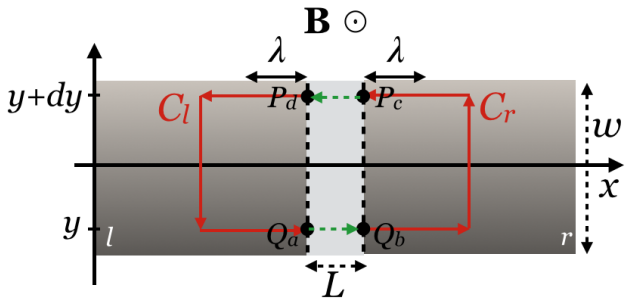

Figure 2.6: *Sketch of the junction under consideration, having width w and barrier's thickness L. The two superconductors are labeled by r, l and assumed to have the same London penetration depth λ. The London penetration depth represents the characteristic decay length over which an applied field decays exponentially inside a superconductor.*

With reference to Fig. 2.6, we determine the phase shift introduced by $\mathbf{B}$ between two positions P and Q along the y-axis separated by an infinitesimal distance dy. The

starting point is

$$\oint_C \nabla\theta \cdot d\mathbf{l} = 2\pi n$$
$$= \underbrace{(\theta_{Q_b} - \theta_{Q_a})}_{I} + \underbrace{(\theta_{P_c} - \theta_{Q_b})}_{II} + \underbrace{(\theta_{P_d} - \theta_{P_c})}_{III} + \underbrace{(\theta_{Q_a} - \theta_{P_d})}_{IV} + 2\pi n, \quad (2.38)$$

where n is an integer, θ is the gauge-invariant superconducting phase difference and C is the closed loop in Fig. 2.6, made by the solid red lines C_r and C_l and the dashed green ones. From Eq. (2.6) in the previous Subsection, we know that within each superconductor (labeled by r, l) the gauge-invariant phase gradient is

$$\boldsymbol{\nabla}\theta_{l,r} = \frac{2e}{\hbar c}\left(\frac{mc}{2e^2\rho}\mathbf{J}_S + \mathbf{A}\right), \quad (2.39)$$

where $\boldsymbol{\nabla}\times\mathbf{A} = \mathbf{B}$. We will neglect self-fields originated by the Josephson supercurrent itself, and assume that the magnetic field throughout the junction coincides with the external $\mathbf{B}$. Terms II and IV in Eq. (2.38) are hence

$$\theta_{P_c} - \theta_{Q_b} = \int_{Q_b}^{P_c} \nabla\theta \cdot d\mathbf{l} = \frac{2e}{\hbar c}\int_{Q_b}^{P_c}\left(\frac{mc}{2e^2\rho}\mathbf{J}_S + \mathbf{A}\right)\cdot d\mathbf{l}, \quad (2.40a)$$

$$\theta_{Q_a} - \theta_{P_d} = \int_{P_d}^{Q_a} \nabla\theta \cdot d\mathbf{l} = \frac{2e}{\hbar c}\int_{P_d}^{Q_a}\left(\frac{mc}{2e^2\rho}\mathbf{J}_S + \mathbf{A}\right)\cdot d\mathbf{l}. \quad (2.40b)$$

On the other hand, the gauge-invariant phase difference between two points on opposite sides l and r across the barrier, at a same position y, reads as [75] (see also footnote 4 of this Chapter)

$$\varphi = \int_l^r \boldsymbol{\gamma}\cdot d\mathbf{l} = (\theta_r - \theta_l) - \frac{2e}{\hbar c}\int_l^r \mathbf{A}\cdot d\mathbf{l}. \quad (2.41)$$

This is the case for terms I and III in Eq. (2.38), whence (being careful about signs)

$$\theta_{Q_b} - \theta_{Q_a} = \varphi(Q) + \frac{2e}{\hbar c}\int_{Q_a}^{Q_b}\mathbf{A}\cdot d\mathbf{l}$$
$$\Rightarrow \varphi(Q) = (\theta_{Q_b} - \theta_{Q_a}) - \frac{2e}{\hbar c}\int_{Q_a}^{Q_b}\mathbf{A}\cdot d\mathbf{l}, \quad (2.42a)$$

$$\theta_{P_d} - \theta_{P_c} = -\varphi(P) + \frac{2e}{\hbar c}\int_{P_c}^{P_d}\mathbf{A}\cdot d\mathbf{l}$$
$$\Rightarrow -\varphi(P) = (\theta_{P_d} - \theta_{P_c}) - \frac{2e}{\hbar c}\int_{P_c}^{P_d}\mathbf{A}\cdot d\mathbf{l}. \quad (2.42b)$$

Altogether, Eqs. (2.40), (2.42) give the change in the gauge-invariant phase difference

$$\begin{aligned}\varphi(Q)-\varphi(P) =&(\theta_{Q_b}-\theta_{Q_a}+\theta_{P_d}-\theta_{P_c})-\frac{2e}{\hbar c}\int_{Q_a}^{Q_b}\mathbf{A}\cdot d\mathbf{l}-\frac{2e}{\hbar c}\int_{P_c}^{P_d}\mathbf{A}\cdot d\mathbf{l}\\ =&-\frac{2e}{\hbar c}\int_{Q_b}^{P_c}\left(\frac{mc}{2e^2\rho}\mathbf{J}_S+\mathbf{A}\right)\cdot d\mathbf{l}-\frac{2e}{\hbar c}\int_{P_d}^{Q_a}\left(\frac{mc}{2e^2\rho}\mathbf{J}_S+\mathbf{A}\right)\cdot d\mathbf{l}\\ &-\frac{2e}{\hbar c}\int_{Q_a}^{Q_b}\mathbf{A}\cdot d\mathbf{l}-\frac{2e}{\hbar c}\int_{P_c}^{P_d}\mathbf{A}\cdot d\mathbf{l}\\ =&-\frac{2e}{\hbar c}\oint_C\mathbf{A}\cdot d\mathbf{l}-\frac{2e}{\hbar c}\int_{Q_b}^{P_c}\frac{mc}{2e^2\rho}\mathbf{J}_S\cdot d\mathbf{l}-\frac{2e}{\hbar c}\int_{P_d}^{Q_a}\frac{mc}{2e^2\rho}\mathbf{J}_S\cdot d\mathbf{l}.\end{aligned} \tag{2.43}$$

The second and third integrals, which are performed on $C_{r,l}$, can be neglected. Indeed, if the superconductors' thickness along x is larger than the London penetration depth[7] λ, we can choose $C_{r,l}$ such that the vertical lines lie outside the penetration regions. Here the shielding current density $\mathbf{J}_S$ is zero (it decreases exponentially moving away from the interfaces). Also, the line integrals along the two horizontal sections of $C_r(C_l)$ within the penetration regions cancel with each other in the limit $dy\to 0$, which we are about to perform[8]. Under these hypothesis, and substituting $P,\ Q$ with their coordinates $y+dy,\ y$, we have

$$\varphi(y+dy)-\varphi(y)=\frac{2e}{\hbar c}\oint_C\mathbf{A}\cdot d\mathbf{l} \tag{2.44}$$

The line integral can be replaced by the surface integral of the magnetic field[9],

$$d\varphi=\frac{2e}{\hbar c}B(2\lambda+L)dy\Rightarrow\frac{d\varphi}{dy}=\frac{2e}{\hbar c}B(2\lambda+L). \tag{2.45}$$

After integration, we get

$$\varphi(y)=\frac{2e}{\hbar c}B(2\lambda+L)y+\varphi(0), \tag{2.46}$$

which is the gauge-invariant phase difference across the junction at any y, in the presence of a piercing magnetic field. The integration constant $\varphi(0)$ is the phase difference across the junction at $y=0$. The superconducting flux quantum $\phi_0=hc/2e$ has also been introduced. In Gaussian units, $\phi_0=2.07\times10^{-7}$ G·cm^2. In SI units[10], the factor c is absent and $\phi_0=h/2e=2.07\times10^{-15}$ Wb. Denoting by $L^*=(2\lambda+L)$, in Eq. (2.46) we can resort to the total flux piercing the junction, $\phi=BL^*w$, where w is its width (see Fig. 2.6). Doing so,

$$\varphi(y)=\frac{2\pi\phi}{\phi_0}\frac{y}{w}+\varphi(0). \tag{2.47}$$

[7] We assume it to be the same for both superconductors.

[8] A different argument, used by [12], is that these sections can be chosen to be perpendicular to $\mathbf{J}_S$.

[9] We recall that λ defines the region over which the field penetrates into the superconducting electrodes.

[10] Gaussian units are used in much of the old physics literature on these topics, and on which the previous Sections are based. This is a good time to switch to SI units for practical convenience.

To summarize, we have found that the phase entering the sinusoidal part of the supercurrent density – see Eq. (2.22) – is spatially modulated by the magnetic field. We then have

$$J_S(y) = J_c \sin\left(\frac{2\pi\phi}{\phi_0}\frac{y}{w} + \varphi(0)\right), \tag{2.48}$$

where we recall that J_c is the critical supercurrent density per unit length. The Josephson supercurrent density $J_S(y)$ exhibits a periodic distribution inside the junction. We will soon discuss the computation of the total supercurrent, including the generalization to a non-uniform J_c. In Ref. [180] the gauge-invariant phase difference in the presence of a magnetic field is computed in a slightly different way, but Eq. (2.48) is still recovered.

The flux ϕ introduced above is the magnetic flux through an effective junction area, which depends on the screening properties of the leads. In most cases, screening in the superconducting leads is not taken into account[11]. For simplicity, in the following we will also assume that it can be neglected. This approximation is justified as long as $w/(2\lambda_P) \ll 1$, where $\lambda_P = 2\lambda^2/d$ is the Pearl penetration depth and d is the superconductors' thickness in the z direction. This is the appropriate screening length if $d \ll \lambda$. Under these assumptions, which are valid in a wide range of scenarios, we can safely use $L^* = L$ and $\phi = BLw$. If the magnetic field is fully screened by the superconductors, we can assume their superconducting phases $\theta_{r,l}$ to remain unchanged and identify $\varphi(0)$ with the superconducting phase difference in the absence of magnetic field.

The interference pattern

For any $y = \overline{y}$, through the sinusoidal current-phase relation in Eq. (2.48), we get the supercurrent contribution associated to transport along $\overline{y}$. The total supercurrent can be obtained by integrating over all the possible horizontal trajectories, namely

$$I(\theta_r - \theta_l, \phi) = \int_{-w/2}^{w/2} J_S(y)dy = \int_{-w/2}^{w/2} J_c \sin\left(\frac{2\pi\phi}{\phi_0}\frac{y}{w} + \theta_r - \theta_l\right)dy, \tag{2.49}$$

where we have emphasized the two dependencies on the superconducting bare phase difference and on the magnetic contribution. The maximum supercurrent with respect to the difference $(\theta_r - \theta_l)$, which becomes a function of the mere magnetic flux, and taken in absolute value, is the so-called interference pattern:

$$I_c(\phi) \equiv \left|\max\left[I(\theta_r - \theta_l, \phi), \theta_r - \theta_l\right]\right|, \tag{2.50}$$

whose name is due to the fact that the magnetic field dependence results from a spatial interference effect of the macroscopic wavefunctions in the two superconducting electrodes. The effect emerges through the spatial change in y of the gauge-invariant phase difference. To compute the interference pattern, we first rewrite Eq. (2.49) as

$$I(\theta_r - \theta_l, \phi) = J_c \sin(\theta_r - \theta_l) \int_{-w/2}^{w/2} \left[\cos\left(\frac{2\pi\phi}{\phi_0}\frac{y}{w}\right)\right] dy = I_c \sin(\theta_r - \theta_l) \frac{\sin\left(\frac{\pi\phi}{\phi_0}\right)}{\frac{\pi\phi}{\phi_0}}, \tag{2.51}$$

[11] Be careful that so far we neglected screening effects *in the tunnel barrier* and not in the leads.

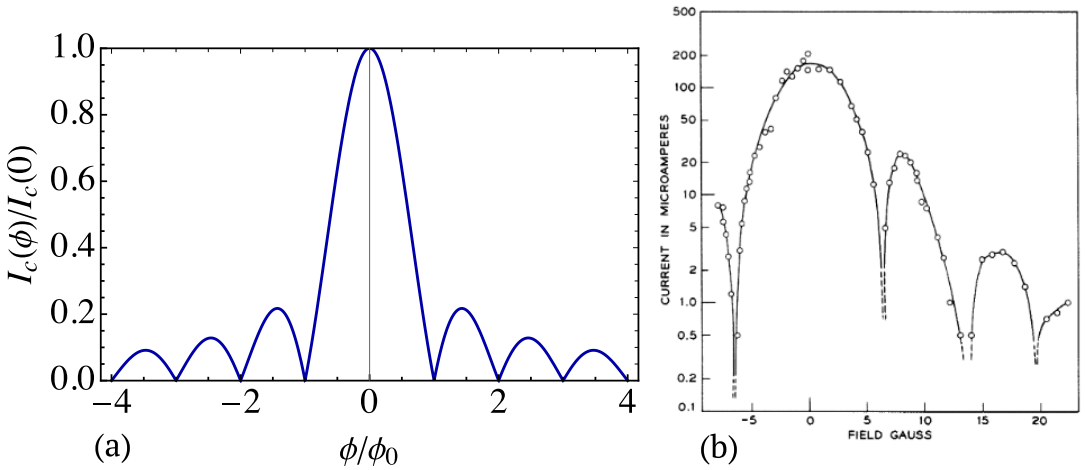

Figure 2.7: *(a) Fraunhofer interference pattern, corresponding to uniform transport across the junction. The minima occur at values of ϕ which are multiples of the flux quantum. (b) Rowell's measurements of the critical current of a Pb-I-Pb junctions as a function of the magnetic field and at a temperature of 1.3 K. The expected (and verified) effect of the external magnetic field was the reduction of the direct current to a minimum whenever the junction contained integral numbers of flux units. Reprinted with permission from [146]. Copyright 2024 by the American Physical Society.*

with $I_c = J_c w$. Notice that, since a uniform J_c is an even function of y, we could decouple the y- and the $(\theta_r - \theta_l)$-dependence. In this case, the maximization mentioned above is easily obtained with $\sin(\theta_r - \theta_l) = 1$, and the corresponding interference pattern is

$$I_c(\phi) = I_c \left| \frac{\sin\left(\frac{\pi\phi}{\phi_0}\right)}{\frac{\pi\phi}{\phi_0}} \right| \Rightarrow \frac{I_c(\phi)}{I_c(0)} = \left| \frac{\sin\left(\frac{\pi\phi}{\phi_0}\right)}{\frac{\pi\phi}{\phi_0}} \right| . \tag{2.52}$$

This is the Fraunhofer pattern and is shown in Fig. 2.7(a). The first observations in this direction were made by J. M. Rowell in 1963 [146]. Fig. 2.7(b) shows his measures on a Pb-I-Pb junction. Further measurements followed in later years [10, 58, 154, 201].

Notice that, so far, we have neglected effects due to nonuniformities of tunneling barriers (and of supercurrent densities). Physically, we can think of a metallic weak link which allows for a uniform current flow. A clearer insight comes from rewriting Eq. (2.49) as

$$\begin{aligned} I(\theta_r - \theta_l, \phi) &= \mathrm{Im}\left[J_c\, e^{i(\theta_r - \theta_l)} \int_{-w/2}^{w/2} e^{i2\pi\phi/\phi_0\, y/w} dy \right] \\ \Rightarrow I_c(\phi) &= J_c \left| \int_{-w/2}^{w/w} e^{i2\pi\phi/\phi_0\, y/w} dy \right| \\ &= J_c \left| \int_{-\infty}^{+\infty} [\Theta(|y| + w/2) - \Theta(|y| - w/2)] e^{i2\pi\phi/\phi_0\, y/w} dy \right| . \end{aligned} \tag{2.53}$$

The Fraunhofer pattern emerges as the Fourier transform of the supercurrent density distribution, which is here rectangular-shaped, equivalently to the optical diffraction pattern of a slit with the same shape as the barrier (and a constant transmission). The observed interference effect is completely analogous to the diffraction of light in optics.

The experimental detection of Fraunhofer patterns was a very important step towards the understanding of the Josephson tunneling of Cooper pairs. Since then, from the experimental point of view, it was still unclear whether the measured supercurrent was flowing as a homogeneous Josephson tunneling current or just through small holes in the tunneling barrier. Only the former possibility is compatible with the observed Fraunhofer pattern.

Dynes and Fulton description

In what follows, we no longer assume that the critical supercurrent density J_c is uniform, for instance due to local inhomogeneities in the junction (or, more interestingly, because of the edge states in a topological insulator, as we shall see). The simple Fraunhofer result in Eq. (2.53) is replaced by a more general Fourier transform, as discussed by R. C. Dynes and T. A. Fulton [54] (we keep neglecting all screening effects). In particular, for a given $J_c(y)$, Eq. (2.49) becomes

$$I(\theta_r - \theta_l, \phi) = \int_{-w/2}^{w/2} J_c(y) \sin\left(\frac{2\pi\phi}{\phi_0}\frac{y}{w} + \theta_r - \theta_l\right) dy. \tag{2.54}$$

With the same procedure used above, we obtain

$$I_c(\phi) = \left| \int_{-w/2}^{+w/2} J_c(y) e^{i2\pi\phi/\phi_0\, y/w} dy \right|. \tag{2.55}$$

It is instructive to revise some results of the application of Eq. (2.55).

- If the critical supercurrent density $J_c(y)$ is sharply peaked around a specific y^*, then we have
$$I(\theta_r - \theta_l, \phi) \propto \sin\left(\frac{2\pi\phi}{\phi_0}\frac{y^*}{w} + \theta_r - \theta_l\right), \tag{2.56}$$
which results in a flux-independent maximal current (as could be expected, since no interference between different paths can arise).

- If there is only edge transport, which is expected, for instance, if the tunnel barrier is a two-dimensional topological insulator, then ideally
$$J_c(y) = \frac{I_0}{2}\left[\delta\left(y + \frac{w}{2}\right) + \delta\left(y - \frac{w}{2}\right)\right], \tag{2.57}$$
and
$$\frac{I_c(\phi)}{I_c(0)} = \frac{1}{2}\left|e^{i\pi\phi/\phi_0} + e^{-i\pi\phi/\phi_0}\right| = \left|\cos\left(\frac{\pi\phi}{\phi_0}\right)\right|, \tag{2.58}$$
named SQUID pattern (see Fig. 2.8(a)) after the Superconducting Quantum Interference Device, which shows the same features. Such device, shown in Fig. 2.8(b), is a superconducting circuit made of two Josephson junctions in parallel.

- Related to the previous case, one can more realistically include some broadening of $J_c(y)$, possibly also across the bulk. This is for instance done in [12] with several examples. The main consequence of broadening is a decay of the interference pattern, see Fig. 2.9.

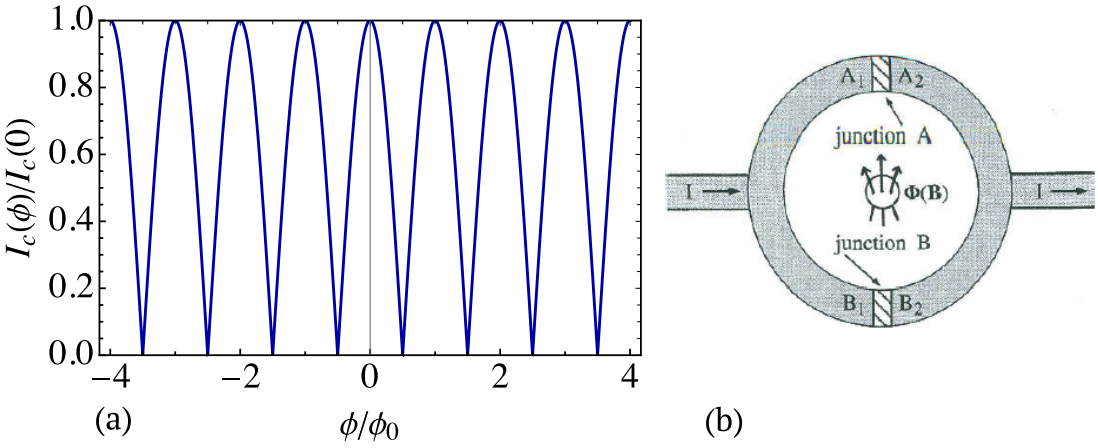

Figure 2.8: *(a) SQUID interference pattern arising from a supercurrent density sharply peaked at the edges of the junction. (b) Sketch of a Superconducting Quantum Interference Device. Figure from [76], copyright © 2000 ACADEMIC PRESS. Published by Elsevier Ltd All rights reserved.*

To conclude this part, we underline the main limitations of the Dynes-Fulton approach. (i) First, we have assumed from the beginning a sinusoidal current-phase relation, which holds in the so-called tunneling regime. This is not always the case, and corresponds to low-transparency interfaces between the superconductors and the non-superconducting region. (ii) A second implied hypothesis is the local nature of the supercurrent, flowing perpendicularly to the superconducting contacts. This means that the supercurrent density only depends on a y coordinate while the current flows in the x direction. Although Dynes and Fulton's analysis is straightforward and informative, this second assumption can lead to false results, as we will discuss in the next Subsection for the particular case of topological Josephson junctions. More in general, this assumption has been relaxed also in some works on mesoscopic Josephson junctions [13, 85, 108], for instance by including an angular distribution for the paths of Cooper pairs, or the effects of normal reflection at the superconductors' boundaries [158].

Before moving on, it is worth noticing that Dynes and Fulton's description is also interesting if applied backwards, namely to obtain a supercurrent density profile given the interference pattern (which can be measured in transport experiments). This is not a trivial matter, in principle. From Eq. (2.55), the measured quantity is the absolute value of

$$\mathcal{I}(\phi) = \int_{-w/2}^{+w/2} J_c(y) e^{i2\pi\phi/\phi_0\, y/w} dy. \tag{2.59}$$

Hence, $\mathcal{I}(\phi) = I_c(\phi)e^{i\theta(\phi)}$, where $\theta(\phi)$ is real. To determine $J_c(y)$, both $I_c(\phi)$ and $\theta(\phi)$ are needed. The difficulty in determining the latter can be overcome if $J_c(y)$ is assumed to be an even function, $J_c(y) \approx J_c(-y)$. More details can be found in [54] on how to consider an additional small odd component.

2.2.2 Experiments on topological Josephson junctions

This Subsection finally merges concepts introduced in Chapter 1 and 2. Indeed, we discuss the first experiment on a topological Josephson junction, namely a Joseph-

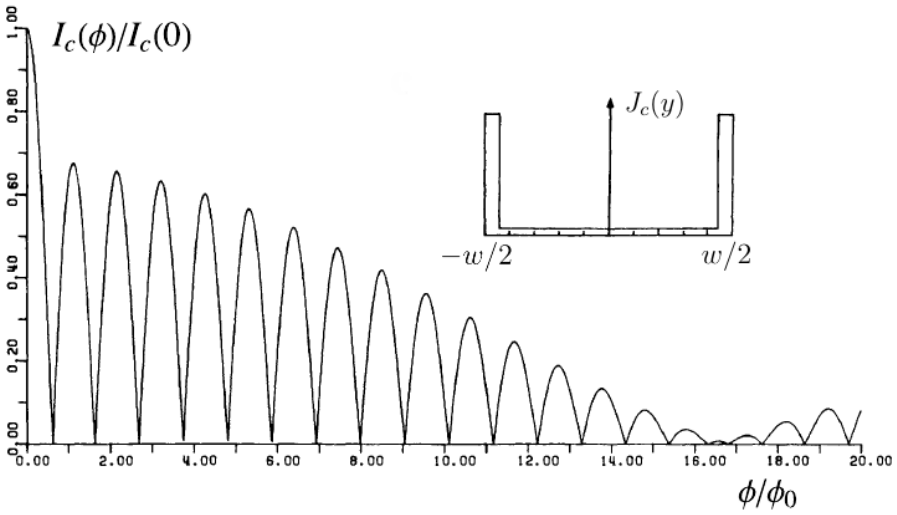

Figure 2.9: *Interference pattern for the supercurrent density distribution shown in the inset. The non-vanishing density in the central part and the finite width of the side peaks are responsible for the pattern's decay (to be compared for instance with the SQUID pattern). Figure adapted from [12], copyright © 1982 by John Wiley & Sons, Inc.*

son junction where the non-superconducting part is a (two-dimensional) topological insulator [82]. In particular, in the experiment, the setup consists of a proximitized HgTe/HgCdTe quantum well, pierced by a perpendicular magnetic field. We have already presented, in the previous Chapter, experimental evidencies for the Quantum Spin Hall Effect [27, 103, 126, 145]. The aim of [82] is to demonstrate that superconductivity can be induced in the Quantum Spin Hall edge: in other words, that a supercurrent is carried across the device (solely) along the helical edges. In this regime, the system is said to be a Quantum Spin Hall superconductor. For a discussion of the proximity effect, we refer the reader to Subsec. 1.2.4.

The essential idea is to leverage the quantum interference effects we have just discussed. Being the interference pattern highly sensitive to the supercurrent density distribution, it is expected to clearly discriminate between the trivial and the topological regime. At a given bulk carrier density, a uniform supercurrent density is expected for a non-topological junction (quantum well thinner than d_C), or in a topological junction (quantum well thicker than d_C, see Subsec. 1.2.2 on the BHZ model) far from the bulk insulating regime. Over a range of bulk densities, the Quantum Spin Hall edge channels coexist with bulk states. In this case, the helical edge contribution appears as peaks in the supercurrent density at each edge, quite similarly to the inset of Fig. 2.9. However, if the bulk carriers' density is decreased, the edge peaks are the only features in the supercurrent density, as in the SQUID case. These different scenarios, together with the interference patterns predicted by the Dynes and Fulton description, are shown in Fig. 2.10.

In the experiment, the interference pattern is measured and the Dynes-Fulton approach is applied backwards to infer the supercurrent density. The effective area pierced by the magnetic field includes not only the quantum well, but also part of the superconducting leads due to screening effects (as we commented at the end of Subsec. 2.2.1). The supercurrent density is not simply assumed to be symmetric, and a small

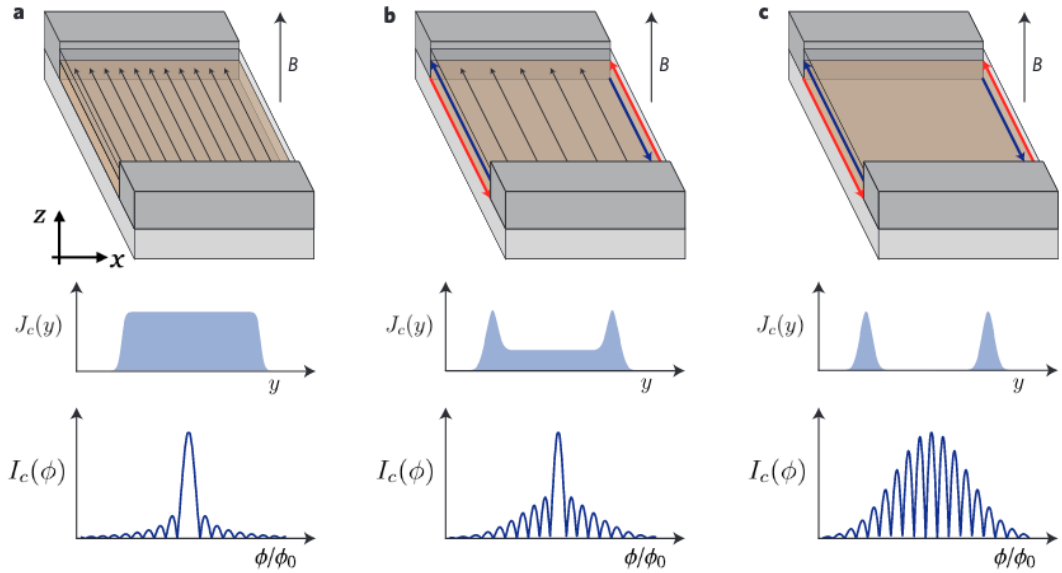

Figure 2.10: *Each column shows a sketch of the conducting states in the sample, the corresponding supercurrent density and the interference pattern predicted by the Dynes and Fulton approach. (a) The quantum well is in the trivial regime, and the bulk is filled with charge carriers, the supercurrent density has a uniform profile and the expected interference pattern is a Fraunhofer, see Eq.* (2.52)*. (b) The quantum well is in the topological regime. Bulk carriers are depleted, and in the supercurrent density two peaks emerge owing to the helical edge states. Side lobes are more pronounced and the central one gets thinner. Notice that this case is similar to the one shown in Fig. 2.9.(c) The quantum well is still in the topological regime, but bulk carriers are completely depleted. The supercurrent is carried solely by the edge states, giving rise to a sinusoidal double-slit pattern, with a decay related to edge states' width. Figure adapted from [82], reproduced with permission from Springer Nature.*

but non-vanishing odd component is also considered (see the Supplementary Information of [82]).

Some of the main plots are shown in Fig. 2.11, and correspond to measures on a quantum well of thickness $d = 7.5$ nm, contacted by Titanium/Aluminum superconducting leads, with a width of $4\,\mu$m[12]. The first and second rows are associated to different values of the top-gate voltage V_G and bulk carriers' density. At a more positive gate voltage, which means higher bulk density, the critical current envelope is similar to a Fraunhofer (single-slit) pattern (Fig. 2.11(a)). Accordingly, the extracted supercurrent density profile is almost rectangular shaped (Fig. 2.11(b)): this means that the quantum well is in the regime of high bulk carrier density of a trivial conductor. On the other hand, at more negative gate voltage and lower bulk density, the critical current envelope gets similar to a sinusoidal oscillation (Fig. 2.11(c)). Such transformation towards a SQUID-like interference pattern is accompanied by the development of sharp peaks in the supercurrent density, spatially located at the edges of the sample (Fig. 2.11(d)). At the most negative voltage, that is $V_G = -0.45$ V (gating further would make the critical current too small to get reliable measurements), and assuming a Gaussian shape, the widths of the two supercurrent-carrying edge channels are estimated to be 408 nm and 319 nm, see Fig. (2.12). This was the first direct measure of the helical edges' spatial

[12]We underline here that the thickness of the quantum well is related to the width of the sample (the distance between the opposite edges). In particular, a larger thickness allows for smaller values of the width. For instance, in [168], $d = 10.5$ nm and the width of the Quantum Spin Hall constriction is only 25 nm. This comment will come in handy later on in this Thesis.

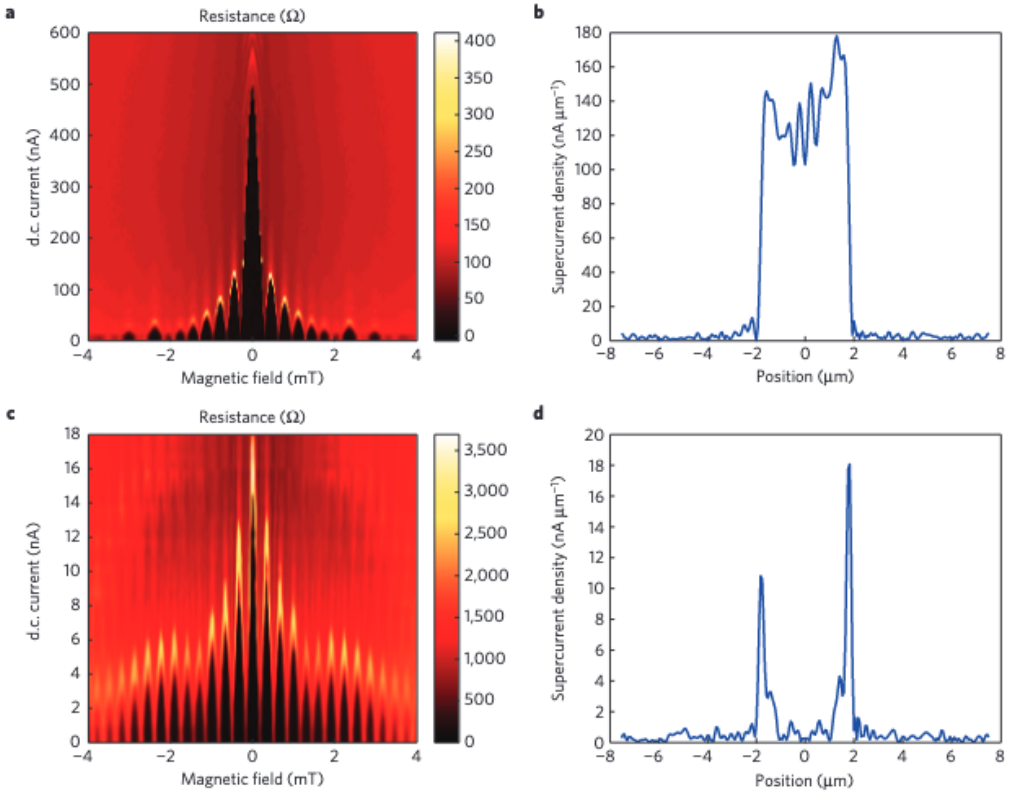

Figure 2.11: *(a) and (c) show a map of the differential resistance across the junction at $V_G = 1.05$ V and $V_G = -0.425$ V, respectively. The former case results in a single-slit interference which is typical of a uniform supercurrent profile. This is in agreement with the extracted supercurrent profile, shown in panel (b). In the latter case, on the other hand, the differential resistance exhibits a more sinusoidal interference pattern. The supercurrent density, shown in panel (d), turns out to be dominated by the contribution from the edges, with almost no supercurrent through the bulk. Figure from [82], reproduced with permission from Springer Nature.*

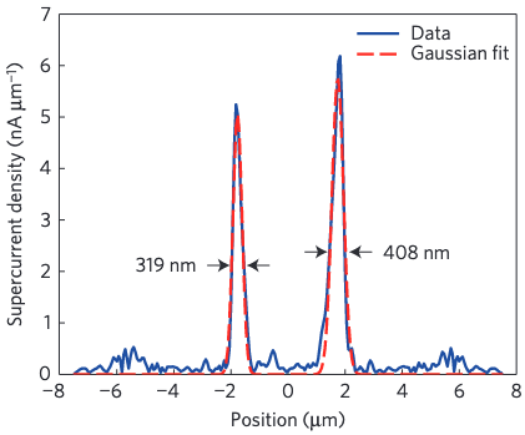

Figure 2.12: *Supercurrent density profile for $V_G = -0.45$ V with a Gaussian fit to extract the edge states' width. Figure from [82], reproduced with permission from Springer Nature.*

extent. Measures on different devices with similar dimensions, however, led to quite different values. These width variations were ascribed by the authors to the presence of additional edge modes or of bulk modes coupled too weakly across the junction to carry a supercurrent.

The same measurements were performed on a heterostructure with a quantum well thickness of 4.5 nm, much lower than the critical thickness of $d_c = 6.3$ nm. In this case, the quantum well should never enter the Quantum Spin Hall regime. It was verified that, in fact, the supercurrent density profile remains uniformly distributed throughout the whole junction. Being the edge supercurrents present only in the Quantum Spin Hall regime, it was concluded that superconductivity had been actually induced in the helical Quantum Spin Hall edge states.

Shortfall of Dynes and Fulton description

A similar experiment was carried out a year later in Josephson junctions based on InAs/-GaSb quantum wells [134], which are also platforms for two-dimensional topological insulators [53, 114]. In the edge dominated regime, an interesting feature was observed in the interference pattern: in addition to the expected SQUID-like pattern, the authors observed a modulation between even and odd peaks amplitudes, usually referred to as even-odd effect or $2\phi_0$-periodicity [16, 24, 42, 43, 78] (see Fig. 2.13(a)). Assuming the validity of the Dynes and Fulton approach, a current density profile featuring three peaks is found: two at the edges (responsible for the SQUID-like flux dependence) and a third peak located in the middle of the junction (originating the different heights of even and odd peaks), as shown in Fig. 2.13(b). Even more strangely, simulations indicated that the middle channel should be within 10% of the device centre. While such a peculiar current distribution might make sense for certain physical devices, it is for sure unsatisfactory for systems where only edge transport is expected. Different explanations of the effect are guessed in the paper, and in any case it is needed to go beyond the Dynes and Fulton description. Among others, it is suggested the possibility that the Cooper pair transmission through the junction involves both edges simultaneously, clearly violating the Dynes and Fulton's hypothesis of local transport. This scenario is

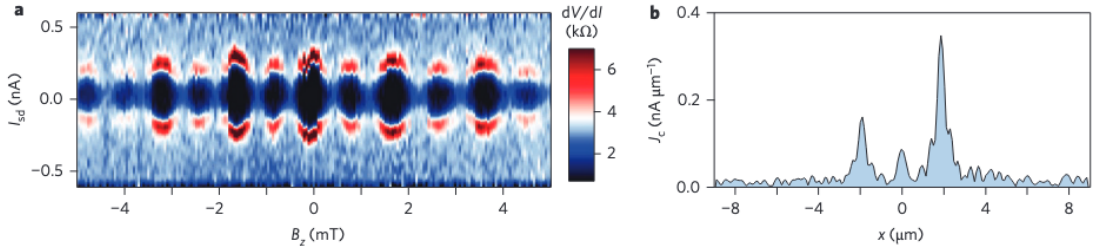

Figure 2.13: *(a) Quantum interference pattern in a Josephson junctions based on an InAs/GaSb quantum well, in the edge dominated transport regime. A $2\phi_0$-periodicity, instead of the ϕ_0 standard SQUID periodicity, is well visible. (b) Current profile assuming the validity of Dynes and Fulton analysis, featuring two peaks at the edges of the sample and a third peak in the middle. Figure from [134], reproduced with permission from Springer Nature.*

the subject of the next Section and will be crucial for the results of this Thesis.

2.3 Beyond Dynes and Fulton: non-local transport

2.3.1 Andreev Reflection in a nutshell

Before moving on, it is useful to shortly revise the mechanism of Andreev Reflection. Even before discussing the Josephson effect, in Chapter 1 we have mentioned the possibility to introduce Cooper pairs – and, consequently, to induce a superconducting pairing – in a non-superconducting material (the proximity effect). Here we discuss how it is possible that Cooper pairs, that are only generated inside a superconductor (below the critical temperature), are not confined to the interior of the superconductor itself. Let us consider an interface between a superconductor (S) and a normal metal (N). At first glance, the transfer of Cooper pairs seems impossible, as they are not eigenfunctions of a non-superconducting material. On the other hand, normal electrons cannot enter S owing to the superconducting gap Δ. Let us suppose that an electron with energy $\epsilon < \Delta$ reaches the interface from the N side. Instead of being simply reflected, it drags a second electron with opposite energy, momentum and spin to enter S as a Cooper pair. The second electron is taken from the valence band, where a hole is consequently left and is retro-reflected. The electric charge is not conserved during the process, as a charge $2e$ is transfered from N to S. However, there is no energy transfer, because on the N side the electronic excitation is replaced by a hole with same energy, and on the S side the Cooper pair simply adds to the condensate (which is the superconductor's ground state). This special kind of scattering, which is called Andreev reflection, is schematically shown in Fig. 2.14.

2.3.2 Crossed Andreev Reflection (CAR) and Local Andreev Reflection (LAR)

Transport in Josephson junctions whose non-superconducting region hosts edge channels, such as the one mentioned at the end of Sec. 2.2 [134], is dominated by the interplay of two charge quanta: charge e and charge $2e$. Although charge can only enter or leave the superconductors in units of $2e$ (Cooper pairs), in the normal region a pair can be split over opposite edges. In terms of Andreev reflections, this corresponds to an electron impinging on the normal metal/superconductor interface along one edge

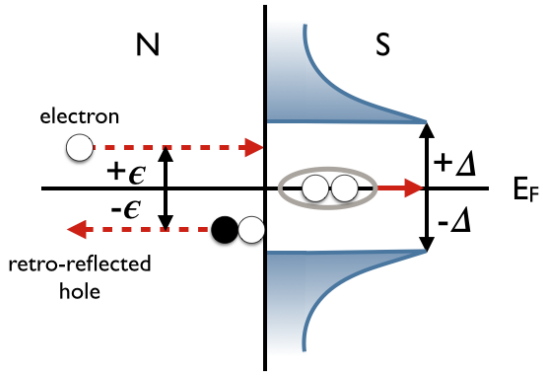

Figure 2.14: *Andreev reflection at the interface between a normal metal (N) and a superconductor (S). The incident electron with energy ϵ (measured with respect to the Fermi energy E_F) and less than Δ is retro-reflected as a hole (in black). Together, they form a correlated electron-hole pair. The incident electron and the missing electron in the valence band enter the superconductor as a Cooper pair. Their energies must be opposite to each other since Cooper pairs have energy E_F.*

and being Andreev reflected as a hole along the opposite edge, see Fig. 2.15(a). This process is referred to as Crossed Andreev Reflections (CAR) [47] and produces oscillations of the critical current as a function of the magnetic flux with a periodicity h/e, twice to the usual one. Due to their non-local character, CAR processes are appealing, for instance, for applications in quantum communication. Several systems have been proposed as potential candidates to observe CAR [23,25,35,37,57,66,142,144,204] and some experimental observations have been reported [40, 86, 88, 148, 151]. If the edge channels are chiral, as in the case of the Quantum Hall Effect, Fig. 2.15(a) represents the only possible current-carrying path.

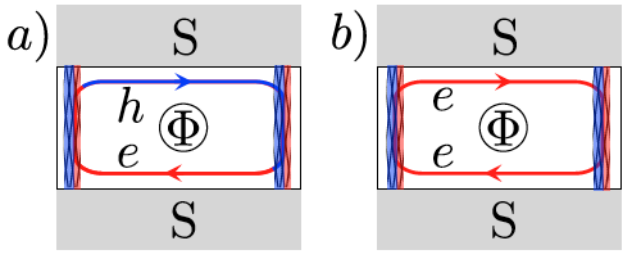

Figure 2.15: *Even-odd effect mechanism for interference oscillations. In the case of uncoupled edges, the standard flux periodicity is $h/2e$, due to a charge transfer of $2e$ (Cooper pair) along the left or right edge channel (represented by the blue/red thick vertical lines). Here the edge channels are coupled by a conducting path along the normal metal/superconductor interface, and a circulating loop of charge $\pm e$ becomes possible. The associated flux periodicity in this case is h/e. Such circulating loop may be (a) half electron-type (red line) and half hole-type (blue line), or (b) totally electron/-totally hole-type. Reprinted with permission from [16]. Copyright 2024 by the American Physical Society.*

If the edge channels allow for propagation in both directions, such as in the Quantum Spin Hall Effect, there are further possibilities. First, the critical current has also a standard $h/2e$-periodic term, stemming from Andreev reflections along a single edge (this process is called Local Andreev Reflection, LAR). Moreover, there is another type

of h/e-periodic term, arising from the circulating path depicted in Fig. 2.15(b). This is not relevant for our following discussions. The competition between these processes has been extensively analyzed in [16], motivated by [134].

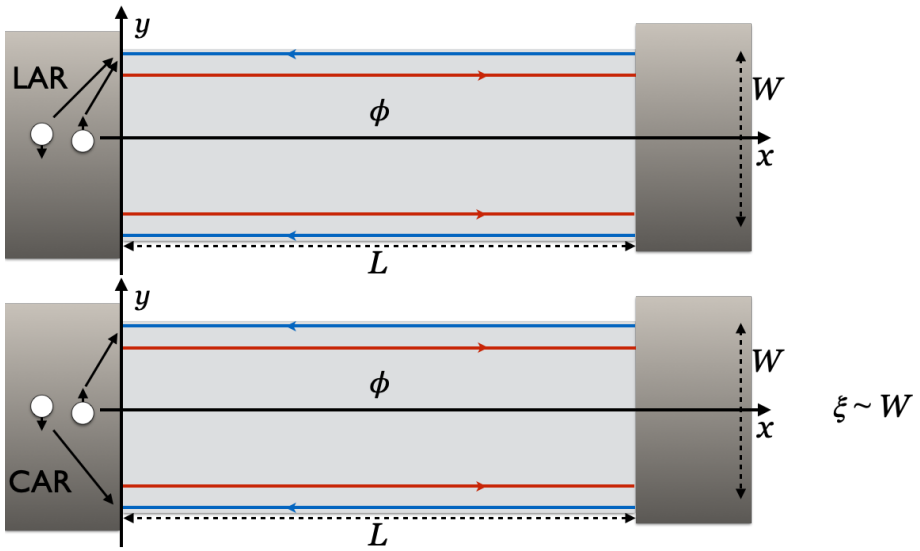

Figure 2.16: *The system mainly analyzed in this Thesis will consist of a topological Josephson junction, having length L and width W, pierced by a magnetic flux ϕ, with a point-like injection of Cooper pairs at the intersection between the edge states and the superconductors (represented by the left and right leads in dark grey). We will call "LAR" the intraedge injection (upper panel) and "CAR" the interedge one (lower panel). The second possibility, as we will see, is allowed as long as $W \sim \xi$, with ξ the superconducting coherence length.*

The description of LAR and CAR is usually done by considering them within a scattering matrix approach, as in [16]. In the remainder of this Thesis, we will follow a different route, entirely tunneling-based. We will always deal with Quantum Spin Hall-based Josephson junctions, and call "LAR" the tunneling injection of both electrons of a Cooper pair into a same edge, and "CAR" the tunneling injection of the two electrons into opposite edges (see Fig. 2.16). The latter process, as we will discuss, is possible as long as $W \sim \xi$, with W the junction's width and ξ the superconducting coherence length.

2.3.3 LAR and CAR in a topological Josephson junction: a tunneling description

Introduction

We now revise a work which will be of major importance for the rest of this Thesis [78]. The system under investigation is a Josephson junction where the non-superconducting part is represented by either a trivial or a topological insulator, shown in Fig. 2.17. In a trivial insulator, non-helical, whereas in a topological insulator, helical edge states may contribute to subgap transport.

As we know from the previous discussion, a SQUID-like interference pattern is associated to a supercurrent density peaked at the edges of the sample. In particular, in the experiment discussed in the previous Section, such a supercurrent density was related to the topological regime of the system. However, edge states can also have a

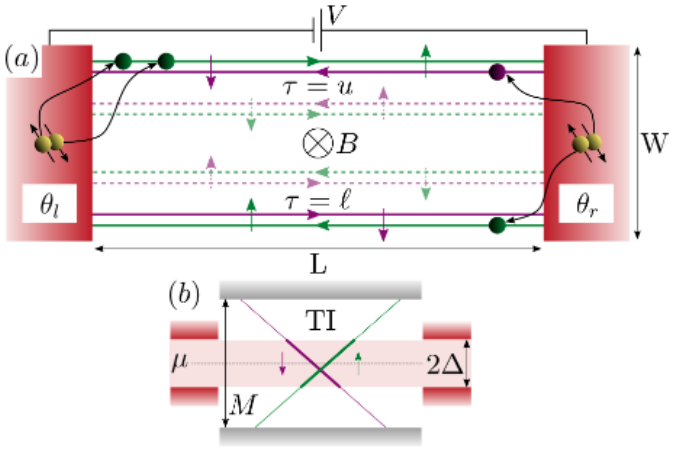

Figure 2.17: *(a) Sketch of the long and narrow Josephson junction under consideration, biased by a voltage V and pierced by the perpendicular magnetic field B. The solid lines represent the helical edge states corresponding to a topological insulator as a link between the superconductors. The edge states corresponding to the dashed lines would be present for a trivial insulator, a scenario which we do not focus on. The upper and lower edge are labeled by τ. (b) Energy spectrum of the upper edge, with the bare bandwidth M and the relevant subgap region 2Δ. μ denotes the chemical potential in the superconductors. Adapted with permission from [78]. Copyright 2024 by the American Physical Society.*

non-topological origin [42,43], and lead to experimental signatures which are similar to the helical scenario. In particular, the even-odd effect may occur in such trivial systems as well, and it is thus not sufficient to decisively identify the topological or trivial case. Its h/e periodicity is often explained by the Crossed Andreev Reflection processes we discussed above. However, in [78] it is shown that the flux-dependent nonequilibrium supercurrent, for long[13] and narrow Josephson junctions, exhibits striking differences in the interference pattern of helical and non-helical edge states, further enhanced by electron-electron interactions in the edge states. This allows for an unambiguous identification of the topological nature of the insulator.

In the following, we will be particularly interested in Josephson junctions based on topological insulators. Therefore, we will not focus on the non-helical case, and rather focus on carefully setting up the formalism, which will be applied also in the next Chapters. Moreover, we will neglect electron-electron interactions, as they are not crucial for the original results we will present.

Model

The considered Josephson junction is made of two s-wave superconducting leads grown on a two-dimensional topological insulator, which is pierced by a magnetic flux ϕ. The bulk gap of the insulator is assumed to be sufficiently large, such that transport between the superconductors occurs only via the one-dimensional edge states. Also, the presence of the superconductors pushes the underlying insulating regions into a metallic phase [141] and destroys the edge states under them abruptly. All in all, as shown in Fig. 2.17(a), the system consists of two one-dimensional channels of length

[13] These are junctions with the separation L between the superconductors being much larger than the coherence length $\xi = \hbar v_F/\Delta$, where v_F is the Fermi velocity in the normal region of the junction and Δ is the superconducting gap.

L, separated by a width W, with a weak and point-like injection of Cooper pairs at the ends, where the edge states and the superconductors intersect. Such injection can be intraedge (what we defined before as LAR) or interedge (what we defined before as CAR). As a starting point, the full Hamiltonian is made of three contributions

$$H = H_E + H_S + H_T, \tag{2.60}$$

which describe the edge states, the superconductors and the tunneling connecting them. As said before, we will focus on the case of helical edge states. The non-helical scenario is easily derived by considering two copies of H_E distinguished by a helicity index (and would correspond to the dashed lines in Fig. 2.17(a)). We can now refer to the previous Chapter. Indeed, H_E is given by Eq. (1.138) written now for both edges. In a matricial form

$$H_E = \int_{-\infty}^{+\infty} dx\, \boldsymbol{\psi}^\dagger(x)(-i\hbar v_F \partial_x)\rho_z \boldsymbol{\psi}(x), \tag{2.61}$$

where ρ_z is the z Pauli matrix acting in the right-mover/left-mover space and by bold font we denote the vector basis $\boldsymbol{\psi}(x) = (\psi_{11}(x), \psi_{-11}(x), \psi_{1-1}(x), \psi_{-1-1}(x))^T$. Here $\psi_{\rho\tau}(x)$ is the Fermi operator that annihilates an electron at position x propagating in the ρ-direction channel of the τ edge. In particular, $\rho = 1/-1$ stands for the right/left direction of motion and $\tau = 1/-1$ for the upper/lower edge. Due to the spin-momentum locking, these two indices completely define the edge states, since the spin polarization is determined by their helical nature. Notice also that the integral between $-L/2$ and $L/2$ has been extended to $(-\infty, +\infty)$, because the main focus of the paper is on long junctions where boundary effects are negligible.

The contribution H_S refers to the two three-dimensional and BCS-like superconductors, and reads as

$$H_S = \sum_{j=l,r} H_S^j = \frac{1}{2}\int d\mathbf{r}\, \mathbf{\Psi}_{S,j}^\dagger \mathcal{H}_S^j \mathbf{\Psi}_{S,j}, \tag{2.62}$$

where

$$\mathbf{\Psi}_{S,j} = \left(\Psi_j(\mathbf{r}), \Psi_j^\dagger(\mathbf{r})\right)^T = \left(\Psi_{j,\uparrow}(\mathbf{r}), \Psi_{j,\downarrow}(\mathbf{r}), \Psi_{j,\uparrow}^\dagger(\mathbf{r}), \Psi_{j,\downarrow}^\dagger(\mathbf{r})\right)^T \tag{2.63}$$

and $\Psi_{j,\sigma'}(\mathbf{r})$ is the annihilation operator of an electron in the j^{th} superconducting lead ($j = -1$ for the left one, $j = 1$ for the right one[14]), with $\sigma = \uparrow / \downarrow$ spin polarization (with respect to the same axis as the spin polarization defined in the edges) and at position $\mathbf{r}$. The Hamiltonian density is

$$\mathcal{H}_S^j = \begin{pmatrix} -\frac{\hbar^2\nabla_{\mathbf{r}}^2}{2m} - \mu & 0 & 0 & -\Delta e^{-i\theta_j} \\ 0 & -\frac{\hbar^2\nabla_{\mathbf{r}}^2}{2m} - \mu & \Delta e^{-i\theta_j} & 0 \\ 0 & \Delta e^{i\theta_j} & \frac{\hbar^2\nabla_{\mathbf{r}}^2}{2m} + \mu & 0 \\ -\Delta e^{i\theta_j} & 0 & 0 & \frac{\hbar^2\nabla_{\mathbf{r}}^2}{2m} + \mu \end{pmatrix}. \tag{2.64}$$

Δ is the superconducting pairing amplitude, μ the chemical potential – which is assumed to be the same in the two superconductors – while θ_j are the bare pairing phases that are kept distinguished in order to achieve the Josephson effect.

[14] In some cases, for the sake of clarity, $j = l, r$ will be preferred to $j = -1, 1$.

Lastly, H_T represents the tunneling Hamiltonian connecting the superconductors and the edges[15]. Is it given by

$$H_T = \sum_{j=\pm 1} H_T^j = \sum_{j=\pm 1} \int dx \int d\mathbf{r}\, \Psi_j^\dagger(\mathbf{r}) \mathcal{T}^j(\mathbf{r}, x) \boldsymbol{\psi}(x) + h.c., \tag{2.65}$$

where the tunneling matrix is

$$[\mathcal{T}^j(\mathbf{r}, x)]_{\sigma',\rho\tau} = \frac{\mathfrak{T}}{\sqrt{1+f_T^2}} (i f_T)^{\frac{1-\sigma'\tau\rho}{2}} e^{i\rho k_F x}\, \delta(x - j\frac{L}{2})\, \delta(\mathbf{r} - \mathbf{r}_{\mathbf{j}\tau}). \tag{2.66}$$

Here k_F is the Fermi momentum resulting from the doping of the topological insulator, whence the Dirac point is shifted away from zero energy. Moreover $\mathbf{r}_{j,\tau} = (jL/2, \tau W/2, 0)^T$ are the contact points between the j-th superconductor and the edges ($\mathbf{r}_{j,1}$ for the upper and $\mathbf{r}_{j,-1}$ for the lower edge channel respectively). As anticipated, the tunneling is assumed to occur locally at the intersections between the superconductors and the edges. Two more parameters have been introduced: f_T and $\mathfrak{T}$. The quantity f_T is the ratio of spin-reversing processes over the spin-conserving ones. It is reasonable to include such a parameter in the model since it allows to take into account the Rashba coupling in the material, which makes spin flips possible [87, 128, 193]. Typically, it is $f_T \ll 1$. The other parameter $\mathfrak{T}$ is the tunneling coefficient related to the opacity of the barrier. Notice that the tunneling Hamiltonian H_T has the same form as the one introduced in Eq. (1.140), when discussing the proximity effect.

Effective Hamiltonian for the edge states

In order to obtain an effective Hamiltonian of the proximitized system, we need to integrate out the superconductors. This procedure is quite long and can be found in Sec. A.2 of Appendix A. The calculation is performed in the absence of the magnetic field. We will discuss soon how the magnetic field is reinserted, keeping in mind the gauge-invariance of the phase.

After the integration over the superconductors' degrees of freedom, the total effective Hamiltonian is $H_E + \delta H_E$, with the extra term δH_E written as [78]

$$\delta H_E \approx \sum_{\zeta,\zeta',j} \left[\Gamma^j_{\zeta,\zeta'} \psi_\zeta(x_j^-) \psi_{\zeta'}(x_j^+) + h.c.\right], \tag{2.67}$$

Here, ζ, ζ' are collective indices standing for $\rho\tau, \rho'\tau'$, and $x_j^\pm = jL/2 \pm \delta_{\zeta,\zeta'}\xi/2$, where $\xi = \hbar v_F/\Delta$ is the coherence length in the edges, which represents the short distance cut-off of our system, $\xi \ll L$. The approximation is done focusing on the low temperature and small voltage regime $T, V \ll \Delta$. In this regime, as commented in Appendix A, transport between the superconductors and the edges is essentially carried out by Cooper pairs, and there is no contribution of single quasi-particles.

Eq. (2.67) accommodates all the possible injection processes for the two electrons, shown in Fig. 2.18: either in a spin-singlet or spin-triplet state (the triplet processes being proportional to a factor $\tilde{f}_T = f_T/\sqrt{1+f_T^2}$; and either into the same edges ("Local Andreev Reflection", LAR) or into different ones ("Crossed Andreev Reflection",

[15] As for H_E, for nonhelical edge states it would have a larger dimension. It is here written for the helical case.

CAR). CAR is possible since we assume $\xi_S > W$, where $\xi_S = \hbar v_{F,S}/\Delta$ (with $v_{F,S}$ the Fermi velocity in the superconductors) is the coherence length of the superconductors, and its suppression compared to LAR will be denoted by f_C[16]. The splitting $x_j^{\pm}$ is introduced to make tunneling of spin-triplet Cooper pairs into or out of the same edge possible.

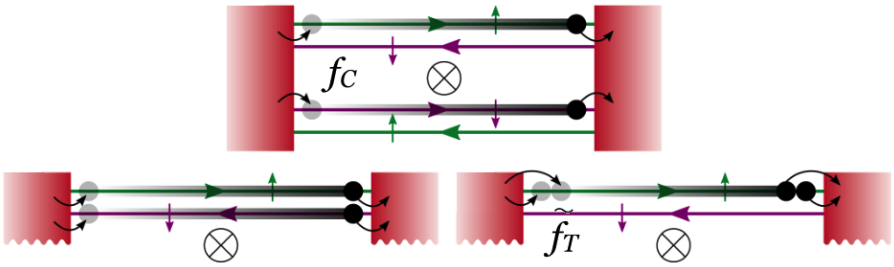

Figure 2.18: *Examples of processes of injection of Cooper pair from the left superconductor into the edge channels, and then from the latters into the right superconductor. The injection into (or out of) opposite edges is associated to a suppression factor of f_C, and the injection in a spin triplet state is associated to a suppression factor of $\tilde{f}_T$. Adapted with permission from [78]. Copyright 2024 by the American Physical Society.*

The summation in Eq. (2.67) is antisymmetrized for each $\zeta \neq \zeta'$. This means that the summed terms are only ten:

$$\Gamma^j_{11,11} \quad \Gamma^j_{11,-11} \quad \Gamma^j_{11,1-1} \quad \Gamma^j_{11,-1-1} \quad \Gamma^j_{-11,-11}$$
$$\Gamma^j_{-11,1-1} \quad \Gamma^j_{-11,-1-1} \quad \Gamma^j_{1-1,1-1} \quad \Gamma^j_{1-1,-1-1} \quad \Gamma^j_{-1-1,-1-1}.$$

Each of the $\Gamma^j_{\zeta,\zeta'}$ coefficients contains all the details specifying the tunneling process, i.e. species of the electrons forming the Cooper pair, spin-flipping, Local/Crossed Andreev Reflection. They are all proportional to the tunneling rate $\Gamma = \pi \mathfrak{T}^2 N_S$, with N_S the normal density of states per spin at the Fermi-level in the superconductors. The full expression for the $\Gamma^j_{\zeta,\zeta'}$ coefficients is [78]

$$\Gamma^j_{\zeta,\zeta'} = \Gamma \left(i\tilde{f}_T\right)^{\delta_{\rho*\tau,\rho'*\tau'}} (f_C)^{\delta_{\tau,-\tau'}} e^{i[\frac{j}{2}k_F L(\rho+\rho')-\theta_j]}. \tag{2.68}$$

Notice that, as expected, the factor f_C is present only if $\tau \neq \tau'$ (CAR) and $\tilde{f}_T$ is present only if the spins of the two electrons of the Cooper pair are the same (triplet injection).

Effect of the magnetic field and the voltage bias

The magnetic field and the voltage bias piercing the junction have not been included yet. They both have an effect on the superconducting phase difference, and the tunneling coefficients $\Gamma^j_{\zeta,\zeta'}$ need to be modified accordingly. The effect of a magnetic flux has been discussed extensively in the first part of this Chapter, arriving at the expression in Eq. (2.47) as the phase difference perceived by a Cooper pair transmitted from the left to the right superconductor. The only paths allowed for electrons through the junction

[16] Here, $f_C \sim \mathtt{f}(k_{F,S}W)e^{-W/\xi_S}$, with $\mathtt{f}$ an oscillatory and decaying function and $k_{F,S}$ the Fermi momentum in the superconductors. This quantity naturally emerges while integrating out the superconductors, see [78] for the details.

are now $y = \pm W/2$. If both electrons are injected into the upper edge ($\tau = \tau' = 1$) or into the lower edge ($\tau = \tau' = -1$), Eq. (2.47) returns

$$\varphi(y = \tau W/2) = \frac{\tau\pi\phi}{\phi_0} + \theta_r - \theta_l, \tag{2.69}$$

These two cases correspond to LAR processes. It can be easily shown that for a single transmitted electron on the τ edge, the magnetic flux contribution is $\tau\pi\phi/2\phi_0$. Therefore, if a Cooper pair is split over the two edges via a CAR process, the two single-electron phases cancel, and no-flux dependence arises. The effect can be simply included in the model just by adding flux-dependent factors to the $\Gamma^j_{\zeta,\zeta'}$ coefficients. In particular, it is sufficient to substitute

$$e^{-i\theta_j} \to e^{-i\left[\theta_j + \frac{j}{2}\frac{\pi\phi(\tau+\tau')}{2\phi_0}\right]}. \tag{2.70}$$

We can check that Eq. (2.70) returns the correct phase differences we discussed. The Cooper pair tunneling from the left superconductor to the edges is described by $(\Gamma^l_{\zeta,\zeta'})^*$, and the one from the edges to the right superconductor is described by $\Gamma^r_{\zeta,\zeta'}$. For two CAR processes $\tau = -\tau'$,

$$\underbrace{e^{-i\left[\theta_r + \frac{1}{2}\frac{\pi\phi(\tau+\tau')}{2\phi_0}\right]}}_{\text{From } \Gamma^r_{\zeta,\zeta'}} \underbrace{e^{i\left[\theta_l - \frac{1}{2}\frac{\pi\phi(\tau+\tau')}{2\phi_0}\right]}}_{\text{From } (\Gamma^l_{\zeta,\zeta'})^*} = e^{-i(\theta_r - \theta_l)}, \tag{2.71}$$

hence there is no flux dependence. On the other hand, for two LAR processes $\tau = \tau'$, and

$$\underbrace{e^{-i\left[\theta_r + \frac{1}{2}\frac{\pi\phi(\tau+\tau')}{2\phi_0}\right]}}_{\text{From } \Gamma^r_{\zeta,\zeta'}} \underbrace{e^{i\left[\theta_l - \frac{1}{2}\frac{\pi\phi(\tau+\tau')}{2\phi_0}\right]}}_{\text{From } (\Gamma^l_{\zeta,\zeta'})^*} = e^{-i\left[(\theta_r - \theta_l) + \frac{\tau\pi\phi}{\phi_0}\right]}, \tag{2.72}$$

in agreement with Eq. (2.69).

Notice that the collected geometric Aharonov-Bohm phase is the only magnetic effect included, while orbital- and Zeeman effects are neglected.

The last element is the voltage bias, which brings a time dependence into the superconducting phase difference (the AC Josephson effect). This is implemented by

$$e^{-i\left[\theta_j + \frac{j}{2}\frac{\pi\phi(\tau+\tau')}{2\phi_0}\right]} \to e^{-i\left[\theta_j + \frac{j}{2}\frac{\pi\phi(\tau+\tau')}{2\phi_0} + \frac{j}{2}\omega_J t\right]}, \tag{2.73}$$

with $\omega_J = 2eV/\hbar$, so that the overall superconducting phase difference reads as

$$\varphi = \frac{(\tau+\tau')\pi\phi}{2\phi_0} + \omega_J t + \theta_r - \theta_l. \tag{2.74}$$

To conclude, the new expressions for the $\Gamma^j_{\zeta,\zeta'}$ coefficients are

$$\Gamma^j_{\zeta,\zeta'} = \Gamma\left(i\tilde{f}_T\right)^{\delta_{\rho\tau,\rho'\tau'}} (f_C)^{\delta_{\tau,-\tau'}} e^{i\left[\frac{j}{2}k_F L(\rho+\rho') - \theta_j - \frac{j}{2}\frac{\pi\phi(\tau+\tau')}{2\phi_0} - \frac{j}{2}\omega_J t\right]}. \tag{2.75}$$

Computation of the supercurrent

Having assessed the effective Hamiltonian of the system at low-energies $E \ll \Delta$, $H_{\text{eff}} = H_E + \delta H_E$, including the effect of the magnetic field and the bias, it is now possible to go through the supercurrent calculation.

The total number operator relative to the electrons in the edge states is given by

$$N = \sum_{\zeta} \int dx\, \psi^{\dagger}_{\zeta}(x)\psi_{\zeta}(x). \tag{2.76}$$

The unperturbed edge system is clearly particle number conserving, namely $[H_E, N] = 0$, while a net change in the number of electrons arises due to the coupling to the superconductors. In particular, we denote as $\dot{N}^r(\dot{N}^l)$ the variation originated by the right(left) superconductor. In the Heisenberg picture,

$$\dot{N}^r = \frac{i}{\hbar}[H_E + \delta H^r_E, N] = \frac{i}{\hbar}[\delta H^r_E, N], \tag{2.77}$$

$$\dot{N}^l = \frac{i}{\hbar}[H_E + \delta H^l_E, N] = \frac{i}{\hbar}[\delta H^l_E, N]. \tag{2.78}$$

The operator I^j, relative to the current flowing in the edges reads as[17] $I^j(t) = e\dot{N}^j$. Specifically, $I^r(t)(I^l(t))$ are the currents injected from the superconducting leads in the edges. Since the procedure is independent of the choice of the lead, the authors report the calculation of the generic j-th term.

Given the form of δH^j_E, carrying out the anticommutation leads to

$$I^j = \frac{2ie}{\hbar} \sum_{\zeta,\zeta'} \left[\Gamma^j_{\zeta,\zeta'} \psi_{\zeta}(x^-_j)\psi_{\zeta'}(x^+_j) - h.c.\right]. \tag{2.79}$$

The next step is to compute the expectation value

$$I^j(t) \equiv \left\langle U(-\infty, t) I^j(t) U(t, -\infty) \right\rangle, \tag{2.80}$$

taken with respect to the unperturbed edge state system in the far past. Here, $U(-\infty, t) = U^{\dagger}(t, +\infty) = T_+ e^{-\frac{i}{\hbar}\int_{-\infty}^{t} d\tau \delta H_E(\tau)}$ is the time-evolution operator in the interaction picture representation, with T_+ the time-ordering operator.

Assuming the coupling between the lead j and the edges to be weak (namely $\Gamma N_E \ll 1$, with N_E the density of states at the Fermi-level in the edge system), δH_E can be regarded as a small perturbation. According to the linear response theory, up to linear order in δH_E (corresponding to second order in Γ), we get

$$I^j(t) \approx \frac{i}{\hbar} \int_{-\infty}^{t} d\tau \left\langle \left[\delta H_E(\tau), I^j(t)\right] \right\rangle_E. \tag{2.81}$$

The subscript "E" serves as a reminder of the fact that we are considering an initial (at $t = -\infty$) equilibrium average calculated with respect to the unperturbed system (described by H_E) in the past. In the calculation of $I^j(t)$, the relevant perturbation is the one induced by the $-j$-th superconductor, namely δH^{-j}_E. This can be understood by looking at the expressions of the $\Gamma^j_{\zeta,\zeta'}$ coefficients: since they keep trace of the phase of the superconductor to whom they are related, the superconducting phase difference-dependent supercurrent originates from the $-j$, j terms.

[17] We remind that the perturbation δH^j_E - and therefore also I^j - acquires a time dependence in the $\Gamma^j_{\zeta,\zeta'}$ coefficients as the bias V is non-zero.

The calculation in full detail can be found in Appendix A. Skipping some steps, one gets

$$I^j(t) = \frac{4e\Gamma^2}{\hbar^2}\mathrm{Re}\Bigg\{ e^{-i(\omega_J t+\varphi_0)} \sum_{\zeta,\zeta'} f_{\zeta,\zeta'} \int_{-\infty}^{\infty} dt'\, e^{i\frac{eV}{\hbar}t'}\theta(t') \\ \Big\langle \Big[\psi_\zeta(x_j^-,t')\psi_{\zeta'}(x_j^+,t'), \psi_{\zeta'}^\dagger(x_{-j}^+,0)\psi_\zeta^\dagger(x_{-j}^-,0)\Big]\Big\rangle_E \Bigg\}, \tag{2.82}$$

where

$$f_{\zeta,\zeta'} = (\tilde{f}_T)^{2\delta_{\rho*\tau,\rho'*\tau'}} f_C^{2\delta_{\tau,-\tau'}} e^{i\left[k_F L(\rho+\rho') - \frac{\pi\phi}{2\phi_0}(\tau+\tau')\right]}. \tag{2.83}$$

Such prefactor emerges from the product $\Gamma^j_{\zeta,\zeta'}(t)\left[\Gamma^{-j}_{\zeta,\zeta'}(t-t')\right]^*$, and is reminescent of the injection out of the $-j$-th superconductor and into the j-th superconductor. For instance, a spin-flip factor $\tilde{f}_T$ is collected if the spin polarizations ($\rho\tau$ and $\rho'\tau'$) of the two electrons are the same. Along the same line of reasoning, a CAR factor f_C is acquired if the Cooper pair is split over the two edges, $\tau = -\tau'$, neutralizing the SQUID phase factor $\pi\phi/\phi_0$ which is expected in the LAR case only. From now on, it is set $j = r$, $-j = l$. With further manipulation and by applying Wick's theorem, the current finally reads as

$$I^r(t) = \frac{2e\Delta\Gamma^2}{\hbar^3\pi^2 v_F^2}\mathrm{Im}\Bigg\{ e^{-i(\omega_J t+\varphi_0)} \sum_{\zeta,\zeta'} f_{\zeta,\zeta'} \int_0^{\infty} ds\, e^{i\tilde{V}s}\mathrm{Im}\,\Pi_{\zeta,\zeta'}\left(\tilde{T},\tilde{L},s\right)\Bigg\}, \tag{2.84}$$

where each addend corresponds to a process (the transport of a Cooper pair through the junction) contributing to the current. In Eq. (2.84), $\tilde{V} = eV/\Delta$, $\tilde{L} = L\Delta/\hbar v_F$, $\tilde{T} = \pi k_B T/\Delta$ and $s = t'\Delta/\hbar$ are dimensionless quantities, and the function $\Pi_{\zeta,\zeta'}$ is given by a combination of products of two Green functions,

$$\Pi_{\zeta,\zeta'}\left(\tilde{T},\tilde{L},s\right) = \delta_{\zeta,\zeta'}\frac{\tilde{T}}{\sinh\left[\tilde{T}\left(\tilde{L}-\delta_{\zeta,\zeta'}-\rho s+i\rho\right)\right]}\frac{\tilde{T}}{\sinh\left[\tilde{T}\left(\tilde{L}+\delta_{\zeta,\zeta'}-\rho s+i\rho\right)\right]} \\ -\rho\rho'\frac{\tilde{T}}{\sinh\left[\tilde{T}\left(\tilde{L}-\rho s+i\rho\right)\right]}\frac{\tilde{T}}{\sinh\left[\tilde{T}\left(\tilde{L}-\rho' s+i\rho'\right)\right]}. \tag{2.85}$$

If $\zeta = \zeta'$, which means that the two electrons within a Cooper pair are injected in a spin-triplet state and into the same edge, the above expression can be expanded in $\xi/L \ll 1$. At the second order, this leads to

$$\Pi_{\zeta,\zeta}\left(\tilde{T},\tilde{L},s\right) = \frac{\tilde{T}^4}{\sinh^4\left[\tilde{T}\left(\tilde{L}-\rho s+i\rho\right)\right]}. \tag{2.86}$$

Notice that the absence of the Cooper pair splitting $\pm\xi/2$ introduced before would have resulted in $\Pi_{\zeta,\zeta}\left(\tilde{T},\tilde{L},s\right) = 0$, in accordance with Pauli principle.

The temperature and bias dependence is encoded by the integrals over s, which are

essentially five, which in [78] are denoted as

$$\mathcal{I}_1 = \int_0^{+\infty} ds\, e^{i\tilde{V}s} \mathrm{Im} \frac{\tilde{T}^2}{\sinh\left[\tilde{T}\left(\tilde{L}-s+i\right)\right]\sinh\left[\tilde{T}\left(\tilde{L}+s-i\right)\right]}, \tag{2.87a}$$

$$\mathcal{I}_{2+} = -\int_0^{+\infty} ds\, e^{i\tilde{V}s} \mathrm{Im} \frac{\tilde{T}^2}{\sinh^2\left[\tilde{T}\left(\tilde{L}-s+i\right)\right]}, \tag{2.87b}$$

$$\mathcal{I}_{2-} = -\int_0^{+\infty} ds\, e^{i\tilde{V}s} \mathrm{Im} \frac{\tilde{T}^2}{\sinh^2\left[\tilde{T}\left(\tilde{L}+s-i\right)\right]}, \tag{2.87c}$$

$$\mathcal{I}_{4+} = \int_0^{+\infty} ds\, e^{i\tilde{V}s} \mathrm{Im} \frac{\tilde{T}^4}{\sinh^4\left[\tilde{T}\left(\tilde{L}-s+i\right)\right]}, \tag{2.87d}$$

$$\mathcal{I}_{4-} = \int_0^{+\infty} ds\, e^{i\tilde{V}s} \mathrm{Im} \frac{\tilde{T}^4}{\sinh^4\left[\tilde{T}\left(\tilde{L}+s-i\right)\right]}. \tag{2.87e}$$

In the following, we will use the notation

$$\mathcal{I}_2 = e^{i2k_F L}\mathcal{I}_{2+} + e^{-i2k_F L}\mathcal{I}_{2-}, \qquad \mathcal{I}_4 = e^{i2k_F L}\mathcal{I}_{4+} + e^{-i2k_F L}\mathcal{I}_{4-}. \tag{2.88}$$

In particular, the paper especially analyzes the long junction regime, $\tilde{L} \gg 1$, and since the current computation considered low sub-gap energies, we have $\tilde{V}, \tilde{T} \ll 1$. Details on the integrals' behavior can be found in the Supplemental Material to [78].

Results and discussion

The quantity which is inspected in [78] is the magnitude of the ω_J Fourier component of the time dependent supercurrent $I^r(t)$, namely

$$I^r_{\omega_J} = \left| \frac{1}{T}\int_{-T/2}^{T/2} dt\, e^{-i\omega_J t} I^r(t) \right| = \frac{1}{2}\frac{2e\Delta\Gamma^2}{\hbar^3\pi^2 v_F^2} \left| \sum_{\zeta,\zeta'} f_{\zeta,\zeta'} \int_0^{\infty} ds\, e^{i\tilde{V}s} \mathrm{Im}\, \Pi_{\zeta,\zeta'}\left(\tilde{T}, \tilde{L}, s\right) \right|, \tag{2.89}$$

as a function of the magnetic flux ϕ. Here, $T = 2\pi/\omega_J$. At zero-bias, the corresponding quantity is the critical current associated to I^r. In this case, the prefactor $1/2$ is absent. In terms of flux dependence, the above expression admits a simple form

$$I^r_{\omega_J} = \left| A\cos\frac{\pi\phi}{\phi_0} + f_C^2 B \right|, \tag{2.90}$$

where, as expected, we recognize the SQUID term originating from LAR and the flux-independent term originating from CAR. The coefficients A and B contain all the amplitudes associated to the current contributing processes, and therefore all the details of the underlying model. They might have cumbersome expressions as a function of the parameters and are in general complex-valued. In particular,

$$A = 2(\mathcal{I}_1 + \tilde{f}_T^2\mathcal{I}_4), \qquad B = (\mathcal{I}_2 + 2\tilde{f}_T^2\mathcal{I}_1). \tag{2.91}$$

The resulting plots are shown in Fig. 2.19. We omit those relative to electron-electron interactions, which we did not review. Apart from the zero-bias case (Fig. 2.19(a)),

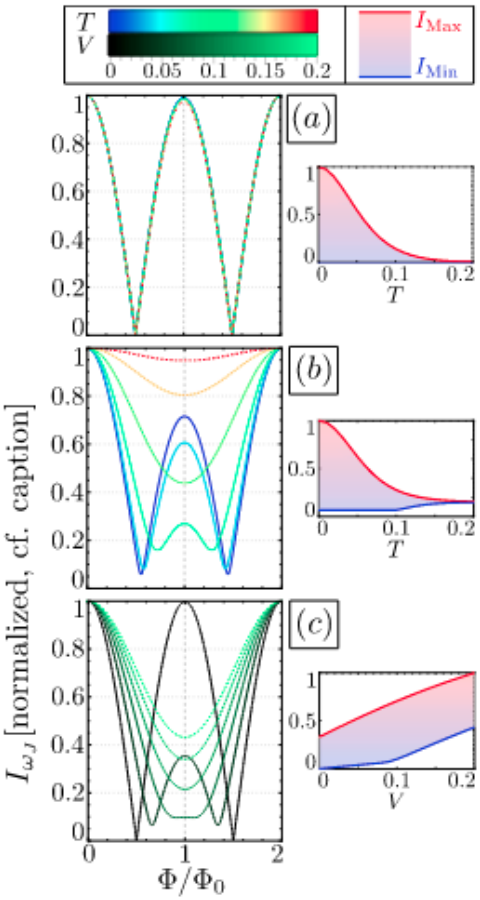

Figure 2.19: *Different plots of $I^r_{\omega_J}$, with each curve normalized with respect to its maximum. In all panels, $\tilde{L} = 20$, $\tilde{f}_T = 0$, $k_F L = \pi(4n+3)/4$, $f_C = 0.3$. The insets show the maximum and minimum value of $I^r_{\omega_J}$ as a function of the sweeping parameter and normalized with respect to the overall maximum value. (a) $\tilde{V} = 0$ and $\tilde{T}$ varies between 0 and 0.2. (b) Same range for temperature, but $\tilde{V} = 0.1$. (c) Bias $\tilde{V}$ varying between 0 and 0.2 while $\tilde{T} = 0.1$. Adapted with permission from [78]. Copyright 2024 by the American Physical Society.*

different values of temperature and bias give rise to different features, and the even-odd effect can be more or less visible. Unlike the helical case, for non-helical edge channels (not discussed here) the plots are highly robust in the parameter space. The papers hence suggests to measure the flux-dependent Josephson-frequency Fourier component of the supercurrent, for various values of bias voltage and temperature, as a way to identify the topological or non-topological nature of the edge states carrying the supercurrent.

As a last comment we emphasize that, within this model, the two electrons within a Cooper pair enter and leave the junction in the same spin state and via the same type of Andreev reflection process. In the next Chapter we will see that, in the presence of a constriction between the helical edge states, this fact does not hold true anymore, and a new interplay of Local and Crossed Andreev Reflection emerges.

CHAPTER 3

The proximitized Quantum Spin Hall constriction

In this Chapter, we delve into the theoretical analysis of a long constriction between the helical edge states of a two-dimensional topological insulator. The constriction is laterally tunnel-coupled to two superconductors and a magnetic field is applied perpendicularly to the plane of the two-dimensional topological insulator. This configuration merges many of the concepts we have previously introduced. Despite its technological importance, it remains largely uncharted in the realm of theoretical investigation. While the complete implementation of a proximitized constriction has yet to be realized in experimental settings, both the constriction itself and the proximization of topological insulators have been achieved. Therefore, the assembly of the entire structure appears to be a feasible endeavor, and its theoretical analysis holds significant relevance. Moreover, the only result reported in literature dealing with a long Quantum Spin Hall constriction, and mentioned in Chapter 1, is about an interaction-induced reduction of the conductance [168], which might disappear in the presence of superconductors, due to screening. It is hence even more challenging to demonstrate the formation of topological constrictions in the presence of superconductivity, and our analysis addresses this issue. At the same time, we provide a characterization of the device and pinpoint an experimental signature of the coupling between the edges. These original results have been published in [188], and this Chapter is largely based upon that.

More specifically, we characterize theoretically the Josephson current in the presence of a magnetic field perpendicular to the plane defined by the edges. We find that the constriction leads to a $4\phi_0$-periodicity of the maximal current as a function of the magnetic flux. Such a periodicity is new compared to the SQUID and the even-odd effect ones, and is visible both if a finite bias is applied to the junction and in the zero-bias regime. We also show that the signature is robust - or even enhanced - at finite temperature. We emphasize that the anomalous periodicity we find is not strictly

related to crossings in the Andreev bound states and to Majorana physics [96]. Unconventional periodicities have been previously reported in [122], but based on different physics and in a Josephson junction with a nanowire as non-superconducting element and not a quantum spin Hall constriction. Ours is instead due to a new interplay of Local and Crossed Andreev Reflection allowed by the constriction, as schematically shown in Fig. 3.1: differently from the case without inter-edge tunneling, a Cooper pair can now enter and leave the junction with Andreev Reflection processes of different type. Being the junction pierced by a magnetic flux, this gives rise to a new possibility for the Aharonov-Bohm phase acquired, distinguished from that of a LAR-LAR or CAR-CAR propagation. As we will discuss, the processes responsible for the anomalous $4\phi_0$-periodicity are exactly those where, within the constriction, one of the two electrons forming the Cooper pair tunnels between the two edges.

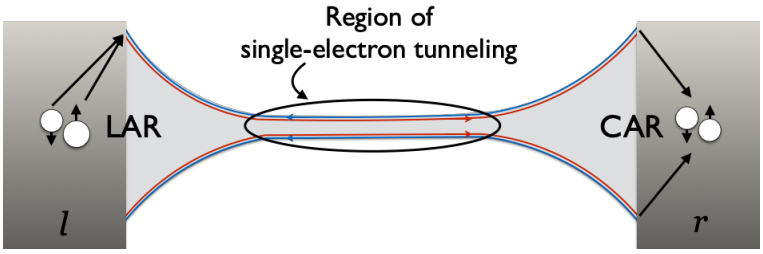

Figure 3.1: *An innovative feature of Josephson junctions based on Quantum Spin Hall constrictions: the possible interplay of Local (LAR) and Crossed Andreev Reflection (CAR) due to single-electron inter-edge tunneling within the constriction.*

The starting point for our formalism is the tunneling model for the topological Josephson junction we described in Subsec. 2.3.3. On top of that, we embed the presence of the inter-edge tunneling events discussed in 1.2.4.

At the end of the Chapter we will further comment on two points: first, the robustness of the results against edge reconstruction [187]; second, their generalization to the case of uniform inter-edge tunneling, and not confined to a subregion of the system as it is in Fig. 3.1.

3.1 Anomalous flux periodicities

3.1.1 Model

Fig. 3.2 shows the setup under investigation, consisting of a Josephson junction made of a two-dimensional topological insulator sample of length L and width W tunnel-coupled to two s-wave superconductors, right (r) and left (l). The superconducting part is a proximitized region of the topological structure. Halfway in the non-superconducting region there is a constriction between the helical edge states, having length ℓ ($\ell < L$, $\ell > {k_F}^{-1}$, with k_F the Fermi momentum) and width $w \ll W$. As will be soon discussed, within the constriction inter-edge tunneling events may occurr, namely an electron can move from the upper edge to the lower one or viceversa. We additionaly include a magnetic field B applied perpendicularly to the plane of the two-dimensional topological insulator, and a bias V. We will now examine in detail each of the components.

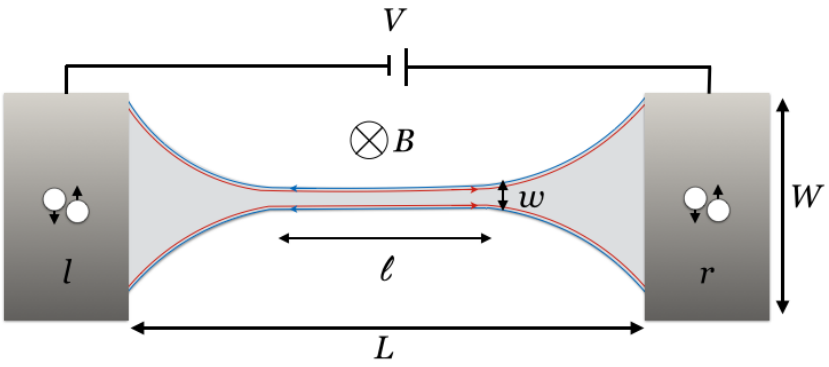

Figure 3.2: *Schematic of the setup: a sample of two-dimensional topological insulator of length L and width W is laterally tunnel-coupled to two superconductors (right, r and left, l); a magnetic field B, applied perpendicularly to the plane of the topological insulator, and a bias V are also included. Halfway in the non-superconducting region, there is a constriction of length ℓ and width w between the helical edges. Figure adapted from [188].*

The constriction

Central to our investigation is the constriction formed between the helical edges of the two-dimensional topological insulator. These edges span the range $-L/2 < x < L/2$. Their separation W at the interfaces with the superconductors diminishes significantly to $w \ll W$ within the constriction of length $\ell < L$ (where $\ell > k_F^{-1}$), as shown in Fig. 3.3. Since $L \gg k_F^{-1}$, the system under inspection acquires translational invariance and we retain momentum k as an eligible quantum number. The Hamiltonian describing the helical states H_E^0 is given by

$$H_E^0 = \sum_k \boldsymbol{c}_k^\dagger \mathcal{H}_E^0 \boldsymbol{c}_k, \tag{3.1}$$

where

$$\boldsymbol{c}_k = \left(c_{k,11}, c_{k,-11}, c_{k,-1-1}, c_{k,1-1}\right)^T, \tag{3.2}$$

with $c_{k,\rho\tau}$ the Fermi operator that annihilates an electron with momentum k propagating in the ρ-direction channel of the τ edge. As in the previous Chapter, we denote by $\rho = 1(-1)$ the right (left) direction of motion and by $\tau = 1(-1)$ the upper (lower) edge. The bare Hamiltonian is made of two terms,

$$\mathcal{H}_E^0 = \mathcal{H}_{kin.} + \mathcal{H}_{f.s.}. \tag{3.3}$$

The kinetic part $\mathcal{H}_{kin.}$ is described by two copies of Eq. (1.138) with opposite helicity,

$$\mathcal{H}_{kin.} = \hbar v_F k \tau_z \otimes \rho_z \tag{3.4}$$

with v_F the Fermi velocity. Here ρ_i and τ_i, $i = 0, x, y, z$ represent the identity and the three Pauli matrices acting on right/left mover and upper/lower edge space, respectively. The second term,

$$\mathcal{H}_{f.s.} = f \tau_x \otimes \rho_x \tag{3.5}$$

describes the forward scattering tunneling across the edges parametrized by f (as introduced in Eq. (1.143)). We recall that it originates from processes where one electron

changes the edge while preserving the direction of motion – hence flipping its spin and breaking axial spin symmetry – and that it preserves time-reversal symmetry. It is important to highlight that, while the parameter f is taken as constant over the entire junction, the assumption is that tunneling takes place exclusively within the constriction of length ℓ, owing to the smaller separation of the helical edges $w \ll W$. However, in the case of long constriction ($\ell > k_F^{-1}$), we only take into account momentum-conserving tunneling events, neglecting finite size effects related to ℓ. Sec. 3.3 will deal with inter-edge tunneling uniformly present in the whole junction L.

When discussing Quantum Spin Hall constrictions, a backward scattering term of the type $\mathcal{H}_{b.s.} = b\tau_x \otimes \rho_0$ was also introduced (see Eq. (1.142)). In the present context, this term is neglected, along with any gapping of the edges due to intra-edge mechanisms. As discussed in Subsec. 1.2.4, the former (but also the latter) does not exert significant influence on the system away from the Dirac point, which for thick heterostructures is located deep in the valence band [168]. We can thus focus on this circumstance and ignore such effects. They could be included perturbatively but we do not expect them to affect our results.

Given the coherent transport observed over distances comparable to the sample dimensions in state-of-the-art devices, we assume the absence of impurities [18]. For a schematic of the system and of the couplings, see Fig. 3.3. Diagonalizing Eq. (3.1), we

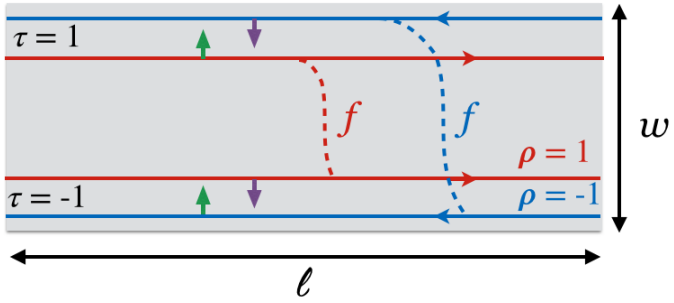

Figure 3.3: *Schematic of the constriction of length ℓ and width w. The direction-conserving couplings between the upper and lower edge of the two-dimensional topological insulator, with amplitude f, are also shown. Figure adapted from [188].*

obtain

$$H_E^0 = \sum_{i=1}^{4} \sum_k E_{A_i}(k) A_{k,i}^\dagger A_{k,i}, \tag{3.6}$$

with

$$\begin{aligned} A_{k,1} &= \frac{1}{\sqrt{2}} \left(-c_{k,-11} + c_{k,-1-1}\right) \\ A_{k,2} &= \frac{1}{\sqrt{2}} \left(c_{k,-11} + c_{k,-1-1}\right) \\ A_{k,3} &= \frac{1}{\sqrt{2}} \left(-c_{k,11} + c_{k,1-1}\right) \\ A_{k,4} &= \frac{1}{\sqrt{2}} \left(c_{k,11} + c_{k,1-1}\right), \end{aligned} \tag{3.7}$$

and the spectrum is

$$\begin{aligned} E_{A_1}(k) &= -f - \hbar v_F k \\ E_{A_2}(k) &= f - \hbar v_F k \\ E_{A_3}(k) &= -f + \hbar v_F k \\ E_{A_4}(k) &= f + \hbar v_F k. \end{aligned} \tag{3.8}$$

The four operators in Eq. (3.7) have well-defined chirality (left for $A_{k,1}$, $A_{k,2}$ and right for $A_{k,3}$, $A_{k,4}$). We highlight the $1/\sqrt{2}$ weight in each term $A_{k,i}$, due to the equal superposition of an upper-edge state and a lower-edge state. We re-establish that the role of f is to split the dispersion in energy, analogously to the Rashba coupling in quantum wires [74, 84, 132, 138, 166].

In the following we will rediscuss the tunneling processes in connection with the magnetic flux ϕ through the plane of the topological insulator.

Superconducting leads and effective Hamiltonian

The edges just described are proximitized, for $x < -L/2$ and $x > L/2$, with two standard BCS superconductors [1]. The left superconductor, extending for $x < -L/2$, is indexed by $j = -1$ while the right one, extending for $x > L/2$, by $j = 1$. In some later expressions, and especially with several indices involved, we will resort back to l and r. The superconducting pairing is denoted by $\Delta_j = \Delta e^{i\theta_j}$, with θ_j the bare superconducting pairing phases - that we keep distinguished in principle. Moreover, we assume the chemical potential to be the same in the two superconductors. Their Hamiltonian H_S^j and the tunneling Hamiltonian between the superconductors and the constriction, $H_T = \sum_j H_T^j$, are kept identical to the ones in [78] introduced in the previous Chapter. As shown in Appendix A, they lead to the effective Hamiltonian of the proximitized system in Eq. (2.67), approximately written as[2] [78]

$$\delta H_E \approx \sum_{\zeta_1,\zeta_2,j} \left[\Gamma^j_{\zeta_1,\zeta_2} \psi_{\zeta_1}(x_j^-)\psi_{\zeta_2}(x_j^+) + h.c.\right], \tag{3.9}$$

with $\psi_\zeta(x) = \psi_{\rho\tau}(x) = 1/\sqrt{L}\sum_k c_{k,\rho\tau}e^{ikx}$. Compared to Eq. (2.67), and for future convenience, we denote by ζ_1, ζ_2 – instead of ζ, ζ' – the collective indices for the two injected electrons. In particular, $\zeta_1 = \rho_1\tau_1$, $\zeta_2 = \rho_2\tau_2$ and $x_j^\pm = jL/2 \pm \delta_{\zeta_1,\zeta_2}\xi/2$, where $\xi = \hbar v_F/\Delta$ is the coherence length in the edges, with $\xi \ll L$. The approximation is done for the regime $E_{A_i} \ll \Delta$. The possible processes of injection of the two electrons, already present in [78], are schematized in Fig. 3.4. The triplet processes, enabled by spin-orbit coupling [193], are rescaled by a factor $\tilde{f}_T = f_T/\sqrt{1+f_T^2}$ if compared to the singlet ones. The parameter f_T is included in the single-electron tunneling Hamiltonian associated to the interfaces between the superconductor and the topological insulator (see Eq. (2.65)), to take into account spin-flip events. The injection into different edges via CAR is suppressed by the factor f_C if compared to LAR. In particular, $f_C \propto e^{-W/\xi_S}$, and in order to allow for a significant amount of CAR we assume $\xi_S > W$, $\xi_S = \hbar v_{F,S}/\Delta$ being the coherence length of the superconductors ($v_{F,S}$ is their Fermi velocity). All this information is encoded in each of the $\Gamma^j_{\zeta_1,\zeta_2}$ coefficients.

[1] In experiments on two-dimensional topological insulators, Niobium is the prime example of employed superconductor.

[2] We remind that the summation is antisymmetrized for each $\zeta_1 \neq \zeta_2$.

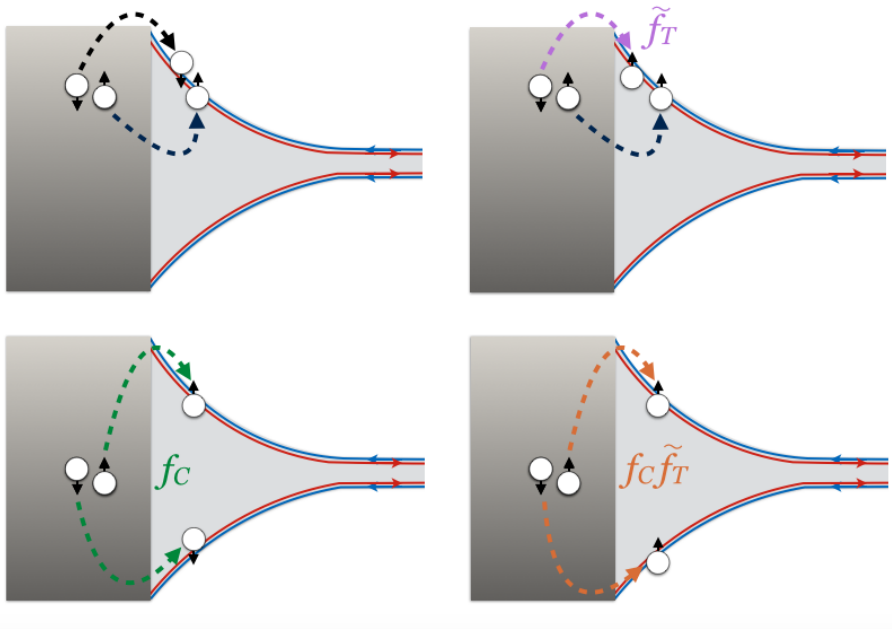

Figure 3.4: *Possible processes of injection of two electrons: in a spin-singlet or spin-triplet state (left or right panels) and either into the same edge or into different ones (upper or lower panels). Figure adapted from [188].*

In momentum space, the effective Hamiltonian becomes

$$\delta H_E = \sum_{\zeta_1,\zeta_2,j} \left[\Gamma^j_{\zeta_1,\zeta_2} \frac{1}{L} \sum_{k_1} \sum_{k_2} c_{k_1,\zeta_1} e^{ik_1 x_j^-} c_{k_2,\zeta_2} e^{ik_2 x_j^+} + h.c. \right] = \delta H_E^r + \delta H_E^l, \quad (3.10)$$

where

$$\Gamma^j_{\zeta_1,\zeta_2} = (-1)^{\delta_{\zeta_1,-1-1}\delta_{\zeta_2,1-1}} \Gamma \left(\tilde{f}_T\right)^{\delta_{\rho_1*\tau_1,\rho_2*\tau_2}} (f_C)^{\delta_{\tau_1,-\tau_2}} e^{i[\frac{j}{2}k_F L(\rho_1+\rho_2)-\theta_j]}. \quad (3.11)$$

Here Γ is the tunneling rate of Cooper pairs[3]. Compared to [78], the additional minus sign in Eq. (3.11) is due to a different choice of the order for our edges basis[4]. This choice obviously does not affect the results.

Introduction of magnetic field and bias

So far we didn't include the applied bias V across the two superconductors and the magnetic flux ϕ piercing the junction perpendicularly, and it is now necessary to modify the rates properly. While the bias simply introduces a time dependence $(2eV/\hbar)t$ (see Eq. (2.23)), it is not a trivial question, in principle, whether we can use the same approach of [78] concerning the magnetic field. As in that work, we neglect the Zeeman coupling since it only provides a small energy splitting of the energy bands without significantly contributing to our results. The orbital effect is encoded by the minimal

[3] $\Gamma \propto \mathfrak{T}^2$, where $\mathfrak{T}$ parametrizes the magnitude of single-electron tunneling, see Eq. 2.66.

[4] This naturally leads to the definition of $\Gamma^j_{-1-1,1-1} \equiv \Gamma^j_{-1-1,1-1} - \Gamma^j_{1-1,-1-1}$ instead of $\Gamma^j_{1-1,-1-1} \equiv \Gamma^j_{1-1,-1-1} - \Gamma^j_{-1-1,1-1}$ as in the original paper. The difference in sign between the right hand side in the two cases originates the minus in Eq. (3.11).

coupling $-i\hbar\nabla \to -i\hbar\nabla + e\mathbf{A}$, with $e > 0$ the absolute value of the electron charge. We use the Landau gauge $\mathbf{A} = B(-y, 0, 0)$, such that the upper and lower edge states acquire opposite contributions $\mp\frac{ev_F\phi}{2L}$ to the energy. In the long junction limit $L \to \infty$, this contribution can hence also be neglected.

In the absence of inter-edge tunneling, the Aharonov-Bohm phase is $\pm\pi\phi/\phi_0$ for a Cooper pair entering and exiting the edge channels through two LAR processes both on the upper/lower edge. By contrast, when both processes are CAR, the Aharonov-Bohm phase is $\gamma^{AB} = 0$, as the phases acquired by the two electrons cancel with each other. However, the distinctive feature of our system is that an arbitrary number of inter-edge tunnelings may occur within the constriction, originating new processes that transfer a Cooper pair through the junction, as sketched in Fig. 3.1. A more careful discussion is hence in order, in particular distinguishing between even and odd numbers of tunneling events.

- With an even number of tunnelings, a Cooper pair can now enter the junction with a LAR process on the upper/lower edge and leave it with a LAR process on the opposite (lower/upper) one. This process is flux-independent, since the Aharonov-Bohm phase picked by the two electrons on the upper edge is canceled by the one picked on the lower one.

- With an odd number of tunnelings, by contrast, a Cooper pair can enter the junction with a LAR and exit with a CAR (or viceversa). This unusual scenario is associated to an unconventional Aharonov-Bohm phase of $\pm\pi\phi/2\phi_0$. For instance, if the Cooper pair enters the junction from the left superconductor with a LAR in the upper edge and exits to the right superconductor with a CAR, the two electrons accumulate the same phase while traveling on the upper edge, until the constriction. After the constriction, they travel on opposite edges and their phases cancel with each other. The resulting magnetic phase is $\pi\phi/2\phi_0$. The opposite phase $-\pi\phi/2\phi_0$ is obtained when the LAR process happens on the lower edge.

Importantly, the discussion of the Aharonov-Bohm phases above holds true if the flux enclosed in the constriction is negligible. This is fully justified by the assumption $\ell w \ll LW$. The relevance of this approximation is that it allows us not to care about the exact number of tunneling events and their precise location within the constriction. The inter-edge tunneling is effectively treated as occurring halfway across the junction. For this reason, in the following calculations, the lengthscale ℓ will not intervene explicitely, and only L will appear. If the flux enclosed in the constriction were included in our calculation, it would just add a weak Fraunhofer-like decay to the flux-dependence. However, our results would be qualitatively unchanged. At the end of the Chapter we will comment on how to deal with the case of extended tunneling, namely with a constriction as long as the junction, $\ell = L$. Thanks to the assumption above, we can include in our previous description all the phases described before, just by adding the same flux-dependent factors of [78] to the tunneling amplitudes in Eq. (3.11):

$$e^{-i\theta_j} \to e^{-i\left[\theta_j + \frac{j}{2}\left(\frac{\pi\phi(\tau_1+\tau_2)}{2\phi_0} + \omega_J t\right)\right]}, \tag{3.12}$$

with $\omega_J = 2eV/\hbar$. Since the gauge-invariant phase difference mentioned above is among the superconductors, it will involve one tunneling with $j = -1$ ($(\Gamma^l_{\zeta_1,\zeta_2})^*$, from

the left superconductor to the edges) and one with $j = 1$ ($\Gamma^r_{\zeta_3,\zeta_4}$, from the edges to the right superconductor). Even in the presence of inter-edge tunneling, Eq. (3.12) returns the correct phase differences we discussed: for two CAR processes ($\tau_1 = -\tau_2$ and $\tau_3 = -\tau_4$), there is no flux-dependence; for two LAR processes on the same edge ($\tau_1 = \tau_2 = \tau_3 = \tau_4 \equiv \tau$), we get a flux-dependent phase $\tau\pi\phi/\phi_0$; for two LAR on opposite edges ($\tau_1 = \tau_2 \neq \tau_3 = \tau_4$) we get zero; for a CAR and a LAR ($\tau_1 = \tau_2 \equiv \tau$ and $\tau_3 = -\tau_4$, or $\tau_1 = -\tau_2$ and $\tau_3 = \tau_4 \equiv \tau$) we get the anomalous term, with the sign depending on the τ of the LAR. This term will be essential for our results.

To conclude this part, we move to the $A_{k,i}$ basis by making the unitary transformation inverse to the one of Eq. (3.7). Let $a_{\zeta_i,i}$, with $\zeta_i = 11, -11, -1-1, 1-1$ and $i = 1, 2, 3, 4$, be the elements of such unitary matrix. Then, for each of the four operators c_{k,ζ_i}, we have

$$c_{k,\zeta_i} = a_{\zeta_i,1}A_{k,1} + a_{\zeta_i,2}A_{k,2} + a_{\zeta_i,3}A_{k,3} + a_{\zeta_i,4}A_{k,4}. \tag{3.13}$$

Substituting Eq. (3.13) in Eq. (3.10), we obtain

$$\begin{aligned}\delta H_E &= \sum_{i_1,i_2}\sum_{k_1,k_2}\sum_{\zeta_1,\zeta_2,j}\frac{1}{L}\left[\Gamma^j_{\zeta_1,\zeta_2}a_{\zeta_1,i_1}a_{\zeta_2,i_2}e^{ik_1x_j^-}e^{ik_2x_j^+}A_{k_1,i_1}A_{k_2,i_2} + h.c.\right] \\ &\equiv \sum_{i_1,i_2,j}\sum_{k_1,k_2}\frac{1}{L}\left[\Gamma^j_{i_1,i_2}(k_1,k_2)A_{k_1,i_1}A_{k_2,i_2} + h.c.\right],\end{aligned} \tag{3.14}$$

where we have defined

$$\Gamma^j_{i_1,i_2}(k_1,k_2) \equiv \sum_{\zeta_1,\zeta_2}\Gamma^j_{\zeta_1,\zeta_2}a_{\zeta_1,i_1}a_{\zeta_2,i_2}e^{ik_1x_j^-}e^{ik_2x_j^+}. \tag{3.15}$$

Until now, the summation over i_1, i_2 runs over 16 terms. We can reduce them up to 10 by antisymmetrizing the coefficients when $i_1 \neq i_2$, introducing the new coefficients $\alpha_{i_1,i_2,j}$[5]. We obtain

$$\delta H_E = \sum_j \delta H_E^j = \sum_j\sum_{i_1,i_2}\sum_{k_1,k_2}\frac{1}{L}\left[\alpha_{i_1,i_2,j}(k_1,k_2)A_{k_1,i_1}A_{k_2,i_2} + h.c.\right], \tag{3.16}$$

where now $\alpha_{i_1,i_2} = \alpha_{1,1} \quad \alpha_{1,2} \quad \alpha_{1,3} \quad \alpha_{1,4} \quad \alpha_{2,2} \quad \alpha_{2,3} \quad \alpha_{2,4} \quad \alpha_{3,3} \quad \alpha_{3,4} \quad \alpha_{4,4}$.

[5]E.g., for $i_1, i_2 = 1, 2$:

$$\begin{aligned}&\sum_{k_1,k_2}\Gamma^j_{1,2}(k_1,k_2)A_{k_1,1}A_{k_2,2} + \sum_{k_1,k_2}\Gamma^j_{2,1}(k_1,k_2)A_{k_1,2}A_{k_2,1} = \\ &= \sum_{k_1,k_2}\Gamma^j_{1,2}(k_1,k_2)A_{k_1,1}A_{k_2,2} + \sum_{k_1,k_2}\Gamma^j_{2,1}(k_2,k_1)A_{k_2,2}A_{k_1,1} = \\ &= \sum_{k_1,k_2}\Gamma^j_{1,2}(k_1,k_2)A_{k_1,1}A_{k_2,2} - \sum_{k_1,k_2}\Gamma^j_{2,1}(k_2,k_1)A_{k_1,1}A_{k_2,2} = \\ &= \sum_{k_1,k_2}\left(\Gamma^j_{1,2}(k_1,k_2) - \Gamma^j_{2,1}(k_2,k_1)\right)A_{k_1,1}A_{k_2,2} \equiv \\ &\equiv \sum_{k_1,k_2}\alpha_{1,2,j}(k_1,k_2)A_{k_1,1}A_{k_2,2}.\end{aligned}$$

The effective Hamiltonian H_E of the edges, which reads

$$H_E = H_E^0 + \delta H_E, \tag{3.17}$$

is now expressed on the basis that diagonalizes H_E^0. In the next Subsection, we show how to adapt the formalism of [78] for the evaluation of the Josephson current in our system, as the number of terms in the presence of the constriction is noticeably larger.

3.1.2 Formalism for the transport properties

Let $N = \sum_i \sum_k A^\dagger_{k,i} A_{k,i}$ be the total number operator relative to the electrons. The net change in the number of electrons, different from zero due to the coupling to the superconductors, is given by $\dot{N}$, with

$$\dot{N} = \frac{i}{\hbar}[H_E^0 + \delta H_E, N] = \frac{i}{\hbar}\left([H_E^0 + \delta H_E^r, N] + [H_E^0 + \delta H_E^l, N]\right) \equiv \dot{N}^r + \dot{N}^l, \tag{3.18}$$

where $[\cdot,\cdot]$ is the commutator and

$$\begin{aligned} \dot{N}^r &= \frac{i}{\hbar}[H_E^0 + \delta H_E^r, N] = \frac{i}{\hbar}[\delta H_E^r, N] \\ \dot{N}^l &= \frac{i}{\hbar}[H_E^0 + \delta H_E^l, N] = \frac{i}{\hbar}[\delta H_E^l, N] \end{aligned} \tag{3.19}$$

in the Heisenberg picture.

The current operator describing the exchange of electrons between the j^{th} superconductor and the edges is given by $I^j(t) = e\dot{N}^j$. According to our convention, $I^r(t)$ and $I^l(t)$ are the currents injected from the superconducting leads into the edges, as shown in Fig. 3.5 by the blue arrows. The total current is

$$I^{tot}(t) = I^r(t) - I^l(t), \tag{3.20}$$

flowing in the direction shown by the yellow arrow in the Figure. In the following we

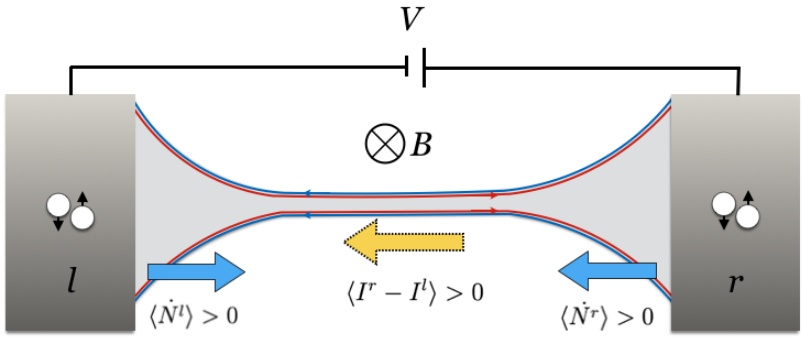

Figure 3.5: *Direction of the right, left and total current flow according to our conventions. Figure adapted from [188].*

sketch the calculation of the generic j^{th} term.

The anticommutation leads to

$$I^j = \frac{2ie}{\hbar L} \sum_{i_1,i_2} \sum_{k_1,k_2} \frac{1}{L} \left[\alpha_{i_1,i_2,j}(k_1,k_2) A_{k_1,i_1} A_{k_2,i_2} - h.c.\right]. \tag{3.21}$$

In the weak coupling regime between leads and edges, δH_E can be treated perturbatively. We are interested in the mean value

$$\langle I^j(t)\rangle = \left\langle U(-\infty,t) I^j(t) U(t,-\infty)\right\rangle, \tag{3.22}$$

taken with respect to the unperturbed edge state system in the far past, and where I^j time-evolves according to the unperturbed edge Hamiltonian H_E^0. With a little abuse of notation, in the following we will drop the angle brackets and simply denote it as $I^j(t)$. Here, $U(-\infty,t) = U^\dagger(t,+\infty) = T_+ e^{-\frac{i}{\hbar}\int_{-\infty}^{t} d\tau \delta H_E(\tau)}$ is the time-evolution operator in the interaction picture representation, with T_+ the time-ordering operator. Up to linear order in δH_E (second order in the tunneling rate Γ in this case), we get

$$I^j(t) \approx \frac{i}{\hbar}\int_{-\infty}^{t} d\tau \left\langle \left[\delta H_E(\tau), I^j(t)\right]\right\rangle_0 . \tag{3.23}$$

The subscript "0" specifies that the average is calculated with respect to the unperturbed system described by H_E^0. As in the previous Chapter, the relevant perturbation (leading to the superconducting phase difference-dependent supercurrent) is the one induced by the $-j^{th}$ superconductor, namely δH_E^{-j}.

Moving forward with the calculations (see Appendix B), we get

$$\begin{aligned} I^j(t) =& \frac{8e}{\hbar^2}\mathrm{Im}\Bigg\{ \int_{-\infty}^{\infty} dt' \theta(t') \sum_{i_1,i_2} \sum_{k_1,k_2,k_1',k_2'} \frac{1}{L^2} \alpha_{i_1,i_2,j}(k_1',k_2',t)\alpha^*_{i_1,i_2,-j}(k_1,k_2,t-t') \\ & \left\langle \left[A_{k_1',i_1}(t) A_{k_2',i_2}(t), A^\dagger_{k_2,i_2}(t-t') A^\dagger_{k_1,i_1}(t-t')\right]\right\rangle_0 \Bigg\}, \end{aligned} \tag{3.24}$$

where we have recovered the explicit time dependence of the coefficients α[6], and the correlation functions from now on will be time-ordered. Since the unperturbed edge system is time-translation invariant, Eq. (3.24) is equivalent to

$$\begin{aligned} I^j(t) =& \frac{8e}{\hbar^2}\mathrm{Im}\Bigg\{ \int_{-\infty}^{\infty} dt' \theta(t') \sum_{i_1,i_2} \sum_{k_1,k_2,k_1',k_2'} \frac{1}{L^2} \alpha_{i_1,i_2,j}(k_1',k_2',t)\alpha^*_{i_1,i_2,-j}(k_1,k_2,t-t') \\ & \left\langle \left[A_{k_1',i_1}(t') A_{k_2',i_2}(t'), A^\dagger_{k_2,i_2}(0) A^\dagger_{k_1,i_1}(0)\right]\right\rangle_0 \Bigg\}, \end{aligned} \tag{3.25}$$

where the time-evolved operators in the expectation value are simply given by

$$A_{k_1',i_1}(t') = A_{k_1',i_1} e^{-iE_{A_{i_1}}(k_1')t'/\hbar},\ A_{k_2',i_2}(t') = A_{k_2',i_2} e^{-iE_{A_{i_2}}(k_2')t'/\hbar}. \tag{3.26}$$

Making use of Wick's theorem and recalling that

$$\left\langle A_{k_1,i_1}(t') A^\dagger_{k_2,i_2}(0)\right\rangle_0 = \delta_{i_1,i_2}\delta_{k_1,k_2}\frac{1}{1+e^{\beta E_{A_{i_1}}(k)}}, \tag{3.27}$$

[6]They depend on time as the $\Gamma^j_{\zeta_1,\zeta_2}$ coefficients, due to the presence of the bias V.

with $\beta = 1/k_B T$, we obtain

$$\sum_{k_1,k_2,k_1',k_2'} \frac{1}{L^2}\alpha_{i_1,i_2,j}(k_1',k_2',t)\alpha^*_{i_1,i_2,-j}(k_1,k_2,t-t')\left\langle\left[A_{k_1',i_1}(t')A_{k_2',i_2}(t'),A^\dagger_{k_2,i_2}(0)A^\dagger_{k_1,i_1}(0)\right]\right\rangle_0$$
$$= \frac{1}{(2\pi)^2}\Bigg\{-\delta_{i_1,i_2}\int_{-\infty}^{+\infty} dk_1\, e^{-iE_{A_{i_1}}(k_1)t'/\hbar}\frac{e^{\beta E_{A_{i_1}}(k_1)}}{1+e^{\beta E_{A_{i_1}}(k_1)}}$$
$$\cdot\int_{-\infty}^{+\infty} dk_2\,\alpha_{i_1,i_1,j}(k_1,k_2,t)\alpha^*_{i_1,i_1,-j}(k_1,k_2,t-t')e^{-iE_{A_{i_1}}(k_2)t'/\hbar}\frac{e^{\beta E_{A_{i_1}}(k_2)}}{1+e^{\beta E_{A_{i_1}}(k_2)}}$$
$$+\int_{-\infty}^{+\infty} dk_1\, e^{-iE_{A_{i_1}}(k_1)t'/\hbar}\frac{e^{\beta E_{A_{i_1}}(k_1)}}{1+e^{\beta E_{A_{i_1}}(k_1)}}$$
$$\cdot\int_{-\infty}^{+\infty} dk_2\,\alpha_{i_1,i_2,j}(k_1,k_2,t)\alpha^*_{i_1,i_2,-j}(k_1,k_2,t-t')e^{-iE_{A_{i_2}}(k_2)t'/\hbar}\frac{e^{\beta E_{A_{i_2}}(k_2)}}{1+e^{\beta E_{A_{i_2}}(k_2)}}\Bigg\}. \tag{3.28}$$

The full expansion of Eq. (3.25) is cumbersome. However, by looking at Eqs. (3.25)-(3.28) we can identify the typical structure of each term: a product of two α coefficients - which, through the Γs, contain all the details specifying the tunneling process - and two Green functions given by the two integrals.

3.1.3 Results

Analytical results

The long and intricate calculation sketched in the previous Section leads to the following expression for the right/left current (more details can be found in Appendix B)

$$I^{r/l}(t) = \mathcal{C}\,\mathrm{Im}\left\{e^{\mp i(\omega_J t+\theta_r-\theta_l)}\int_0^{+\infty} ds\, e^{\pm i s\tilde{V}}\left[A_1\cos\left(\pi\frac{\phi}{\phi_0}\right)+A_2\sin\left(\frac{\pi}{2}\frac{\phi}{\phi_0}\right)+A_3\right]\right\}$$
$$= \mathcal{C}\,\mathrm{Im}\left\{e^{\mp i(\omega_J t+\theta_r-\theta_l)}\left[\tilde{A}_1^{r/l}\cos\left(\pi\frac{\phi}{\phi_0}\right)+\tilde{A}_2^{r/l}\sin\left(\frac{\pi}{2}\frac{\phi}{\phi_0}\right)+\tilde{A}_3^{r/l}\right]\right\}. \tag{3.29}$$

Here, $\mathcal{C} \equiv (-2e\Delta\Gamma^2)/(\pi^2\hbar^3 v_F^2)$ is a constant. We have introduced $\tilde{V} = eV/\Delta$ and $s = \frac{t'\Delta}{\hbar}$, with t' a time variable. The three complex factors A_1, A_2 and A_3 depend on all the parameters except for the flux ϕ. Likewise, $\tilde{A}_1^{r/l}$, $\tilde{A}_2^{r/l}$, $\tilde{A}_3^{r/l}$ stand for the three coefficients A_1, A_2, A_3 once the integration over s is done, and the indices r/l are related to the sign in $e^{\pm is\tilde{V}}$. To give an idea of their form, we report explicitly

$\tilde{A}_1^r$, $\tilde{A}_2^r$, $\tilde{A}_3^r$:

$$\tilde{A}_1^r = \frac{\pi e^{\tilde{V}(-1+i\tilde{L})}}{6}\Bigg\{ie^{i2k_F L}\tilde{f}_T^2\tilde{V}\Bigg[6+\cos\left(2\tilde{f}\right)\left(-6+4\tilde{T}^2+\tilde{V}^2\right)$$
$$+\cosh\left(2\tilde{f}-i2\tilde{f}\tilde{L}\right)\left(4\tilde{T}^2+\tilde{V}^2\right)\Bigg]+\frac{12\tilde{T}}{\sinh\left(2\tilde{L}\tilde{T}\right)}\cosh\left(\tilde{f}-i\tilde{f}\tilde{L}\right)\cosh\left(\tilde{f}+i\tilde{f}\tilde{L}\right)\Bigg\},$$

$$\tilde{A}_2^r = \frac{\pi f_C \tilde{f}_T \tilde{V}}{6}e^{i2k_F L}e^{\tilde{V}(-1+i\tilde{L})}\sin\left(2\tilde{f}\right)\left(24-4\tilde{T}^2-\tilde{V}^2\right),$$

$$\tilde{A}_3^r = \frac{\pi}{6}e^{\tilde{V}(-1+i\tilde{L})}\Bigg\{i\tilde{V}e^{2ik_F L}\Bigg[6\left(f_C^2-\tilde{f}_T^2\right)-\tilde{f}_T^2\left(-6+4\tilde{T}^2+\tilde{V}^2\right)\cos\left(2\tilde{f}\right)$$
$$+\tilde{f}_T^2\left(4\tilde{T}^2+\tilde{V}^2\right)\cosh\left(2\tilde{f}-2i\tilde{f}\tilde{L}\right)\Bigg]+\frac{6\tilde{T}}{\sinh\left(2\tilde{L}\tilde{T}\right)}\Bigg[\left(-1+2f_C^2\tilde{f}_T^2\right)\cosh\left(2\tilde{f}\right)$$
$$+\cosh\left(2i\tilde{f}\tilde{L}\right)\Bigg]\Bigg\},$$

where the dimensionless quantities $\tilde{f} = f/\Delta$, $\tilde{L} = L\Delta/\hbar v_F$ and $\tilde{T} = \pi k_B T/\Delta$ are referred to the superconducting gap Δ[7].

The different scattering processes contributing to the current can be singled out. Table 3.1 lists all the processes giving a nonzero contribution to $I^r(t)$, specifying the coefficient $\tilde{A}_i$ they enter.

Table 3.1: *Transport processes contributing to $I^r(t)$: the initial state (after the tunneling from the left superconductor) and final state (before the tunneling to the right superconductor) of the Cooper pair are indicated, together with the $\tilde{A}_i$ coefficient they are associated with. To clarify the notation, $u\uparrow u\uparrow\rightarrow l\downarrow l\downarrow$ means that both electrons are injected in the upper edge with spin up, and extracted from the lower edge with spin down.*

$\tilde{A}_1$:	$u\uparrow u\uparrow\rightarrow u\uparrow u\uparrow$, $l\uparrow l\downarrow\rightarrow u\uparrow u\downarrow$	$l\downarrow l\downarrow\rightarrow l\downarrow l\downarrow$, $u\uparrow u\downarrow\rightarrow l\uparrow l\downarrow$,	$u\uparrow u\uparrow\rightarrow l\downarrow l\downarrow$, $u\uparrow u\downarrow\rightarrow u\uparrow u\downarrow$,	$l\downarrow l\downarrow\rightarrow u\uparrow u\uparrow$, $l\uparrow l\downarrow\rightarrow l\uparrow l\downarrow$.
$\tilde{A}_2$:	$u\uparrow l\downarrow\rightarrow u\uparrow u\uparrow$,	$u\uparrow l\downarrow\rightarrow l\downarrow l\downarrow$,	$u\uparrow u\uparrow\rightarrow u\uparrow l\downarrow$,	$l\downarrow l\downarrow\rightarrow u\uparrow l\downarrow$.
$\tilde{A}_3$:	$u\downarrow l\downarrow\rightarrow u\downarrow l\downarrow$, $u\uparrow l\downarrow\rightarrow u\uparrow l\downarrow$.	$u\uparrow l\uparrow\rightarrow u\uparrow l\uparrow$,	$u\downarrow l\downarrow\rightarrow u\uparrow l\uparrow$,	$u\uparrow l\uparrow\rightarrow u\downarrow l\downarrow$,

We focus on the term proportional to $\sin\left(\frac{\pi}{2}\frac{\phi}{\phi_0}\right)$ in Eq. (3.29), which is responsible for the resulting 4π-periodicity with respect to the magnetic flux (or, equivalently, a $4\phi_0$-dependence). This term is absent in the absence of forward tunneling among the two edges ($f = 0$). Moreover, in order to have a nonzero $\tilde{A}_2^{r/l}$ one must additionally have $\tilde{f}_T \neq 0$, which is reasonable due to the strong spin-orbit coupling characterizing the structure. The need for its presence is easily understood: an odd number of tunneling events within the constriction necessarily leads to a spin-flip of one electron of the pair; since we assume to deal with standard BCS superdonducors, an additional spin-flip at the superconductor-topological insulator interface is required to recover the spin singlet state. The anomalous periodicity is found analytically to be brought about by processes where the Cooper pair switches from being on one edge only to being

[7]Notice that our previous assumption of sub-gap energy regime requires $\tilde{V}$, $\tilde{T} \ll 1$.

delocalized between the two edges (see Table 3.1). These processes are proportional to $\tilde{f}_T f_C$ and must include an odd number of forward tunneling in the constriction.

This is shown in Fig. 3.6 with an example. A Cooper pair enters the junction with a LAR in the upper edge and leaves it with a CAR after one electron tunnels in the constriction. Before the constriction, the two electrons pick up equal Aharonov-Bohm phases which sum up, while after the constriction they cancel with each other. Within the constriction, the acquired phase is negligible (making the precise location of the tunneling within the constriction irrelevant, as we already pointed out). The amplitude of the process just described is proportional to $\Gamma^r_{11,1-1}(\Gamma^l_{11,11})^*$, explicitly

$$\Gamma^r_{11,1-1}(\Gamma^l_{11,11})^* = \left(\Gamma f_C\, e^{-i\left(\theta_r+\frac{1}{2}\omega_J t\right)}\right)\left(\Gamma \tilde{f}_T\, e^{i\left(\theta_l-\frac{1}{2}\omega_J t-\frac{\pi\phi}{2\phi_0}\right)}\right) = \\ = \Gamma^2 f_C \tilde{f}_T e^{-i[(\theta_r-\theta_l)+\omega_J t]} e^{-i\frac{\pi\phi}{2\phi_0}}.$$

Notice that the flux-dependence does correspond to the anomalous term we commented before. A spin-flip $\tilde{f}_T$ is needed due to the fact that in (1) and (5) in the Figure we have a singlet state and that within the constriction an odd number (one) of inter-edge tunneling events results in a spin-flip of one electron. The anomalous periodicity hence

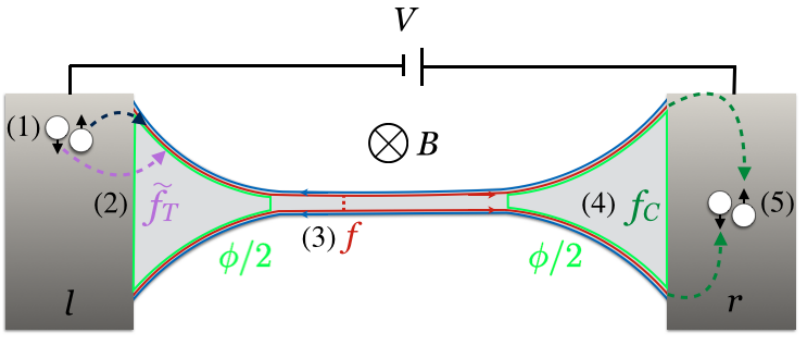

Figure 3.6: *A prototypical example of a process carrying a 4π-periodic dependence on the flux ϕ: (1) a Cooper pair is injected from the left superconductor in the upper edge; (2) during the injection, one of the electrons is spin-flipped, and thus the Cooper pair enters the edge system in a spin-triplet state, acquiring a $\tilde{f}_T$ factor accounting for the spin-flip. (3) Having enclosed a flux $\phi/2$, in the constriction an electron tunnels to the lower edge; no flux is enclosed in the remaining path. (4) When the opposite end of the junction is reached, a final f_C factor keeps track of the CAR; (5) clearly, the Cooper pair reaches the right superconductor in a spin-singlet state. Figure adapted from [188].*

represents a hallmark of the presence of forward scattering and the coupling between the edges. It is important to note the general difficulty in demonstrating such coupling. Indeed, as already discussed, in long constrictions the single particle backscattering is only able to open a gap at the Dirac point. However such point is often hidden in the valence band of the structure [109,163,168]. Achieving zero conductance as a function of the gate voltage, that would strongly indicate the formation of the constriction, is hence not always achievable and remains unverified in experimental settings. At present, the only signature that is related to the existence of the constriction is a reduction of the conductance from $2e^2/h$ to e^2/h. However, this behavior is originated by electronic interactions, leaving uncertainty about its persistence in the presence of superconductors in close proximity to the constriction. Therefore, a more conclusive signature of formation of the constriction is needed.

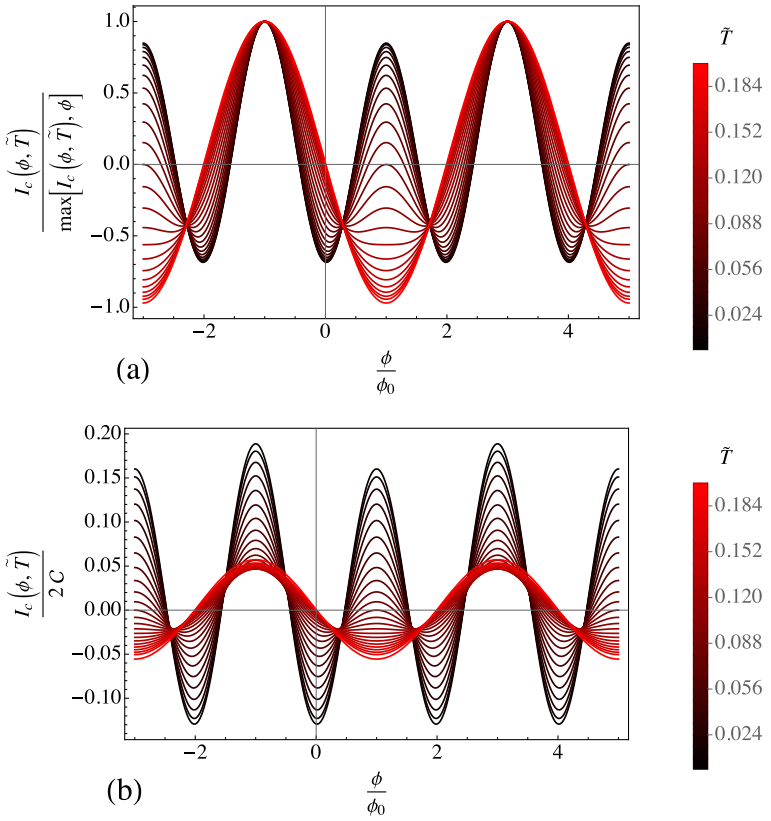

Figure 3.7: *(a) I_c, normalized with respect to its maximum, for $\tilde{L} = 20$, $k_F L = 6\pi$, $\tilde{f}_T = 0.4$, $f_C = 0.3$ and $\tilde{f} = 0.3$. The plot is represented as a function of ϕ (in units of ϕ_0) and for $\tilde{V} = 0$. $\tilde{T}$ is varying between 0.008 and 0.2 (see the red bar legend aside). (b) Same but without the normalisation to the maximum. Figure adapted from [188].*

Quantitative analysis

In the limit $\tilde{V} \to 0$, we analyze the critical current $I_c(\phi)$ shown in Fig. 3.7, given by the total current $I^r - I^l$ (from Eq. (3.29)) for $\theta_r - \theta_l = \pi/2$. As we can see, the anomalous periodicity is more pronounced at high temperature $\tilde{T}$, while at low temperature, a $2\phi_0$-periodicity is almost recovered, as shown in Fig. 3.7(a). There, the current at different temperatures, normalized to its maximum value, is shown as a function of the flux. This rescaling facilitates the comparison of periodicity in the different curves. In the picture, darker lines correspond to lower temperatures. However, the magnitude of the current itself decreases as temperature is raised, as shown in Fig. 3.7(b), where the plots are not scaled.

For finite values of $\tilde{V}$, owing to the AC Josephson effect, the current becomes time-dependent. As in Ref. [78], we hence analyze the Fourier component of the current at the frequency ω_J given by the voltage. Quantitatively, what we plot is

$$I^r_{\omega_J} = \left| \frac{1}{\mathrm{T}} \int_{-\mathrm{T}/2}^{\mathrm{T}/2} e^{-i\omega_J t} I^r(t) \right|, \tag{3.31}$$

with $\mathrm{T} = 2\pi/\omega_J$. The Fourier transform of the total current is qualitatively similar. The applied bias generates additional features in the curves which increase the visibility

of the anomalous periodicity, see Fig. 3.8. On top of that, and differently from the zero-bias case, the $4\phi_0$ component becomes more pronounced for lower temperature (Fig. 3.9(a)). Moreover, as in the zero-bias limit, higher temperature makes the signal smaller. This fact is shown in Fig. 3.9(b), which represents the same plots as Fig. 3.9(a) but without scaling. The zero-bias and finite-bias regimes, showing distinct behaviors in response to variations in parameters, can prove beneficial for different materials.

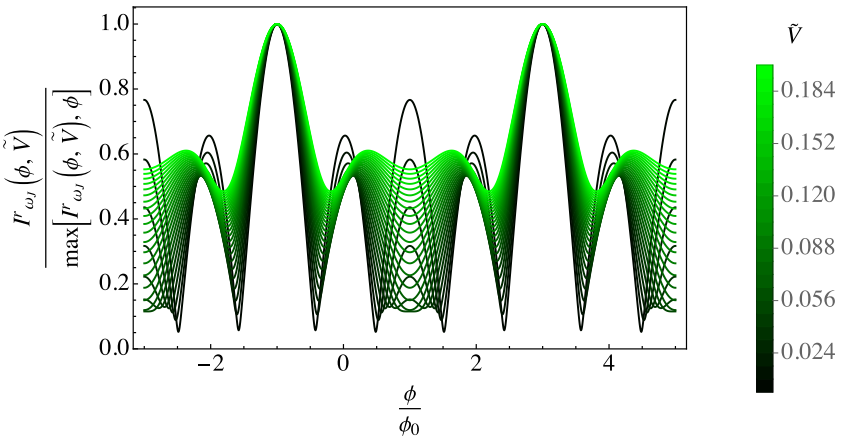

Figure 3.8: *$I^r_{\omega_J}$, normalized with respect to its maximum, for $\tilde{L} = 20$, $k_F L = 6\pi$, $\tilde{f}_T = 0.4$, $f_C = 0.3$, $\tilde{f} = 0.3$ and $\tilde{T} = 0.1$. The plot is represented as a function of ϕ (in units of ϕ_0) and for $\tilde{V}$ varying between 0.008 and 0.2 (see the green bar legend aside). Figure adapted from [188].*

3.1.4 Discussion and conclusions

In this Section, we have inspected a Josephson junction having a long constriction between helical edge states as a non-superconducting element, and pierced by a magnetic flux. The interplay between the possibility of spin-flips through the coefficient $\tilde{f}_T$ (enabled by the strong spin-orbit interaction characterizing the system) and the coupling between opposite edges (through inter-edge tunneling) results in an anomalous $4\phi_0$-periodicity of the Josephson current with respect to the flux.

This behavior is present both in the presence and in the absence of external bias. It is robust with respect to temperature and doesn't need for fine tuning. The effect in our system needs the occurrence of three steps: a LAR with spin-flipping, a tunneling between the edges and a CAR, as shown in Fig. 3.6. Throughout our discussion, we neglected the magnetic flux enclosed in the constriction; if included, it would just add a weak Fraunhofer-like decay to the pattern, without substantially affecting our findings. Instead, a following Section will discuss how to describe the system if the constriction constitutes the entire junction.

The anomalous periodicity we found represents a cut signature of a constriction between edges tunnel-coupled to superconducting leads. Its physical origin resides in the possibility of switching the Cooper pair nature from localized on one edge to delocalized on both edges. This is allowed by the single-electron tunneling within the narrow region. In the absence of inter-edge tunneling, the fate of the Cooper pairs is predetermined: Cooper pairs entering the weak link in LAR on the left end ($x = -L/2, y = \pm W/2$) necessarily end up on the right end of the same edge

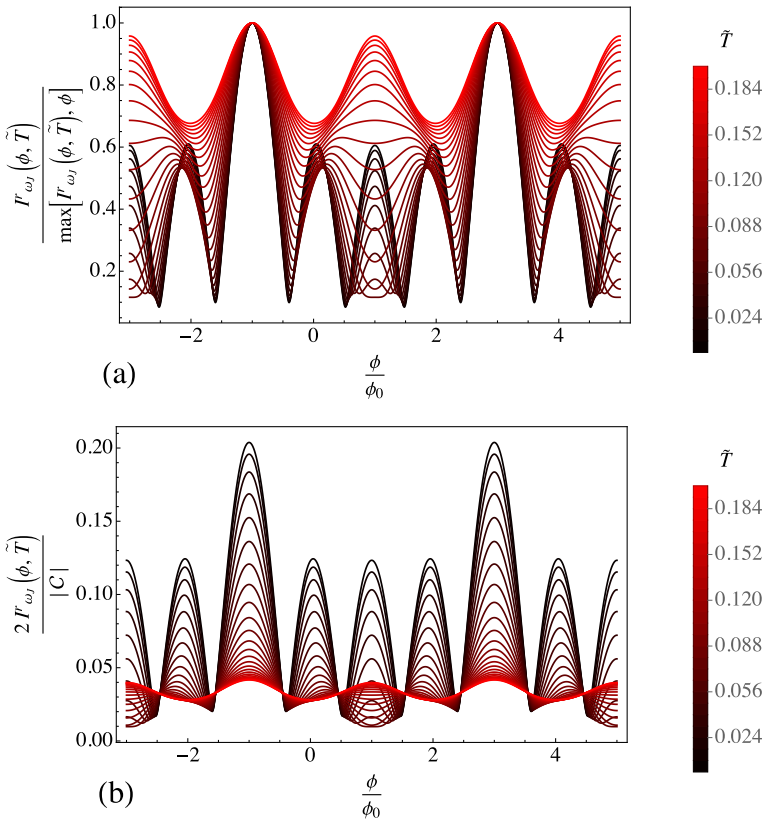

Figure 3.9: *(a) $I^r_{\omega_J}$, normalized with respect to its maximum, for $\tilde{L} = 20$, $k_F L = 6\pi$, $\tilde{f}_T = 0.4$, $f_C = 0.3$, $\tilde{f} = 0.3$ and $\tilde{V} = 0.1$. The plot is represented as a function of ϕ (in units of ϕ_0) and for $\tilde{T}$ varying between 0.008 and 0.2 (see the red bar legend aside). (b) Same but without the normalization to the maximum. Figure adapted from [188].*

($x = L/2$, $y = \pm W/2$), picking a phase difference $\pm\pi\phi/\phi_0$; similarly, Cooper pairs entering the link in CAR unavoidably exit in CAR without accumulating any phase, as discussed in Subsec. (3.1.1). This scenario corresponds to a standard SQUID pattern or an even-odd effect, similar to [78], and is plotted in Fig. 3.10. The inclusion of inter-edge tunneling notably allows for a third possibility: a Cooper pair can enter the junction in LAR and exit in CAR, or viceversa. The single-electron tunneling is the boundary between two types of Cooper pairs, having different insights of the magnetic flux. For the setup we considered, the resulting phase difference is $\pm\pi\phi/2\phi_0$, ultimately leading to a $4\phi_0$-periodic contribution to the Josephson current.

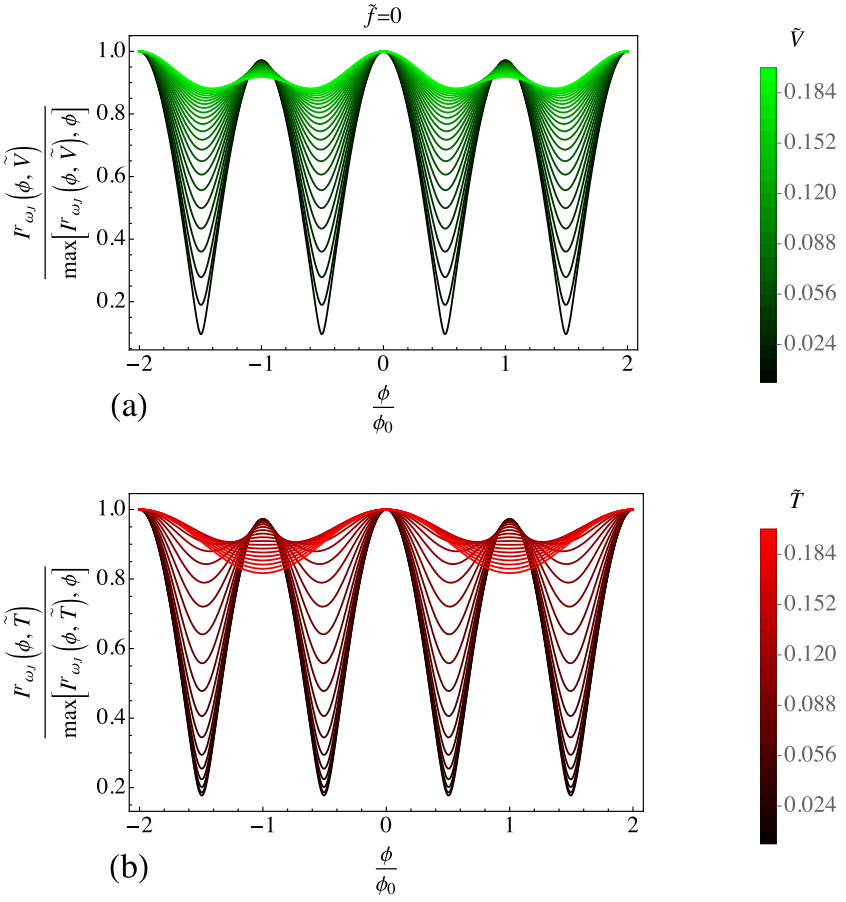

Figure 3.10: *(a) $I^r_{\omega_J}$, normalized with respect to its maximum, for $\tilde{L} = 20$, $k_F L = 6\pi$, $\tilde{f}_T = 0.4$, $f_C = 0.3$, $\tilde{f} = 0$ and $\tilde{T} = 0.1$. The plot is represented as a function of ϕ (in units of ϕ_0) and for $\tilde{V}$ varying between 0.008 and 0.2 (see the green bar legend aside). (b) Same parameters values, but now $\tilde{V} = 0.1$ and $\tilde{T}$ varies between 0.008 and 0.2 (see the red bar legend aside). Figure adapted from [188].*

To summarize our original results:

- If the edges are not coupled ($f = 0$, see Fig. 3.10), there are only two possible contributions, a ϕ_0 and a $2\phi_0$ terms. The former originates a SQUID pattern, while the latter comes from the presence of CAR and leads to the even-odd effect, that we discussed in the previous Chapter of this Thesis (Subsec. 2.3.2). Depending on the parameters at play (in particular, temperature and bias), the $2\phi_0$ component

can be more or less pronounced. This is the main point of [78].

- If f is finite, an additional $4\phi_0$ component emerges (see Figs. 3.7-3.9). Whenever a constriction allows to switch from a Cooper pair propagating on one side to a Cooper pair delocalized on both sides, we argue that novel periodicities can emerge. They are, more in general, connected to single-electron physics in the superconducting context. This explanation of the phenomenon, applied to our setup, substantiates the robustness of the anomalous periodicity with respect to slight spatial variations of the parameters.

Although our considerations apply, in principle, to all the Quantum Spin Hall (candidate) systems, we argue in particular our results to be readily observable in HgTe-CdTe heterostructures. Assuming the realistic lengthscales

$$L \simeq 3\,\mu\text{m}, \qquad \ell \simeq 1\,\mu\text{m}, \qquad W \simeq 200\,\text{nm}, \qquad w \simeq 30\,\text{nm},$$

the magnetic field necessary to observe the effect is of the order $B \simeq 10^{-3}\,\text{T}$. The temperature and bias ranges are limited by the pairing potential $\Delta \sim 0.40\,\text{meV}$ (a reasonable value for HgTe-based systems [79, 198]), which determines an upper bound of $\sim 300\,\text{mK}$ and $\sim 80\mu\text{eV}$. We conclude by recalling from Subsec. 1.2.3 that the edge states have been proved to be robust even in the presence of magnetic fields that are much stronger than those needed for our proposal [53, 116, 205].

3.2 Unbalanced tunneling amplitudes

We now shortly discuss the more general and experimentally realistic case of a reconstructed constriction. As elucitated in [197], and briefly mentioned in Chapter 1, unlike the infinitely sharp edge potential assumed in traditional calculations, it is experimentally more realistic to consider a smooth one. If the density of electrons is determined by an external gate, it is electrostatically convenient for it to mimic the positive charge distribution on the gate. If the latter goes to zero smoothly close to the edge of the system, the electron density can do likewise via a separation of the opposite spin channels, see Fig. 3.11. As a consequence, the two direction-conserving tunnel couplings of our model should have different intensities, $f_1 \neq f_2$. In this Section we introduce such distinction and rediscuss the interference pattern of the system. As in the absence of edge reconstruction, we find the occurrence of a $4\phi_0$-periodic component in the AC Josephson current as a function of the magnetic flux, robust in a wide range of parameters. We also discuss the temperature dependence in more detail. Other interesting consequences of reconstruction will be discussed in the next Chapter.

The Hamiltonian associated to the reconstructed constriction is modified as

$$H_E^0 = \int_{-\infty}^{+\infty} dx\, \psi^\dagger(x) \begin{pmatrix} -i\hbar v_F \partial_x & 0 & 0 & f_1 \\ 0 & i\hbar v_F \partial_x & f_2 & 0 \\ 0 & f_2 & i\hbar v_F \partial_x & 0 \\ f_1 & 0 & 0 & -i\hbar v_F \partial_x \end{pmatrix} \psi(x), \tag{3.32}$$

where $\psi(x) = (\psi_{11}(x), \psi_{-11}(x), \psi_{-1-1}(x), \psi_{1-1}(x))^T$ as before. The possible edge reconstruction is taken into account by allowing in principle the two couplings to take

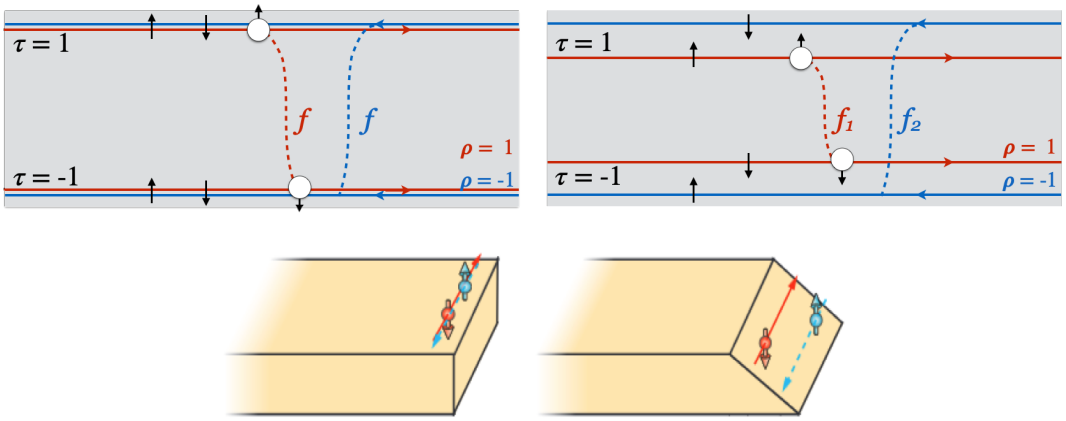

Figure 3.11: *Comparison between the non-reconstructed and the reconstructed constriction. In the first case, corresponding to the left panels, the edge potential is sharp and the two right- and left-moving channels are equally distant. In the second case, corresponding to the right panels, the edge potential is smooth, leading to a spatial separation of the two channels on each edge. As a consequence, the right-moving channels (for instance) are closer to each other than the left-moving ones, resulting in the unbalance $f_1 \neq f_2$. Lower panels are reprinted with permission from [197]. Copyright 2024 by the American Physical Society.*

different values (on the same line of thought as before, we neglect backward scattering and only consider forward scattering).

After the Fourier transformation $\psi_{\rho\tau}(x) = \frac{1}{\sqrt{L}} \sum_k c_{k,\rho\tau}\, e^{ikx}$, the diagonalization of Eq. (3.32) leads to the four eigenstates and eigenvalues

$$A_{k,1} = \frac{1}{\sqrt{2}}\left(-c_{k,-11} + c_{k,-1-1}\right) \qquad E_{A_1}(k) = -f_2 - \hbar v_F k, \tag{3.33a}$$

$$A_{k,2} = \frac{1}{\sqrt{2}}\left(c_{k,-11} + c_{k,-1-1}\right) \qquad E_{A_2}(k) = f_2 - \hbar v_F k, \tag{3.33b}$$

$$A_{k,3} = \frac{1}{\sqrt{2}}\left(-c_{k,11} + c_{k,1-1}\right) \qquad E_{A_3}(k) = -f_1 + \hbar v_F k, \tag{3.33c}$$

$$A_{k,4} = \frac{1}{\sqrt{2}}\left(c_{k,11} + c_{k,1-1}\right) \qquad E_{A_4}(k) = f_1 + \hbar v_F k. \tag{3.33d}$$

The f_1/f_2 couplings split by different amounts the two right-mover/left-mover branches.

The two current contributions in Eq. (3.29) are now dependent on both f_1, f_2. Developing calculations similar to those of the previous Section, we obtain the following expression for the right component

$$I^r(t) = \mathcal{C}\,\mathrm{Im}\Bigg\{ e^{-i(\omega_J t + \theta_r - \theta_l)} \int_0^{+\infty} ds\, e^{is\tilde{V}} \Bigg[A_1\left(\tilde{f}_1, \tilde{f}_2\right) \cos\left(\pi \frac{\phi}{\phi_0}\right) + A_2\left(\tilde{f}_1\right) \sin\left(\frac{\pi}{2}\frac{\phi}{\phi_0}\right) + A_3\left(\tilde{f}_1, \tilde{f}_2\right) \Bigg] \Bigg\}, \tag{3.34}$$

where the dimensionless quantities and $\mathcal{C}$ have been already introduced. The left current $I^l(t)$ is straightforwardly obtained by conjugating the two complex exponentials and exchanging $\tilde{f}_1$ and $\tilde{f}_2$. We confine our discussion to the current contribution that is

aligned with the bias direction according to Fig. 3.5, that is $I^r(t)$. After integration, the full analytical expression for $\tilde{V} > 0$ is

$$I^r(t) = \mathcal{C}\,\mathrm{Im}\Bigg\{ e^{-i(\omega_J t+\theta_r-\theta_l)} \Bigg[\tilde{A}_1\left(\tilde{f}_1,\tilde{f}_2\right)\cos\left(\pi\frac{\phi}{\phi_0}\right) + \tilde{A}_2\left(\tilde{f}_1\right)\sin\left(\frac{\pi}{2}\frac{\phi}{\phi_0}\right) + \tilde{A}_3\left(\tilde{f}_1,\tilde{f}_2\right)\Bigg]\Bigg\}, \tag{3.35}$$

with the new coefficients

$$\tilde{A}_1 = \frac{\pi e^{\tilde{V}(-1+i\tilde{L})}}{6}\Bigg\{ ie^{i2k_F L}\tilde{f}_T^2\tilde{V}\Bigg[6+\cos\left(2\tilde{f}_1\right)\left(-6+4\tilde{T}^2+\tilde{V}^2\right)+\cosh\left(2\tilde{f}_1-i2\tilde{f}_1\tilde{L}\right)\left(4\tilde{T}^2+\tilde{V}^2\right)\Bigg] + \frac{12\tilde{T}}{\sinh\left(2\tilde{L}\tilde{T}\right)}\cosh\left(\tilde{f}_1-i\tilde{f}_1\tilde{L}\right)\cosh\left(\tilde{f}_2+i\tilde{f}_2\tilde{L}\right)\Bigg\}, \tag{3.36a}$$

$$\tilde{A}_2 = \frac{\pi f_C\tilde{f}_T\tilde{V}}{6}e^{i2k_F L}e^{\tilde{V}(-1+i\tilde{L})}\sin\left(2\tilde{f}_1\right)\left(24-4\tilde{T}^2-\tilde{V}^2\right), \tag{3.36b}$$

$$\tilde{A}_3 = \frac{\pi}{6}e^{\tilde{V}(-1+i\tilde{L})}\Bigg\{ i\tilde{V}e^{2ik_F L}\Bigg[6\left(f_C^2-\tilde{f}_T^2\right)-\tilde{f}_T^2\left(-6+4\tilde{T}^2+\tilde{V}^2\right)\cos\left(2\tilde{f}_1\right) + \tilde{f}_T^2\left(4\tilde{T}^2+\tilde{V}^2\right)\cosh\left(2\tilde{f}_1-2i\tilde{f}_1\tilde{L}\right)\Bigg] + \frac{6\tilde{T}}{\sinh\left(2\tilde{L}\tilde{T}\right)}\Bigg[\left(-1+2f_C^2\tilde{f}_T^2\right) \cosh\left(\tilde{f}_1+\tilde{f}_2-i\tilde{f}_1\tilde{L}+i\tilde{f}_2\tilde{L}\right)+\cosh\left(\tilde{f}_1-\tilde{f}_2-i\tilde{f}_1\tilde{L}-i\tilde{f}_2\tilde{L}\right)\Bigg]\Bigg\}. \tag{3.36c}$$

The explicit form of $I^l(t)$ is not reported here.

Eq. (3.35) shows that the $4\phi_0$-periodic term, emerged for the non-reconstructed case, is present even if the constriction is reconstructed. This means that the anomalous periodicity is not accidentally related to the particular restriction $\tilde{f}_1 = \tilde{f}_2$. The anomalous contribution is proportional to $\tilde{A}_2$ and depends, for each current component, on one single tunneling coefficient: the right-mover coefficient $\tilde{f}_1$ in the case of $I^r(t)$ and the left-mover coefficient $\tilde{f}_2$ in the case of $I^l(t)$. With given values for $\tilde{f}_1$ and $\tilde{f}_2$, the relative weight of the $4\phi_0$-component differs between the two currents. Consequently, it may exhibit a better or worse visibility in $I^r(t)$ and $I^l(t)$. Moreover, by looking for instance at $I^r(t)$, and considering that $\tilde{A}_2 \propto f_C\tilde{f}_T\sin\left(2\tilde{f}_1\right)$, it is clear the necessity of f_C, $\tilde{f}_T \neq 0$, as in [188]. However, while without reconstruction we needed $\tilde{f}_1 = \tilde{f}_2 \equiv \tilde{f} \neq 0$, in our present analysis a single coupling is sufficient.

Fig. 3.12 shows the ω_J-Fourier component of $I^r(t)$,

$$I^r_{\omega_J} = \left|\mathcal{C}\left[\tilde{A}_1\left(\tilde{f}_1,\tilde{f}_2\right)\cos\left(\pi\frac{\phi}{\phi_0}\right)+\tilde{A}_2\left(\tilde{f}_1\right)\sin\left(\frac{\pi}{2}\frac{\phi}{\phi_0}\right)+\tilde{A}_3\left(\tilde{f}_1,\tilde{f}_2\right)\right]\right|, \tag{3.37}$$

for different values of the tunneling coefficients and at a fixed temperature and bias $\tilde{T} = \tilde{V} = 0.1$. It is well visible that, whenever $\tilde{f}_1 = 0$, a standard $2\phi_0$-periodicity is recovered (see dashed and dotted lines), while all the other cases, either with edge reconstruction (including $\tilde{f}_2 = 0$) or not, exhibit the $4\phi_0$-feature. We find that $I^l_{\omega_J} =$

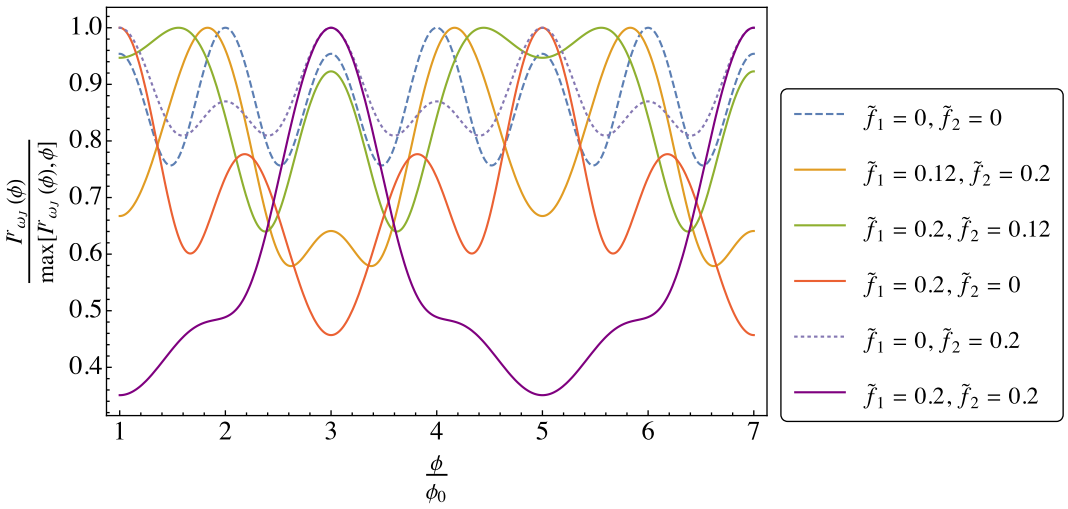

Figure 3.12: *$I^r_{\omega_J}$, normalized with respect to its maximum, for $\tilde{L} = 20$, $k_F L = 6\pi$, $\tilde{f}_T = 0.4$, $f_C = 0.3$, $\tilde{T} = 0.1$ and $\tilde{V} = 0.1$, as a function of ϕ (in units of ϕ_0). The different curves correspond to different values of $\tilde{f}_1$, $\tilde{f}_2$. Whenever $\tilde{f}_1 = 0$, a standard $2\phi_0$-periodicity is recovered (dashed and dotted lines), while in all the other cases, either in presence of edge reconstruction or not, and regardless of the value of $\tilde{f}_2$, $I^r_{\omega_J}$ is $4\phi_0$-periodic. Figure adapted from [187], with kind permission of Società Italiana di Fisica.*

$I^r_{\omega_J}$, provided that $\tilde{f}_1$ and $\tilde{f}_2$ are interchanged in $\tilde{A}_{1/2/3}$ and that the bias is reversed, $\tilde{V} \to -\tilde{V}$.

So far, we have discussed the occurrence of the $4\phi_0$-signature, which isn't affected by the edge reconstruction. However, the visibility of the feature depends on which one among the differently periodic terms dominates; this is related to both $\tilde{f}_1$ and $\tilde{f}_2$ and is, therefore, sensitive to the edge reconstruction. To better appreciate the relevance of the different periodicities, since Eq. 3.37) contains several interfering terms, we rewrite it conveniently as

$$I^r_{\omega_J} = |\mathcal{C}| \sqrt{\alpha + \beta \cos\left(2\pi \frac{\phi}{\phi_0}\right) + \gamma \sin\left(\frac{3\pi}{2} \frac{\phi}{\phi_0}\right) + \delta \cos\left(\pi \frac{\phi}{\phi_0}\right) + \epsilon \sin\left(\frac{\pi}{2} \frac{\phi}{\phi_0}\right)}, \tag{3.38}$$

where

$$\alpha = \frac{|\tilde{A}_1|^2}{2} + \frac{|\tilde{A}_2|^2}{2} + |\tilde{A}_3|^2, \qquad \beta = \frac{|\tilde{A}_1|^2}{2}, \qquad \gamma = \mathrm{Re}\tilde{A}_1 \mathrm{Re}\tilde{A}_2 + \mathrm{Im}\tilde{A}_1 \mathrm{Im}\tilde{A}_2,$$
$$\delta = -\frac{|\tilde{A}_2|^2}{2} + 2\mathrm{Re}\tilde{A}_1 \mathrm{Re}\tilde{A}_3 + 2\mathrm{Im}\tilde{A}_1 \mathrm{Im}\tilde{A}_3,$$
$$\epsilon = 2\mathrm{Re}\tilde{A}_2 \mathrm{Re}\tilde{A}_3 + 2\mathrm{Im}\tilde{A}_2 \mathrm{Im}\tilde{A}_3 - \mathrm{Re}\tilde{A}_1 \mathrm{Re}\tilde{A}_2 - \mathrm{Im}\tilde{A}_1 \mathrm{Im}\tilde{A}_2.$$

Although the processes originating the $4\phi_0$-periodicity (those contributing to $\tilde{A}_2$, and listed in Table 3.1) are just a few, they are connected to all the others through the interference pattern. The resulting periodicity depends on the coefficients β, γ, δ, ϵ, whereas α is a flux-independent offset. We focus on their dependence on temperature, since in the non-reconstructed case [188] some challenges arose at high temperature.

Given $\tilde{f}_1,\ \tilde{f}_2$, all the coefficients have a higher sensitivity to temperature in the lower-temperature regime, as shown in Figs. 3.13(a)-3.14(a) (where we considered $\tilde{f}_1 = 0.12,\ \tilde{f}_2 = 0.2$ and the viceversa). At high temperature (but keeping $\tilde{T} \ll 1$ due to our former approximations), we find that the prefactors of the flux-dependent terms β, γ and ϵ approach zero or settle to very small values if compared to the offset α. However δ, which brings the standard periodicity, behaves differently: it may increase with temperature, as in Fig. 3.13(b), or reach a plateau with greater magnitude than the others, as in Fig. 3.14(b). In the first case, the $4\phi_0$-periodicity can survive at high temperature, since the different periodicities have a comparable weight (Fig. 3.13(c)). However, this weight being small, the curves are flattened and their peak structure is weakened. By contrast, in the second case the $2\phi_0$-periodic contribution becomes dominant and the $4\phi_0$-periodic one almost vanishes (Fig. 3.14(c)). As in [188], where $\tilde{f}_1,\ \tilde{f}_2$ are equal, we recover that the intensity of $I^r_{\omega_J}$ (namely, the peak-to-peak distance) drops down at high temperature. The occurrence of the anomalous periodicity is in general worsened, but can persist at high temperature, depending on $\tilde{f}_1,\ \tilde{f}_2$.

Given our comments below Eq. (3.37), we can interpret Fig. 3.13(c) and Fig. 3.14(c) respectively as $I^r_{\omega_J}$ for $\tilde{V} > 0$ and $I^l_{\omega_J}$ for $\tilde{V} < 0$ of a constriction with $\tilde{f}_1 = 0.12,\ \tilde{f}_2 = 0.2$. This link between the two quantities offers a doubled possibility of inspection of the anomalous periodicity – more or less visible – that can all rely on the same analytical results.

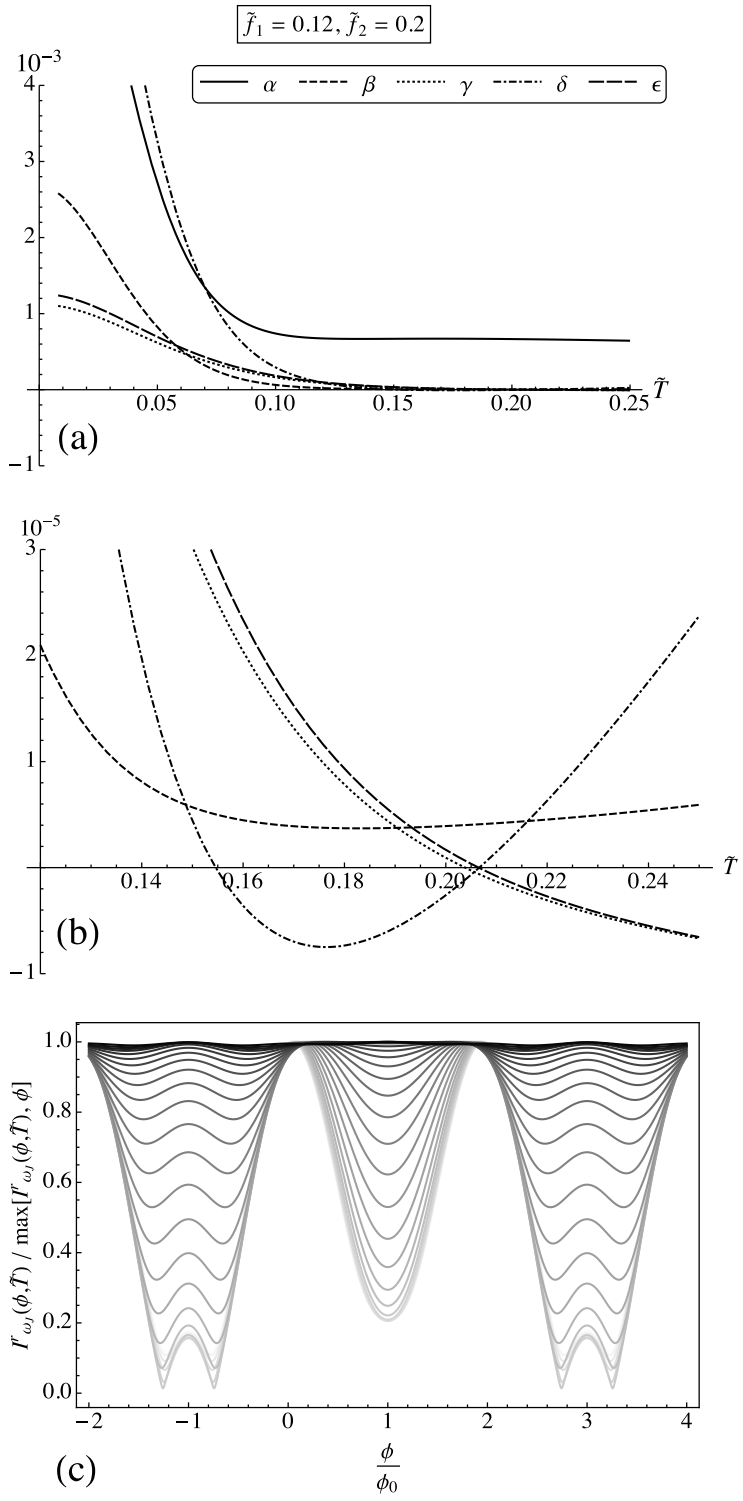

Figure 3.13: *(a) Temperature dependence of the coefficients α, β, γ, δ, ϵ, for $\tilde{T}$ varying between 0.008 and 0.25. (b) Zoom of (a) on the high-temperature range, from $\tilde{T} = 0.12$ to $\tilde{T} = 0.25$, only for the prefactors of the flux-dependent terms β, γ, δ and ϵ. (c) $I^r_{\omega_J}$, normalized with respect to its maximum, as a function of ϕ (in units of ϕ_0) and for $\tilde{T}$ varying between 0.008 (lighter grey) and 0.2 (darker grey) with steps of 0.008. Here, $\tilde{f}_1 = 0.12$, $\tilde{f}_2 = 0.2$, $\tilde{L} = 20$, $k_F L = 6\pi$, $\tilde{f}_T = 0.4$, $f_C = 0.3$ and $\tilde{V} = 0.1$. Figure adapted from [187], with kind permission of Società Italiana di Fisica.*

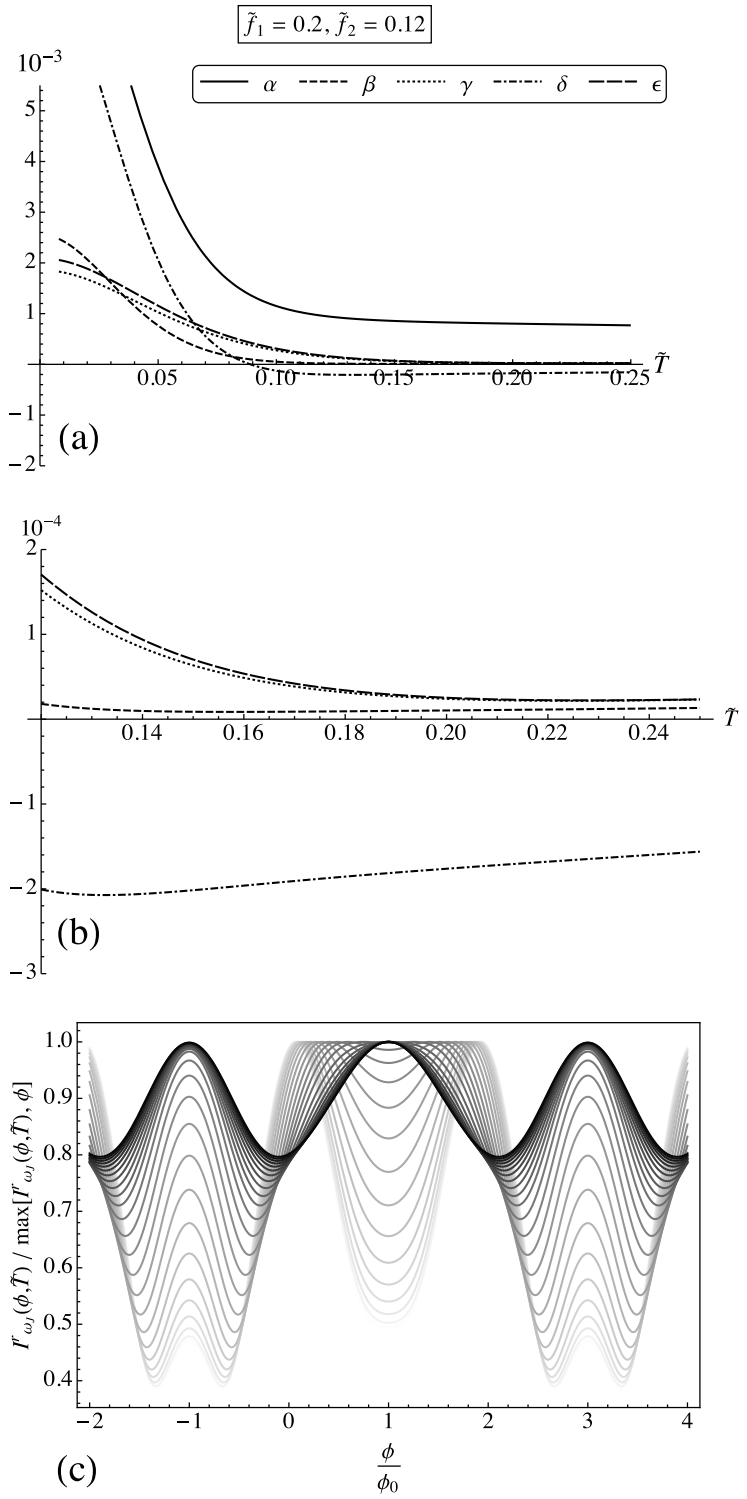

Figure 3.14: *(a) Temperature dependence of the coefficients α, β, γ, δ, ϵ, for $\tilde{T}$ varying between 0.008 and 0.25. (b) Zoom of (a) on the high-temperature range, from $\tilde{T} = 0.12$ to $\tilde{T} = 0.25$, only for the prefactors of the flux-dependent terms β, γ, δ and ϵ. (c) $I^r_{\omega_J}$, normalized with respect to its maximum, as a function of ϕ (in units of ϕ_0) and for $\tilde{T}$ varying between 0.008 (lighter grey) and 0.2 (darker grey) with steps of 0.008. Here, $\tilde{f}_1 = 0.2$, $\tilde{f}_2 = 0.12$, $\tilde{L} = 20$, $k_F L = 6\pi$, $\tilde{f}_T = 0.4$, $f_C = 0.3$ and $\tilde{V} = 0.1$. Figure adapted from [187], with kind permission of Società Italiana di Fisica.*

3.3 Hints about the extended tunneling

To conclude this Chapter, we discuss how the description should be modified if the inter-edge tunneling were extended throughout the whole structure instead of confined to a subregion of it. These two scenarios are compared in Fig. 3.15. So far, in deriving the Aharonov-Bohm phases associated to Cooper pairs transport, we assumed negligible flux enclosed in the constriction ($\ell w \ll WL$, see panel (a)). This allowed us not to worry about the exact number of tunneling events and their exact location within the constriction: we could effectively treat them as occurring halfway across the junction. In the case of panel (b), where $w = W$ and $\ell = L$, this semplification is not possible anymore, and a more detailed description is in order.

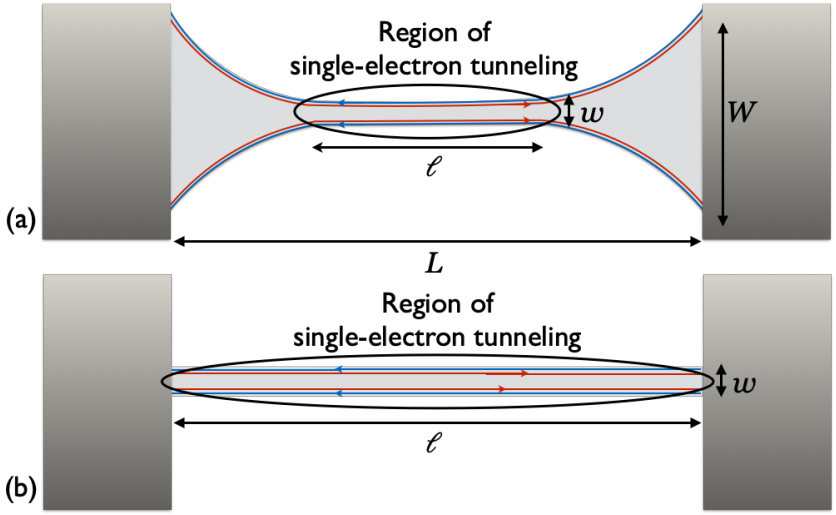

Figure 3.15: *Comparison between a constriction confined to a portion of the junction (a) and the extended constriction (b).*

Let us start from an illustrative case, depicted in Fig. 3.16. The process consists in a Cooper pair entering and leaving the junction via CAR, which in the former description was associated to no flux dependence. Within the new setup, this is true only if no inter-edge tunneling occurs, and a perturbative approach in the tunneling amplitude f is needed. Given the initial and final states, the first higher order to which the process is allowed is f^2, namely the two electrons change the edge of propagation with each other. Let us assume that the electron injected in the upper edge undergoes inter-edge tunneling at position $x_2 = \epsilon_2 L$ along the junction. Until that, the two Aharonov-Bohm phases cancel. Then, till the second electron tunnels at $x_1 = \epsilon_1 L$, a phase $\gamma^{AB} = -\frac{\pi\phi}{\phi_0}(\epsilon_1 - \epsilon_2)$ is accumulated. After the second tunneling event, the phases compensate again. Since x_1, x_2 can assume any value between 0 and L, we have to integrate ϵ_1, ϵ_2 between 0 and 1:

$$\int_0^1 d\epsilon_1 \int_0^1 d\epsilon_2 e^{-\frac{\pi\phi}{\phi_0}(\epsilon_1-\epsilon_2)} = 2\frac{1-\cos\left(\frac{\pi\phi}{\phi_0}\right)}{\left(\frac{\pi\phi}{\phi_0}\right)^2}. \tag{3.39}$$

In the calculation of the current presented in this Chapter, one should then isolate the amplitude associated to the process just described, expand it in powers of f - for in-

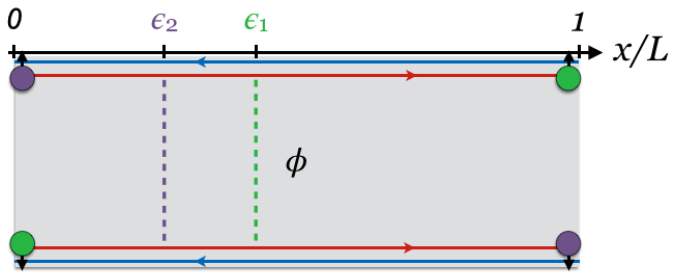

Figure 3.16: *Injection and extraction of a Cooper pair through CAR processes with two inter-edge tunneling events at $x = \epsilon_1 L$, $\epsilon_2 L$. The different colors (green/purple) are introduced to keep trace of the path of each electron.*

stance, up to the second order - and complement the term f^2 with the Aharonov-Bohm contribution computed above.

This has to be done for all the processes involved, and the new flux dependencies are summarized in Table 3.2. Preliminary results show an interference pattern more similar to a Fraunhofer pattern than a SQUID pattern, with two main peculiar features:

- a side lobe decay faster compared to that of a standard Fraunhofer pattern;
- traces of a "doubled" minima periodicity compared to the standard Fraunhofer pattern, just as a doubled periodicity compared to the standard SQUID pattern emerged in [188].

We conclude that the presence of a constriction remains highly influential on the interference pattern. Fig. 3.17 shows $I^r_{\omega_J}$ for the two setups (a) and (b) of Fig. 3.15. It displays that the extended tunneling in setup (b) makes the effect of the constriction visible even for parameter values at which it is weak for setup (a).

Table 3.2: *Aharonov-Bohm phases to be associated to the different types of processes up to the second order in the inter-edge coupling.*

Injection-Extraction	Flux dependence	Order in the inter-edge tunneling
LAR-CAR	$\int_0^1 d\epsilon \left(e^{-i\frac{\pi\phi\epsilon}{\phi_0}} - e^{-i\frac{\pi\phi\epsilon}{\phi_0}}\right) = 2i\frac{\cos\left(\frac{\pi\phi}{\phi_0}\right)-1}{\frac{\pi\phi}{\phi_0}}$	f
LAR-LAR with edge change	$\int_0^1 d\epsilon_1 \int_{\epsilon_1}^1 d\epsilon_2 e^{-i\frac{\pi\phi}{\phi_0}(\epsilon_1+\epsilon_2-1)} = \frac{1-\cos\left(\frac{\pi\phi}{\phi_0}\right)}{\left(\frac{\pi\phi}{\phi_0}\right)^2}$	f^2
CAR-CAR	1	f^0
	$\int_0^1 d\epsilon_1 \int_0^1 d\epsilon_2 e^{-\frac{\pi\phi}{\phi_0}(\epsilon_1-\epsilon_2)} = 2\frac{1-\cos\left(\frac{\pi\phi}{\phi_0}\right)}{\left(\frac{\pi\phi}{\phi_0}\right)^2}$	f^2
LAR-LAR on a same edge	$\cos\left(\frac{\pi\phi}{\phi_0}\right)$	f^0
	$\int_0^1 d\epsilon_1 \int_{\epsilon_1}^1 d\epsilon_2 e^{-i\frac{\pi\phi}{\phi_0}(\epsilon_1-\epsilon_2+1)} + (\phi \to -\phi)$	f^2
	$= -2\left[\frac{\cos\left(\frac{2\pi\phi}{\phi_0}\right)-\cos\left(\frac{\pi\phi}{\phi_0}\right)}{\left(\frac{\pi\phi}{\phi_0}\right)^2} + \frac{\sin\left(\frac{\pi\phi}{\phi_0}\right)}{\frac{\pi\phi}{\phi_0}}\right]$	

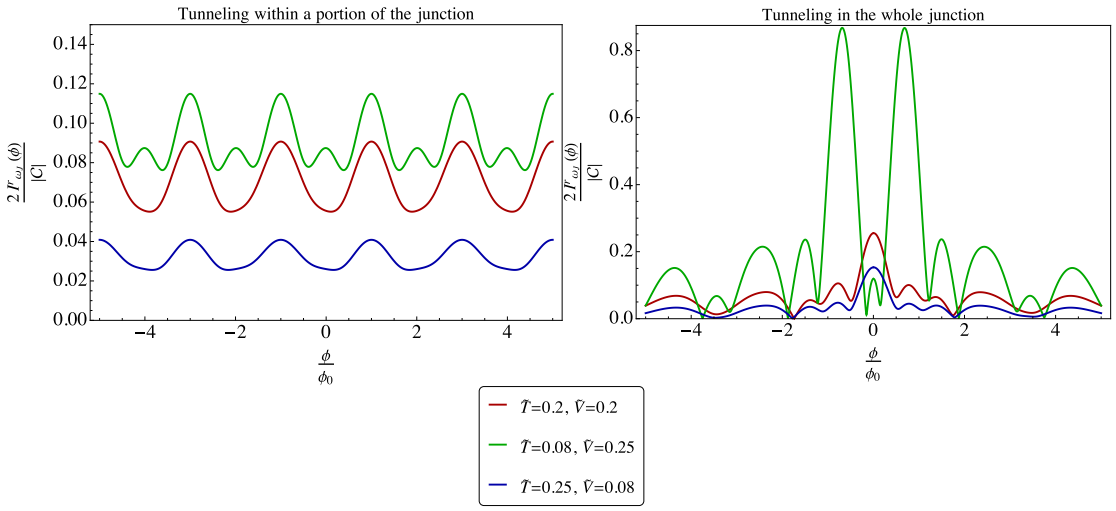

Figure 3.17: *$I^r_{\omega J}$ as a function of ϕ (in units of ϕ_0) for the two cases of Fig. 3.15. Here $\tilde{L} = 20$, $k_F L = 23\pi/4$, $\tilde{f}_T = 0.5$, $f_C = 0.3$, $\tilde{f} = 0.3$. The values of $\tilde{T}$ and $\tilde{V}$ are indicated in the legend.*

CHAPTER 4

The anomalous Josephson effect

In this Chapter, we focus on another declination of the Josephson effect which may occur if the junction satisfies specific symmetry conditions: the anomalous Josephson effect. Leaving aside the AC Josephson effect and magnetic interference, we have seen that the minimal requirement for a Josephson current to flow is a phase difference between the superconducting leads. However, this is not a truly exhaustive formulation of the effect, and an "anomalous" current can arise even in the absence of any phase difference [9, 15, 19, 34, 50, 64, 65, 70, 89, 100, 117, 143, 153, 156, 160–162, 167, 169, 170, 173, 202]. To this aim, the system must break time-reversal and spatial inversion symmetry [72, 115, 139]. In Sec. 4.1 we briefly explain why, by looking at the generic current-phase relation and its properties. Then, in Sec. 4.2, we revise the technological perspectives inspired by this effect and introduce a closely related phenomenon, the superconducting diode effect [90,206]. We conclude the Section by mentioning some of the suitable experimental platforms. Lastly, in Sec. 4.3, we show that among them there is also the Quantum Spin Hall constriction with reconstructed edge channels introduced in Chapter 3. There, not only the anomalous effect appears, but it is also interestingly increased by temperature.

4.1 Supercurrent properties and origin of the phase shift

Before delving into the anomalous Josephson effect and its occurrence in our Quantum Spin Hall-based system, let us revise some basic properties satisfied by the Josephson current (in particular, by the current-phase relation) [72]. Let us assume that the two superconductors defining the junction are described by the order parameters $\Delta_r = |\Delta|e^{i\theta_r}$ and $\Delta_l = |\Delta|e^{i\theta_l}$.

1. First of all, any change of 2π in the wavefunctions of the superconducting elec-

trodes cannot affect the wavefunctions themselves. In other words, a shift of $n2\pi$, $n \in \mathbb{Z}$, of θ_r or θ_l, is irrelevant. This forces the supercurrent I, which depends on their difference, to be a 2π-periodic function,

$$I(\theta_r - \theta_l) = I[(\theta_r - \theta_l) + n2\pi]. \tag{4.1}$$

2. Reversing the direction of the supercurrent flow must introduce a change of sign of the phase difference, namely the current-phase relation is an odd function

$$I(\theta_r - \theta_l) = -I(\theta_l - \theta_r). \tag{4.2}$$

Notably, this property does not hold in every case, but only if either time-reversal symmetry or spatial inversion symmetry are preserved. An easy way to understand this fact is the following [139]. It can be shown that the Josephson supercurrent can be computed from the free energy of the junction F as [6]

$$I(\theta) = \frac{2e}{\hbar}\frac{\partial F}{\partial \theta}, \tag{4.3}$$

where $\theta = \theta_r - \theta_l$ and $F = -k_B T \ln \mathrm{Tr}\{e^{-H/k_B T}\}$ is the free energy. H is the Hamiltonian of the junction, T the temperature and k_B the Boltzmann constant. It is well known that any two Hamiltonians H and H' have identical spectra if and only if they are connected by a unitary or antiunitary transformation: $H = UH'U^\dagger$. In these cases, the transformation has no consequences on the free energy, $F' = F$. By investigating transformations between given pairs of H and H', we can infer the symmetries that the Josephson current must possess, and the requirements to obtain asymmetries. For instance, for a finite supercurrent at zero phase difference to flow, $I(\theta = 0) \neq 0$, it is necessary that the free energy is not symmetric under $\theta \to -\theta$. Otherwise, $F(\theta) = F(-\theta)$ implies $I(\theta) = -I(-\theta)$ with $I(\theta = 0) = 0$. When does a transformation U, such that $H(-\theta) = UH(\theta)U^\dagger$, exist? A swap in the sign of θ in the Hamiltonian is produced by the parity operator (which effectively exchanges the two superconducting electrodes) or by the time-reversal operator. As long as (at least) one of these symmetries is preserved, we can conclude $I(\theta) = -I(-\theta)$. If they are all broken, $I(\theta = 0) \neq 0$ is allowed: this is the anomalous Josephson effect, and the associated current is called anomalous Josephson current. In a following Section we will explain the interest in such effect in view of applications in superconducting electronics and spintronics, and refer to some possible experimental platforms. We mention in passing that, if only time-reversal symmetry is broken, which is a necessary but not sufficient condition to get the anomalous Josephson effect, the junction typically exhibits a π shift in the current-phase relation. Such junction is called a π-junction [30].

3. As a direct consequence of Eq. (4.2) in point 2., a DC supercurrent can flow only in the presence of a superconducting phase gradient,

$$I(n2\pi) = 0,\ n \in \mathbb{Z}. \tag{4.4}$$

4. Lastly, from points 1. and 2., the supercurrent should also vanish at $\theta = n\pi$,

$$I(n\pi) = 0,\ n \in \mathbb{Z}, \tag{4.5}$$

therefore one can consider $I(\theta)$ only in the interval $0 < \theta < \pi$.

In general, without specifying the symmetries of the system, $I(\theta)$ can be decomposed into a Fourier series (see for instance [173])

$$I(\theta) = \sum_{n\geq 1}[I_n \sin(n\theta) + J_n \cos(n\theta)], \tag{4.6}$$

where I_n and J_n are coefficients to be determined. Hence, the current-phase relation is not always simply sinusoidal, but might be "skewed". Notice that, if time-reversal and inversion symmetries are not broken, the current-phase relation has to be antisymmetric even in presence of the higher harmonics, that is $J_n = 0$. If the temperature is close to the critical temperature, or if the junction is relatively opaque – the so-called tunneling limit – the first harmonic $n = 1$ dominates and the higher ones, $n > 1$, are usually neglected. However, if these conditions are relaxed, their contribution can be observed. For $n = 1$,

$$I(\theta) = I_1 \sin(\theta) + J_1 \cos(\theta) = \bar{I} \sin(\theta + \varphi_0), \tag{4.7}$$

where $\bar{I} = \sqrt{I_1^2 + J_1^2}$ and $\varphi_0 = \arctan I_1/J_1$ is the anomalous phase shift, whose microscopic form depends on the system under consideration and specific model assumptions. Junctions featuring the current-phase relation in Eq. (4.7) are called φ_0-junctions.

4.2 Experimental implementations and technological applications

In the previous Section, we have pointed out the two essential requirements for the anomalous Josephson effect to occurr: both time-reversal and inversion symmetry have to be broken. The most common tool to break time-reversal symmetry is the application of a magnetic field [115]. A popular alternative is to attach a ferromagnetic insulator to the superconductor. This kind of systems have been widely discussed in the literature [81,119,172,181]. Besides, π-junctions can be realized in Josephson junctions with non-equilibrium normal metal interlayer [14], semiconductor nanowires [185], d-wave superconductors [186], gated carbon nanotubes [36]. The appeal of π-junctions resides in their potential as building blocks for superconducting circuit elements, such as superconducting programmable logic [67], superconducting digital quantum circuits [55], and scalable superconducting logic circuits [184]. In particular, they can be exploited as on-chip batteries for biasing quantum circuits, providing a constant phase shift between the two superconductors. In analogy to a traditional battery, with supplies a voltage, these junctions are said to be "phase batteries". Significantly, they allow to remove bias lines and reduce decoherence.

Concerning inversion symmetry breaking to realize a φ_0-junction, it can happen intrinsically, such as in topological insulators [50, 83] or in superconductors with Rashba spin-orbit coupling [19, 100, 143, 202], but it can also be provoked by asymmetries of the junction geometry [156] or asymmetries of the device originated during the fabrication process [89]. Compared to a π-junction, a φ_0-junction allows to realize a phase battery which provides an arbitrary phase shift, rather than just 0 or π [130]. Initially, it was suggested to combine 0 and π-junctions, but it is not a trivial task to balance them properly [29]. Apart from junctions which combine conventional superconductors with magnetism and spin-orbital interaction, other systems in which the effect has

been predicted are unconventional superconductors [64, 65, 169, 173] and topologically nontrivial superconductors [153]. The anomalous Josephson effect has also been experimentally observed [9, 77, 89, 117, 161, 167, 170]. We notice that, even for a φ_0-junction (see Eq. (4.7)), the positive critical current $I_c^+ = \max_\theta[I(\theta)]$ is clearly equal in modulus to the negative one $I_c^- = \min_\theta[I(\theta)]$. The critical supercurrent is said to be reciprocal.

Let us look back at Eq. (4.6). In the presence of higher harmonics – for instance, if the junction transparency is high – the cosine terms cannot be absorbed in a mere phase shift as in Eq. (4.7), and a further effect occurs. As a consequence, it might happen that the critical current is different for opposite current directions, namely $I_c^+ \neq |I_c^-|$. Since, for an applied current which is higher than the critical value, a superconductor becomes a normal metal with a finite resistance, it follows that a current I, with $\min(|I_c^-|, I_c^+) < I < \max(|I_c^-|, I_c^+)$, is a supercurrent in one direction, and a dissipative current in the opposite direction (see the cartoon in Fig. 4.1). Such a device is called a superconducting diode. The name is reminescent of the semiconducting diode, namely the $p - n$ junction, which conducts current primarily in one direction [92]. This nonreciprocal charge transport has several applications, including rectification of current, detection of radio signals, temperature sensors. But most importantly it basically opened the way to modern electronics, being the basic component of computer memories and logic circuits. Given the analogy to its semiconducting counterpart, the superconducting diode inspires great perspectives, and has already been experimentally observed [8, 111, 129].

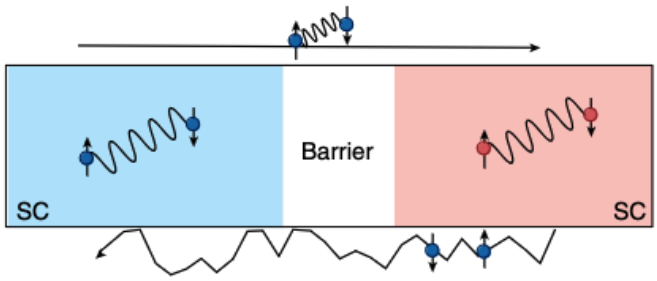

Figure 4.1: *Schematic representation of the diode effect in a Josephson junction: for proper intensities (see the main text), a current flows with no resistance in one direction (the right one in the Figure, denoted by the straight arrow), while it dissipates in the other (denoted by the rugged arrow). Figure adapted from [92], reproduced with permission from Springer Nature.*

In view of the following Section, among the several studies on the anomalous Josephson effect, it is useful to mention in particular the work by Dolcini *et al.* [50]. The authors consider a junction based on a two-dimensional topological insulator and subjected to a Zeeman field along the spin quantization axis of the edge states. The model initially focuses on a single edge, and satisfies the symmetry requirements to realize both the anomalous Josephson effect and the diode effect, since the calculations include all the harmonics. If the width of the topological insulator is sufficiently large[1], the system may be simply described as two junctions in parallel, and the contribution of the second edge can be easily accounted for by a copy of the single-edge Hamiltonian with opposite helicity. Interestingly, when both edges are considered and contribute

[1]The reference scale is the superconducting coherence length ξ.

to the Josephson current, their anomalous current contributions might compensate with each other, leading to the conventional Josephson effect. However, only if the two junctions on either side of the sample have the same length the compensation is exact, and the conventional result is recovered. If the two junctions have different lengths, as depicted in Fig. 4.2, the compensation is only partial and a residual effect persists. In the next Section, we will elucidate some analogies and differences between this work and our results about a Josephson junction based on a constriction between reconstructed edge channels.

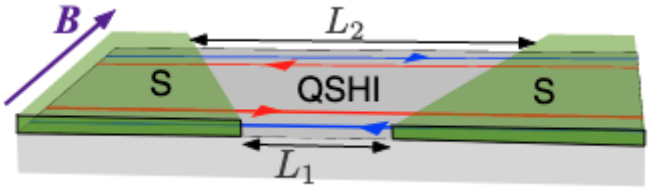

Figure 4.2: *The topological Josephson junction based on a topological insulator inspected in [50] (whence the Figure is taken, reprinted with permission, copyright 2024 by the American Physical Society). When both edges are considered, in order to get a non-vanishing anomalous Josephson current, it is mandatory that the two sides of the sample have different length, $L_1 \neq L_2$.*

4.3 Edge reconstruction-induced anomalous effect

This Section is largely based on the publication [191], where we point out a further property of the proximitized Quantum Spin Hall constriction. Under certain experimental circumstances, which are discussed below, the edge states might be reconstructed, meaning that the differently spin polarized states on each edge are spatially separated. We have discussed in the previous Chapter how this condition affects only marginally the anomalous periodicities emerging in the interference pattern. However, in the absence of magnetic field and external bias, it takes on a fundamental importance. Indeed, it allows the system to host the anomalous Josephson effect presented in the previous Section. We find that, intriguingly, the effect is reinforced by a temperature increase in a range of parameters. Explicitly, for low temperature and weak inter-edge tunneling between the topological channels, the anomalous current has a small zero temperature contribution and a quadratic one. We explain these features on the basis of a simple perturbative argument.

4.3.1 Model and formalism for the transport properties

Let us reconsider the particular case of Josephson junction based on a two-dimensional topological insulator that we analyzed in the previous Chapter, namely the proximitized Quantum Spin Hall constriction, with a particular focus on symmetries and symmetry breakings. We report a scheme in Fig. 4.3(a). For the purposes of this Chapter, it is not relevant whether the constriction corresponds to the whole junction or not, as distinguished in Sec. 3.3, because we will not deal with magnetic interference effects.

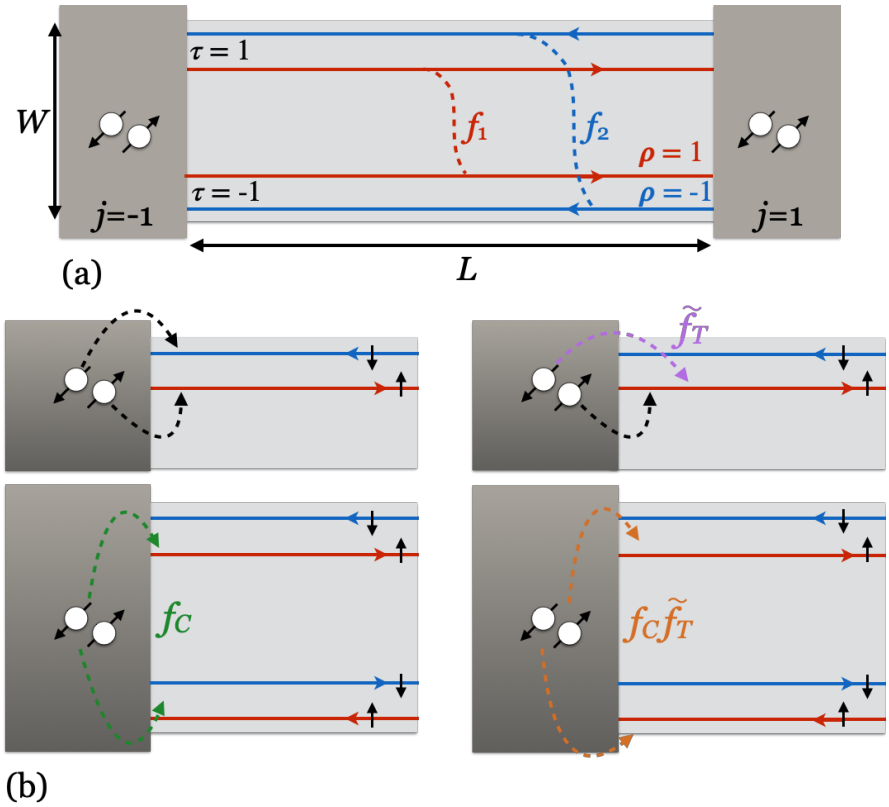

Figure 4.3: *(a) The system under investigation: a Josephson junction having length L and width W, with the edge channels of a two-dimensional topological insulator serving as the non-superconducting region. The superconductors are assumed to be of BCS type. As in the previous Chapters, $\rho = \pm 1$ labels the right/left-mover metallic channels, $\tau = \pm 1$ the upper/lower edge, and $j = \pm 1$ the right/left superconductor. Importantly, $f_{1/2}$ denotes the amplitude of the inter-edge tunneling for right/left-moving electrons. Due to the unbalance between the tunneling amplitudes $f_1 \neq f_2$, both inversion symmetry and time-reversal symmetry are broken. (b) Injection processes of Cooper pairs from the superconductors to the edges of the topological insulator: either a single edge (upper panels, which correspond to a Local Andreev Reflection) or both edges (lower panels, which correspond to a Crossed Andreev Reflection) might be involved. In the proximitized system, Cooper pairs can flow either in a singlet (left panels) or in a triplet (right panels) spin state. Triplet injections and Crossed Andreev Reflections affect the tunneling amplitudes with a factor of $\tilde{f}_T$ and f_C, respectively. Figure adapted from [191].*

Referring to the Figure, on the upper edge, right/left moving electrons have spin up-/down projection. On the lower edge, the situation is reversed, in other words electrons with spin down/up move right/left. At this stage, inversion symmetry is already broken at the level of the single edges, but time-reversal symmetry is not [83]. To do so, we can combine the constriction and edge reconstruction. Let us recap one last time the three main conceptual steps of this scheme:

- Through etching, the edge channels are brought at a distance that is comparable with their localization length, such that electrons can tunnel between the upper and lower edge. This can happen in two ways [48, 61, 110]: via backscattering, which preserves the spin polarization, or via forward scattering, which flips it.
- The constriction is fabricated long with respect to the inverse Fermi momentum.

As we already commented in this Thesis, it is in some sense unavoidable to this date: currently, constrictions between helical edge states have only been realized in thick HgTe quantum wells, where the Dirac point is hidden in the bulk valence band [168]. The spin-preserving backscattering is hence irrelevant, and the only process remaining is the spin-flipping forward scattering [168], denoted by $f_1,\ f_2$ in Fig. 4.3(a). However, even alone, this process is still time-reversal invariant.

- The third point consists in the edge reconstruction: as proposed in Ref. [197], if the potential confining the edge channels is soft, the spin up and spin down channels can separate in real space in order to mimic the positive charge distribution of the gate and minimize the Coulomb energy. This creates an unbalance in the tunneling rates for spin up and spin down electrons (see Fig. 4.3(a), $f_1 \neq f_2$). Time-reversal symmetry is hence also broken, as well as inversion symmetry at the level of the full structure.

Thanks to these three considerations, according to what was said at the beginning of this Chapter, the Josephson junction with reconstructed helical edges as a link is hence expected to exhibit a φ_0 Josephson effect in the absence of external fields. Such anomalous effect has similarities to the one previously discussed in [50], where, however, a magnetic field is crucially required. Furthermore, in that case, the effect is mainly present when a single edge is considered as a weak link, while it tends to vanish when both edges are considered. Additional comments on this comparison will follow at the end of the Chapter.

We now provide a quantitative analysis of what we have just described. Consistently with the previous Chapters, the fermionic operators $\psi_{\rho\tau}(x)$ annihilate an electron at position x propagating in the ρ-direction channel of the τ edge. In particular, $\rho = 1\ (-1)$ stands for the right (left) direction of motion and $\tau = 1\ (-1)$ for the upper (lower) edge. The spin polarization is hence $\tau\rho$. For notational convenience, we previously introduced the spinor $\boldsymbol{\psi}(x) = (\psi_{11}(x), \psi_{-11}(x), \psi_{-1,-1}(x), \psi_{1-1}(x))^T$. The Hamiltonian could hence be recast in the quadratic form

$$H = H_E^0 + \delta H_E, \tag{4.8}$$

with H_E^0 describing the two-dimensional topological insulator and δH_E the coupling to the superconductors, that are considered of s-wave type. From Eq. (3.32),

$$H_E^0 = \int_{-\infty}^{+\infty} dx\, \boldsymbol{\psi}^\dagger(x) \mathcal{H}_E^0 \boldsymbol{\psi}(x), \tag{4.9}$$

where the separation L between the superconductors has been effectively taken as infinite for long junctions, and $\mathcal{H}_E^0$ is the Hamiltonian density of the edge channels, made up of the two contributions $\mathcal{H}_E^0 = \mathcal{H}_{kin.} + \mathcal{H}_{f.s.}$, that are the kinetic term and the forward scattering term, respectively. In a compact form,

$$\mathcal{H}_{kin.} = \hbar v_F (-i\partial_x) \tau_z \otimes \rho_z, \tag{4.10}$$

$$\begin{aligned} \mathcal{H}_{f.s.} &= \frac{f_1}{2}(-\tau_y \otimes \rho_y + \tau_x \otimes \rho_x) + \frac{f_2}{2}(\tau_y \otimes \rho_y + \tau_x \otimes \rho_x) \\ &= \frac{-f_1 + f_2}{2} \tau_y \otimes \rho_y + \frac{f_1 + f_2}{2} \tau_x \otimes \rho_x, \end{aligned} \tag{4.11}$$

with ρ_i and τ_i, $i = 0, x, y, z$, the identity and the three Pauli matrices acting in the right/left-movers and the upper/lower edge space, respectively, and v_F the Fermi velocity. The couplings f_1 and f_2 parametrize the tunneling between the edges, and we emphasize that as $f_1 \neq f_2$ and the edges are reconstructed, time-reversal symmetry is broken. Our model does not include magnetic impurities, that would introduce intra-edge backscattering (and, for the present discussion, other sources of symmetry-breakings), due to the fact that long and ballistic edges can nowadays be accomplished [18]. We also neglect charge puddles in the bulk of the two-dimensional topological insulator sample, owing to its narrowness.

In terms of energy spectrum, the non-superconducting part just discussed represents a pair of one-dimensional Dirac cones, in which the two right-moving branches are shifted with respect to the left-moving ones proportionally to $f_1 - f_2$. Moreover, branches with fixed chirality do not have fixed spin projection anymore, due to the spin non-conserving tunneling. We will come back on considerations about the effect of $f_1,\ f_2$ on the spectrum.

Before focusing on the anomalous current, let us recall our previous perturbative formalism in a few lines. We know that the superconducting leads, assumed to have a large superconducting gap Δ with respect to all the other energy scales at play, affect the system via the perturbative Hamiltonian δH_E. Besides the large gap hypothesis, its derivation required both the Hamiltonian model of the superconductors (in our case, it is the standard BCS one), and a weak coupling between the latters and the edges, see [78]. Ultimately, the coupling to the superconductors ($j = \pm 1$ denoting the right/left one) was found to be [78, 188]

$$\delta H_E = \sum_{\zeta_1,\zeta_2,j} \left[\Gamma^j_{\zeta_1,\zeta_2} \psi_{\zeta_1}(x_j^-)\psi_{\zeta_2}(x_j^+) + h.c.\right], \tag{4.12}$$

with ζ_i collective indices standing for $\rho_i\tau_i$, $x_j^\pm = jL/2 \pm \delta_{\zeta_1,\zeta_2}\xi/2$ ($\xi \ll L$ the coherence length in the edges). We recall that the sum has been antisymmetrized for each $\zeta_1 \neq \zeta_2$ term, and all the possible injection processes are collected in Fig. 4.3(b). The generic coefficient reads as

$$\Gamma^j_{\zeta_1,\zeta_2} = \Gamma(-1)^{\delta_{\zeta_1,-1-1}\delta_{\zeta_2,1-1}} \left(\tilde{f}_T\right)^{\delta_{\rho_1\tau_1,\ \rho_2\tau_2}} (f_C)^{\delta_{\tau_1,-\tau_2}} e^{i[\frac{j}{2}k_F L(\rho_1+\rho_2)-\theta_j]}. \tag{4.13}$$

Here, Γ parametrizes the typical amplitude of the tunneling processes across the superconductors/topological insulator interfaces, θ_j are the bare phases of the superconductors, k_F is the Fermi momentum, $\tilde{f}_T = f_T/\sqrt{1+f_T^2}$ and $f_{T/C}$ are coefficients related to the occurrence of spin flips and tunneling into different edges (Crossed Andreev Reflection), respectively. In the following discussions, a main role will be played by f_T. Indeed, the propagation of triplet Cooper pairs on a same reconstructed edge, that $f_T \neq 0$ enables, breaks inversion symmetry and is found to be the origin of our anomalous current. A finite f_T is justified by the strong spin-orbit coupling characterizing HgTe quantum wells. Although expected as well, f_C is not essential for the following, while it was pivotal for our former results involving a perpendicular magnetic field [188].

We are now ready to investigate the direct Josephson current through the junction. With a standard perturbative Kubo-like approach with respect to δH, we can find the

right and left current contributions in the reconstructed case, see Eq. (3.34) with $\phi = \tilde{V} = 0$ (and see Appendix A for all the details of the method in the non-reconstructed case). By combining them together, the Josephson current reads as

$$I^{tot} = \mathcal{C}\,\mathrm{Im}\Big\{e^{-i(\theta_r-\theta_l)}\mathcal{I}(\tilde{f}_1,\tilde{f}_2) - e^{i(\theta_r-\theta_l)}\mathcal{I}(\tilde{f}_2,\tilde{f}_1)\Big\}, \tag{4.14}$$

with $\mathcal{C} \equiv (-2e\Delta\Gamma^2)/(\pi^2\hbar^3 v_F^2)$. The function $\mathcal{I}$ has the following structure

$$\mathcal{I}(\tilde{f}_1,\tilde{f}_2) = \frac{1}{\Gamma^2}\sum_{\zeta_1,\zeta_2,\zeta_3,\zeta_4}\Gamma^r_{\zeta_1,\zeta_2}(\Gamma^l_{\zeta_3,\zeta_4})^*\int_0^{+\infty} ds\,\mathrm{Im}\left[\Pi_{\zeta_1,\zeta_2,\zeta_3,\zeta_4}\left(\tilde{L},\tilde{f}_1,\tilde{f}_2,\tilde{T},s\right)\right]. \tag{4.15}$$

The integral evaluates the amplitude associated to the transport of a Cooper pair whose electrons are in the initial states ζ_3,ζ_4 and in the final states ζ_1,ζ_2, encoding all the relevant information. More quantitatively, $\Pi_{\zeta_1,\zeta_2,\zeta_3,\zeta_4}$ arises as a combination of products of two Green functions (see [188] for the details) calculated over the Hamiltonian in the absence of superconductors. As before, we resort to the adimensional quantities

$$\tilde{L} = \frac{L\Delta}{\hbar v_F}, \qquad \tilde{T} = \frac{\pi k_B T}{\Delta}, \qquad \tilde{f}_{1,2} = \frac{f_{1,2}}{\Delta}.$$

Apparently, in Eq. (4.14) only the difference between the bare phases of the two superconductors appears. However, in the next Subsection, we will bring out the anomalous phase shift.

4.3.2 Results

To better characterize the anomalous effect, we first recast the current as

$$I^{tot} = \mathcal{C}\left[\mathcal{A}\cos(\theta_r-\theta_l) + \mathcal{B}\sin(\theta_r-\theta_l)\right] \equiv \mathcal{C}\mathcal{D}\sin\left[(\theta_r-\theta_l)+\varphi_0\right], \tag{4.16}$$

where we have defined

$$\begin{aligned} &\mathcal{A} \equiv \mathrm{Im}\left[\mathcal{I}\left(\tilde{f}_1,\tilde{f}_2\right) - \mathcal{I}\left(\tilde{f}_2,\tilde{f}_1\right)\right], \qquad \mathcal{B} \equiv -\mathrm{Re}\left[\mathcal{I}\left(\tilde{f}_1,\tilde{f}_2\right) + \mathcal{I}\left(\tilde{f}_2,\tilde{f}_1\right)\right], \\ &\mathcal{D} \equiv \sqrt{\mathcal{A}^2+\mathcal{B}^2}, \qquad\qquad \tan\varphi_0 \equiv \frac{\mathcal{A}}{\mathcal{B}}. \end{aligned} \tag{4.17}$$

This way we have singled out the parameter φ_0, that is the one describing the anomalous Josephson effect. When $\varphi_0 = 0 \bmod 2\pi$, there is no anomalous Josephson effect. It is present otherwise.

To move towards the quantitative description of the φ_0 effect, let us consider the current in the absence of phase difference between the superconductors, $\theta_r = \theta_l$. What we explicitly have is

$$I_a \equiv I^{tot}\|_{\theta_r=\theta_l} = \mathcal{C}\,\mathrm{Im}\left[\mathcal{I}\left(\tilde{f}_1,\tilde{f}_2\right) - \mathcal{I}\left(\tilde{f}_2,\tilde{f}_1\right)\right], \tag{4.18}$$

which makes evident that processes contributing to $\mathcal{I}$ symmetrically under the exchange $\tilde{f}_1 \leftrightarrow \tilde{f}_2$ do not give rise to an anomalous current ($I_a = 0$). A deeper analysis, supported by Eq. (4.15) and the expressions of $\Pi_{\zeta_1,\zeta_2,\zeta_3,\zeta_4}$, excludes processes where one

electron is injected in a right-moving channel and the other in a left-moving channel. Specifically, we find that the processes responsible for the anomalous effect are $\propto \tilde{f}_T^2$ and independent of f_C. They correspond to injections as depicted in the upper-right panel of Fig. 4.3(b). Quantitatively, we have

$$I_a = \frac{\mathcal{C}}{\Gamma^2}\left\{\mathrm{Im}\left[\sum_{i=1}^{8}\Lambda_i\int_0^{+\infty} ds\,\mathrm{Im}\,\Pi_i(s)\right] - \tilde{f}_1 \leftrightarrow \tilde{f}_2\right\}, \tag{4.19}$$

where the coefficients Λ_i are listed in the Table below.

Table 4.1: *Coefficients Λ_i and processes contributing to the anomalous Josephson current.*

Coefficient Λ_i	Corresponding $\Gamma^r_{\zeta_1,\zeta_2}(\Gamma^l_{\zeta_3,\zeta_4})^*$
$\Lambda_1 = \Gamma^2\tilde{f}_T^2 e^{-i2k_FL}$	$= \Gamma^r_{-11,-11}(\Gamma^l_{-11,-11})^*$
$\Lambda_2 = \Gamma^2\tilde{f}_T^2 e^{-i2k_FL}$	$= \Gamma^r_{-1-1,-1-1}(\Gamma^l_{-1-1,-1-1})^*$
$\Lambda_3 = \Gamma^2\tilde{f}_T^2 e^{-i2k_FL}$	$= \Gamma^r_{-11,-11}(\Gamma^l_{-1-1,-1-1})^*$
$\Lambda_4 = \Gamma^2\tilde{f}_T^2 e^{-i2k_FL}$	$= \Gamma^r_{-1-1,-1-1}(\Gamma^l_{-11,-11})^*$
$\Lambda_5 = \Gamma^2\tilde{f}_T^2 e^{i2k_FL}$	$= \Gamma^r_{11,11}(\Gamma^l_{11,11})^*$
$\Lambda_6 = \Gamma^2\tilde{f}_T^2 e^{i2k_FL}$	$= \Gamma^r_{1-1,1-1}(\Gamma^l_{1-1,1-1})^*$
$\Lambda_7 = \Gamma^2\tilde{f}_T^2 e^{i2k_FL}$	$= \Gamma^r_{11,11}(\Gamma^l_{1-1,1-1})^*$
$\Lambda_8 = \Gamma^2\tilde{f}_T^2 e^{i2k_FL}$	$= \Gamma^r_{1-1,1-1}(\Gamma^l_{11,11})^*$

The Π_i functions are not all independent of each other, and can be written in a unified form. In particular, it can be shown that

$$\Pi_1(s) = \Pi_2(s) \qquad \Pi_3(s) = \Pi_4(s) \qquad \Pi_5(s) = \Pi_6(s) \qquad \Pi_7(s) = \Pi_8(s),$$

where, from calculations that we skip here, but can be inferred by following [188] and Appendix B,

$$\Pi_1(s) = \frac{\tilde{T}^2}{2}\left\{[\cosh(\lambda_2)+1]K^2(s) - \left[\cosh(\lambda_2)+\cos\left(2\tilde{f}_2\right)\right]K(s+1)K(s-1)\right\},$$

$$\Pi_3(s) = \frac{\tilde{T}^2}{2}\left\{[\cosh(\lambda_2)-1]K^2(s) - \left[\cosh(\lambda_2)-\cos\left(2\tilde{f}_2\right)\right]K(s+1)K(s-1)\right\},$$

$$\Pi_5(s) = \frac{\tilde{T}^2}{2}\left\{[\cosh(\lambda_1)+1](K^*(-s))^2 - \left[\cosh(\lambda_1)+\cos\left(2\tilde{f}_1\right)\right]K^*(-s-1)K^*(-s+1)\right\},$$

$$\Pi_7(s) = \frac{\tilde{T}^2}{2}\left\{[\cosh(\lambda_1)-1](K^*(-s))^2 - \left[\cosh(\lambda_1)-\cos\left(2\tilde{f}_1\right)\right]K^*(-s-1)K^*(-s+1)\right\}.$$

Here,

$$K(s) = \frac{1}{\sinh\left[\tilde{T}\left(\tilde{L}+s-i\right)\right]}, \tag{4.20}$$

with $s \in \mathbb{R}$, and

$$\lambda_\nu = 2\tilde{f}_\nu\left(1+i\tilde{L}\right), \tag{4.21}$$

with $\nu = 1, 2$. We stop for a moment to further manipulate these expressions. The reader wishing to proceed straightforwardly to the results can move to Eq. (4.29).

We first notice the symmetry relation

$$K^*(-s) = \frac{1}{\sinh\left[\tilde{T}\left(\tilde{L} - s + i\right)\right]} \equiv K(-s+2i),$$

thanks to which we can rewrite the functions $\Pi_5(s)$ and $\Pi_7(s)$ as

$$\begin{aligned}\Pi_5(s) =& \frac{\tilde{T}^2}{2}\Big\{[\cosh(\lambda_1)+1]K^2(-s+2i) - \left[\cosh(\lambda_1) + \cos\left(2\tilde{f}_1\right)\right] \\ & K(-s+2i-1)K(-s+2i+1)\Big\}, \end{aligned} \tag{4.22}$$

$$\begin{aligned}\Pi_7(s) =& \frac{\tilde{T}^2}{2}\Big\{[\cosh(\lambda_1)-1]K^2(-s+2i) - \left[\cosh(\lambda_1) - \cos\left(2\tilde{f}_1\right)\right] \\ & K(-s+2i-1)K(-s+2i+1)\Big\}. \end{aligned} \tag{4.23}$$

Hence, in a unified form, we obtain

$$\Pi_1(s) \equiv \Pi_+^{(2)}(s), \tag{4.24a}$$

$$\Pi_3(s) \equiv \Pi_-^{(2)}(s), \tag{4.24b}$$

$$\Pi_5(s) \equiv \Pi_+^{(1)}(-s+2i), \tag{4.24c}$$

$$\Pi_7(s) \equiv \Pi_-^{(1)}(-s+2i), \tag{4.24d}$$

where

$$\Pi_\pm^{(\nu)}(s) = \frac{\tilde{T}^2}{2}\left\{[\cosh(\lambda_\nu)\pm 1]K^2(s) - \left[\cosh(\lambda_\nu)\pm\cos\left(2\tilde{f}_\nu\right)\right]K(s+1)K(s-1)\right\}. \tag{4.25}$$

Since ξ is the short distance cut-off, and since we are interested in the long junction regime, we can expand the functions K at the lowest order in ξ/L. In this case, what we obtain is

$$K(s+1)K(s-1) \simeq \tilde{T}^2K^4(s) + K^2(s), \tag{4.26}$$

and hence Eq. (4.25) becomes

$$\Pi_\pm^{(\nu)}(s) = \frac{\tilde{T}^2}{2}\left\{\left[\mp\cos\left(2\tilde{f}_\nu\right)\pm 1\right]K^2(s) - \left[\cosh(\lambda_\nu)\pm\cos\left(2\tilde{f}_\nu\right)\right]\tilde{T}^2K^4(s)\right\}. \tag{4.27}$$

Plugging this result into Eq. (4.19) and extracting the imaginary parts, the terms $\propto K^2(s)$ cancel out exactly and we are left with the following expression for the anomalous current, which represents the central result of our analysis

$$\begin{aligned}\frac{I_a}{\mathcal{C}} =& -2\tilde{f}_T^2\sin(2k_FL)\Big[\cosh(2\tilde{f}_1)\cos(2\tilde{f}_1\tilde{L})(I_1+I_2) \\ & -\sinh(2\tilde{f}_1)\sin(2\tilde{f}_1\tilde{L})(I_4-I_3) + \tilde{f}_1 \leftrightarrow \tilde{f}_2\Big]. \end{aligned} \tag{4.28}$$

Here

$$I_1 = \tilde{T}^4 \,\mathrm{Im}\left[\int_0^{+\infty} ds\, K^4(s)\right], \quad I_2 = \tilde{T}^4 \,\mathrm{Im}\left[\int_0^{+\infty} ds\, (K^*(-s))^4\right],$$
$$I_3 = \tilde{T}^4 \,\mathrm{Re}\left[\int_0^{+\infty} ds\, K^4(s)\right], \quad I_4 = \tilde{T}^4 \,\mathrm{Re}\left[\int_0^{+\infty} ds\, (K^*(-s))^4\right].$$

The building block is given by

$$\tilde{T}^4 \int_0^{+\infty} ds\, K^4(s) = \frac{4}{3}\tilde{T}^3 \frac{1 - 3e^{2\left(\tilde{L}-i\right)\tilde{T}}}{\left[1 - e^{2\left(\tilde{L}-i\right)\tilde{T}}\right]^3} \equiv \mathcal{F}\left(\tilde{L}, \tilde{T}\right),$$
$$\tilde{T}^4 \int_0^{+\infty} ds\, (K^*(-s))^4 = \mathcal{F}\left(-\tilde{L}, \tilde{T}\right),$$

and we notice that

$$I_1 = I_2 \qquad I_3 + I_4 = \frac{4}{3}\tilde{T}^3.$$

With some more simple algebraic manipulations, one can now finally reach the final expression for the anomalous current characterizing the system,

$$I_a = \mathcal{C}\mathcal{D}\sin(\varphi_0) = 4\mathcal{C}\tilde{f}_T^2 \sin(2k_F L)\mathrm{Im}\left\{[\cosh(\lambda_2) - \cosh(\lambda_1)]\left[\mathcal{F}\left(\tilde{L}, \tilde{T}\right) - \frac{2}{3}\tilde{T}^3\right]\right\}. \tag{4.29}$$

The function $\mathcal{F}\left(\tilde{L}, \tilde{T}\right)$ is explicitly

$$\mathcal{F}\left(\tilde{L}, \tilde{T}\right) = \frac{4}{3}\tilde{T}^3 \frac{1 - 3e^{2\left(\tilde{L}-i\right)\tilde{T}}}{\left[1 - e^{2\left(\tilde{L}-i\right)\tilde{T}}\right]^3}.$$

4.3.3 Discussion and conclusions

Let us start from the inspection of the anomalous current in Eq. (4.29) as a function of the two tunneling amplitudes, as shown in Fig. 4.4(a).

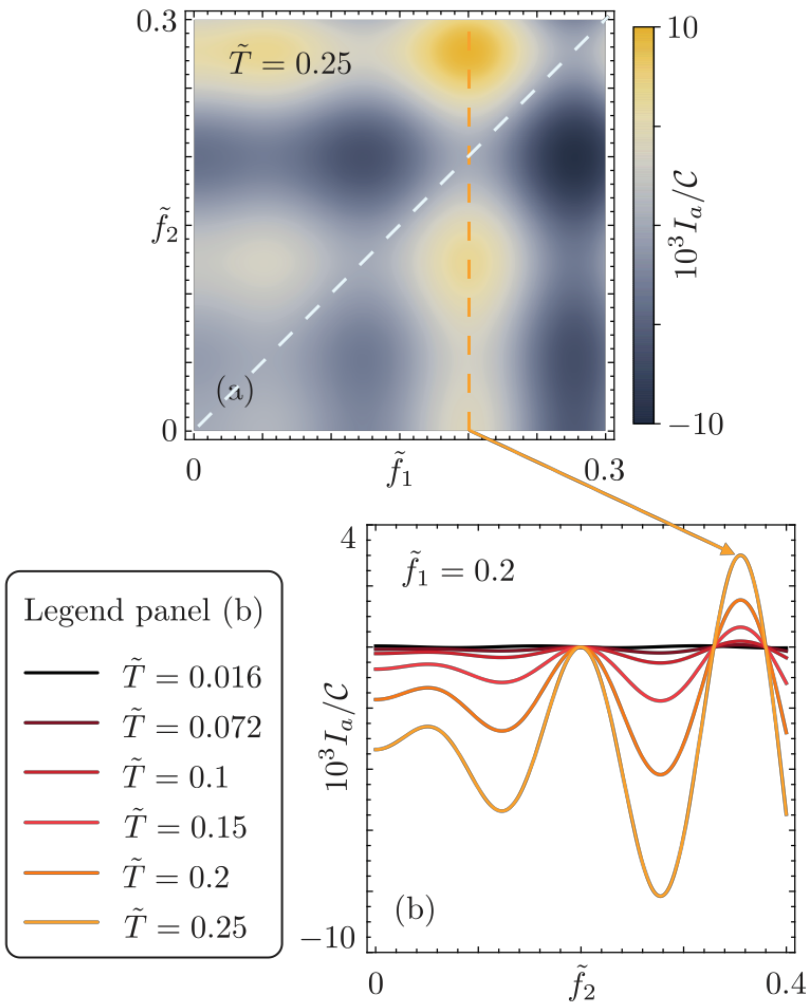

Figure 4.4: *Anomalous current $I_a = I^{tot}\|_{\theta_r=\theta_l}$ flowing in the system. (a) Density plot of $I_a/\mathcal{C}$ as a function of $\tilde{f}_1$, $\tilde{f}_2$, with $f_C = 0.3$, $\tilde{f}_T = 0.4$, $k_F L = 23/4\pi$, $\tilde{L} = 20$ and $\tilde{T} = 0.25$ (color scale at the right). (b) $I_a/\mathcal{C}$ as a function of $\tilde{f}_2$, for different values of $\tilde{T}$ (see the plot legend) and $\tilde{f}_1 = 0.2$. The other parameters remain unchanged from panel (a). Figure adapted from [191].*

As a first observation, the anomalous current does not have a well-defined sign. Just like the ordinary current, it obviously has to be antisymmetric in the exchange of the right and left current contributions, being proportional to their difference – see Eq. (4.14). But from the same Equation and the previous Chapter, we know that I^r and I^l are related to each other simply by $\tilde{f}_1 \leftrightarrow \tilde{f}_2$, if $\theta_r = \theta_l$. Accordingly, in Fig. 4.4(a) I_a appears odd under the exchange $\tilde{f}_1 \leftrightarrow \tilde{f}_2$. In terms of symmetries, such exchange essentially realizes the inversion of the structure. Consistently, we find $I_a = 0$ for $\tilde{f}_1 = \tilde{f}_2$, and in that case Eq. (4.16) recovers the standard Josephson effect (see the dashed white line on the diagonal). This could be expected from the beginning since for $\tilde{f}_1 = \tilde{f}_2$ time-reversal symmetry is preserved, and the conditions for the anomalous effect are no longer met. An oscillatory behavior is also present as a function of $\tilde{f}_1$ and $\tilde{f}_2$ (see again Fig. 4.4(a)). This fact is not surprising since oscillations in the amplitude of the DC and AC (non-anomalous) Josephson currents were also present for $\tilde{f}_1 = \tilde{f}_2$ [188]. As a second interesting fact, thanks to such oscillations, I_a increases

rapidly as soon as an asymmetry between the couplings, although small, is introduced. This is visible in Fig. 4.4(b), where we set $\tilde{f}_1 = 0.2$: the anomalous current assumes a finite value as $\tilde{f}_2$ deviates, even slightly, from 0.2. Finally, it is here worth noticing a peculiar effect: the anomalous current increases as the temperature is increased, having to keep, however, $k_B T$ smaller than the induced gap. This effect is better shown in Fig. 4.5. Surprising at first, it can be understood with a simple "perturbative" argument: the inter-edge scattering proportional to $f_{1/2}$ mixes states with the same kinetic energy $\pm\hbar v_F k$; in a Fermi's golden rule approach where $H_{f.s.}$ is the perturbation, its effects are strongly suppressed at low temperature due to the Fermi functions. Such a temperature dependence is hence a clear cut signature of the constriction.

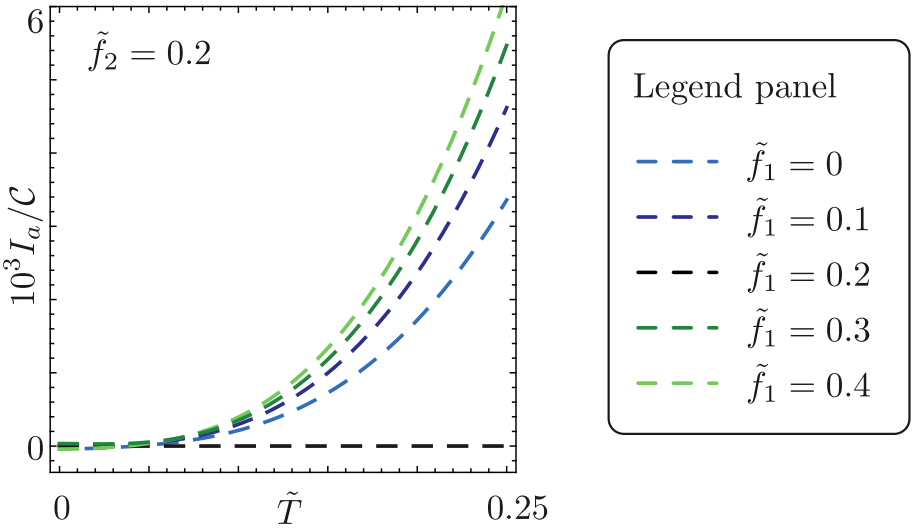

Figure 4.5: *$I_a/\mathcal{C}$ as a function of $\tilde{T}$, for different values of $\tilde{f}_1$ (see the plot legend), at $\tilde{f}_2 = 0.2$. Here $f_C = 0.3$, $\tilde{f}_T = 0.4$, $k_F L = 23/4\pi$, $\tilde{L} = 20$. Figure adapted from [191].*

In order to catch the essential physics underlying such temperature behavior, an expansion of Eq. (4.29) is particularly illuminating. First of all, the anomalous current has a zero temperature contribution, although hardly visible in Fig. 4.5:

$$\left.\frac{I_a}{\mathcal{C}\tilde{f}_T^2 \sin(2k_F L)}\right|_{\tilde{T}=0} = \frac{4}{3}\mathrm{Im}\left\{\frac{\cosh(\lambda_2)-\cosh(\lambda_1)}{\left(\tilde{L}-i\right)^3}\right\}. \tag{4.30}$$

Despite its low visibility, the presence of this term is significant and will be discussed in a while. Restoring finite temperature, without assumptions on $\tilde{L}$ but expanding for small $\tilde{T}$ and $\tilde{f}_\nu$, we obtain

$$\frac{I_a}{\mathcal{C}\tilde{f}_T^2 \sin(2k_F L)} \overset{\tilde{T},\tilde{f}_\nu \ll 1}{\simeq} \frac{8}{3}\left(\tilde{f}_1^2 - \tilde{f}_2^2\right)\left[\frac{1}{1+\tilde{L}^2} + 2\tilde{T}^2\right], \tag{4.31}$$

which is the quadratic temperature scaling well visible in Fig. 4.5[2].

We can now interpret the temperature dependence of the anomalous current. As we already commented, at zero temperature (see Eq. (4.30)), and for small $\tilde{f}_{1/2}$, the inter-edge tunneling events are suppressed by phase space arguments. In this case, the effect has a different origin: the coupling between the edges, for $\tilde{f}_1 \neq \tilde{f}_2$, splits the energies of electrons having different chiralities. In terms of the spin degree of freedom, it is analogous to the application of two magnetic fields in the z-direction opposite to each other on the two edges. Under this perspective, our system realizes two replica of the single-edge φ_0 effect reported in [50], and discussed at the end of the previous Section. However, while in [50] the anomalous current vanishes when both edges are considered, in our case the effect is opposite for the two edges and the cancellation doesn't occur. The energy splitting just mentioned is independent of the length $\tilde{L}$ of the system and, accordingly, the associated current decays as the distance between the superconductors is increased (Eq. (4.30)), as usual for Josephson currents. When the temperature is finite, as in Eq. (4.31), the second mechanism for the φ_0 effect comes into play: the inter-edge tunneling. Just as the zero temperature contribution, the finite temperature one scales as $\tilde{f}_{1/2}^2$. It thus involves two inter-edge tunneling events, consistently with the processes we identified in Table 4.1, which require at least two tunnelings. The probability of each tunneling event scales as $\tilde{L}$, so that the finite temperature term scales, compared to the zero temperature one, with a factor $\tilde{L}^2$ more. Moreover, each tunneling corresponds to a product $\mathsf{f}(1-\mathsf{f})$, with $\mathsf{f} = 1/(e^{E/k_BT}+1)$ the Fermi function. Under integration over the energies $E = \pm\hbar v_F k$, such a product contributes with a factor $\tilde{T}$, and since we are in the presence of a double tunneling, the leading order becomes $\tilde{T}^2$. The probability of the events contributing to the temperature activated anomalous current is hence favored by both the junction length and temperature. Our qualitative interpretation is able to capture the scaling of the φ_0 effect at finite temperature, its non-zero value at zero temperature, and the better scaling with the length of the junction characterizing the thermally activated processes.

To summarize, the Quantum Spin Hall-based Josephson junction we conceived turns out to be an experimentally relevant system hosting the φ_0 Josephson effect, remarkably in the absence of applied magnetic fields. The necessary symmetry breakings are provided by the edge reconstruction, a phenomenon which can take place with soft confinement potentials. The anomalous Josephson current, surprisingly at first, increases as the temperature is increased. We have analyzed in detail such an increase resorting to a perturbative expansion and we have qualitatively interpreted that on the basis of the thermal activation of the inter-edge tunneling processes in the constriction. Our results open the way to the design of phase batteries in these systems, without the need of external magnetic fields. Being the building block of our system a two-dimensional topological insulator, it is possible to envision the direct integration of the φ_0 junction just considered with other functional nanostructures built on the same topological insulator. Lastly, going beyond the low-transparency interfaces assumption, and hence

[2]On the other hand, we can also write analytically the thermodynamic limit of Eq. (4.29)

$$\frac{I_a}{\mathcal{C}\tilde{f}_{\tilde{T}}^2 \sin(2k_F L)} \overset{\tilde{T}\tilde{L}\gg 1}{\simeq} 16\left[\cos\left(2\tilde{f}_2\tilde{L}\right)\cosh\left(2\tilde{f}_2\right) - \cos\left(2\tilde{f}_1\tilde{L}\right)\cosh\left(2\tilde{f}_1\right)\right]\tilde{T}^3$$
$$e^{-4\tilde{L}\tilde{T}}\sin\left(4\tilde{T}\right) - \frac{8}{3}\left[\sin\left(2\tilde{f}_2\tilde{L}\right)\sinh\left(2\tilde{f}_2\right) - \sin\left(2\tilde{f}_1\tilde{L}\right)\sinh\left(2\tilde{f}_1\right)\right]\tilde{T}^3, \tag{4.32}$$

but we will rather focus on Eq. (4.31).

including higher order contributions of δH_E in the calculation of the current, our setup satisfies the requirements to exhibit the superconducting diode effect.

CHAPTER 5

Role of the spatial extension of the edge channels

In this last Chapter, we summarize the main results on how to describe transport through a Quantum Spin Hall-based Josephson junction in the presence of edges with large spatial extension. This situation is shown in Fig. 5.1(c)-(d).

In Chapter 2 (Subsec. 2.2.1), we have discussed the Dynes and Fulton description of supercurrents in the presence of a magnetic field, emphasizing that such description is not able to capture any Cooper pair splitting. Then, in Sec. 2.3, we have introduced the Crossed Andreev Reflection, which is the most common splitting mechanism when dealing with edge states. In what follows, we discuss a heuristic approach that generalizes Dynes and Fulton's one. It is still built on the supercurrent density, but includes any distinguished trajectories for the two electrons, provided that they are not further away from each other than the coherence length ξ. This can involve a single edge (a generalization of Local Andreev Reflection, LAR) or both edges (a generalization of Crossed Andreev Reflection, CAR). We will see that the wider the edges, the more pronounced are the consequences on the interference pattern, which is highly sensitive to the electrons' path. The pattern's periodicity resulting from this phenomenology will be discussed and compared to the case of localized edge states. This Chapter is largely based on the original results in Ref. [189].

5.1 Local and non-local transport of Cooper pairs

Before moving to the description of extended channels, we shortly recap how the interference pattern looks like when they have a strongly localized profile. To this aim, let us consider a Josephson junction of length L and width w. Let the non-superconducting part be tunnel-coupled to a right and a left superconducting leads, and subjected to a uniform perpendicular magnetic field, $\mathbf{B} = B\mathbf{e_3}$, with a magnetic flux $\phi = BLw$

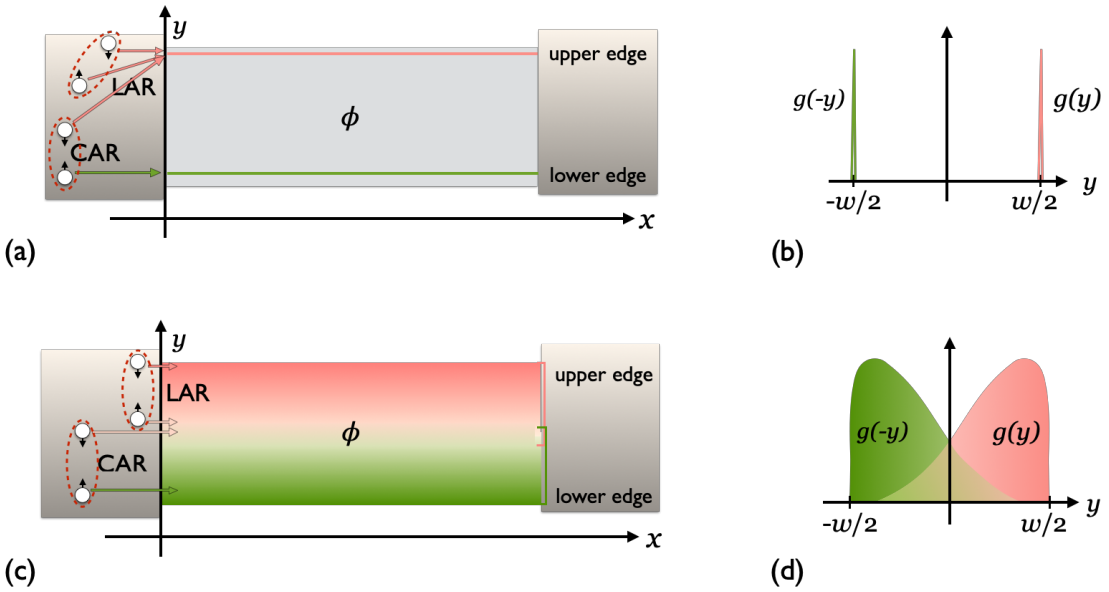

Figure 5.1: *(a) A topological Josephson junction with strongly localized edge states on the boundaries, marked in pink and green. Each boundary hosts two counter-propagating channels with identical profiles. For clarity of the picture, only one colored shape per boundary is shown. The electrons of a Cooper pair can be both injected into a same edge (LAR) or split over opposite edges (CAR), if the superconducting coherence length ξ is larger or comparable with the width of the junction. (b) The colored shapes represent the edges' profiles for the junction (a): $g(y)$ for the upper edge (pink) and $g(-y)$ for the lower edge (green). They are assumed to be symmetric around $y = 0$. (c) The same sample as (a) for the case of broadened edge states, which allow different trajectories for electrons injected in LAR and a wider range of possibilities for CAR. As an example, both panels (a) and (c) show LAR processes involving only the upper edge. (d) Edges' profiles $g(y)$ and $g(-y)$ as in (b), but for the junction (c), where they also overlap to some extent. Figure adapted from [189].*

piercing the junction.

In the simplest case, when Cooper pair splitting is forbidden or neglected, the gauge-invariant phase difference picked up by the two tied electrons reads as [179]

$$\varphi = (\theta_r - \theta_l) - \frac{2\pi}{\phi_0} \int \mathbf{A} \cdot d\mathbf{r}, \tag{5.1}$$

where $\theta_r(\theta_l)$ is the phase characterizing the right(left) superconductor, $\mathbf{A}$ is the vector potential, and the line integral has to be evaluated over the path of the Cooper pair from a side of the junction to the other. We are here assuming that the magnetic field is fully screened from the superconducting electrodes, see Subsec. 2.2.1. With the gauge choice $\mathbf{A} = -By\mathbf{e}_1$, and by considering horizontal (ballistic) paths labeled by y, with $-w/2 \leq y \leq w/2$, Eq. (5.1) becomes

$$\varphi(y) = (\theta_r - \theta_l) + \frac{2\pi\phi}{\phi_0} \frac{y}{w}. \tag{5.2}$$

The second addend in Eq. (5.2) represents the Aharonov-Bohm contribution, which for a single electron would read as $(\pi\phi/\phi_0)(y/w)$.

Following Dynes and Fulton prescription, the total supercurrent through the junction

is given by (see Eq. (2.54)),

$$I(\theta_r - \theta_l, \phi) = \int_{-w/2}^{w/2} J_c(y) \sin\left(\theta_r - \theta_l + \frac{2\pi\phi}{\phi_0}\frac{y}{w}\right) dy. \tag{5.3}$$

with $J_c(y)$ the critical supercurrent density. Maximizing with respect to $(\theta_r - \theta_l)$ and getting the absolute value, this returns the critical supercurrent as a function of the magnetic flux, or interference pattern, $I_c(\phi)$. In Chapter 2, we have presented two cases:

- If $J_c(y)$ is uniform, one obtains the Fraunhofer pattern,

  $$I_c(\phi)/I_c(0) = \left|\sin\left(\pi\phi/\phi_0\right)/(\pi\phi/\phi_0)\right|.$$

  More complicated settings, for instance including diagonal trajectories for Cooper pairs, have been addressed in the literature for different realizations of Josephson junctions [13, 85, 108, 158].

- If there is only edge transport, and the edge channels are assumed to be extremely narrow, then $J_c(y) = I_0[\delta(y + w/2) + \delta(y - w/2)]/2$, and one gets the SQUID pattern,

  $$I_c(\phi)/I_c(0) = \left|\cos\left(\pi\phi/\phi_0\right)\right|.$$

We are interested in this second situation, in particular in Josephson junctions having a two-dimensional topological insulator as a weak link. If $w \sim \xi$, a first step beyond Dynes and Fulton is the introduction of Cooper pair splitting over the narrow edges via CAR processes (Sec. 2.3). This is shown in Fig. 5.1(a). The Aharonov-Bohm phases acquired on opposite edges cancel with each other, resulting in a flux-independent process that modifies the SQUID pattern into the even-odd effect [16, 24, 42, 43, 78, 134], with a doubled periodicity of $2\phi_0$,

$$I_c(\phi)/I_c(0) = \left|\cos\left(\pi\phi/\phi_0\right) + f\right|.$$

The next Section is devoted to the case of two-dimensional systems with extended edge states. Different interference patterns depending on the extension of the edge states and on the width of the junction will be found.

5.2 From narrow to extended edge channels

We now move to the scenario depicted in Fig. 5.1(c). In the proximitized regions, the edge states are gapped out, while in the central part they have a spatial profile qualitatively sketched in Fig. 5.1(d). Each boundary hosts two counter-propagating channels with identical profile and opposite spin polarization, although for clarity a single colored shape per boundary is shown.

We first introduce two distinguished coordinates in Eq. (5.3) (one for each electron of the Cooper pair), $y_\uparrow$ and $y_\downarrow$:

$$\begin{aligned} I(\theta_r - \theta_l, \phi) &= \int_{-w/2}^{w/2} dy_\uparrow\, dy_\downarrow\, J_c(y_\uparrow, y_\downarrow) \sin\left(\theta_r - \theta_l + \frac{\pi\phi}{\phi_0}\frac{(y_\uparrow + y_\downarrow)}{w}\right) \\ &= \mathrm{Im}\left[e^{i(\theta_r - \theta_l)} \int_{-w/2}^{w/2} dy_\uparrow\, dy_\downarrow\, J_c(y_\uparrow, y_\downarrow) e^{i\frac{\pi\phi}{\phi_0}\frac{y_\uparrow}{w}} e^{i\frac{\pi\phi}{\phi_0}\frac{y_\downarrow}{w}}\right], \end{aligned} \tag{5.4}$$

Here $\uparrow$ / $\downarrow$ refers to the electron's spin projection, and we keep considering only horizontal trajectories. We also maintain the sinusoidal current-phase relation of the former approach, valid for low-transparency interfaces. The function $J_c(y_\uparrow, y_\downarrow)$, which weights how each specific path contributes to the total supercurrent, is a generalization of the critical supercurrent density and to enclose the main physical properties of the normal region. The main point is to comprise the possibility for a Cooper pair to split into different trajectories within a same edge, as far as they lie within a distance ξ. To this aim, an overall constraint function to take into account the Cooper pair's size should be included. Our ansatz is

$$J_c(y_\uparrow, y_\downarrow) = J_0 e^{-|y_\uparrow - y_\downarrow|/\xi}[\underbrace{s g(y_\uparrow)g(y_\downarrow) + s g(-y_\uparrow)g(-y_\downarrow)}_{LAR} + \underbrace{g(-y_\uparrow)g(y_\downarrow)}_{CAR}], \tag{5.5}$$

where J_0 has the dimensions of a current per unit length and $g(\pm y)$ will be connected to the spatial profile of the upper/lower edge states, which are assumed to be symmetric around $y = 0$ (see Fig. 5.1(d)). Each term is the product of a factor involving only $y_\uparrow$ and a factor involving only $y_\downarrow$. As marked in the Equation, the first two addends are identified as a generalization of LAR, into the upper or lower edge, to the case of extended edge states. The third term represents CAR. The parameter s is the ratio of the amplitudes of LAR and CAR. Indeed, owing to the helicity of the edge channels, LAR and CAR are clearly different processes: as we do not consider spin-flips here, in the LAR case, spin up and spin down electrons have opposite directions of propagation; on the contrary, in the CAR case, they are either right-movers or left-movers [78, 188]. In general, s might depend on temperature, applied bias, and length of the junction. Such dependence is not specified here, and it is rather treated as a phenomenological parameter to unbalance the presence of LAR and CAR.

Two unusual features are incorporated in Eqs. (5.4)-(5.5):

1. the electrons can tunnel into the same edge but at different positions;
2. the electrons can tunnel into different edges acquiring Aharonov-Bohm phases that do not cancel each other out. This implies the unconventional possibility of flux-dependent CAR processes.

The part within square brackets has the flavor of a probability density. We argue that $g(y) \equiv |\psi_u(y)| = |\psi_l(-y)|$, where $\psi_{u/l}(y)$ is the wavefunction of the upper/lower edge state.

We can check two limiting cases of the last two Equations:

- For $\xi \ll w$, we should recover Dynes and Fulton. In the constraint function $e^{-|y_\uparrow - y_\downarrow|/\xi} = e^{-\frac{|y_\uparrow - y_\downarrow|}{w}\frac{w}{\xi}}$, the first fraction necessarily takes values between 0 and 1. Therefore $e^{-|y_\uparrow - y_\downarrow|/\xi} \xrightarrow{\xi \ll w} 0$, and the supercurrent density vanishes unless $y_\uparrow = y_\downarrow \equiv y$. The Cooper pairs' electrons are labeled by a same coordinate back again[1]. Moreover, if the edge states' extent is $\lesssim \xi \ll w$, they do not overlap and in the CAR term $g(-y)g(y) = |\psi_l(y)||\psi_u(y)| = 0$. Concerning LAR, from Dynes and Fulton we should get

$$J_c(y) = I_0(|\psi_u(y)|^2 + |\psi_l(y)|^2), \tag{5.6}$$

[1] More precisely, $e^{-|y_\uparrow - y_\downarrow|/\xi} \xrightarrow{\xi \ll w} 2\xi\delta(y_\uparrow - y_\downarrow)$.

and indeed (apart from the factor s) our supercurrent becomes

$$I(\theta_r - \theta_l, \phi) = 2\xi J_0 \mathrm{Im}\left[e^{i(\theta_r - \theta_l)} \int_{-w/2}^{w/2} dy \, \left(|\psi_u(y)|^2 + |\psi_l(y)|^2 \right) e^{i \frac{2\pi\phi}{\phi_0} \frac{y}{w}} \right], \quad (5.7)$$

where we can identify $2\xi J_0 \equiv I_0$. By specifying $|\psi_{u/l}(y)| \propto \delta(y \mp w/2)$, it leads to a SQUID interference pattern.

- On the contrary, if $\xi \gg w$, then $e^{-|y_\uparrow - y_\downarrow|/\xi} \overset{\xi \gg w}{\longrightarrow} 1$, and the integrals over $y_\uparrow$ and $y_\downarrow$ in Eq. (5.4) factorize, unsurprisingly corresponding to completely independent trajectories for the two electrons.

For what concerns CAR, if the conduction can only happen on narrow edges $|\psi_{u/l}(y)| \propto \delta(y \mp w/2)$ (such as in the upper panel of Fig. 5.1(a)), this results in a flux-independent contribution to the critical current, as expected.

In the next Section, we focus on the interference pattern arising from differently extended edges and for different values of ξ, s. In particular, we aim at identifying a parameter regime in which the interference pattern is $2\phi_0$-periodic. Indeed, as the doubled periodicity is a widely studied signature, it is interesting to investigate new mechanisms that can give rise to it. Moreover, it has been previously discussed that it usually emerges in the presence of Cooper pair splitting, which is a cornerstone in our description of broadened edge states. We therefore expect it to arise also in our system. In particular, we find that this unusual periodicity in our model corresponds to a markedly non-local transport regime, when the edge states are highly broadened and CAR are the dominating processes. To move in this direction, we inspect the CAR-dominated regime, and set $s < 1$ from now on[2]. This circumstance has been experimentally observed. In Ref. [42], an InSb Josephson junction is analyzed, and CAR processes turn out to be larger than expected and to even exceed the LAR ones[3]. It would be interesting to pinpoint rather general conditions under which CAR processes are more important than LAR processes, but this open issue is beyond the scope of the present discussion.

5.3 Results

We draw the attention to the interference pattern of the junction, to discuss the role of the edges' profile $g(y)$ and of the two parameters ξ and s. From Eq. (5.4), the pattern reads as[4]

$$I_c(\phi) = \left| \int_{-w/2}^{w/2} dy_\uparrow \, dy_\downarrow \, J_c(y_\uparrow, y_\downarrow) e^{i \frac{\pi\phi}{\phi_0} \frac{y_\uparrow}{w}} e^{i \frac{\pi\phi}{\phi_0} \frac{y_\downarrow}{w}} \right|, \quad (5.8)$$

with $J_c(y_\uparrow, y_\downarrow)$ from Eq. (5.5).

[2] A second CAR contribution should be proportional to s^2. Since $s < 1$, it will be neglected, and only the first order in s will be included.

[3] The authors measured an entirely $2\phi_0$-periodic pattern, in combination with an enhanced conduction at both edges. We know from Chapter 2 that a $2\phi_0$ periodicity can result from the flux-independent supercurrent due to CAR interfering with the standard ϕ_0-periodic SQUID current. If LAR dominates over CAR, a ϕ_0 oscillation should be simultaneously present, otherwise the CAR amplitude must be larger than the LAR one.

[4] We recall that the interference pattern is obtained as the maximum supercurrent with respect to the difference $(\theta_r - \theta_l)$, taken in absolute value.

As we commented in Chapter 2, any extended supercurrent density profile leads to decaying patterns. We obtain also here a fast side lobe decay. Reminescent of the even-odd pattern, which is $2\phi_0$-periodic, in the non-local transport regime our model features an interference pattern approaching a $2\phi_0$-periodicity. This is shown in Fig. 5.2.

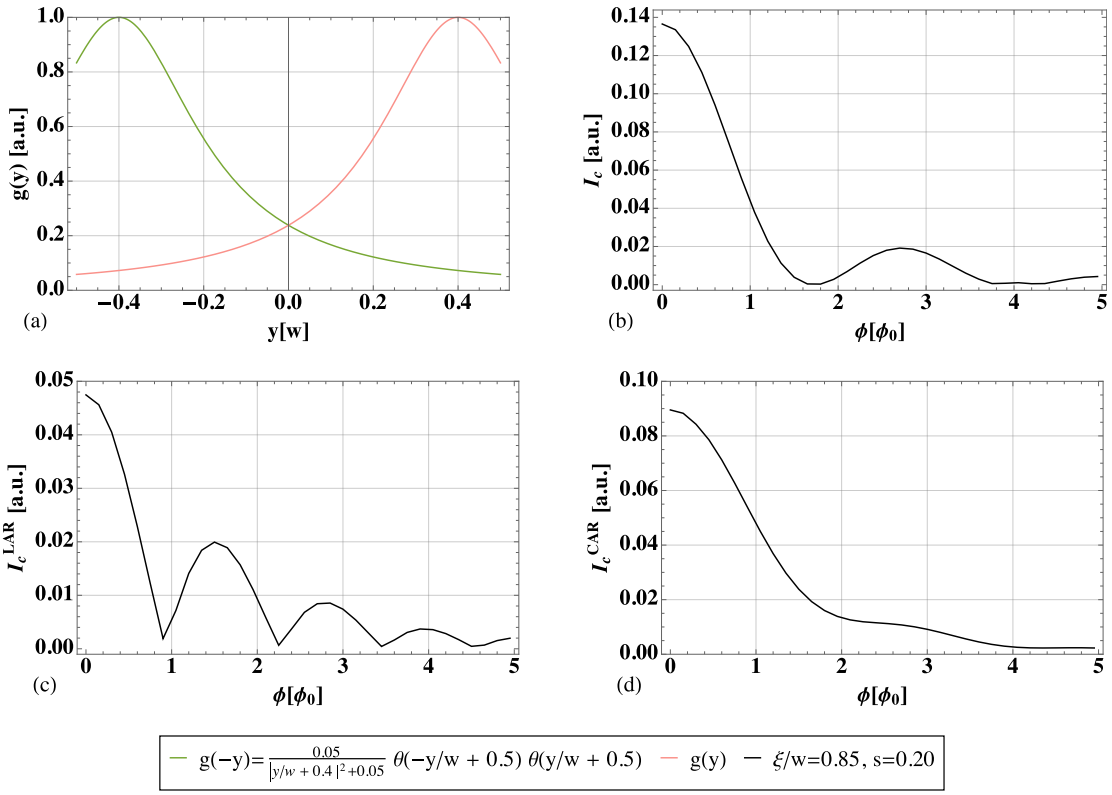

Figure 5.2: *Resultant interference pattern $I_c(\phi)$ (panel (b)) and the separated contributions of LAR (panel (c)) and CAR (panel (d)) for the edge's profiles shown in panel (a), with $\xi/w = 0.85$ and $s = 0.2$. All plots are in arbitrary units. Figure from [189].*

The edge profile is visible in panel (a), and we set $\xi/w = 0.85$ and $s = 0.2$. Panel (b) is the total interference pattern. As anticipated, it is fastly decaying and its minima approach multiples of $2\phi_0$. Panels (c) and (d) isolate the LAR and the CAR term ($s = 0$), respectively, to pinpoint the interplay of the two contributions. The LAR pattern on its own, despite Cooper pair splitting is strongly favored by the large ratio ξ/w, shares similarities with a standard Fraunhofer pattern, although a shift of the minima away from ϕ_0 multiples is visible. On the other hand, CAR processes exhibit a pronounced decay with only a mild $2\phi_0$ modulation on top. In panel (b), the $2\phi_0$ oscillation arise from the interaction of these two terms. The minima in the odd multiples of ϕ_0, $\phi = \phi_0, 3\phi_0, 5\phi_0$, are not present. Fig. 5.3 covers a larger interval for the same plot, showing that this trend persists. While $\phi \approx 2\phi_0$ hosts a minimum, for $\phi = 4\phi_0, 6\phi_0, 8\phi_0$ very lowered bumps, reminiscent of the peak structure of the LAR contribution, are still visible. This is indeed dominant over the CAR one for large values of ϕ, due to its slower decay.

Fig. 5.4 shows the interference pattern obtained for different values of coherence length, a more or less prevalent role played by LAR and CAR (represented by the parameter s), and different spatial profiles for the edge states. In particular, we consider

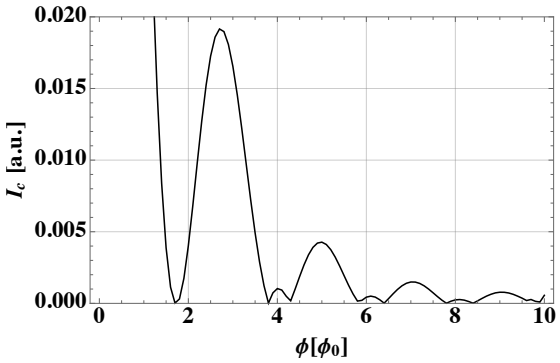

Figure 5.3: *Resultant interference pattern $I_c(\phi)$ in Fig. 5.2b for a larger interval for the magnetic flux. Figure from [189].*

two different edge states' shapes for the plots in panels (b) and (d).
For panel (b), we assume the shape in panel (a), the same as Fig. 5.2,

$$g(-y) = \frac{0.05}{|y/w + 0.4|^2 + 0.05}\theta(-y/w + 0.5)\theta(y/w + 0.5). \tag{5.9}$$

For panel (d), we assume the shape in panel (c),

$$g(-y) = e^{-(y/w-0.45)^2/(2*0.2^2)}\theta(-y/w + 0.5)\theta(y/w + 0.5), \tag{5.10}$$

but fine details about the functional form describing the edge profile are not crucial. Both functions are peaked at the opposite ends of the junction, around $y = \pm w/2$, but have a different overlap. The full interference pattern, arising from both LAR and CAR, is plotted for different combinations of ξ/w and s (see the plot legend). From the patterns obtained, we see that the finite extension of the edge states leads to a pattern with a main central lobe and decaying side lobes. Moreover, if CARs are dominant and the edge states overlap, the resulting periodicity approaches $2\phi_0$. In the next Section we discuss the various cases in more detail.

5.4 Discussion and conclusions

In Fig. 5.4(b), the orange curve is the one presented in Fig. 5.2(b), with a high coherence length ($\xi/w = 0.85$) and the prominent presence of CAR ($s = 0.2$), featuring a minima periodicity approaching $2\phi_0$. We use it now as a reference plot. For the black curve, CAR is almost missing ($s = 0.7$). Owing to $\xi/w \ll 1$, this situation can be captured by Dynes and Fulton description applied to a supercurrent density $\propto g(y)^2 + g(-y)^2$. If s is decreased, LAR is also suppressed, and the entire pattern is lowered. Increasing the coherence length, the possibility of a non-local propagation of the two electrons is increased, although not sufficiently to get a clearly visible $2\phi_0$-periodicity. A LAR-dominated scenario (a weak suppression $s \sim 1$), despite high coherence lengths, still leads to Fraunhofer-like behavior with more minima and a slower decay (light blue curve, with $\xi/w = 0.85$ and $s = 0.7$).

Panel (d) is associated to edge states with a smaller overlap. Tuning the parameters as in the black and light blue curves, gives a result similar to panel (b). This had to be the case, because we are not in the appropriate parameter regime to appreciate non-local

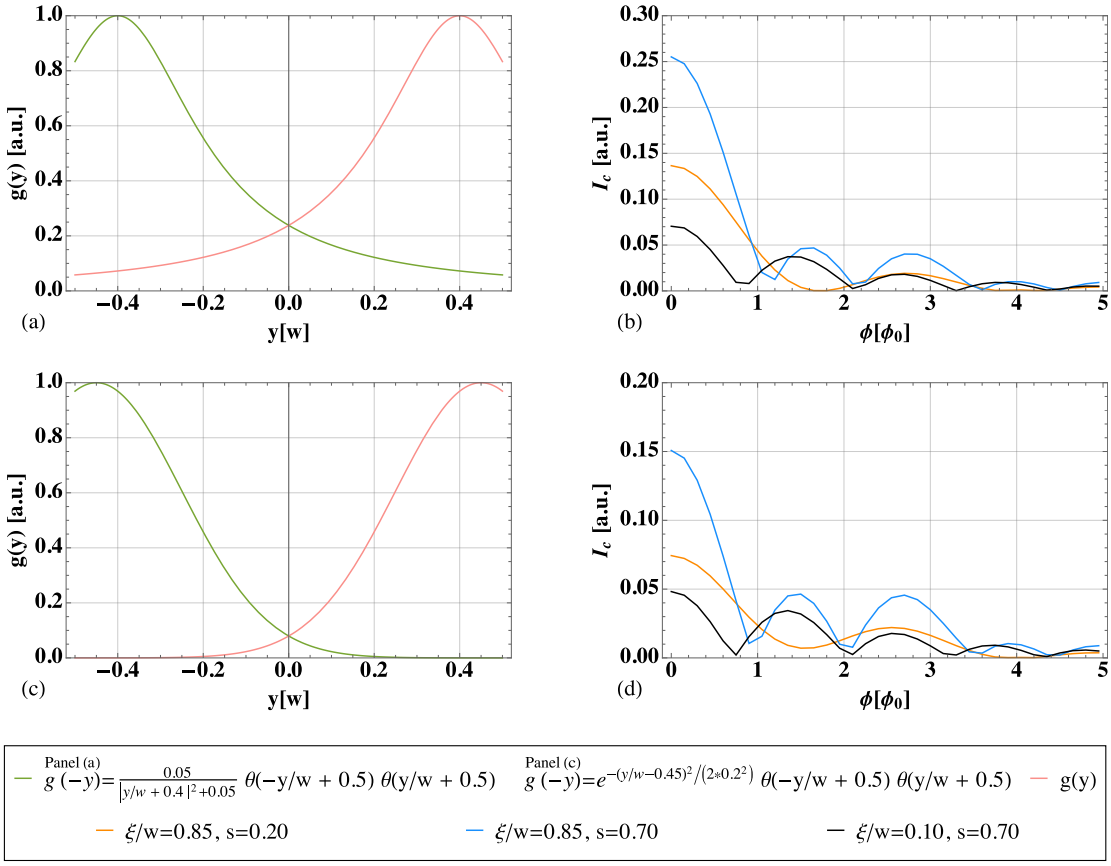

Figure 5.4: *Panels (a), (c) show two possible profiles $g(y)$ and $g(-y)$ for the edge states. Panels (b), (d), are the corresponding interference patterns, arising from both LAR and CAR. Different colors are associated to different values of ξ and s, see the plot legend. Figure from [189].*

transport significantly, hence the different shape doesn't produce striking differences. However, choosing both parameters to favor non-local transport (orange curve, with $\xi/w = 0.85$ and $s = 0.2$), the periodicity starts to approach $2\phi_0$, with weak minima. This shows the need for highly extended states as in (a) to better see the $2\phi_0$-periodicity. To summarize, to this aim:

1. A high coherence length ξ ($\xi \gtrsim w$) is necessary because short values of ξ/w suppress the occurrence of CAR. This first requirement depends on the choice of the superconductors and on the sample width, and it is not hard to fulfill.

2. Second, the ratio s has to be low (at least $s < 1/2$), which means that CAR dominate over LAR.

3. Lastly, a significant overlap of the edge states is needed. If the edge states do not overlap, there start to emerge features expected for perfectly localized edges: a SQUID-like pattern with the additional even-odd effect, which is $2\phi_0$-periodic but not decaying. See Fig. 5.5.

To sum up, in this Chapter we have described a way to compute the supercurrent – and the interference pattern – of a Josephson junction with spatially extended edge states. We argued that, as a consequence of their spatial extension, the edge states can

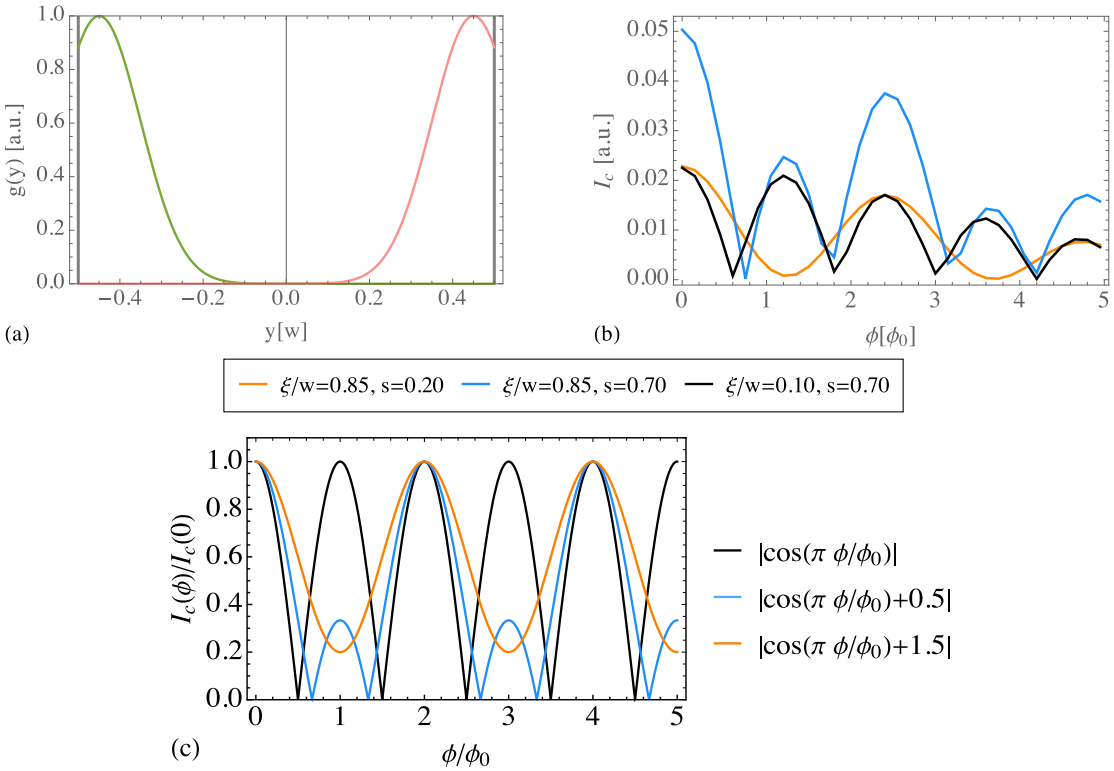

Figure 5.5: *Interference pattern (b) obtained with our approach applied to the more localized and non-overlapping edge states in (a), with* $g(-y) = e^{-(y/w-0.45)^2/(2*0.1^2)}\theta(-y/w+0.5)\theta(y/w+0.5)$. *The parameters are specified in the plot legend. There start to emerge features expected for perfectly localized edges. For comparison with (b), panel (c) shows patterns associated to perfectly localized edge states: a SQUID pattern (black), an even-odd pattern with prevalence of LAR (light blue), an even-odd pattern with prevalence of CAR (orange).*

host different trajectories for the two electrons. Our approach, although not technically demanding, maintains the straightforward and informative nature of the Dynes and Fulton's one. At the same time, it fills one of its main gaps, that is the assumption that both electrons within a Cooper pair follow the same path. Our generalization allows to take into account also CAR processes. Some limiting cases have been discussed, showing that the new approach correctly captures the already studied regimes. The Dynes and Fulton hypothesis of sinusoidal current-phase relation, which holds in the tunneling regime between the superconductors and the middle region, has been maintained. A further assumption we made is that the two edge states have a symmetric profile. On the other hand, their specific functional form is not crucial.

While strongly localized edge states give rise to a pattern with no decay and a period ϕ_0 or $2\phi_0$, including a finite extent of the edge states in the model gives rise to wider possibilities. We particularly focused on the role played by LAR and CAR processes in determining the interference pattern, together with the edge states' broadening and the superconducting coherence length. The periodicity of the resulting pattern can vary from ϕ_0 to $2\phi_0$, depending on the dominating process. In particular, we find that the doubled periodicity goes together with non-local transport, when the two electrons within a pair can separately explore the two edges and the latter are widely broadened through the junction.

This work can help in developing a more realistic description of experimentally realized systems, and opens up further generalizations and refinements. Among these, a justification at the microscopic level of the phenomenological parameters would be an interesting follow-up.

Conclusions and perspectives

In this Thesis we have considered Josephson junctions where the non-superconducting part is respresented by a Quantum Spin Hall system. In particular, we have addressed experimentally relevant features of this setup which were still lacking a theoretical description. The common thread has been the investigation of phenomena having lengthscales comparable or less than the superconducting coherence length ξ, such that Cooper pair splitting, in different ways, plays a key role. Our attention was drawn to three main aspects. First, in **Chapter 3**, we have analyzed the effects on the interference pattern of inter-edge tunneling within a Quantum Spin Hall constriction. Second, in **Chapter 4**, the occurrence of edge reconstruction was discussed, together with its impact on the current-phase relation of the junction. Lastly, in **Chapter 5**, we have considered the role of the spatial distribution of the edge states instead of considering them as perfectly localized. In what follows we summarize in more details each of the raised problems.
Although we suggested that nanostructures exploiting constrictions between helical edges are entitled to a huge variety of functionalities, their potential is by far not exhausted with the results of this Thesis. At the end of each bullet below, we mention examples of open problems which might be the subject of further studies.

- **Summary and outlook of Chapter 3**

  In this Chapter we established a model to describe a Josephson junction realized by a helical constriction between superconducting leads, and addressed its properties in the presence of a magnetic field and an external bias, as well as tunneling events between the two edges of the topological insulator occurring in the narrow region, located halfway along the junction. The object of our analysis was the functional dependence of the critical current on the magnetic field via the interference pattern.

  We showed that the interference pattern corresponds to an unusual $4\phi_0$-periodic SQUID-like interference pattern ($\phi_0 = h/2e$) – which in the absence of inter-edge tunneling is only $2\phi_0$-periodic – persisting in a wide range of parameters. This robustness makes it a convenient tool to test our theoretical model for a superconducting quantum point contact in experiments. The physical explanation

we proposed resides in the fact that the dominant effect induced by the tunneling involves a single electron within the Cooper pair, with elemental charge e and not $2e$ as for the pair. This effectively doubles the relevant flux quantum, resulting in a new Aharonov-Bohm phase $\gamma^{AB} = \pm\pi\phi/\mathbf{2}\phi_0$. We argued that, more generally, whenever in a constriction there is the possibility to switch from a Cooper pair living on one side to a Cooper pair split over both sides, anomalous periodicities can emerge. Also, the system allows for an unusual interplay of Local and Crossed Andreev Reflection for the transmission of a same Cooper pair.

This work opens up to interesting follow-ups. First, the generalization of the results to extended inter-edge tunneling, uniformly present in the junction and not confined to a small subregion. In this case, the computation of the gauge-invariant phases requires closer attention, and it is interesting to determine the resultant period of the interference pattern. The outcome would be the characterization of a complex though experimentally relevant setup. Our preliminary results show an interference pattern more similar to a Fraunhofer pattern than a SQUID pattern, with traces of a doubled minima periodicity compared to the standard Fraunhofer pattern, just as a doubled periodicity compared to the standard SQUID pattern emerged in [188]. Afterwards, it would be meaningful to inspect the AC-driven behavior of the system, to test whether the anomalous periodicities can also show up in the Shapiro step structure. This evaluation will be crucial when the formation of Majorana fermions in the structure will be assessed.

- **Summary and outlook of Chapter 4**

  Elaborating over the previous results, in this Chapter we analyzed the consequences of the edge reconstruction, which is a spatial separation arising between the two channels on each edge. If the potential confining the edge states is smooth, this might happen as a result of electron-electron interactions, which make such rearrangement electrostatically convenient. The edge reconstruction has been implemented in our theoretical model through an unbalance between the different inter-edge tunneling amplitudes at play. Interestingly, this breaks both time-reversal symmetry and inversion symmetry, allowing for two connected and promising behaviors: the φ_0 Josephson effect and the superconducting diode effect. The first consists in the presence of a finite Josephson current – called "anomalous Josephson current" – in the absence of a phase difference between the two superconductors, and has recently been experimentally observed. It is attractive because it can be exploited to design phase batteries, and to drive superconducting circuits and superconducting memories. The second, experimentally observed as well, inspires great perspectives given the analogy to its semiconducting counterpart, that laid the foundation for modern electronics.

  Whereas the breaking of inversion symmetry can be provided by the geometry of the nanostructure or by the microscopic lattice, the breaking of time-reversal symmetry is often driven externally by means of applied magnetic fields. Notably, for our reconstructed edge system, no external magnetic field is needed.

  We analytically showed that, unexpectedly at first, the anomalous effect is reinforced by a temperature increase in a range of parameters. The peculiar temperature dependence has been substantiated by a simple argument based on Fermi's

golden rule approach, and attributed to the thermal activation of the inter-edge tunneling processes in the constriction. For this reason, it represents a clear trademark of the constriction.

Our results open the way to design phase batteries, remarkably in the absence of external magnetic fields, and make it possible to envision the direct integration of the φ_0 junction we considered with other functional nanostructures built on a same Quantum Spin Hall sample. Lastly, going beyond the tunneling regime (namely, the hypothesis of opaque interfaces between the superconductors and their link), we expect the reconstructed system to realize a superconducting diode, which would deserve a full characterization.

- **Summary and outlook of Chapter 5**

  This Chapter was devoted to the role of the spatial extent of the edges' wavefunctions on transport through the junction. While the edge states are usually modeled as strongly localized, we inspected the uncharted situation where they are broadened through the junction over appreciable lengthscales for Cooper pairs, or even overlap with each other.

  In this cases, since the two electrons of a Cooper pair can propagate and explore the junction independently over lengthscales comparable to ξ, the number of paths they can follow remarkably increases, both via Local Andreev Reflection (the injection of both into a same edge) and via Crossed Andreev Reflection (their splitting over opposite edges). If the junction is pierced by a magnetic flux, this gives rise to wider possibilities for the Aharonov-Bohm phases they acquire. The maximal current as a function of the magnetic flux, which results from the interference of all these paths, becomes rapidly decaying and can exhibit different periods in terms of the superconducting flux quantum $\phi_0 = h/2e$. Both features are absent in the case of localized states.

  We suggested a way of describing this phenomenology, generalizing the long-lasting Dynes and Fulton approach, and addressed the question whether Crossed Andreev Reflection processes can bring along interference oscillations with a periodicity $2\phi_0$ as in the case of Crossed Andreev Reflection for localized edge states. We found that the answer is affirmative and identified the best regime to observe such periodicity, finding that it requires a prevalence of Crossed over Local Andreev Reflection.

  Our main findings are the derivation of an expression that allows for the computation of supercurrents in the experimentally relevant scenario of topological Josephson junctions featuring edge states with finite spatial extent, and the introduction of a new way of taking into account the non-local character of Cooper pairs.

  This proposal can help in developing a more realistic description of experimentally realized systems and opens up further generalizations and refinements, first of all a justification at a microscopic level of the phenomenological parameters involved.

APPENDIX $\mathcal{A}$

Complements to Chapter 2

A.1 Details on the calculation of Eq. (2.84)

This Section contains all the missing calculations in the current computation of Sec. 2.3 to reach Eq. (2.84). Let us restart from Eq. (2.81), where it has already been selected the relevant perturbation $-j$,

$$I^j(t) \approx \frac{i}{\hbar}\int_{-\infty}^{t} d\tau \left\langle \left[\delta H_E^{-j}(\tau), I^j(t)\right]\right\rangle_E . \tag{A.1}$$

Let us define $A(j,t) = \Gamma^j_{\zeta,\zeta'}(t)\psi_\zeta(x_j^-,t)\psi_{\zeta'}(x_j^+,t)$ as in [78]. Then

$$\begin{aligned} I^j(t) =& \frac{i}{\hbar}\int_{-\infty}^{t} d\tau \sum_{\zeta,\zeta'} \left\langle \left[A(-j,\tau)+A^\dagger(-j,\tau), \frac{2ie}{\hbar}(A(j,t)-A^\dagger(j,t))\right]\right\rangle_E \\ =& \frac{-2e}{\hbar^2}\sum_{\zeta,\zeta'}\int_{-\infty}^{t} d\tau \left\langle \left[A(-j,\tau)+A^\dagger(-j,\tau), A(j,t)-A^\dagger(j,t)\right]\right\rangle_E . \end{aligned} \tag{A.2}$$

The average value can be rewritten as

$$\begin{aligned} &\left\langle \left[A(-j,\tau)+A^\dagger(-j,\tau), A(j,t)-A^\dagger(j,t)\right]\right\rangle_E \\ =& \left\langle [A(-j,\tau),A(j,t)] - \left[A(-j,\tau),A^\dagger(j,t)\right] + \left[A^\dagger(-j,\tau),A(j,t)\right] - \left[A^\dagger(-j,\tau),A^\dagger(j,t)\right]\right\rangle_E \\ =& \left\langle [A(-j,\tau),A(j,t)] + \left[A^\dagger(-j,\tau),A(j,t)\right]^\dagger + \left[A^\dagger(-j,\tau),A(j,t)\right] + [A(-j,\tau),A(j,t)]^\dagger\right\rangle_E \\ =& 2\left\langle \mathrm{Re}\,[A(-j,\tau),A(j,t)] + \mathrm{Re}\left[A^\dagger(-j,\tau),A(j,t)\right]\right\rangle_E . \end{aligned} \tag{A.3}$$

The first term mediated on the unperturbed edge system returns zero, since it is not particle number conserving. Substituting in the above expression,

$$I^j(t) = \frac{4e}{\hbar^2}\sum_{\zeta,\zeta'}\int_{-\infty}^{t} d\tau \mathrm{Re}\left\langle\left[A(j,t), A^\dagger(-j,\tau)\right]\right\rangle_E . \tag{A.4}$$

By making the change of variable $t' = t - \tau$,

$$\begin{aligned}
I^j(t) &= \frac{4e}{\hbar^2}\mathrm{Re}\left\{\sum_{\zeta,\zeta'}\int_0^{+\infty} dt' \left\langle\left[A(j,t), A^\dagger(-j,t-t')\right]\right\rangle_E\right\} \\
&= \frac{4e}{\hbar^2}\mathrm{Re}\left\{\sum_{\zeta,\zeta'}\int_{-\infty}^{+\infty} dt'\theta(t') \left\langle\left[A(j,t), A^\dagger(-j,t-t')\right]\right\rangle_E\right\} \\
&= \frac{4e}{\hbar^2}\mathrm{Re}\left\{\sum_{\zeta,\zeta'}\int_{-\infty}^{+\infty} dt'\theta(t')\Gamma^j_{\zeta,\zeta'}(t)(\Gamma^{-j}_{\zeta,\zeta'}(t-t'))^* \right. \\
&\qquad \left.\left\langle\left[\psi_\zeta(x_j^-,t)\psi_{\zeta'}(x_j^+,t), \psi^\dagger_{\zeta'}(x^+_{-j},t-t')\psi^\dagger_\zeta(x^-_{-j},t-t')\right]\right\rangle_E\right\} \\
&= \frac{4e}{\hbar^2}\mathrm{Re}\left\{\sum_{\zeta,\zeta'}\int_{-\infty}^{+\infty} dt'\theta(t')\Gamma^j_{\zeta,\zeta'}(t)(\Gamma^{-j}_{\zeta,\zeta'}(t-t'))^* \right. \\
&\qquad \left.\left\langle\left[\psi_\zeta(x_j^-,t')\psi_{\zeta'}(x_j^+,t'), \psi^\dagger_{\zeta'}(x^+_{-j},0)\psi^\dagger_\zeta(x^-_{-j},0)\right]\right\rangle_E\right\},
\end{aligned} \tag{A.5}$$

where in the last step we made a translation in time of the fermionic operator leveraging the time-translation invariance of the unperturbed edge system. Notice that, in principle, there should be two sums over ζ, ζ' and ζ'', ζ'''. However, since these sums are ordered, the only non-zero average value corresponds to $\zeta'', \zeta''' = \zeta, \zeta'$. The prefactor is

$$\begin{aligned}
&\Gamma^j_{\zeta,\zeta'}(t)(\Gamma^{-j}_{\zeta,\zeta'}(t-t'))^* \\
=&\Gamma^2(\tilde{f}_T)^{2\delta_{\rho\tau,\rho'\tau'}}(f_C)^{2\delta_{\tau,-\tau'}} e^{\frac{ij}{2}\left[k_F L(\rho+\rho')-\omega_J t-\varphi_0-\frac{\pi\phi}{2\phi_0}(\tau+\tau')\right]} e^{\frac{ij}{2}\left[k_F L(\rho+\rho')-\omega_J (t-t')-\varphi_0-\frac{\pi\phi}{2\phi_0}(\tau+\tau')\right]} \\
=&\Gamma^2(\tilde{f}_T)^{2\delta_{\rho\tau,\rho'\tau'}}(f_C)^{2\delta_{\tau,-\tau'}} e^{ij\left[k_F L(\rho+\rho')-\frac{\pi\phi}{2\phi_0}(\tau+\tau')\right]} e^{-ij(\omega_J t+\varphi_0)} e^{ij\frac{\omega_J t'}{2}} \\
\equiv&\Gamma^2 f_{\zeta,\zeta'} e^{-ij(\omega_J t+\varphi_0)} e^{ij\frac{\omega_J t'}{2}}.
\end{aligned} \tag{A.6}$$

Plugging it into Eq. (A.5), we get

$$\begin{aligned}
I^j(t) = \frac{4e\Gamma^2}{\hbar^2}\mathrm{Re}\left\{ e^{-ij(\omega_J t+\varphi_0)}\sum_{\zeta,\zeta'} f_{\zeta,\zeta'}\int_{-\infty}^{+\infty} dt'\theta(t')\, e^{ij\frac{eVt'}{\hbar}} \right. \\
\left.\left\langle\left[\psi_\zeta(x_j^-,t')\psi_{\zeta'}(x_j^+,t'), \psi^\dagger_{\zeta'}(x^+_{-j},0)\psi^\dagger_\zeta(x^-_{-j},0)\right]\right\rangle_E\right\},
\end{aligned} \tag{A.7}$$

where we used $\omega_J = 2eV/\hbar$. The next step is to compute the average value. It can be shown that

$$\begin{aligned}
&\theta(t')\left\langle\left[\psi_\zeta(x_j^-,t')\psi_{\zeta'}(x_j^+,t'), \psi^\dagger_{\zeta'}(x^+_{-j},0)\psi^\dagger_\zeta(x^-_{-j},0)\right]\right\rangle_E \\
=&-2i\theta(t')\mathrm{Im}\left\langle\mathcal{T}\psi_\zeta(x_j^-,t')\psi_{\zeta'}(x_j^+,t')\psi^\dagger_{\zeta'}(x^+_{-j},0)\psi^\dagger_\zeta(x^-_{-j},0)\right\rangle_E,
\end{aligned} \tag{A.8}$$

which is a time-ordered correlation function. Due to the former presence of $\theta(t')$, we have $t' > 0$ and

$$\begin{aligned}&\left\langle \mathcal{T}\psi_\zeta(x_j^-,t')\psi_{\zeta'}(x_j^+,t')\psi^\dagger_{\zeta'}(x^+_{-j},0)\psi^\dagger_\zeta(x^-_{-j},0)\right\rangle_E\\ =&\left\langle \psi_\zeta(x_j^-,t')\psi_{\zeta'}(x_j^+,t')\psi^\dagger_{\zeta'}(x^+_{-j},0)\psi^\dagger_\zeta(x^-_{-j},0)\right\rangle_E.\end{aligned} \tag{A.9}$$

Thanks to the spatial translation invariance of the infinite edges, we can move to momentum space by Fourier transforming

$$\psi_\zeta(x,t)=\frac{1}{\sqrt{L}}\sum_k e^{ik(x-\rho v_F t)}c_{k,\zeta},\qquad \psi^\dagger_\zeta(x,t)=\frac{1}{\sqrt{L}}\sum_k e^{-ik(x-\rho v_F t)}c^\dagger_{k,\zeta}, \tag{A.10}$$

whence

$$\begin{aligned}&\left\langle \psi_\zeta(x_j^-,t')\psi_{\zeta'}(x_j^+,t')\psi^\dagger_{\zeta'}(x^+_{-j},0)\psi^\dagger_\zeta(x^-_{-j},0)\right\rangle_E\\ =&\frac{1}{L^2}\left\langle \sum_{k=-\infty}^{+\infty} e^{ik(x_j^--\rho v_F t')}c_{k,\zeta}\sum_{k'=-\infty}^{+\infty} e^{ik'(x_j^+-\rho' v_F t')}c_{k',\zeta'}\sum_{k''=-\infty}^{+\infty} e^{-ik''x^+_{-j}}c^\dagger_{k'',\zeta'}\sum_{k'''=-\infty}^{+\infty} e^{-ik'''x^-_{-j}}c^\dagger_{k''',\zeta}\right\rangle_E\\ =&\frac{1}{L^2}\sum_{k,k',k'',k'''=-\infty}^{+\infty} e^{ik(x_j^--\rho v_F t')}e^{ik'(x_j^+-\rho' v_F t')}e^{-ik''x^+_{-j}}e^{-ik'''x^-_{-j}}\left\langle c_{k,\zeta}c_{k',\zeta'}c^\dagger_{k'',\zeta'}c^\dagger_{k''',\zeta}\right\rangle_E.\end{aligned} \tag{A.11}$$

with

$$\{c_{k,\zeta},c_{k',\zeta'}\}=\{c^\dagger_{k,\zeta},c^\dagger_{k',\zeta'}\}=0,\qquad \{c_{k,\zeta},c^\dagger_{k',\zeta'}\}=\delta_{\zeta,\zeta'}\delta_{k,k'}. \tag{A.12}$$

Making use of Wick's theorem

$$\begin{aligned}&\left\langle \psi_\zeta(x_j^-,t')\psi_{\zeta'}(x_j^+,t')\psi^\dagger_{\zeta'}(x^+_{-j},0)\psi^\dagger_\zeta(x^-_{-j},0)\right\rangle_E\\ =&\frac{1}{L^2}\sum_{k,k',k'',k'''=-\infty}^{+\infty} e^{ik(x_j^--\rho v_F t')}e^{ik'(x_j^+-\rho' v_F t')}e^{-ik''x^+_{-j}}e^{-ik'''x^-_{-j}}\\ &-\left\langle c_{k,\zeta}c^\dagger_{k'',\zeta'}\right\rangle_E\left\langle c_{k',\zeta'}c^\dagger_{k''',\zeta}\right\rangle_E+\left\langle c_{k,\zeta}c^\dagger_{k''',\zeta}\right\rangle_E\left\langle c_{k',\zeta'}c^\dagger_{k'',\zeta'}\right\rangle_E.\end{aligned} \tag{A.13}$$

Recalling that

$$\left\langle c^\dagger_{k,\zeta}c_{k',\zeta'}\right\rangle_E=\delta_{\zeta,\zeta'}\delta_{k,k'}f_k,\quad f_k=\frac{1}{1+e^{\beta\hbar v_F k\rho}},\quad \beta=\frac{1}{k_BT}, \tag{A.14}$$

we have

$$\begin{aligned}
&\left\langle \psi_\zeta(x_j^-,t')\psi_{\zeta'}(x_j^+,t')\psi^\dagger_{\zeta'}(x^+_{-j},0)\psi^\dagger_\zeta(x^-_{-j},0)\right\rangle_E \\
=&\frac{1}{L^2}\sum_{k,k',k'',k'''=-\infty}^{+\infty}\Big\{e^{ik(x_j^- -\rho v_F t')}e^{ik'(x_j^+-\rho' v_F t')}e^{-ik'' x^+_{-j}}e^{-ik''' x^-_{-j}} \\
&-(1-f_k)(1-f_{k'})\delta_{k,k''}\delta_{\zeta,\zeta'}\delta_{k',k'''}+(1-f_k)(1-f_{k'})\delta_{k,k'''}\delta_{k',k''}\Big\} \\
=&\frac{1}{L^2}\Big\{-\sum_k(1-f_k)e^{ik(x_j^- -\rho v_F t'-x^+_{-j})}\sum_{k'}(1-f_{k'})e^{ik'(x_j^+-\rho v_F t'-x^-_{-j})}\delta_{\zeta,\zeta'} \\
&+\sum_k(1-f_k)e^{ik(x_j^- -\rho v_F t'-x^-_{-j})}\sum_{k'}(1-f_{k'})e^{ik'(x_j^+-\rho' v_F t'-x^+_{-j})}\Big\}. \qquad \text{(A.15)}
\end{aligned}$$

Moving to integrals,

$$\begin{aligned}
&\left\langle \psi_\zeta(x_j^-,t')\psi_{\zeta'}(x_j^+,t')\psi^\dagger_{\zeta'}(x^+_{-j},0)\psi^\dagger_\zeta(x^-_{-j},0)\right\rangle_E \\
=&\frac{1}{(2\pi)^2}\Big\{-\int_{-\infty}^{+\infty}dk\,(1-f_k)e^{ik(x_j^- -\rho v_F t'-x^+_{-j})}\int_{-\infty}^{+\infty}dk'\,(1-f_{k'})e^{ik'(x_j^+-\rho v_F t'-x^-_{-j})}\delta_{\zeta,\zeta'} \\
&+\int_{-\infty}^{+\infty}dk\,(1-f_k)e^{ik(x_j^- -\rho v_F t'-x^-_{-j})}\int_{-\infty}^{+\infty}dk'\,(1-f_{k'})e^{ik'(x_j^+-\rho' v_F t'-x^+_{-j})}\Big\}. \qquad \text{(A.16)}
\end{aligned}$$

In order to simplify the exponentials, we look for instance at $j=r$, $-j=l$. In this case

$$\begin{aligned}
&x_j^+-x^+_{-j}=x_r^+-x_l^+=L, && x_j^--x^-_{-j}=x_r^--x_l^-=L, \\
&x_j^--x^+_{-j}=x_r^--x_l^+=L-\delta_{\zeta,\zeta'}\xi, && x_j^+-x^-_{-j}=x_r^+-x_l^-=L+\delta_{\zeta,\zeta'}\xi. \qquad \text{(A.17)}
\end{aligned}$$

This finally leads to

$$\begin{aligned}
&\left\langle \psi_\zeta(x_j^-,t')\psi_{\zeta'}(x_j^+,t')\psi^\dagger_{\zeta'}(x^+_{-j},0)\psi^\dagger_\zeta(x^-_{-j},0)\right\rangle_E \\
=&\frac{1}{(2\pi)^2}\Big\{-\int_{-\infty}^{+\infty}dk\,(1-f_k)e^{ik(L-\delta_{\zeta,\zeta'}\xi-\rho v_F t')}\int_{-\infty}^{+\infty}dk'\,(1-f_{k'})e^{ik'(L+\delta_{\zeta,\zeta'}\xi-\rho v_F t')}\delta_{\zeta,\zeta'} \\
&+\int_{-\infty}^{+\infty}dk\,(1-f_k)e^{ik(L-\rho v_F t')}\int_{-\infty}^{+\infty}dk'\,(1-f_{k'})e^{ik'(L-\rho' v_F t')}\Big\}. \qquad \text{(A.18)}
\end{aligned}$$

The last thing to do is the evaluation of the four integrals, each corresponding to a propagator. By moving to the complex plane and using the residue theorem, it can be shown that

$$\begin{aligned}
&\int_{-\infty}^{+\infty}dk\,(1-f_k)e^{ik(L-\delta_{\zeta,\zeta'}\xi-\rho v_F t')}e^{-\rho k\xi}=\int_{-\infty}^{+\infty}dk\,\frac{e^{\rho\beta\hbar v_F k}}{1+e^{\rho\beta\hbar v_F k}}e^{ik(L-\delta_{\zeta,\zeta'}\xi-\rho v_F t')}e^{-\rho k\xi} \\
=&\frac{i\Delta}{\rho\hbar v_F}\frac{\tilde T}{\sinh\left[\tilde T\left(\tilde L-\delta_{\zeta,\zeta'}-\rho s+i\rho\right)\right]}, \qquad \text{(A.19)}
\end{aligned}$$

where we have introduced the dimensionless quantities of the main text, $\tilde{L} = L\Delta/\hbar v_F$, $\tilde{T} = \pi k_B T/\Delta$, $s = t'\Delta/\hbar$. In the integral, the cut-off $e^{-\rho k\xi}$ has been introduced to ensure the convergence at $+\infty(-\infty)$ for $\rho = 1(-1)$. Notice that, since $\xi = \hbar v_F/\Delta \ll v_F\beta$, we have not introduced any divergence in the opposite direction, at $-\infty(+\infty)$.

Finally, looking back at Eq. (A.8),

$$\begin{aligned}
&\theta(t')\left\langle\left[\psi_\zeta(x_j^-,t')\psi_{\zeta'}(x_j^+,t'),\psi_{\zeta'}^\dagger(x_{-j}^+,0)\psi_\zeta^\dagger(x_{-j}^-,0)\right]\right\rangle_E \\
=&\frac{i\theta(t')}{2\pi^2}\,\mathrm{Im}\left\{\left(\frac{i\Delta}{\hbar v_F}\right)^2\left[\delta_{\zeta,\zeta'}\frac{\tilde{T}}{\sinh\left[\tilde{T}\left(\tilde{L}-\delta_{\zeta,\zeta'}-\rho s+i\rho\right)\right]}\frac{\tilde{T}}{\sinh\left[\tilde{T}\left(\tilde{L}+\delta_{\zeta,\zeta'}-\rho s+i\rho\right)\right]}\right.\right. \\
&\left.\left.-\rho\rho'\frac{\tilde{T}}{\sinh\left[\tilde{T}\left(\tilde{L}-\rho s+i\rho\right)\right]}\frac{\tilde{T}}{\sinh\left[\tilde{T}\left(\tilde{L}-\rho' s+i\rho'\right)\right]}\right]\right\} \\
\equiv&\frac{-i\Delta^2}{2\pi^2\hbar^2 v_F^2}\,\theta(t')\,\mathrm{Im}\,\Pi_{\zeta,\zeta'}\left(\tilde{T},\tilde{L},s\right),
\end{aligned} \tag{A.20}$$

with $\Pi_{\zeta,\zeta'}\left(\tilde{T},\tilde{L},s\right)$ as introduced in the main text. Inserting this into Eq. (A.7), making the change of variable $t' \to s$ and substituting $\tilde{V} = eV/\Delta$ in the integration,

$$I^r(t) = \frac{4e\Gamma^2}{\hbar^2}\frac{\Delta}{2\pi^2\hbar v_F^2}\mathrm{Im}\left\{e^{-i(\omega_J t+\varphi_0)}\sum_{\zeta,\zeta'}f_{\zeta,\zeta'}\int_{-\infty}^{+\infty}ds\,\theta(s)\,e^{i\tilde{V}s}\mathrm{Im}\,\Pi_{\zeta,\zeta'}\left(\tilde{T},\tilde{L},s\right)\right\}, \tag{A.21}$$

which is exactly Eq. (2.84).

A.2 About integrating out the superconductors

The aim of this Section is to show the procedure to derive an effective edge Hamiltonian which includes the low-energy proximity effect of the superconductors on the edge states. The strategy is to get through the path integral for fermionic fields. In this formalism, one can express the partition function in terms of the actions for the edge states, for the superconductors, and for the tunneling contribution. By completing the square in the superconductor fields, a Gaussian integral, which can be carried out, is obtained. Having integrated out the degrees of freedom of the superconductors, an effective action containing only the edge state fields remains, representing effectively their coupling to the superconductors. Then, under the appropriate conditions it is possible to get back to an effective edge Hamiltonian.

Without delving into the details of the formalism, which can be found for instance in [4] and go beyond the purpose of this Thesis, we recall just some essential concepts. Throughout this Section, $\hbar = 1$.

Given a Hamiltonian of the form

$$H(a^\dagger,a) = \sum_{ij}h_{ij}a_i^\dagger a_j, \tag{A.22}$$

the path integral representation of the partition function[1]

$$\mathcal{Z} = \mathrm{tr} e^{-\beta H} = \sum_n \langle n| \, e^{-\beta H} \, |n\rangle \, , \tag{A.23}$$

where $\beta \equiv 1/T$ and the sum runs over a completes set of Fock space states $\{|n\rangle\}$, is given by

$$\mathcal{Z} = \int D(\overline{\psi}, \psi) e^{-\int_0^\beta d\tau [\overline{\psi} \partial_\tau \psi + H(\overline{\psi}, \psi)]} = \int D(\overline{\psi}, \psi) e^{-S[\overline{\psi}, \psi)]}, \tag{A.24}$$

with

$$S[\overline{\psi}, \psi)] = \int_0^\beta d\tau [\overline{\psi}(\tau) \partial_\tau \psi(\tau) + H(\overline{\psi}(\tau), \psi(\tau))] = \int_0^\beta d\tau \left[\sum_{ij} \overline{\psi}_i(\tau) (\partial_\tau \delta_{ij} + h_{ij}) \psi_j(\tau) \right] . \tag{A.25}$$

$\overline{\psi}$, ψ are vectors made of the Grassmann variables corresponding to the fermionic operators $a^\dagger$, a. They satisfy the boundary condition $\psi_i(0) = -\psi_i(\beta)$, $\overline{\psi}_i(0) = -\overline{\psi}_i(\beta)$.

Grassmann variables arise from the construction of fermionic coherent states: let us suppose that the annihilation operators are characterized by a set of coherent states such that, for all i,

$$a_i \, |\psi\rangle = \psi_i \, |\psi\rangle \, . \tag{A.26}$$

The anticommutativity of fermionic operators implies that the eigenvalues ψ_i have to anticommute with each other as well,

$$\psi_i \psi_j = -\psi_j \psi_i. \tag{A.27}$$

Hence, they are clearly not ordinary numbers. A set of such objects can be defined in a mathematically rigorous way, but here we just take Eq. (A.27) as a working definition. It is straightforward to demonstrate that a fermionic coherent state, namely a state which simultaneously diagonalizes all annihilation operators, is defined by

$$|\psi\rangle = e^{-\sum_i \psi_i a_i^\dagger} \, |0\rangle \, . \tag{A.28}$$

To get Eq. (A.24) from Eq. (A.23), we first insert into the latter the resolution of identity in terms of coherent states

$$\mathbb{I}_\mathcal{F} = \int d(\overline{\psi}, \psi) e^{-\sum_i \overline{\psi}_i \psi_i} \, |\psi\rangle \, \langle\psi| \, , \tag{A.29}$$

obtaining

$$\mathcal{Z} = \int d(\overline{\psi}, \psi) e^{-\sum_i \overline{\psi}_i \psi_i} \sum_n \langle n|\psi\rangle \, \langle\psi| \, e^{-\beta H} \, |n\rangle \, . \tag{A.30}$$

In order to remove the resolution of identity $\mathbb{I}_\mathcal{F} = \sum_n |n\rangle \, \langle n|$, the factor $\langle n|\psi\rangle$ has to be commuted to the right-hand side. It can be verified that the fermionic coherent states acquire a minus sign under permutation, $\langle n|\psi\rangle \, \langle\psi|n\rangle = - \langle\psi|n\rangle \, \langle n|\psi\rangle$ (notice that, on

[1] Notice that the partition function can be interpreted as a trace over the transition amplitude $\langle n| \, e^{-iHt} \, |n\rangle$ evaluated at an imaginary time $t = -i\beta = -i\tau$. The transformation $t \to -i\tau$ is described as a Wick rotation. The variable τ appearing from now on indicates the imaginary time.

the other hand, no sign is acquired by bringing $\langle n|\psi\rangle$ to the right of $e^{-\beta H}$, because H contains even numbers of creation/annihilation operators). We get

$$\mathcal{Z} = \int d(\overline{\psi},\psi) e^{-\sum_i \overline{\psi}_i \psi_i} \sum_n - \langle\psi| e^{-\beta H} |n\rangle \langle n|\psi\rangle = \int d(\overline{\psi},\psi) e^{-\sum_i \overline{\psi}_i \psi_i} - \langle\psi| e^{-\beta H} |\psi\rangle . \tag{A.31}$$

The next step, which we do not cover here explicitly, is to divide the time interval β in N segments $\delta = \beta/N$

$$e^{-\beta H} = (e^{-\delta H})^N = e^{-\delta H} \cdot \cdots \cdot e^{-\delta H}. \tag{A.32}$$

We insert in the above expression $N-1$ resolutions of identity in terms of coherent states, each indicized by $n = 1, \ldots, N$

$$\mathbb{I}_{\mathcal{F}} = \int d(\overline{\psi}^n,\psi^n) e^{-\sum_i \overline{\psi}_i^n \psi_i^n} |\psi^n\rangle \langle\psi^n| . \tag{A.33}$$

After some manipulations, the result can be plugged into (A.31). Lastly, identifying $|\psi^0\rangle = -|\psi^N\rangle$, namely $\overline{\psi}^0 = -\overline{\psi}^N$, $\psi^0 = -\psi^N$, and sending $N \to \infty$ while keeping $\beta = N\delta$ fixed, one obtains Eq. (A.24).

We have derived Eqs. (A.24-A.25) starting from a Hamiltonian $H(a^\dagger, a) = \sum_{ij} h_{ij} a_i^\dagger a_j$. The Hamiltonians of our problem are of the form

$$H_S^j = \frac{1}{2}\int d\mathbf{r}'\, \mathbf{\Psi}_{S,j}^\dagger(\mathbf{r}') \mathcal{H}_S^j(\mathbf{r}') \mathbf{\Psi}_{S,j}(\mathbf{r}') = \frac{1}{2}\int d\mathbf{r}' \sum_{\alpha\beta} \mathbf{\Psi}_{S,j}^{\dagger\alpha}(\mathbf{r}') \mathcal{H}_S^{j\,\alpha\beta}(\mathbf{r}') \mathbf{\Psi}_{S,j}^{\beta}(\mathbf{r}'), \tag{A.34a}$$

$$H_E = \frac{1}{2}\int dx\, \boldsymbol{\psi}_E^\dagger(x) \tilde{\mathcal{H}}_E(x) \boldsymbol{\psi}_E(x) = \frac{1}{2}\int dx \sum_{\alpha\beta} \boldsymbol{\psi}_E^{\dagger\alpha}(x) \tilde{\mathcal{H}}_E^{\alpha\beta}(x) \boldsymbol{\psi}_E^{\beta}(x), \tag{A.34b}$$

$$H_T^j = \frac{1}{2}\int dx \int d\mathbf{r}'\, \{\mathbf{\Psi}_{S,j}^\dagger(\mathbf{r}') \tilde{\mathcal{T}}^j(\mathbf{r}',x) \boldsymbol{\psi}_E(x) + \boldsymbol{\psi}_E^\dagger(x) \left[\tilde{\mathcal{T}}^j(\mathbf{r}',x)\right]^\dagger \mathbf{\Psi}_{S,j}(\mathbf{r}')\}, \tag{A.34c}$$

where we have doubled the original space for the edge states to introduce particle-hole symmetry,

$$\begin{aligned}\boldsymbol{\psi}_E(x) &= (\boldsymbol{\psi}(x), \boldsymbol{\psi}^\dagger(x))^T \\ &= \Big(\psi_{11}(x), \psi_{-11}(x), \psi_{1-1}(x), \psi_{-1-1}(x), \psi_{11}^\dagger(x), \psi_{-11}^\dagger(x), \psi_{1-1}^\dagger(x), \psi_{-1-1}^\dagger(x)\Big)^T ,\end{aligned} \tag{A.35}$$

and

$$\tilde{\mathcal{H}}_E = \begin{pmatrix} \mathcal{H}_E & 0 \\ 0 & \mathcal{H}_E \end{pmatrix}, \qquad \tilde{\mathcal{T}}^j(\mathbf{r}',x) = \begin{pmatrix} \mathcal{T}^j(\mathbf{r}',x) & 0 \\ 0 & -[\mathcal{T}^j(\mathbf{r}',x)]^* \end{pmatrix}, \tag{A.36}$$

with $\mathcal{H}_E$ and $\mathcal{T}^j(\mathbf{r}',x)$ as in the main text. For what follows, it is useful to express $\mathcal{H}_S^j(\mathbf{r}')$ in the compact form

$$\mathcal{H}_S^j(\mathbf{r}') = \left(-\frac{\boldsymbol{\nabla}_{\mathbf{r}'}^2}{2m} - \mu\right) \eta_z \otimes \sigma_0 + i\Delta(e^{i\theta_j}\eta_- - e^{-i\theta_j}\eta_+) \otimes \sigma_y, \tag{A.37}$$

where η_z, $\eta_\pm$ are Pauli matrices acting in particle-hole space, with $\eta_\pm = (\eta_x \pm \eta_y)/2$, while σ_0, σ_y acts in spin space (σ_0 is the identity).

With a slight abuse of notation, from now on we will denote by $\mathbf{\Psi}_{S,j}$, $\overline{\mathbf{\Psi}}_{S,j}$, $\boldsymbol{\psi}_E$, $\overline{\boldsymbol{\psi}}_E$ the Grassman variables associated to the operators $\mathbf{\Psi}_{S,j}$, $\mathbf{\Psi}^\dagger_{S,j}$, $\boldsymbol{\psi}_E$, $\boldsymbol{\psi}^\dagger_E$. Inspired by Eqs. (A.24-A.25), the actions written in terms of Grassman variables read as

$$S^j_S[\overline{\mathbf{\Psi}}_{S,j}, \mathbf{\Psi}_{S,j}] = \frac{1}{2}\int_0^\beta d\tau \int d\mathbf{r}'\, \overline{\mathbf{\Psi}}_{S,j}(\mathbf{r}',\tau)(\partial_\tau + \mathcal{H}^j_S(\mathbf{r}'))\mathbf{\Psi}_{S,j}(\mathbf{r}',\tau), \tag{A.38a}$$

$$S_E[\overline{\boldsymbol{\psi}}_E, \boldsymbol{\psi}_E] = \frac{1}{2}\int_0^\beta d\tau \int dx\, \overline{\boldsymbol{\psi}}_E(x,\tau)(\partial_\tau + \tilde{\mathcal{H}}_E(x))\boldsymbol{\psi}_E(x,\tau), \tag{A.38b}$$

$$\begin{aligned} S^j_T[\overline{\mathbf{\Psi}}_{S,j}, \mathbf{\Psi}_{S,j}, \overline{\boldsymbol{\psi}}_E, \boldsymbol{\psi}_E] = \frac{1}{2}\int_0^\beta d\tau \int dx \int d\mathbf{r}' \{&\overline{\mathbf{\Psi}}_{S,j}(\mathbf{r}',\tau)\tilde{\mathcal{T}}^j(\mathbf{r}',x)\boldsymbol{\psi}_E(x,\tau) \\ &+ \overline{\boldsymbol{\psi}}_E(x,\tau)\left[\tilde{\mathcal{T}}^j(\mathbf{r}',x)\right]^\dagger \mathbf{\Psi}_{S,j}(\mathbf{r}',\tau)\}. \end{aligned} \tag{A.38c}$$

In this case, the partition function will be

$$\begin{aligned} \mathcal{Z} = &\prod_j \int D(\overline{\mathbf{\Psi}}_{S,j}, \mathbf{\Psi}_{S,j}) \\ &\int D(\overline{\boldsymbol{\psi}}_E, \boldsymbol{\psi}_E) e^{-\sum_j S^j_S[\overline{\mathbf{\Psi}}_{S,j},\mathbf{\Psi}_{S,j}] - S_E[\overline{\boldsymbol{\psi}}_E,\boldsymbol{\psi}_E] - \sum_j S^j_T[\overline{\mathbf{\Psi}}_{S,j},\mathbf{\Psi}_{S,j},\overline{\boldsymbol{\psi}}_E,\boldsymbol{\psi}_E]}. \end{aligned} \tag{A.39}$$

The actions containing the superconductor fields, $S^j_S[\overline{\mathbf{\Psi}}_{S,j}, \mathbf{\Psi}_{S,j}]$ and $S^j_T[\overline{\mathbf{\Psi}}_{S,j}, \mathbf{\Psi}_{S,j}, \overline{\boldsymbol{\psi}}_E, \boldsymbol{\psi}_E]$, are at most quadratic in the fields. It is hence possible to complete the square such that, in the partition function, a Gaussian integral can be factorized[2]. Let us consider the sum

$$\begin{aligned} &S^j_S[\overline{\mathbf{\Psi}}_{S,j}, \mathbf{\Psi}_{S,j}] + S^j_T[\overline{\mathbf{\Psi}}_{S,j}, \mathbf{\Psi}_{S,j}, \overline{\boldsymbol{\psi}}_E, \boldsymbol{\psi}_E] = \\ &= \frac{1}{2}\int_0^\beta d\tau \Bigg\{ \int d\mathbf{r}'\, \overline{\mathbf{\Psi}}_{S,j}(\mathbf{r}',\tau)(\partial_\tau + \mathcal{H}^j_S(\mathbf{r}'))\mathbf{\Psi}_{S,j}(\mathbf{r}',\tau) \\ &+ \int dx \int d\mathbf{r}' \{\overline{\mathbf{\Psi}}_{S,j}(\mathbf{r}',\tau)\tilde{\mathcal{T}}^j(\mathbf{r}',x)\boldsymbol{\psi}_E(x,\tau) + \overline{\boldsymbol{\psi}}_E(x,\tau)\left[\tilde{\mathcal{T}}^j(\mathbf{r}',x)\right]^\dagger \mathbf{\Psi}_{S,j}(\mathbf{r}',\tau)\}\Bigg\}. \end{aligned} \tag{A.40}$$

In order to complete the square, we make use of the definition of the superconductor Green's function $\mathcal{G}^j_S(\mathbf{r}\tau, \mathbf{r}'\tau')$ as the inverse of the superconductor kernel,

$$-\partial_\tau \mathcal{G}^j_S(\mathbf{r}\tau,\mathbf{r}'\tau') - \mathcal{H}^j_S(\mathbf{r}')\mathcal{G}^j_S(\mathbf{r}\tau,\mathbf{r}'\tau') = (-\partial_\tau - \mathcal{H}^j_S(\mathbf{r}'))\mathcal{G}^j_S(\mathbf{r}\tau,\mathbf{r}'\tau') = \delta(\mathbf{r}-\mathbf{r}')\delta(\tau-\tau'). \tag{A.41}$$

[2]We remind in passing that $\int d(\overline{\phi},\phi) e^{-\phi^T \mathbf{A}\phi} = \det \mathbf{A}$, where $\overline{\phi}$ and ϕ are N-components vectors of Grassmann variables, the measure is $d(\overline{\phi},\phi) \equiv \prod_{i=1}^N d\overline{\phi}_i d\phi_i = \prod_{i=1}^N d\mathrm{Re}\phi_i d\mathrm{Im}\phi_i$, and $\mathbf{A}$ is an arbitrary complex matrix.

Eq. (A.40) can then be recast as

$$
\begin{aligned}
&S_S^j[\overline{\mathbf{\Psi}}_{S,j}, \mathbf{\Psi}_{S,j}] + S_T^j[\overline{\mathbf{\Psi}}_{S,j}, \mathbf{\Psi}_{S,j}, \overline{\boldsymbol{\psi}}_E, \boldsymbol{\psi}_E] = \\
=&\frac{1}{2}\int_0^\beta d\tau \int d\mathbf{r}' \Bigg\{ \overline{\mathbf{\Psi}}_{S,j}(\mathbf{r}',\tau) - \int_0^\beta d\tau'' \int dx \int d\mathbf{r}'' \left[\overline{\boldsymbol{\psi}}_E(x,\tau'') \left[\tilde{\mathcal{T}}^j(\mathbf{r}'',x)\right]^\dagger \mathcal{G}_S^j(\mathbf{r}''\tau'', \mathbf{r}'\tau) \right] \Bigg\} \\
&(\partial_\tau + \mathcal{H}_S^j(\mathbf{r}')) \Bigg\{ \mathbf{\Psi}_{S,j}(\mathbf{r}',\tau) - \int_0^\beta d\tau' \int dx' \int d\mathbf{r}''' \left[\mathcal{G}_S^j(\mathbf{r}'''\tau, \mathbf{r}'\tau') \tilde{\mathcal{T}}^j(\mathbf{r}''', x') \boldsymbol{\psi}_E(x',\tau') \right] \Bigg\} \\
-&\frac{1}{2}\int_0^\beta d\tau \int_0^\beta d\tau' \int_0^\beta d\tau'' \int dx \int dx' \int d\mathbf{r}' \int d\mathbf{r}'' \int d\mathbf{r}''' \\
&\Bigg\{ \overline{\boldsymbol{\psi}}_E(x,\tau'') \left[\tilde{\mathcal{T}}^j(\mathbf{r}'',x)\right]^\dagger \mathcal{G}_S^j(\mathbf{r}''\tau'', \mathbf{r}'\tau) (\partial_\tau + \mathcal{H}_S^j(\mathbf{r}')) \mathcal{G}_S^j(\mathbf{r}'''\tau, \mathbf{r}'\tau') \tilde{\mathcal{T}}^j(\mathbf{r}''', x') \boldsymbol{\psi}_E(x',\tau') \Bigg\},
\end{aligned}
\tag{A.42}
$$

where the extra term arising from the first two rows is canceled by the last two. The latter can be rewritten as

$$
\begin{aligned}
&\frac{1}{2}\int_0^\beta d\tau \int_0^\beta d\tau' \int_0^\beta d\tau'' \int dx \int dx' \int d\mathbf{r}' \int d\mathbf{r}'' \int d\mathbf{r}''' \\
&\Bigg\{ \overline{\boldsymbol{\psi}}_E(x,\tau'') \left[\tilde{\mathcal{T}}^j(\mathbf{r}'',x)\right]^\dagger \mathcal{G}_S^j(\mathbf{r}''\tau'', \mathbf{r}'\tau) \delta(\mathbf{r}''' - \mathbf{r}') \delta(\tau - \tau') \tilde{\mathcal{T}}^j(\mathbf{r}''', x') \boldsymbol{\psi}_E(x',\tau') \Bigg\} \\
=&\frac{1}{2}\int_0^\beta d\tau' \int_0^\beta d\tau'' \int dx \int dx' \\
&\Bigg\{ \overline{\boldsymbol{\psi}}_E(x,\tau'') \int d\mathbf{r}'' \int d\mathbf{r}''' \left[\tilde{\mathcal{T}}^j(\mathbf{r}'',x)\right]^\dagger \mathcal{G}_S^j(\mathbf{r}''\tau'', \mathbf{r}'''\tau') \tilde{\mathcal{T}}^j(\mathbf{r}''', x') \boldsymbol{\psi}_E(x',\tau') \Bigg\} \\
=&\frac{1}{2}\int_0^\beta d\tau' \int_0^\beta d\tau'' \int dx \int dx' \Bigg\{ \overline{\boldsymbol{\psi}}_E(x,\tau'') \Sigma(\tau', \tau'', x, x') \boldsymbol{\psi}_E(x',\tau') \Bigg\}.
\end{aligned}
\tag{A.43}
$$

In the last equivalence, we have defined the self-energy

$$
\Sigma_j(\tau', \tau'', x, x') \equiv \int d\mathbf{r}'' \int d\mathbf{r}''' \left[\tilde{\mathcal{T}}^j(\mathbf{r}'',x)\right]^\dagger \mathcal{G}_S^j(\mathbf{r}''\tau'', \mathbf{r}'''\tau') \tilde{\mathcal{T}}^j(\mathbf{r}''', x'). \tag{A.44}
$$

We can now make some further remarks. Since $\mathcal{H}_S^j(\mathbf{r}')$ is independent of time, the Green's function $\mathcal{G}_S^j(\mathbf{r}''\tau'', \mathbf{r}'''\tau')$ does not depend on τ', τ'', but rather on their difference $\tau' - \tau''$ [28]. Hence, also $\Sigma_j(\tau', \tau'', x, x') = \Sigma_j(\tau' - \tau'', x, x')$. Moreover, the times at which the two electrons of a Cooper pair tunnel, τ' and τ'', are of the order $1/\Delta$ [26]. Since we are interested in energies $E \ll \Delta$, we can assume them to be equal (Appendix D of [155]), namely $\Sigma_j(\tau' - \tau'', x, x') \propto \delta(\tau' - \tau'')$.

The first two rows of Eq. (A.42) are now in a quadratic form, and hence lead a gaussian contribution, which can be integrated, to the partition function. The extra term Eq. (A.43) has to be added to the edge state action Eq. (A.38b),

$$
\begin{aligned}
S_E^{eff}[\overline{\boldsymbol{\psi}}_E, \boldsymbol{\psi}_E] = &\frac{1}{2}\int_0^\beta d\tau \int dx\, \overline{\boldsymbol{\psi}}_E(x,\tau)(\partial_\tau + \tilde{\mathcal{H}}_E(x)) \boldsymbol{\psi}_E(x,\tau) \\
&+ \frac{1}{2}\sum_j \int_0^\beta d\tau' \int_0^\beta d\tau'' \int dx \int dx' \Bigg\{ \overline{\boldsymbol{\psi}}_E(x,\tau'') \Sigma_j(\tau' - \tau'', x, x') \boldsymbol{\psi}_E(x',\tau') \Bigg\}.
\end{aligned}
\tag{A.45}
$$

Before moving back to Hamiltonians, we need to better specify $\Sigma(\tau' - \tau'', x, x')$. For now, we just deduced that it is proportional to a δ in time.

- Since $\mathcal{G}_S^j$ only depends on the difference $\tau' - \tau''$, it can be expressed in terms of a Fourier transform with just one fermionic Matsubara frequency $i\omega_n$ and not two (here $\omega_n = (2n+1)\pi/\beta$). In particular,

$$\begin{aligned}\Sigma(i\omega_n, x, x') = &\int d\mathbf{r}'' \int d\mathbf{r}''' \left[\hat{\mathcal{T}}^{\nu j}(\mathbf{r}'', x)\right]^\dagger \\ &\left[\int_0^\beta d(\tau' - \tau'')\mathcal{G}_S^j(\tau' - \tau'', \mathbf{r}'', \mathbf{r}''')e^{i\omega_n(\tau' - \tau'')}\right] \hat{\mathcal{T}}^{\nu' j}(\mathbf{r}''', x') \\ = &\int d\mathbf{r}'' \int d\mathbf{r}''' \left[\hat{\mathcal{T}}^{\nu j}(\mathbf{r}'', x)\right]^\dagger \mathcal{G}_S^j(i\omega_n, \mathbf{r}'', \mathbf{r}''')\hat{\mathcal{T}}^{\nu' j}(\mathbf{r}''', x'). \quad \text{(A.46)}\end{aligned}$$

- Being proportional to $\delta(\tau' - \tau'')$, in the frequency space $\Sigma(i\omega_n, x, x')$ has to be constant in ω_n.

This is not enough yet. However, a common approximation in the literature for $E \ll \Delta$ is to consider $i\omega_n \to 0$ [1, 149], that is

$$\Sigma(i\omega_n, x, x') \overset{E \ll \Delta}{\approx} \Sigma(i\omega_n = 0, x, x'). \quad \text{(A.47)}$$

We can hence substitute, in (A.45),

$$\begin{aligned}\Sigma(\tau' - \tau'', x, x') = \frac{1}{\beta}\sum_n e^{-i\omega_n(\tau' - \tau'')}\Sigma(i\omega_n, x, x') = \frac{1}{\beta}\Sigma(i\omega_n = 0, x, x')\sum_n e^{-i\omega_n(\tau' - \tau'')} \\ = \Sigma(i\omega_n = 0, x, x')\delta(\tau' - \tau''). \quad \text{(A.48)}\end{aligned}$$

$\Sigma(i\omega_n = 0, x, x')$ can be written explicitly. First of all,

$$\Sigma(i\omega_n = 0, x, x') = \int d\mathbf{r}'' \int d\mathbf{r}''' \left[\tilde{\mathcal{T}}^j(\mathbf{r}'', x)\right]^\dagger \mathcal{G}_S^j(i\omega_n = 0, \mathbf{r}'', \mathbf{r}''')\tilde{\mathcal{T}}^j(\mathbf{r}''', x'). \quad \text{(A.49)}$$

We need an expression for $\mathcal{G}_S^j(i\omega_n = 0, \mathbf{r}'', \mathbf{r}''')$. We know that

$$(-\partial_\tau - \mathcal{H}_S^j(\mathbf{r}'))\mathcal{G}_S^j(\mathbf{r}\tau, \mathbf{r}'\tau') = \delta(\mathbf{r} - \mathbf{r}')\delta(\tau - \tau'). \quad \text{(A.50)}$$

By Fourier transforming,

$$(i\omega_n - \mathcal{H}_S^j(\mathbf{r}'))\mathcal{G}_S^j(i\omega_n, \mathbf{r}, \mathbf{r}') = \delta(\mathbf{r} - \mathbf{r}'). \quad \text{(A.51)}$$

Assuming that the superconductors can be treated as bulk (translationally invariant) systems in three dimensions, we have $\mathcal{G}_S^j(i\omega_n, \mathbf{r}, \mathbf{r}') = \mathcal{G}_S^j(i\omega_n, \mathbf{r} - \mathbf{r}')$. We can hence obtain their Green's function by moving to $\mathbf{k}$-space, where

$$\mathcal{G}_S^j(i\omega_n, \mathbf{r} - \mathbf{r}') = \int \frac{d\mathbf{k}}{(2\pi)^3} e^{i\mathbf{k}\cdot(\mathbf{r} - \mathbf{r}')}\mathcal{G}_S^j(i\omega_n, \mathbf{k}) \quad \text{(A.52)}$$

and Eq. (A.51) becomes

$$(i\omega_n - \mathcal{H}_S^j(\mathbf{k}))\mathcal{G}_S^j(i\omega_n, \mathbf{k}) = 1. \quad \text{(A.53)}$$

We can conclude that

$$\mathcal{G}_S^j(i\omega_n,\mathbf{k}) = (i\omega_n - \mathcal{H}_S^j(\mathbf{k}))^{-1} = (i\omega_n - \xi_\mathbf{k}\eta_z\otimes\sigma_0 - i\Delta(e^{i\theta_j}\eta_- - e^{-i\theta_j}\eta_+)\otimes\sigma_y)^{-1}$$
$$= -\frac{i\omega_n + \xi_\mathbf{k}\eta_z\otimes\sigma_0 + i\Delta(e^{i\theta_j}\eta_- - e^{-i\theta_j}\eta_+)\otimes\sigma_y}{{\omega_n}^2 + {\xi_\mathbf{k}}^2 + \Delta^2}, \tag{A.54}$$

where $\xi_\mathbf{k} = \mathbf{k}^2/(2m) - \mu$, and $\mathcal{H}_S^j(\mathbf{k})$ was simply obtained by Fourier transforming Eq. (A.37). Evaluating at $\omega_n = 0$,

$$\mathcal{G}_S^j(i\omega_n = 0,\mathbf{k}) = -\frac{\xi_\mathbf{k}\eta_y\otimes\sigma_0 + i\Delta(e^{i\theta_j}\eta_- - e^{-i\theta_j}\eta_+)\otimes\sigma_y}{{\xi_\mathbf{k}}^2 + \Delta^2}, \tag{A.55}$$

and, from Eq. (A.49),

$$\Sigma(i\omega_n = 0, x, x') = \int d\mathbf{r}''\int d\mathbf{r}'''\left[\tilde{\mathcal{T}}^j(\mathbf{r}'',x)\right]^\dagger \mathcal{G}_S^j(i\omega_n = 0,\mathbf{r}'',\mathbf{r}''')\tilde{\mathcal{T}}^j(\mathbf{r}''',x')$$
$$= \int d\mathbf{r}''\int d\mathbf{r}'''\left[\tilde{\mathcal{T}}^j(\mathbf{r}'',x)\right]^\dagger \int \frac{d\mathbf{k}}{(2\pi)^3}e^{i\mathbf{k}\cdot(\mathbf{r}''-\mathbf{r}''')}\mathcal{G}_S^j(i\omega_n = 0,\mathbf{k})\tilde{\mathcal{T}}^j(\mathbf{r}''',x')$$
$$= \int d\mathbf{r}''\int d\mathbf{r}'''\left[\tilde{\mathcal{T}}^j(\mathbf{r}'',x)\right]^\dagger$$
$$\int \frac{d\mathbf{k}}{(2\pi)^3}e^{i\mathbf{k}\cdot(\mathbf{r}''-\mathbf{r}''')}\left[-\frac{\xi_\mathbf{k}\eta_z\otimes\sigma_0 + i\Delta(e^{i\theta_j}\eta_- - e^{-i\theta_j}\eta_+)\otimes\sigma_y}{{\xi_\mathbf{k}}^2 + \Delta^2}\right]\tilde{\mathcal{T}}^j(\mathbf{r}''',x'). \tag{A.56}$$

We can now go back to Eq. (A.45) and substitute Eq. (A.48)

$$S_E^{eff}[\overline{\boldsymbol{\psi}}_E,\boldsymbol{\psi}_E] = \frac{1}{2}\int_0^\beta d\tau\int dx\,\overline{\boldsymbol{\psi}}_E(x,\tau)(\partial_\tau + \tilde{\mathcal{H}}_E(x))\boldsymbol{\psi}_E(x,\tau)$$
$$+\frac{1}{2}\sum_j\int_0^\beta d\tau'\int_0^\beta d\tau''\int dx\int dx'\left\{\overline{\boldsymbol{\psi}}_E(x,\tau'')\Sigma_j(\tau'-\tau'',x,x')\boldsymbol{\psi}_E(x',\tau')\right\}$$
$$=\frac{1}{2}\int_0^\beta d\tau\int dx\,\overline{\boldsymbol{\psi}}_E(x,\tau)(\partial_\tau + \tilde{\mathcal{H}}_E(x))\boldsymbol{\psi}_E(x,\tau)$$
$$+\frac{1}{2}\sum_j\int_0^\beta d\tau'\int_0^\beta d\tau''\int dx\int dx'\left\{\overline{\boldsymbol{\psi}}_E(x,\tau'')\Sigma_j(i\omega_n = 0,x,x')\delta(\tau'-\tau'')\boldsymbol{\psi}_E(x',\tau')\right\}$$
$$=\frac{1}{2}\int_0^\beta d\tau\int dx\,\overline{\boldsymbol{\psi}}_E(x,\tau)(\partial_\tau + \tilde{\mathcal{H}}_E(x))\boldsymbol{\psi}_E(x,\tau)$$
$$+\frac{1}{2}\sum_j\int_0^\beta d\tau'\int dx\int dx'\left\{\overline{\boldsymbol{\psi}}_E(x,\tau')\Sigma_j(i\omega_n = 0,x,x')\boldsymbol{\psi}_E(x',\tau')\right\}$$
$$=\frac{1}{2}\int_0^\beta d\tau\int dx\int dx'\,\left(\overline{\boldsymbol{\psi}}_E(x,\tau)\left\{\delta(x-x')(\partial_\tau + \tilde{\mathcal{H}}_E(x))\right.\right.$$
$$\left.\left.+\sum_j\Sigma_j(i\omega_n = 0,x,x')\right\}\boldsymbol{\psi}_E(x',\tau)\right). \tag{A.57}$$

From this action, by following what said between Eq. (A.34b) and Eq. (A.38), we can infer an effective Hamiltonian for the edge system, containing the edge state operators only

$$\begin{aligned} H_E^{eff} =& \frac{1}{2}\int dx\, \boldsymbol{\psi}_E^\dagger(x)\tilde{\mathcal{H}}_E(x)\boldsymbol{\psi}_E(x) + \frac{1}{2}\sum_j \int dx \int dx'\, \boldsymbol{\psi}_E^\dagger(x)\Sigma_j(i\omega_n = 0, x, x')\boldsymbol{\psi}_E(x') \\ \equiv& H_E + \sum_j \delta H^j. \end{aligned} \tag{A.58}$$

For the remaining calculations, we refer the reader to [78], and just mention what should be done.

By looking at the form of the self-energy, we see that there are two different possibilities, depending on whether we consider the diagonal elements of $\mathcal{G}_S^j(i\omega_n, \mathbf{r} - \mathbf{r}')$ in the particle-hole space, or the anomalous (off-diagonal) elements, which correspond to Cooper pairs. It can be verified that in the sub-gap energy regime there are no contributions from the diagonal quasi-particle sector, but only from the anomalous ones. Moreover, by looking at the structure of the tunneling matrices, it is clear that only two specific spatial separations play a role. The first is $\mathbf{r} - \mathbf{r}' = 0$, when both tunneling processes take place at the same edge. This corresponds to a Local Andreev Reflection in case of the anomalous sector. The second is $|\mathbf{r} - \mathbf{r}'| = W$, when the tunneling processes occur at opposite edges. This realizes a Crossed Andreev Reflection in the anomalous sector. Both contributions are computed in [78], and the conclusion is that the low-energy effect of the superconducting self-energies Σ_j on the edge system is a point-like injection of Cooper pairs at $x_j = jL/2$, either into a same edge or into opposite edges. The channel of injection of each electron is encoded into the indices $\rho\tau$ and $\rho'\tau'$ of the edge state operators. The result is Eq. (2.67) of the main text.

APPENDIX $\mathcal{B}$

Complements to Chapter 3

In the following, we address the calculation of the current $I^j(t)$ in more detail. Let's look back at Eq. (3.28), and make use of the two definitions in the main text

$$\begin{aligned}\alpha_{i_1,i_2,j}(k_1,k_2) &\equiv \Gamma^j_{i_1,i_2}(k_1,k_2) - \Gamma^j_{i_2,i_1}(k_2,k_1)\\ \Gamma^j_{i_1,i_2}(k_1,k_2) &\equiv \sum_{\zeta_1,\zeta_2} \Gamma^j_{\zeta_1,\zeta_2} a_{\zeta_1,i_1} a_{\zeta_2,i_2} e^{ik_1 x_j^-} e^{ik_2 x_j^+},\end{aligned}$$

where we remind that the possible values for i_1, i_2 are

$$1,1 \qquad 1,2 \qquad 1,3 \qquad 1,4 \qquad 2,2 \qquad 2,3 \qquad 2,4 \qquad 3,3 \qquad 3,4 \qquad 4,4 \tag{B.1}$$

while those for ζ_1, ζ_2 are

$$\begin{aligned}&11,11 \qquad 11,-11 \qquad 11,-1-1 \qquad 11,1-1 \qquad -11,-11\\ &-11,-1-1 \qquad -11,1-1 \qquad -1-1,-1-1 \qquad -1-1,1-1 \qquad 1-1,1-1.\end{aligned} \tag{B.2}$$

We focus on the calculation of $I^j(t)$ for $j = r = 1$. In this case, Eq. (3.28) becomes

$$\sum_{k_1,k_2,k_1',k_2'} \frac{1}{L^2}\alpha_{i_1,i_2,1}(k_1',k_2',t)\alpha^*_{i_1,i_2,-1}(k_1,k_2,t-t')\left\langle\left[A_{k_1',i_1}(t')A_{k_2',i_2}(t'),A^\dagger_{k_2,i_2}(0)A^\dagger_{k_1,i_1}(0)\right]\right\rangle_0$$

$$=\frac{1}{(2\pi)^2}\Bigg\{-\delta_{i_1,i_2}\sum_{\zeta_1,\zeta_2}\Gamma^r_{\zeta_1,\zeta_2}\sum_{\zeta_3,\zeta_4}(\Gamma^l_{\zeta_3,\zeta_4})^*$$

$$\Bigg[\int_{-\infty}^{+\infty}dk_1\,e^{-iE_{A_{i_1}}(k_1)t'/\hbar}\frac{e^{\beta E_{A_{i_1}}(k_1)}}{1+e^{\beta E_{A_{i_1}}(k_1)}}a_{\zeta_1,i_1}a_{\zeta_4,i_1}e^{ik_1\left[L-(\delta_{\zeta_1,\zeta_2}+\delta_{\zeta_3,\zeta_4})\frac{\xi}{2}\right]}$$

$$\int_{-\infty}^{+\infty}dk_2\,e^{-iE_{A_{i_1}}(k_2)t'/\hbar}\frac{e^{\beta E_{A_{i_1}}(k_2)}}{1+e^{\beta E_{A_{i_1}}(k_2)}}a_{\zeta_2,i_1}a_{\zeta_3,i_1}e^{ik_2\left[L-(\delta_{\zeta_1,\zeta_2}+\delta_{\zeta_3,\zeta_4})\frac{\xi}{2}\right]}\Bigg]+$$

$$\int_{-\infty}^{+\infty}dk_1\,e^{-iE_{A_{i_1}}(k_1)t'/\hbar}\frac{e^{\beta E_{A_{i_1}}(k_1)}}{1+e^{\beta E_{A_{i_1}}(k_1)}}\int_{-\infty}^{+\infty}dk_2\,e^{-iE_{A_{i_2}}(k_2)t'/\hbar}\frac{e^{\beta E_{A_{i_2}}(k_2)}}{1+e^{\beta E_{A_{i_2}}(k_2)}}$$

$$\Bigg[\sum_{\zeta_1,\zeta_2}\Bigg(\Gamma^r_{\zeta_1,\zeta_2}a_{\zeta_1,i_1}a_{\zeta_2,i_2}e^{ik_1\left(\frac{L}{2}-\delta_{\zeta_1,\zeta_2}\frac{\xi}{2}\right)}e^{ik_2\left(\frac{L}{2}+\delta_{\zeta_1,\zeta_2}\frac{\xi}{2}\right)}-$$

$$\Gamma^r_{\zeta_1,\zeta_2}a_{\zeta_1,i_2}a_{\zeta_2,i_1}e^{ik_2\left(\frac{L}{2}-\delta_{\zeta_1,\zeta_2}\frac{\xi}{2}\right)}e^{ik_1\left(\frac{L}{2}+\delta_{\zeta_1,\zeta_2}\frac{\xi}{2}\right)}\Bigg)$$

$$\sum_{\zeta_3,\zeta_4}\Bigg((\Gamma^l_{\zeta_3,\zeta_4})^*a_{\zeta_3,i_1}a_{\zeta_4,i_2}e^{-ik_1\left(-\frac{L}{2}-\delta_{\zeta_3,\zeta_4}\frac{\xi}{2}\right)}e^{-ik_2\left(-\frac{L}{2}+\delta_{\zeta_3,\zeta_4}\frac{\xi}{2}\right)}-$$

$$(\Gamma^l_{\zeta_3,\zeta_4})^*a_{\zeta_3,i_2}a_{\zeta_4,i_1}e^{-ik_2\left(-\frac{L}{2}-\delta_{\zeta_3,\zeta_4}\frac{\xi}{2}\right)}e^{-ik_1\left(-\frac{L}{2}+\delta_{\zeta_3,\zeta_4}\frac{\xi}{2}\right)}\Bigg)\Bigg]\Bigg\}. \tag{B.3}$$

In the previous expression, the building block is represented by the integral

$$\int_{-\infty}^{+\infty}dk\,e^{-iE_{A_{i_1/i_2}}(k)t'/\hbar}\frac{e^{\beta E_{A_{i_1/i_2}}(k)}}{1+e^{\beta E_{A_{i_1/i_2}}(k)}}e^{ik\left[L+(\pm\delta_{\zeta_1,\zeta_2}\pm\delta_{\zeta_3,\zeta_4})\frac{\xi}{2}\right]}, \tag{B.4}$$

where all the combinations of signs $\pm$ are possible. Let the generic energy dispersion be written as $E_{A_{i_1/i_2}}(k) = f_{i_1/i_2} + \rho_{i_1/i_2}\hbar v_F k$, with $\rho_{i_1/i_2} = \pm 1$ and $f_{i_1/i_2} = \pm f$, then it can be computed

$$\int_{-\infty}^{+\infty}dk\,e^{-iE_{A_{i_1/i_2}}(k)t'/\hbar}\frac{e^{\beta E_{A_{i_1/i_2}}(k)}}{1+e^{\beta E_{A_{i_1/i_2}}(k)}}e^{ik\left[L+(\pm\delta_{\zeta_1,\zeta_2}\pm\delta_{\zeta_3,\zeta_4})\frac{\xi}{2}\right]}=$$

$$=\exp\left\{\left[\left(L+(\pm\delta_{\zeta_1,\zeta_2}\pm\delta_{\zeta_3,\zeta_4})\frac{\xi}{2}\right)i-\rho_{i_1/i_2}\xi\right]\frac{(-f_{i_1/i_2})}{\rho_{i_1/i_2}\hbar v_F}\right\}$$

$$\frac{1}{\sinh\left[\frac{\pi}{\hbar\beta v_F}(L\pm(\delta_{\zeta_1,\zeta_2}\pm\delta_{\zeta_3,\zeta_4})\frac{\xi}{2}-\rho_{i_1/i_2}v_Ft'+i\rho_{i_1/i_2}\xi)\right]}\left(\frac{\pi i}{\rho_{i_1/i_2}\beta\hbar v_F}\right). \tag{B.5}$$

Inserting these results in Eq. (3.25) and distinguishing explicitly the cases $i_1 = i_2$ and $i_1 \neq i_2$ in the sum over $i_1 i_2$, the current $I^r(t)$ reads as follows

$$I^r(t) = \frac{8e}{(2\pi\hbar)^2}\mathrm{Im}\Bigg\{\int_{-\infty}^{+\infty}dt'\Theta(t')\sum_{i_1,i_2}\sum_{\zeta_1,\zeta_2}\sum_{\zeta_3,\zeta_4}\Gamma^r_{\zeta_1,\zeta_2}(\Gamma^l_{\zeta_3,\zeta_4})^*$$

$$\Bigg[-\delta_{i_1,i_2}\mathrm{Im}\Bigg\{ a_{\zeta_1,i_1}a_{\zeta_4,i_1}a_{\zeta_2,i_1}a_{\zeta_3,i_1}e^{\Big\{\big[\big(L-(\delta_{\zeta_1,\zeta_2}+\delta_{\zeta_3,\zeta_4})\frac{\xi}{2}\big)i-\rho_{i_1}\lambda\big]\frac{-f_{i_1}}{\rho_{i_1}\hbar v_F}\Big\}}$$

$$\frac{1}{\sinh\big[\frac{\pi}{\hbar\beta v_F}(L-(\delta_{\zeta_1,\zeta_2}+\delta_{\zeta_3,\zeta_4})\frac{\xi}{2}-\rho_{i_1}v_Ft'+i\rho_{i_1}\lambda)\big]}e^{\Big\{\big[\big(L+(\delta_{\zeta_1,\zeta_2}+\delta_{\zeta_3,\zeta_4})\frac{\xi}{2}\big)i-\rho_{i_1}\lambda\big]\frac{-f_{i_1}}{\rho_{i_1}\hbar v_F}\Big\}}$$

$$\frac{1}{\sinh\big[\frac{\pi}{\hbar\beta v_F}(L+(\delta_{\zeta_1,\zeta_2}+\delta_{\zeta_3,\zeta_4})\frac{\xi}{2}-\rho_{i_1}v_Ft'+i\rho_{i_1}\lambda)\big]}\left(\frac{\pi i}{\rho_{i_1}\beta\hbar v_F}\right)^2\Bigg\}$$

$$+\delta_{i_1,i_2}\mathrm{Im}\Bigg\{ a_{\zeta_1,i_1}a_{\zeta_2,i_2}a_{\zeta_3,i_1}a_{\zeta_4,i_2}e^{\Big\{\big[\big(L+(-\delta_{\zeta_1,\zeta_2}+\delta_{\zeta_3,\zeta_4})\frac{\xi}{2}\big)i-\rho_{i_1}\lambda\big]\frac{-f_{i_1}}{\rho_{i_1}\hbar v_F}\Big\}}$$

$$\frac{1}{\sinh\big[\frac{\pi}{\hbar\beta v_F}(L+(-\delta_{\zeta_1,\zeta_2}+\delta_{\zeta_3,\zeta_4})\frac{\xi}{2}-\rho_{i_1}v_Ft'+i\rho_{i_1}\lambda)\big]}e^{\Big\{\big[\big(L+(\delta_{\zeta_1,\zeta_2}-\delta_{\zeta_3,\zeta_4})\frac{\xi}{2}\big)i-\rho_{i_2}\lambda\big]\frac{-f_{i_2}}{\rho_{i_2}\hbar v_F}\Big\}}$$

$$\frac{1}{\sinh\big[\frac{\pi}{\hbar\beta v_F}(L+(\delta_{\zeta_1,\zeta_2}-\delta_{\zeta_3,\zeta_4})\frac{\xi}{2}-\rho_{i_2}v_Ft'+i\rho_{i_2}\lambda)\big]}\left(\frac{\pi i}{\rho_{i_1}\beta\hbar v_F}\right)\left(\frac{\pi i}{\rho_{i_2}\beta\hbar v_F}\right)\Bigg\}$$

$$+\delta_{i_1,-i_2}\mathrm{Im}\Bigg\{ a_{\zeta_1,i_1}a_{\zeta_2,i_2}a_{\zeta_3,i_1}a_{\zeta_4,i_2}e^{\Big\{\big[\big(L+(-\delta_{\zeta_1,\zeta_2}+\delta_{\zeta_3,\zeta_4})\frac{\xi}{2}\big)i-\rho_{i_1}\lambda\big]\frac{-f_{i_1}}{\rho_{i_1}\hbar v_F}\Big\}}$$

$$\frac{1}{\sinh\big[\frac{\pi}{\hbar\beta v_F}(L+(-\delta_{\zeta_1,\zeta_2}+\delta_{\zeta_3,\zeta_4})\frac{\xi}{2}-\rho_{i_1}v_Ft'+i\rho_{i_1}\lambda)\big]}e^{\Big\{\big[\big(L+(\delta_{\zeta_1,\zeta_2}-\delta_{\zeta_3,\zeta_4})\frac{\xi}{2}\big)i-\rho_{i_2}\lambda\big]\frac{-f_{i_2}}{\rho_{i_2}\hbar v_F}\Big\}}$$

$$\frac{1}{\sinh\big[\frac{\pi}{\hbar\beta v_F}(L+(\delta_{\zeta_1,\zeta_2}-\delta_{\zeta_3,\zeta_4})\frac{\xi}{2}-\rho_{i_2}v_Ft'+i\rho_{i_2}\lambda)\big]}\left(\frac{\pi i}{\rho_{i_1}\beta\hbar v_F}\right)\left(\frac{\pi i}{\rho_{i_2}\beta\hbar v_F}\right)\Bigg\}$$

$$-\delta_{i_1,-i_2}\mathrm{Im}\Bigg\{ a_{\zeta_1,i_1}a_{\zeta_2,i_2}a_{\zeta_3,i_2}a_{\zeta_4,i_1}e^{\Big\{\big[\big(L+(-\delta_{\zeta_1,\zeta_2}-\delta_{\zeta_3,\zeta_4})\frac{\xi}{2}\big)i-\rho_{i_1}\lambda\big]\frac{-f_{i_1}}{\rho_{i_1}\hbar v_F}\Big\}}$$

$$\frac{1}{\sinh\big[\frac{\pi}{\hbar\beta v_F}(L+(-\delta_{\zeta_1,\zeta_2}-\delta_{\zeta_3,\zeta_4})\frac{\xi}{2}-\rho_{i_1}v_Ft'+i\rho_{i_1}\lambda)\big]}e^{\Big\{\big[\big(L+(\delta_{\zeta_1,\zeta_2}+\delta_{\zeta_3,\zeta_4})\frac{\xi}{2}\big)i-\rho_{i_2}\lambda\big]\frac{-f_{i_2}}{\rho_{i_2}\hbar v_F}\Big\}}$$

$$\frac{1}{\sinh\big[\frac{\pi}{\hbar\beta v_F}(L+(\delta_{\zeta_1,\zeta_2}+\delta_{\zeta_3,\zeta_4})\frac{\xi}{2}-\rho_{i_2}v_Ft'+i\rho_{i_2}\lambda)\big]}\left(\frac{\pi i}{\rho_{i_1}\beta\hbar v_F}\right)\left(\frac{\pi i}{\rho_{i_2}\beta\hbar v_F}\right)\Bigg\}$$

$$-\delta_{i_1,-i_2}\mathrm{Im}\Bigg\{ a_{\zeta_1,i_2}a_{\zeta_2,i_1}a_{\zeta_3,i_1}a_{\zeta_4,i_2}e^{\Big\{\big[\big(L+(\delta_{\zeta_1,\zeta_2}+\delta_{\zeta_3,\zeta_4})\frac{\xi}{2}\big)i-\rho_{i_1}\lambda\big]\frac{-f_{i_1}}{\rho_{i_1}\hbar v_F}\Big\}}$$

$$\frac{1}{\sinh\big[\frac{\pi}{\hbar\beta v_F}(L+(\delta_{\zeta_1,\zeta_2}+\delta_{\zeta_3,\zeta_4})\frac{\xi}{2}-\rho_{i_1}v_Ft'+i\rho_{i_1}\lambda)\big]}e^{\Big\{\big[\big(L+(-\delta_{\zeta_1,\zeta_2}-\delta_{\zeta_3,\zeta_4})\frac{\xi}{2}\big)i-\rho_{i_2}\lambda\big]\frac{-f_{i_2}}{\rho_{i_2}\hbar v_F}\Big\}}$$

$$\frac{1}{\sinh\big[\frac{\pi}{\hbar\beta v_F}(L+(-\delta_{\zeta_1,\zeta_2}-\delta_{\zeta_3,\zeta_4})\frac{\xi}{2}-\rho_{i_2}v_Ft'+i\rho_{i_2}\lambda)\big]}\left(\frac{\pi i}{\rho_{i_1}\beta\hbar v_F}\right)\left(\frac{\pi i}{\rho_{i_2}\beta\hbar v_F}\right)\Bigg\}$$

$$+\delta_{i_1,-i_2}\mathrm{Im}\Bigg\{ a_{\zeta_1,i_2}a_{\zeta_2,i_1}a_{\zeta_3,i_2}a_{\zeta_4,i_1}e^{\Big\{\big[\big(L+(\delta_{\zeta_1,\zeta_2}-\delta_{\zeta_3,\zeta_4})\frac{\xi}{2}\big)i-\rho_{i_1}\lambda\big]\frac{-f_{i_1}}{\rho_{i_1}\hbar v_F}\Big\}}$$

$$\frac{1}{\sinh\big[\frac{\pi}{\hbar\beta v_F}(L+(\delta_{\zeta_1,\zeta_2}-\delta_{\zeta_3,\zeta_4})\frac{\xi}{2}-\rho_{i_1}v_Ft'+i\rho_{i_1}\lambda)\big]}e^{\Big\{\big[\big(L+(-\delta_{\zeta_1,\zeta_2}+\delta_{\zeta_3,\zeta_4})\frac{\xi}{2}\big)i-\rho_{i_2}\lambda\big]\frac{-f_{i_2}}{\rho_{i_2}\hbar v_F}\Big\}}$$

$$\frac{1}{\sinh\left[\frac{\pi}{\hbar\beta v_F}(L+(-\delta_{\zeta_1,\zeta_2}+\delta_{\zeta_3,\zeta_4})\frac{\xi}{2}-\rho_{i_2}v_F t'+i\rho_{i_2}\lambda)\right]}\left(\frac{\pi i}{\rho_{i_1}\beta\hbar v_F}\right)\left(\frac{\pi i}{\rho_{i_2}\beta\hbar v_F}\right)\Bigg\}\Bigg]\Bigg\}. \tag{B.6}$$

The summation over i_1, i_2 runs over 10 terms that can be divided into three cases:

1. $i_1 = i_2$, including $i_1, i_2 = 1,1 \quad 2,2 \quad 3,3 \quad 4,4$;
2. $i_1 \neq i_2$, with A_{k_1,i_1} and A_{k_2,i_2} being both right-movers or both left-movers, including $i_1, i_2 = 1,2 \quad 3,4$;
3. $i_1 \neq i_2$, with A_{k_1,i_1} and A_{k_2,i_2} having opposite directions of propagation, including $i_1, i_2 = 1,3 \quad 1,4 \quad 2,3 \quad 2,4$.

Table B.1 makes explicit the three cases, by looking at Eq. (3.8).

		f_{i_1}	f_{i_2}	ρ_{i_1}	ρ_{i_2}
(i)	1, 1	$-f$	$-f$	-1	-1
	2, 2	f	f	-1	-1
	3, 3	$-f$	$-f$	1	1
	4, 4	f	f	1	1
(ii)	1, 2	$-f$	f	-1	-1
	3, 4	$-f$	f	1	1
(iii)	1, 3	$-f$	$-f$	-1	1
	1, 4	$-f$	f	-1	1
	2, 3	f	$-f$	-1	1
	2, 4	f	f	-1	1

Table B.1: *Details concerning the ten terms of the summation over i_1, i_2 in Eq. (B.6).*

The next step consists in developing the summations over ζ_1, ζ_2 and ζ_3, ζ_4, remembering that the possible values are only those listed in (B.2). Since some of the $a_{\zeta,i}$ are zero, the corresponding addends of the sum will not contribute to the current. The last thing to be done is the evaluation of the eighteen integrals intervening once the previous expression is expanded. In particular

$$I_1 = \int_0^{+\infty} ds\, e^{i\tilde{V}s}\mathrm{Im}\frac{\tilde{T}^2}{\sinh\left[\tilde{T}\left(\tilde{L}-s+i\right)\right]\sinh\left[\tilde{T}\left(\tilde{L}+s-i\right)\right]}, \tag{B.7}$$

$$I_2 = \int_0^{+\infty} ds\, e^{i\tilde{V}s}\mathrm{Re}\frac{\tilde{T}^2}{\sinh\left[\tilde{T}\left(\tilde{L}-s+i\right)\right]\sinh\left[\tilde{T}\left(\tilde{L}+s-i\right)\right]}, \tag{B.8}$$

$$I_3 = \int_0^{+\infty} ds\, e^{i\tilde{V}s}\mathrm{Im}\frac{\tilde{T}^2}{\sinh^2\left[\tilde{T}\left(\tilde{L}-s+i\right)\right]}, \tag{B.9}$$

$$I_4 = \int_0^{+\infty} ds\, e^{i\tilde{V}s}\mathrm{Re}\frac{\tilde{T}^2}{\sinh^2\left[\tilde{T}\left(\tilde{L}-s+i\right)\right]}, \tag{B.10}$$

$$I_5 = \int_0^{+\infty} ds\, e^{i\tilde{V}s}\mathrm{Im}\frac{\tilde{T}^2}{\sinh^2\left[\tilde{T}\left(\tilde{L}+s-i\right)\right]}, \tag{B.11}$$

$$I_6 = \int_0^{+\infty} ds\, e^{i\tilde{V}s} \mathrm{Re} \frac{\tilde{T}^2}{\sinh^2\left[\tilde{T}\left(\tilde{L}+s-i\right)\right]}, \tag{B.12}$$

$$I_7 = \int_0^{+\infty} ds\, e^{i\tilde{V}s} \mathrm{Im} \frac{\tilde{T}^2}{\sinh^4\left[\tilde{T}\left(\tilde{L}-s+i\right)\right]}, \tag{B.13}$$

$$I_8 = \int_0^{+\infty} ds\, e^{i\tilde{V}s} \mathrm{Re} \frac{\tilde{T}^2}{\sinh^4\left[\tilde{T}\left(\tilde{L}-s+i\right)\right]}, \tag{B.14}$$

$$I_9 = \int_0^{+\infty} ds\, e^{i\tilde{V}s} \mathrm{Im} \frac{\tilde{T}^2}{\sinh^4\left[\tilde{T}\left(\tilde{L}+s-i\right)\right]}, \tag{B.15}$$

$$I_{10} = \int_0^{+\infty} ds\, e^{i\tilde{V}s} \mathrm{Re} \frac{\tilde{T}^2}{\sinh^4\left[\tilde{T}\left(\tilde{L}+s-i\right)\right]}, \tag{B.16}$$

$$I_{11} = \int_0^{+\infty} ds\, e^{i\tilde{V}s} \mathrm{Im} \frac{\tilde{T}^2}{\sinh\left[\tilde{T}\left(\tilde{L}-1-s+i\right)\right]\sinh\left[\tilde{T}\left(\tilde{L}+1-s+i\right)\right]}, \tag{B.17}$$

$$I_{12} = \int_0^{+\infty} ds\, e^{i\tilde{V}s} \mathrm{Re} \frac{\tilde{T}^2}{\sinh\left[\tilde{T}\left(\tilde{L}-1-s+i\right)\right]\sinh\left[\tilde{T}\left(\tilde{L}+1-s+i\right)\right]}, \tag{B.18}$$

$$I_{13} = \int_0^{+\infty} ds\, e^{i\tilde{V}s} \mathrm{Im} \frac{\tilde{T}^2}{\sinh\left[\tilde{T}\left(\tilde{L}-\frac{1}{2}-s+i\right)\right]\sinh\left[\tilde{T}\left(\tilde{L}+\frac{1}{2}-s+i\right)\right]}, \tag{B.19}$$

$$I_{14} = \int_0^{+\infty} ds\, e^{i\tilde{V}s} \mathrm{Re} \frac{\tilde{T}^2}{\sinh\left[\tilde{T}\left(\tilde{L}-\frac{1}{2}-s+i\right)\right]\sinh\left[\tilde{T}\left(\tilde{L}+\frac{1}{2}-s+i\right)\right]}, \tag{B.20}$$

$$I_{15} = \int_0^{+\infty} ds\, e^{i\tilde{V}s} \mathrm{Im} \frac{\tilde{T}^2}{\sinh\left[\tilde{T}\left(\tilde{L}-1+s-i\right)\right]\sinh\left[\tilde{T}\left(\tilde{L}+1+s-i\right)\right]}, \tag{B.21}$$

$$I_{16} = \int_0^{+\infty} ds\, e^{i\tilde{V}s} \mathrm{Re} \frac{\tilde{T}^2}{\sinh\left[\tilde{T}\left(\tilde{L}-1+s-i\right)\right]\sinh\left[\tilde{T}\left(\tilde{L}+1+s-i\right)\right]}, \tag{B.22}$$

$$I_{17} = \int_0^{+\infty} ds\, e^{i\tilde{V}s} \mathrm{Im} \frac{\tilde{T}^2}{\sinh\left[\tilde{T}\left(\tilde{L}-\frac{1}{2}+s-i\right)\right]\sinh\left[\tilde{T}\left(\tilde{L}+\frac{1}{2}+s-i\right)\right]}, \tag{B.23}$$

$$I_{18} = \int_0^{+\infty} ds\, e^{i\tilde{V}s} \mathrm{Re} \frac{\tilde{T}^2}{\sinh\left[\tilde{T}\left(\tilde{L}-\frac{1}{2}+s-i\right)\right]\sinh\left[\tilde{T}\left(\tilde{L}+\frac{1}{2}+s-i\right)\right]}. \tag{B.24}$$

Only those in Eqs. (B.7)-(B.16) are independent. Indeed, up to the second order in

ξ/L, we have

$$\begin{aligned}
I_{11} &\approx I_7 + I_3,\\
I_{12} &\approx I_8 + I_4,\\
I_{13} &\approx \frac{1}{4} I_7 + I_3,\\
I_{14} &\approx \frac{1}{4} I_8 + I_4,\\
I_{15} &\approx I_9 + I_5,\\
I_{16} &\approx I_{10} + I_6,\\
I_{17} &\approx \frac{1}{4} I_9 + I_5,\\
I_{18} &\approx \frac{1}{4} I_{10} + I_6.
\end{aligned}$$

Some of the independent integrals are already present in [78], the other ones have been evaluated under the same assumptions and up to the same order in ξ. We obtain

$$\begin{aligned}
I_1 &\approx -\frac{\pi \tilde{T} e^{\left(i\tilde{V}\tilde{L}-\tilde{V}\right)}}{\sinh\left(2\tilde{T}\tilde{L}\right)},\\
I_2 &\approx -i\frac{\pi \tilde{T} e^{\left(i\tilde{V}\tilde{L}-\tilde{V}\right)}}{\sinh\left(2\tilde{T}\tilde{L}\right)},\\
I_3 &\approx i\pi \tilde{V} e^{\left(i\tilde{V}\tilde{L}-\tilde{V}\right)},\\
I_4 &\approx -\pi \tilde{V} e^{\left(i\tilde{V}\tilde{L}-\tilde{V}\right)},\\
I_5 &\approx 0,\\
I_6 &\approx 0,\\
I_7 &\approx -i\frac{\pi}{6}\tilde{V}\left(\tilde{V}^2 + 4\tilde{T}^2\right) e^{\left(i\tilde{V}\tilde{L}-\tilde{V}\right)},\\
I_8 &\approx \frac{\pi}{6}\tilde{V}\left(\tilde{V}^2 + 4\tilde{T}^2\right) e^{\left(i\tilde{V}\tilde{L}-\tilde{V}\right)},\\
I_9 &\approx 0,\\
I_{10} &\approx 0.
\end{aligned}$$

Once the integration over s is done, we obtain

$$I^r(t) = \mathcal{C}\,\mathrm{Im}\left\{ e^{-i(\omega_J t+\varphi_0)} \left[\tilde{A}_1^r \cos\left(\pi\frac{\phi}{\phi_0}\right) + \tilde{A}_2^r \sin\left(\frac{\pi}{2}\frac{\phi}{\phi_0}\right) + \tilde{A}_3^r \right] \right\}, \tag{B.25}$$

with $\mathcal{C} = (-2e\Delta\Gamma^2)/(\pi^2\hbar^3 v_F^2)$ as defined in the main text and $\tilde{A}_1^r$, $\tilde{A}_2^r$, $\tilde{A}_3^r$ reported there explicitly.

Bibliography

[1] I. Affleck, J.-S. Caux, and A. M. Zagoskin. Andreev scattering and Josephson current in a one-dimensional electron liquid. *Phys. Rev. B*, 62:1433–1445, 2000. doi:10.1103/PhysRevB.62.1433.

[2] A. R. Akhmerov, J. Nilsson, and C. W. J. Beenakker. Electrically Detected Interferometry of Majorana Fermions in a Topological Insulator. *Phys. Rev. Lett.*, 102:216404, 2009. doi:10.1103/PhysRevLett.102.216404.

[3] J. Alicea. New directions in the pursuit of Majorana fermions in solid state systems. *Reports on Progress in Physics*, 75(7):076501, 2012. doi:10.1088/0034-4885/75/7/076501.

[4] A. Altland and B. Simons. *Condensed Matter Field Theory*. Cambridge University Press, 2010. URL `https://doi.org/10.1017/CBO9780511789984`.

[5] V. Ambegaokar and A. Baratoff. Tunneling Between Superconductors. *Phys. Rev. Lett.*, 10:486–489, 1963. doi:10.1103/PhysRevLett.10.486.

[6] P. W. Anderson. *Ravello - Lectures on the Many-Body Problem*. ed. E. R. Caianello (Academic Press, New York), 1963. URL `https://doi.org/10.1016/B978-0-12-395616-3.X5001-3`.

[7] P. W. Anderson and J. M. Rowell. Probable Observation of the Josephson Superconducting Tunneling Effect. *Phys. Rev. Lett.*, 10:230–232, 1963. doi:10.1103/PhysRevLett.10.230.

[8] F. Ando, Y. Miyasaka, T. Li, J. Ishizuka, T. Arakawa, Y. Shiota, T. Moriyama, Y. Yanase, and T. Ono. Observation of superconducting diode effect. *Nature*, 584(7821):373–376, 2020. doi:10.1038/s41586-020-2590-4.

[9] A. Assouline, C. Feuillet-Palma, N. Bergeal, T. Zhang, A. Mottaghizadeh, A. Zimmers, E. Lhuillier, M. Eddrie, P. Atkinson, M. Aprili, and H. Aubin. Spin-Orbit induced phase-shift in Bi2Se3 Josephson junctions. *Nature Communications*, 10(1):126, 2019. doi:10.1038/s41467-018-08022-y.

[10] E. P. Balsamo, G. Paternò, A. Barone, M. Russo, and R. Vaglio. Temperature and magnetic field dependence of the critical current in Sn-SnxOy-in Josephson junctions. *physica status solidi (a)*, 35(2):K173–K175, 1976, https://onlinelibrary.wiley.com/doi/pdf/10.1002/pssa.2210350266. doi:https://doi.org/10.1002/pssa.2210350266.

[11] J. Bardeen, L. N. Cooper, and J. R. Schrieffer. Theory of Superconductivity. *Phys. Rev.*, 108:1175–1204, 1957. doi:10.1103/PhysRev.108.1175.

[12] A. Barone and G. Paternò. *Physics and Applications of the Josephson Effect*. John Wiley & Sons, Ltd.: Hoboken, NJ, USA, 1982. URL `https://doi.org/10.1002/352760278X`.

[13] V. Barzykin and A. M. Zagoskin. Coherent transport and nonlocality in mesoscopic SNS junctions: anomalous magnetic interference patterns. *Superlattices and Microstructures*, 25(5):797–807, 1999. doi:https://doi.org/10.1006/spmi.1999.0731.

[14] J. J. A. Baselmans, A. F. Morpurgo, B. J. van Wees, and T. M. Klapwijk. Reversing the direction of the supercurrent in a controllable Josephson junction. *Nature*, 397(6714):43–45, 1999. doi:10.1038/16204.

[15] C. Baumgartner, L. Fuchs, A. Costa, J. Picó-Cortés, S. Reinhardt, S. Gronin, G. C. Gardner, T. Lindemann, M. J. Manfra, P. E. Faria Junior, D. Kochan, J. Fabian, N. Paradiso, and C. Strunk. Effect of Rashba and Dresselhaus spin–orbit coupling on supercurrent rectification and magnetochiral anisotropy of ballistic Josephson junctions. *Journal of Physics: Condensed Matter*, 34(15):154005, 2022. doi:10.1088/1361-648X/ac4d5e.

[16] B. Baxevanis, V. P. Ostroukh, and C. W. J. Beenakker. Even-odd flux quanta effect in the Fraunhofer oscillations of an edge-channel Josephson junction. *Phys. Rev. B*, 91:041409, 2015. doi:10.1103/PhysRevB.91.041409.

[17] C. R. Becker, C. Brüne, M. Schäfer, A. Roth, H. Buhmann, and L. W. Molenkamp. The influence of interfaces and the modulation doping technique on the magneto-transport properties of HgTe based quantum wells. *Physica Status Solidi c*, 4(9):3382–3389, 2007, https://onlinelibrary.wiley.com/doi/pdf/10.1002/pssc.200775402. doi:https://doi.org/10.1002/pssc.200775402.

[18] K. Bendias, S. Shamim, O. Herrmann, A. Budewitz, P. Shekhar, P. Leubner, J. Kleinlein, E. Bocquillon, H. Buhmann, and L. W. Molenkamp. High Mobility HgTe Microstructures for Quantum Spin Hall Studies. *Nano Letters*, 18(8):4831–4836, 2018. doi:10.1021/acs.nanolett.8b01405.

[19] F. S. Bergeret and I. V. Tokatly. Theory of diffusive ϕ_0 Josephson junctions in the presence of spin-orbit coupling. *Europhysics Letters*, 110(5):57005, 2015. doi:10.1209/0295-5075/110/57005.

[20] B. A. Bernevig. *Topological Insulators and Topological Superconductors*. Princeton University Press, 2013. URL `https://books.google.at/books?id=w0n7JHSSxrsC`.

[21] B. A. Bernevig, T. L. Hughes, and S.-C. Zhang. Quantum Spin Hall Effect and Topological Phase Transition in HgTe Quantum Wells. *Science*, 314(5806):1757–1761, 2006. doi:10.1126/science.1133734.

[22] A. M. Black-Schaffer and A. V. Balatsky. Odd-frequency superconducting pairing in topological insulators. *Phys. Rev. B*, 86:144506, 2012. doi:10.1103/PhysRevB.86.144506.

[23] G. Blasi, F. Taddei, L. Arrachea, M. Carrega, and A. Braggio. Nonlocal Thermoelectricity in a Superconductor–Topological-Insulator–Superconductor Junction in Contact with a Normal-Metal Probe: Evidence for Helical Edge States. *Phys. Rev. Lett.*, 124:227701, 2020. doi:10.1103/PhysRevLett.124.227701.

[24] G. Blasi, F. Taddei, V. Giovannetti, and A. Braggio. Manipulation of Cooper pair entanglement in hybrid topological Josephson junctions. *Phys. Rev. B*, 99:064514, 2019. doi:10.1103/PhysRevB.99.064514.

[25] D. Breunig, P. Burset, and B. Trauzettel. Creation of Spin-Triplet Cooper Pairs in the Absence of Magnetic Ordering. *Phys. Rev. Lett.*, 120:037701, 2018. doi:10.1103/PhysRevLett.120.037701.

[26] C. Bruder, R. Fazio, and G. Schön. Proximity effect and charging in mesoscopic normal-metal–superconductor junction systems. *Phys. Rev. B*, 50:12766–12769, 1994. doi:10.1103/PhysRevB.50.12766.

[27] C. Brüne, A. Roth, H. Buhmann, E. M. Hankiewicz, L. W. Molenkamp, J. Maciejko, X.-L. Qi, and S.-C. Zhang. Spin polarization of the quantum spin Hall edge states. *Nature Physics*, 8(6):485–490, 2012. doi:10.1038/nphys2322.

[28] H. Bruus and K. Flensberg. *Many-Body Quantum Theory in Condensed Matter Physics: An Introduction*. Oxford Graduate Texts. OUP Oxford, 2004. URL `https://books.google.it/books?id=CktuBAAAQBAJ`.

[29] L. N. Bulaevskii, V. V. Kuzii, and A. A. Sobyanin. On possibility of the spontaneous magnetic flux in a Josephson junction containing magnetic impurities. *Solid State Communications*, 25(12):1053–1057, 1978. doi:https://doi.org/10.1016/0038-1098(78)90906-7.

[30] L. N. Bulaevskiĭ, V. V. Kuziĭ, and A. A. Sobyanin. Superconducting system with weak coupling to the current in the ground state. *Soviet Journal of Experimental and Theoretical Physics Letters*, 25:290, 1977. URL `https://www.osti.gov/biblio/7316063`.

[31] M. Büttiker. Four-terminal phase-coherent conductance. *Phys. Rev. Lett.*, 57:1761–1764, 1986. doi:10.1103/PhysRevLett.57.1761.

[32] M. Büttiker. Absence of backscattering in the quantum Hall effect in multiprobe conductors. *Phys. Rev. B*, 38:9375–9389, 1988. doi:10.1103/PhysRevB.38.9375.

[33] M. Büttiker. Edge-state physics without magnetic fields. *Science*, 325(5938):278–279, 2009, https://www.science.org/doi/pdf/10.1126/science.1177157. doi:10.1126/science.1177157.

[34] A. Buzdin. Direct Coupling Between Magnetism and Superconducting Current in the Josephson φ_0 Junction. *Phys. Rev. Lett.*, 101:107005, 2008. doi:10.1103/PhysRevLett.101.107005.

[35] W. Chen, R. Shen, L. Sheng, B. G. Wang, and D. Y. Xing. Resonant nonlocal Andreev reflection in a narrow quantum spin Hall system. *Phys. Rev. B*, 84:115420, 2011. doi:10.1103/PhysRevB.84.115420.

[36] J.-P. Cleuziou, W. Wernsdorfer, V. Bouchiat, T. Ondarçuhu, and M. Monthioux. Carbon nanotube superconducting quantum interference device. *Nature Nanotechnology*, 1(1):53–59, 2006. doi:10.1038/nnano.2006.54.

[37] A. Cottet, T. Kontos, and A. L. Yeyati. Subradiant Split Cooper Pairs. *Phys. Rev. Lett.*, 108:166803, 2012. doi:10.1103/PhysRevLett.108.166803.

[38] F. Crépin, P. Burset, and B. Trauzettel. Odd-frequency triplet superconductivity at the helical edge of a topological insulator. *Phys. Rev. B*, 92:100507, 2015. doi:10.1103/PhysRevB.92.100507.

[39] F. Crépin, B. Trauzettel, and F. Dolcini. Signatures of Majorana bound states in transport properties of hybrid structures based on helical liquids. *Phys. Rev. B*, 89:205115, 2014. doi:10.1103/PhysRevB.89.205115.

[40] A. Das, Y. Ronen, M. Heiblum, D. Mahalu, A. V. Kretinin, and H. Shtrikman. High-efficiency Cooper pair splitting demonstrated by two-particle conductance resonance and positive noise cross-correlation. *Nature Communications*, 3(1):1165, 2012. doi:10.1038/ncomms2169.

[41] P. G. de Gennes. Self-consistent calculation of the Josephson current. *Physics Letters*, 5(1):22–24, 1963. doi:10.1016/S0375-9601(63)80011-0.

[42] F. K. de Vries, M. L. Sol, S. Gazibegovic, R. L. M. op het Veld, S. C. Balk, D. Car, E. P. A. M. Bakkers, L. P. Kouwenhoven, and J. Shen. Crossed Andreev reflection in InSb flake Josephson junctions. *Phys. Rev. Res.*, 1:032031, 2019. doi:10.1103/PhysRevResearch.1.032031.

[43] F. K. de Vries, T. Timmerman, V. P. Ostroukh, J. van Veen, A. J. A. Beukman, F. Qu, M. Wimmer, B.-M. Nguyen, A. A. Kiselev, W. Yi, M. Sokolich, M. J. Manfra, C. M. Marcus, and L. P. Kouwenhoven. h/e Superconducting Quantum Interference through Trivial Edge States in InAs. *Phys. Rev. Lett.*, 120:047702, 2018. doi:10.1103/PhysRevLett.120.047702.

[44] A. de Waele and R. de Bruyn Ouboter. Quantum-interference phenomena in point contacts between two superconductors. *Physica*, 41(2):225–254, 1969. doi:https://doi.org/10.1016/0031-8914(69)90116-5.

[45] R. S. Deacon, J. Wiedenmann, E. Bocquillon, F. Domínguez, T. M. Klapwijk, P. Leubner, C. Brüne, E. M. Hankiewicz, S. Tarucha, K. Ishibashi, H. Buhmann, and L. W. Molenkamp. Josephson Radiation from Gapless Andreev Bound States in HgTe-Based Topological Junctions. *Phys. Rev. X*, 7:021011, 2017. doi:10.1103/PhysRevX.7.021011.

[46] B. S. Deaver and W. M. Fairbank. Experimental Evidence for Quantized Flux in Superconducting Cylinders. *Phys. Rev. Lett.*, 7:43–46, 1961. doi:10.1103/PhysRevLett.7.43.

[47] G. Deutscher and D. Feinberg. Coupling superconducting-ferromagnetic point contacts by Andreev reflections. *Applied Physics Letters*, 76(4):487–489, 2000. doi:10.1063/1.125796.

[48] G. Dolcetto, M. Sassetti, and T. L. Schmidt. Edge physics in two-dimensional topological insulators. *La Rivista del Nuovo Cimento*, 39:113–154, 2016. doi:10.1393/ncr/i2016-10121-7.

[49] F. Dolcini. Full electrical control of charge and spin conductance through interferometry of edge states in topological insulators. *Phys. Rev. B*, 83:165304, 2011. doi:10.1103/PhysRevB.83.165304.

[50] F. Dolcini, M. Houzet, and J. S. Meyer. Topological Josephson ϕ_0 junctions. *Phys. Rev. B*, 92:035428, 2015. doi:10.1103/PhysRevB.92.035428.

[51] R. Doll and M. Näbauer. Experimental Proof of Magnetic Flux Quantization in a Superconducting Ring. *Phys. Rev. Lett.*, 7:51–52, 1961. doi:10.1103/PhysRevLett.7.51.

[52] P. Drude. Zur Elektronentheorie der Metalle; II. Teil. Galvanomagnetische und thermomagnetische Effecte. *Annalen der Physik*, 308:369–402, 1900. doi:10.1002/andp.19003081102.

[53] L. Du, I. Knez, G. Sullivan, and R.-R. Du. Robust Helical Edge Transport in Gated $\mathrm{InAs/GaSb}$ Bilayers. *Phys. Rev. Lett.*, 114:096802, 2015. doi:10.1103/PhysRevLett.114.096802.

[54] R. C. Dynes and T. A. Fulton. Supercurrent Density Distribution in Josephson Junctions. *Phys. Rev. B*, 3:3015–3023, 1971. doi:10.1103/PhysRevB.3.3015.

[55] A. K. Feofanov, V. A. Oboznov, V. V. Bol'ginov, J. Lisenfeld, S. Poletto, V. V. Ryazanov, A. N. Rossolenko, M. Khabipov, D. Balashov, A. B. Zorin, P. N. Dmitriev, V. P. Koshelets, and A. V. Ustinov. Implementation of superconductor/ferromagnet/ superconductor π-shifters in superconducting digital and quantum circuits. *Nature Physics*, 6(8):593–597, 2010. doi:10.1038/nphys1700.

[56] R. P. Feynman, R. B. Leighton, and M. L. Sands. *The Feynman Lectures on Physics: Quantum Mechanics (Vol. 3)*. Reading, MA: Addison-Wesley, 1965. URL `https://www.feynmanlectures.caltech.edu/III_toc.html`.

[57] F. Finocchiaro, F. Guinea, and P. San-Jose. Topological π Junctions from Crossed Andreev Reflection in the Quantum Hall Regime. *Phys. Rev. Lett.*, 120:116801, 2018. doi:10.1103/PhysRevLett.120.116801.

[58] M. D. Fiske. Temperature and Magnetic Field Dependences of the Josephson Tunneling Current. *Rev. Mod. Phys.*, 36:221–222, 1964. doi:10.1103/RevModPhys.36.221.

[59] C. Fleckenstein, F. Keidel, B. Trauzettel, and N. Traverso Ziani. The invisible Majorana bound state at the helical edge. *The European Physical Journal Special Topics*, 227:1377–1386, 2018. doi:10.1140/epjst/e2018-800093-5.

[60] C. Fleckenstein, N. Traverso Ziani, and B. Trauzettel. Conductance signatures of odd-frequency superconductivity in quantum spin Hall systems using a quantum point contact. *Phys. Rev. B*, 97:134523, 2018. doi:10.1103/PhysRevB.97.134523.

[61] C. Fleckenstein, N. T. Ziani, A. Calzona, M. Sassetti, and B. Trauzettel. Formation and detection of Majorana modes in quantum spin Hall trenches. *Phys. Rev. B*, 103:125303, Mar 2021. doi:10.1103/PhysRevB.103.125303.

[62] L. Fu and C. L. Kane. Superconducting Proximity Effect and Majorana Fermions at the Surface of a Topological Insulator. *Phys. Rev. Lett.*, 100:096407, 2008. doi:10.1103/PhysRevLett.100.096407.

[63] L. Fu and C. L. Kane. Josephson current and noise at a superconductor/quantum-spin-Hall-insulator/superconductor junction. *Phys. Rev. B*, 79:161408, 2009. doi:10.1103/PhysRevB.79.161408.

[64] V. B. Geshkenbe$\breve{\text{i}}$n and A. I. Larkin. The Josephson effect in superconductors with heavy fermions. *Pis'ma Zh. Eksp. Teor. Fiz.*, 43(6), 1986. doi:10.1016/0038-1098(86)90747-7.

[65] V. B. Geshkenbe$\breve{\text{i}}$n, A. I. Larkin, and A. Barone. Vortices with half magnetic flux quanta in "heavy-fermion" superconductors. *Phys. Rev. B*, 36:235–238, 1987. doi:10.1103/PhysRevB.36.235.

[66] F. Giazotto, F. Taddei, F. Beltram, and R. Fazio. Crossed Andreev Reflection-Induced Magnetoresistance. *Phys. Rev. Lett.*, 97:087001, 2006. doi:10.1103/PhysRevLett.97.087001.

[67] E. C. Gingrich, B. M. Niedzielski, J. A. Glick, Y. Wang, D. L. Miller, R. Loloee, W. P. Pratt Jr, and N. O. Birge. Controllable 0–π Josephson junctions containing a ferromagnetic spin valve. *Nature Physics*, 12(6):564–567, 2016. doi:10.1038/nphys3681.

[68] M. Gmitra, S. Konschuh, C. Ertler, C. Ambrosch-Draxl, and J. Fabian. Band-structure topologies of graphene: Spin-orbit coupling effects from first principles. *Phys. Rev. B*, 80:235431, 2009. doi:10.1103/PhysRevB.80.235431.

[69] M. O. Goerbig. *Quantum Hall Effect*. Lecture Notes of the Les Houches Summer School (Singapore Section), arXiv:0909.1998, 2009. doi:10.48550/arXiv.0909.1998.

[70] E. Goldobin, D. Koelle, R. Kleiner, and R. G. Mints. Josephson Junction with a Magnetic-Field Tunable Ground State. *Phys. Rev. Lett.*, 107:227001, 2011. doi:10.1103/PhysRevLett.107.227001.

[71] J. Goldstone and F. Wilczek. Fractional quantum numbers on solitons. *Phys. Rev. Lett.*, 47:986–989, 1981. doi:10.1103/PhysRevLett.47.986.

[72] A. A. Golubov, M. Y. Kupriyanov, and E. Il'ichev. The current-phase relation in Josephson junctions. *Rev. Mod. Phys.*, 76:411–469, 2004. doi:10.1103/RevModPhys.76.411.

[73] L. P. Gor'kov. Microscopic derivation of the Ginzburg-Landau equations in the theory of superconductivity. *Zh. Eksp. Teor. Fiz.*, 36:1918, 1959. URL `https://www.osti.gov/biblio/7264935`.

[74] M. Governale and U. Zülicke. Spin accumulation in quantum wires with strong Rashba spin-orbit coupling. *Phys. Rev. B*, 66:073311, 2002. doi:10.1103/PhysRevB.66.073311.

[75] R. Gross and A. Marx. *Applied Superconductivity: Josephson Effect and Superconducting Electronics*. Lecture notes. 2005. URL `https://www.wmi.badw.de/teaching/lecture-notes`.

[76] G. Grosso and G. Pastori Parravicini. *Solid State Physics*. Elsevier Science, 2000. doi:10.1016/B978-0-12-304460-0.X5000-2.

[77] C. Guarcello and F. Bergeret. Cryogenic Memory Element Based on an Anomalous Josephson Junction. *Phys. Rev. Appl.*, 13:034012, 2020. doi:10.1103/PhysRevApplied.13.034012.

[78] T. Haidekker Galambos, S. Hoffman, P. Recher, J. Klinovaja, and D. Loss. Superconducting Quantum Interference in Edge State Josephson Junctions. *Phys. Rev. Lett.*, 125:157701, 2020. doi:10.1103/PhysRevLett.125.157701.

[79] J. Hajer, M. Kessel, C. Brüne, M. P. Stehno, H. Buhmann, and L. W. Molenkamp. Proximity-Induced Superconductivity in CdTe–HgTe Core–Shell Nanowires. *Nano Letters*, 19(6):4078–4082, 2019, https://doi.org/10.1021/acs.nanolett.9b01472. doi:10.1021/acs.nanolett.9b01472. PMID: 31120766.

[80] F. D. M. Haldane. Model for a Quantum Hall Effect without Landau Levels: Condensed-Matter Realization of the "Parity Anomaly". *Phys. Rev. Lett.*, 61:2015–2018, 1988. doi:10.1103/PhysRevLett.61.2015.

[81] X. Hao, J. S. Moodera, and R. Meservey. Thin-film superconductor in an exchange field. *Phys. Rev. Lett.*, 67:1342–1345, 1991. doi:10.1103/PhysRevLett.67.1342.

[82] S. Hart, H. Ren, T. Wagner, P. Leubner, M. Mühlbauer, C. Brüne, H. Buhmann, L. W. Molenkamp, and A. Yacoby. Induced superconductivity in the quantum spin Hall edge. *Nature Physics*, 10(9):638–643, 2014. doi:10.1038/nphys3036.

[83] M. Z. Hasan and C. L. Kane. Colloquium: Topological insulators. *Rev. Mod. Phys.*, 82:3045–3067, 2010. doi:10.1103/RevModPhys.82.3045.

[84] S. Heedt, N. Traverso Ziani, F. Crépin, W. Prost, S. Trellenkamp, J. Schubert, D. Grützmacher, B. Trauzettel, and T. Schäpers. Signatures of interaction-induced helical gaps in nanowire quantum point contacts. *Nature Physics*, 13(6):563–567, 2017. doi:10.1038/nphys4070.

[85] J. P. Heida, B. J. van Wees, T. M. Klapwijk, and G. Borghs. Nonlocal supercurrent in mesoscopic Josephson junctions. *Phys. Rev. B*, 57:R5618–R5621, 1998. doi:10.1103/PhysRevB.57.R5618.

[86] L. G. Herrmann, F. Portier, P. Roche, A. L. Yeyati, T. Kontos, and C. Strunk. Carbon Nanotubes as Cooper-Pair Beam Splitters. *Phys. Rev. Lett.*, 104:026801, 2010. doi:10.1103/PhysRevLett.104.026801.

[87] S. Hoffman, D. Chevallier, D. Loss, and J. Klinovaja. Spin-dependent coupling between quantum dots and topological quantum wires. *Phys. Rev. B*, 96:045440, 2017. doi:10.1103/PhysRevB.96.045440.

[88] L. Hofstetter, S. Csonka, J. Nygård, and C. Schönenberger. Cooper pair splitter realized in a two-quantum-dot Y-junction. *Nature*, 461(7266):960–963, 2009. doi:10.1038/nature08432.

[89] Y. Hou, F. Nichele, H. Chi, A. Lodesani, Y. Wu, M. F. Ritter, D. Z. Haxell, M. Davydova, S. Ilić, O. Glezakou-Elbert, A. Varambally, F. S. Bergeret, A. Kamra, L. Fu, P. A. Lee, and J. S. Moodera. Ubiquitous Superconducting Diode Effect in Superconductor Thin Films. *Phys. Rev. Lett.*, 131:027001, 2023. doi:10.1103/PhysRevLett.131.027001.

[90] J. Hu, C. Wu, and X. Dai. Proposed Design of a Josephson Diode. *Phys. Rev. Lett.*, 99:067004, 2007. doi:10.1103/PhysRevLett.99.067004.

[91] R. Jackiw and C. Rebbi. Solitons with fermion number ½. *Phys. Rev. D*, 13:3398–3409, 1976. doi:10.1103/PhysRevD.13.3398.

[92] K. Jiang and J. Hu. Superconducting diode effects. *Nature Physics*, 18(10):1145–1146, 2022. doi:10.1038/s41567-022-01701-0.

[93] B. D. Josephson. Possible new effects in superconductive tunnelling. *Physics Letters*, 1(7):251–253, 1962. doi:https://doi.org/10.1016/0031-9163(62)91369-0.

[94] B. D. Josephson. Supercurrents through barriers. *Advances in Physics*, 14(56):419–451, 1965, https://doi.org/10.1080/00018736500101091. doi:10.1080/00018736500101091.

[95] C. L. Kane and E. J. Mele. Quantum Spin Hall Effect in Graphene. *Phys. Rev. Lett.*, 95:226801, 2005. doi:10.1103/PhysRevLett.95.226801.

[96] A. Y. Kitaev. Unpaired Majorana fermions in quantum wires. *Physics-Uspekhi*, 44(10S):131, 2001. doi:10.1070/1063-7869/44/10S/S29.

[97] C. Kittel. *Quantum Theory of Solids*. J. Wiley & Sons, New York, 1986. URL `https://books.google.at/books?id=BcGwQgAACAAJ`.

[98] T. M. Klapwijk. Proximity Effect From an Andreev Perspective. *Journal of Superconductivity*, 17(5):593–611, 2004. doi:10.1007/s10948-004-0773-0.

[99] M. König, H. Buhmann, L. W. Molenkamp, T. Hughes, C.-X. Liu, X.-L. Qi, and S.-C. Zhang. The Quantum Spin Hall Effect: Theory and Experiment. *Journal of the Physical Society of Japan*, 77(3):031007, 2008. doi:10.1143/JPSJ.77.031007.

[100] F. Konschelle, I. V. Tokatly, and F. S. Bergeret. Theory of the spin-galvanic effect and the anomalous phase shift φ_0 in superconductors and Josephson junctions with intrinsic spin-orbit coupling. *Phys. Rev. B*, 92:125443, 2015. doi:10.1103/PhysRevB.92.125443.

[101] N. B. Kopnin and A. S. Melnikov. Proximity-induced superconductivity in two-dimensional electronic systems. *Phys. Rev. B*, 84:064524, 2011. doi:10.1103/PhysRevB.84.064524.

[102] J. M. Kosterlitz and D. J. Thouless. Ordering, metastability and phase transitions in two-dimensional systems. *Journal of Physics C: Solid State Physics*, 6(7):1181, 1973. doi:10.1088/0022-3719/6/7/010.

[103] M. König, S. Wiedmann, C. Brüne, A. Roth, H. Buhmann, L. W. Molenkamp, X.-L. Qi, and S.-C. Zhang. Quantum Spin Hall Insulator State in HgTe Quantum Wells. *Science*, 318(5851):766–770, 2007, https://www.science.org/doi/pdf/10.1126/science.1148047. doi:10.1126/science.1148047.

[104] M. Lababidi and E. Zhao. Microscopic simulation of superconductor/topological insulator proximity structures. *Phys. Rev. B*, 83:184511, 2011. doi:10.1103/PhysRevB.83.184511.

[105] L. D. Landau and V. L. Ginzburg. On the theory of superconductivity. *Zh. Eksp. Teor. Fiz.*, 20:1064, 1950. URL `http://cds.cern.ch/record/486430`.

[106] L. D. Landau, E. M. Lifshitz, and L. P. Pitaevskii. *Course of Theoretical Physics: Statistical Physics, Part 2 : by E.M. Lifshitz and L.P. Pitaevskii*. Number v. 9. 1980. URL `https://books.google.it/books?id=QAcenQAACAAJ`.

[107] R. B. Laughlin. Quantized Hall conductivity in two dimensions. *Phys. Rev. B*, 23:5632–5633, 1981. doi:10.1103/PhysRevB.23.5632.

[108] U. Ledermann, A. L. Fauchère, and G. Blatter. Nonlocality in mesoscopic Josephson junctions with strip geometry. *Phys. Rev. B*, 59:R9027–R9030, 1999. doi:10.1103/PhysRevB.59.R9027.

[109] C.-A. Li, S.-B. Zhang, and S.-Q. Shen. Hidden edge Dirac point and robust quantum edge transport in InAs/GaSb quantum wells. *Phys. Rev. B*, 97:045420, 2018. doi:10.1103/PhysRevB.97.045420.

[110] J. Li, W. Pan, B. A. Bernevig, and R. M. Lutchyn. Detection of Majorana Kramers Pairs Using a Quantum Point Contact. *Phys. Rev. Lett.*, 117:046804, 2016. doi:10.1103/PhysRevLett.117.046804.

[111] J.-X. Lin, P. Siriviboon, H. D. Scammell, S. Liu, D. Rhodes, K. Watanabe, T. Taniguchi, J. Hone, M. S. Scheurer, and J. I. A. Li. Zero-field superconducting diode effect in small-twist-angle trilayer graphene. *Nature Physics*, 18(10):1221–1227, 2022. doi:10.1038/s41567-022-01700-1.

[112] J. Linder and J. W. A. Robinson. Superconducting spintronics. *Nature Physics*, 11(4):307–315, 2015. doi:10.1038/nphys3242.

[113] C.-X. Liu, J. C. Budich, P. Recher, and B. Trauzettel. Charge-spin duality in nonequilibrium transport of helical liquids. *Phys. Rev. B*, 83:035407, 2011. doi:10.1103/PhysRevB.83.035407.

[114] C.-X. Liu, T. L. Hughes, X.-L. Qi, K. Wang, and S.-C. Zhang. Quantum Spin Hall Effect in Inverted Type-II Semiconductors. *Phys. Rev. Lett.*, 100:236601, 2008. doi:10.1103/PhysRevLett.100.236601.

[115] J.-F. Liu and K. S. Chan. Relation between symmetry breaking and the anomalous Josephson effect. *Phys. Rev. B*, 82:125305, Sep 2010. doi:10.1103/PhysRevB.82.125305.

[116] E. Y. Ma, M. R. Calvo, J. Wang, B. Lian, M. Mühlbauer, C. Brüne, Y.-T. Cui, K. Lai, W. Kundhikanjana, Y. Yang, M. Baenninger, M. König, C. Ames, H. Buhmann, P. Leubner, L. W. Molenkamp, S.-C. Zhang, D. Goldhaber-Gordon, M. A. Kelly, and Z.-X. Shen. Unexpected edge conduction in mercury telluride quantum wells under broken time-reversal symmetry. *Nature Communications*, 6(1):7252, 2015. doi:10.1038/ncomms8252.

[117] W. Mayer, M. C. Dartiailh, J. Yuan, K. S. Wickramasinghe, E. Rossi, and J. Shabani. Gate controlled anomalous phase shift in Al/InAs Josephson junctions. *Nature Communications*, 11(1):212, 2020. doi:10.1038/s41467-019-14094-1.

[118] W. L. McMillan. Tunneling Model of the Superconducting Proximity Effect. *Phys. Rev.*, 175:537–542, 1968. doi:10.1103/PhysRev.175.537.

[119] R. Meservey and P. M. Tedrow. Spin-polarized electron tunneling. *Physics Reports*, 238(4):173–243, 1994. doi:https://doi.org/10.1016/0370-1573(94)90105-8.

[120] A. Messiah. *Quantum Mechanics*. Dover Publications, 1999. URL `https://books.google.at/books?id=mwssSDXzkNcC`.

[121] P. Michetti and B. Trauzettel. Devices with electrically tunable topological insulating phases. *Applied Physics Letters*, 102(063503), 2013. doi:https://doi.org/10.1063/1.4792275.

[122] S. V. Mironov, A. S. Mel'nikov, and A. I. Buzdin. Double Path Interference and Magnetic Oscillations in Cooper Pair Transport through a Single Nanowire. *Phys. Rev. Lett.*, 114:227001, 2015. doi:10.1103/PhysRevLett.114.227001.

[123] S. Murakami, N. Nagaosa, and S.-C. Zhang. Spin-Hall Insulator. *Phys. Rev. Lett.*, 93:156804, 2004. doi:10.1103/PhysRevLett.93.156804.

[124] C. Nayak, S. H. Simon, A. Stern, M. Freedman, and S. Das Sarma. Non-Abelian anyons and topological quantum computation. *Rev. Mod. Phys.*, 80:1083–1159, 2008. doi:10.1103/RevModPhys.80.1083.

[125] K. S. Novoselov, A. K. Geim, S. V. Morozov, D. Jiang, Y. Zhang, S. V. Dubonos, I. V. Grigorieva, and A. A. Firsov. Electric Field Effect in Atomically Thin Carbon Films. *Science*, 306(5696):666–669, 2004, https://www.science.org/doi/pdf/10.1126/science.1102896. doi:10.1126/science.1102896.

[126] K. C. Nowack, E. M. Spanton, M. Baenninger, M. König, J. R. Kirtley, B. Kalisky, C. Ames, P. Leubner, C. Brüne, H. Buhmann, L. W. Molenkamp, D. Goldhaber-Gordon, and K. A. Moler. Imaging currents in HgTe quantum wells in the quantum spin Hall regime. *Nature Materials*, 12(9):787–791, 2013. doi:10.1038/nmat3682.

[127] C. P. Orth, R. P. Tiwari, T. Meng, and T. L. Schmidt. Non-Abelian parafermions in time-reversal-invariant interacting helical systems. *Phys. Rev. B*, 91:081406, 2015. doi:10.1103/PhysRevB.91.081406.

[128] L. Ortiz, R. A. Molina, G. Platero, and A. M. Lunde. Generic helical edge states due to Rashba spin-orbit coupling in a topological insulator. *Phys. Rev. B*, 93:205431, 2016. doi:10.1103/PhysRevB.93.205431.

[129] B. Pal, A. Chakraborty, P. K. Sivakumar, M. Davydova, A. K. Gopi, A. K. Pandeya, J. A. Krieger, Y. Zhang, M. Date, S. Ju, N. Yuan, N. B. M. Schröter, L. Fu, and S. S. P. Parkin. Josephson diode effect from Cooper pair momentum in a topological semimetal. *Nature Physics*, 18(10):1228–1233, 2022. doi:10.1038/s41567-022-01699-5.

[130] S. Pal and C. Benjamin. Quantized Josephson phase battery. *Europhysics Letters*, 126(5):57002, 2019. doi:10.1209/0295-5075/126/57002.

[131] D. Pesin and A. H. MacDonald. Spintronics and pseudospintronics in graphene and topological insulators. *Nature Materials*, 11(5):409–416, 2012. doi:10.1038/nmat3305.

[132] K. Plekhanov, F. Ronetti, D. Loss, and J. Klinovaja. Hinge states in a system of coupled Rashba layers. *Phys. Rev. Res.*, 2:013083, 2020. doi:10.1103/PhysRevResearch.2.013083.

[133] A. C. Potter and P. A. Lee. Engineering a $p + ip$ superconductor: Comparison of topological insulator and Rashba spin-orbit-coupled materials. *Phys. Rev. B*, 83:184520, 2011. doi:10.1103/PhysRevB.83.184520.

[134] V. S. Pribiag, A. J. A. Beukman, F. Qu, M. C. Cassidy, C. Charpentier, W. Wegscheider, and L. P. Kouwenhoven. Edge-mode superconductivity in a two-dimensional topological insulator. *Nature Nanotechnology*, 10(7):593–597, 2015. doi:10.1038/nnano.2015.86.

[135] A. Primer and H. Eschrig. Theory of superconductivity. 2008. URL `https://api.semanticscholar.org/CorpusID:16583662`.

[136] X.-L. Qi, T. L. Hughes, and S.-C. Zhang. Fractional charge and quantized current in the quantum spin Hall state. *Nature Physics*, 4(4):273–276, 2008. doi:10.1038/nphys913.

[137] X.-L. Qi and S.-C. Zhang. Topological insulators and superconductors. *Rev. Mod. Phys.*, 83:1057–1110, 2011. doi:10.1103/RevModPhys.83.1057.

[138] C. H. L. Quay, T. L. Hughes, J. A. Sulpizio, L. N. Pfeiffer, K. W. Baldwin, K. W. West, D. Goldhaber-Gordon, and R. de Picciotto. Observation of a one-dimensional spin–orbit gap in a quantum wire. *Nature Physics*, 6(5):336–339, 2010. doi:10.1038/nphys1626.

[139] A. Rasmussen, J. Danon, H. Suominen, F. Nichele, M. Kjaergaard, and K. Flensberg. Effects of spin-orbit coupling and spatial symmetries on the Josephson current in SNS junctions. *Phys. Rev. B*, 93:155406, 2016. doi:10.1103/PhysRevB.93.155406.

[140] G. Rebora. *Consequences of interactions in quantum Hall edge channels*. Doctoral Thesis, Università degli Studi di Genova, 2023. URL `https://hdl.handle.net/11567/1105324`.

[141] C. Reeg, D. Loss, and J. Klinovaja. Metallization of a Rashba wire by a superconducting layer in the strong-proximity regime. *Phys. Rev. B*, 97:165425, 2018. doi:10.1103/PhysRevB.97.165425.

[142] R. W. Reinthaler, P. Recher, and E. M. Hankiewicz. Proposal for an All-Electrical Detection of Crossed Andreev Reflection in Topological Insulators. *Phys. Rev. Lett.*, 110:226802, 2013. doi:10.1103/PhysRevLett.110.226802.

[143] A. A. Reynoso, G. Usaj, C. A. Balseiro, D. Feinberg, and M. Avignon. Anomalous Josephson Current in Junctions with Spin Polarizing Quantum Point Contacts. *Phys. Rev. Lett.*, 101:107001, 2008. doi:10.1103/PhysRevLett.101.107001.

[144] T. O. Rosdahl, A. Vuik, M. Kjaergaard, and A. R. Akhmerov. Andreev rectifier: A nonlocal conductance signature of topological phase transitions. *Phys. Rev. B*, 97:045421, 2018. doi:10.1103/PhysRevB.97.045421.

[145] A. Roth, C. Brüne, H. Buhmann, L. W. Molenkamp, J. Maciejko, X.-L. Qi, and S.-C. Zhang. Nonlocal Transport in the Quantum Spin Hall State. *Science*, 325(5938):294–297, 2009. doi:10.1126/science.1174736.

[146] J. M. Rowell. Magnetic Field Dependence of the Josephson Tunnel Current. *Phys. Rev. Lett.*, 11:200–202, 1963. doi:10.1103/PhysRevLett.11.200.

[147] G. Santoro. *Non-equilibrium quantum systems*. Lecture Notes, 2016. URL `https://indico.ictp.it/event/7644/session/2/contribution/5/material/2/0.pdf`.

[148] K. Sato, D. Loss, and Y. Tserkovnyak. Cooper-Pair Injection into Quantum Spin Hall Insulators. *Phys. Rev. Lett.*, 105:226401, 2010. doi:10.1103/PhysRevLett.105.226401.

[149] J. D. Sau, R. M. Lutchyn, S. Tewari, and S. Das Sarma. Robustness of Majorana fermions in proximity-induced superconductors. *Phys. Rev. B*, 82:094522, 2010. doi:10.1103/PhysRevB.82.094522.

[150] J. D. Sau, S. Tewari, R. M. Lutchyn, T. D. Stanescu, and S. Das Sarma. Non-Abelian quantum order in spin-orbit-coupled semiconductors: Search for topological Majorana particles in solid-state systems. *Phys. Rev. B*, 82:214509, 2010. doi:10.1103/PhysRevB.82.214509.

[151] J. Schindele, A. Baumgartner, and C. Schönenberger. Near-Unity Cooper Pair Splitting Efficiency. *Phys. Rev. Lett.*, 109:157002, 2012. doi:10.1103/PhysRevLett.109.157002.

[152] T. L. Schmidt, S. Rachel, F. von Oppen, and L. I. Glazman. Inelastic Electron Backscattering in a Generic Helical Edge Channel. *Phys. Rev. Lett.*, 108:156402, 2012. doi:10.1103/PhysRevLett.108.156402.

[153] C. Schrade, S. Hoffman, and D. Loss. Detecting topological superconductivity with φ_0 Josephson junctions. *Phys. Rev. B*, 95:195421, 2017. doi:10.1103/PhysRevB.95.195421.

[154] K. Schwidtal and R. D. Finnegan. Barrier-Thickness Dependence of the dc Quantum Interference Effect in Thin-Film Lead Josephson Junctions. *Journal of Applied Physics*, 40(5):2123–2127, 2003. doi:10.1063/1.1657934.

[155] G. Schön and A. Zaikin. Quantum coherent effects, phase transitions, and the dissipative dynamics of ultra small tunnel junctions. *Physics Reports*, 198(5):237–412, 1990. doi:https://doi.org/10.1016/0370-1573(90)90156-V.

[156] R. Seoane Souto, M. Leijnse, and C. Schrade. Josephson Diode Effect in Supercurrent Interferometers. *Phys. Rev. Lett.*, 129:267702, 2022. doi:10.1103/PhysRevLett.129.267702.

[157] S. Shapiro. Josephson Currents in Superconducting Tunneling: The Effect of Microwaves and Other Observations. *Phys. Rev. Lett.*, 11:80–82, 1963. doi:10.1103/PhysRevLett.11.80.

[158] D. E. Sheehy and A. M. Zagoskin. Theory of anomalous magnetic interference pattern in mesoscopic superconducting/normal/superconducting Josephson junctions. *Phys. Rev. B*, 68:144514, 2003. doi:10.1103/PhysRevB.68.144514.

[159] S.-Q. Shen. *Topological Insulators: Dirac Equation in Condensed Matters*. Springer, 2012. doi:10.1007/978-3-642-32858-9.

[160] Y. M. Shukrinov. Anomalous Josephson effect. *Physics-Uspekhi*, 65(4):317, 2022. doi:10.3367/UFNe.2020.11.038894.

[161] H. Sickinger, A. Lipman, M. Weides, R. G. Mints, H. Kohlstedt, D. Koelle, R. Kleiner, and E. Goldobin. Experimental Evidence of a φ Josephson Junction. *Phys. Rev. Lett.*, 109:107002, 2012. doi:10.1103/PhysRevLett.109.107002.

[162] M. A. Silaev, I. V. Tokatly, and F. S. Bergeret. Anomalous current in diffusive ferromagnetic Josephson junctions. *Phys. Rev. B*, 95:184508, 2017. doi:10.1103/PhysRevB.95.184508.

[163] R. Skolasinski, D. I. Pikulin, J. Alicea, and M. Wimmer. Robust helical edge transport in quantum spin Hall quantum wells. *Phys. Rev. B*, 98:201404, 2018. doi:10.1103/PhysRevB.98.201404.

[164] T. I. Smith. Observation of Persistent Currents in a Superconducting Circuit Containing a Josephson Junction. *Phys. Rev. Lett.*, 15:460–462, 1965. doi:10.1103/PhysRevLett.15.460.

[165] T. D. Stanescu, J. D. Sau, R. M. Lutchyn, and S. Das Sarma. Proximity effect at the superconductor–topological insulator interface. *Phys. Rev. B*, 81:241310, 2010. doi:10.1103/PhysRevB.81.241310.

[166] P. Středa and P. Šeba. Antisymmetric Spin Filtering in One-Dimensional Electron Systems with Uniform Spin-Orbit Coupling. *Phys. Rev. Lett.*, 90:256601, 2003. doi:10.1103/PhysRevLett.90.256601.

[167] E. Strambini, A. Iorio, O. Durante, R. Citro, C. Sanz-Fernández, C. Guarcello, I. V. Tokatly, A. Braggio, M. Rocci, N. Ligato, V. Zannier, L. Sorba, F. S. Bergeret, and F. Giazotto. A Josephson phase battery. *Nature Nanotechnology*, 15(8):656–660, 2020. doi:10.1038/s41565-020-0712-7.

[168] J. Strunz, J. Wiedenmann, C. Fleckenstein, L. Lunczer, W. Beugeling, V. L. Müller, P. Shekhar, N. Traverso Ziani, S. Shamim, J. Kleinlein, H. Buhmann, B. Trauzettel, and L. W. Molenkamp. Interacting topological edge channels. *Nature Physics*, 16(1):83–88, 2020. doi:10.1038/s41567-019-0692-4.

[169] Y. Sungkit. Josephson current-phase relationships with unconventional superconductors. *Phys. Rev. B*, 52:3087–3090, 1995. doi:10.1103/PhysRevB.52.3087.

[170] D. B. Szombati, S. Nadj-Perge, D. Car, S. R. Plissard, E. P. A. M. Bakkers, and L. P. Kouwenhoven. Josephson φ_0-junction in nanowire quantum dots. *Nature Physics*, 12(6):568–572, 2016. doi:10.1038/nphys3742.

[171] Y. Tanaka, A. A. Golubov, S. Kashiwaya, and M. Ueda. Anomalous josephson effect between even- and odd-frequency superconductors. *Phys. Rev. Lett.*, 99:037005, 2007. doi:10.1103/PhysRevLett.99.037005.

[172] Y. Tanaka and S. Kashiwaya. Theory of Josephson effect in superconductor-ferromagnetic-insulator-superconductor junction. *Physica C: Superconductivity*, 274(3):357–363, 1997. doi:https://doi.org/10.1016/S0921-4534(97)80002-0.

[173] Y. Tanaka and S. Kashiwaya. Theory of Josephson effects in anisotropic superconductors. *Phys. Rev. B*, 56:892–912, 1997. doi:10.1103/PhysRevB.56.892.

[174] Y. Tanaka, Y. Tanuma, and A. A. Golubov. Odd-frequency pairing in normal-metal/superconductor junctions. *Phys. Rev. B*, 76:054522, 2007. doi:10.1103/PhysRevB.76.054522.

[175] Y. Tanaka, T. Yokoyama, and N. Nagaosa. Manipulation of the Majorana Fermion, Andreev Reflection, and Josephson Current on Topological Insulators. *Phys. Rev. Lett.*, 103:107002, 2009. doi:10.1103/PhysRevLett.103.107002.

[176] J. C. Y. Teo and C. L. Kane. Critical behavior of a point contact in a quantum spin Hall insulator. *Phys. Rev. B*, 79:235321, 2009. doi:10.1103/PhysRevB.79.235321.

[177] D. J. Thouless. Quantization of particle transport. *Phys. Rev. B*, 27:6083–6087, May 1983. doi:10.1103/PhysRevB.27.6083.

[178] C. Timm. *Theory of Superconductivity*. Notes, 2023. URL `https://tu-dresden.de/mn/physik/itp/cmt/ressourcen/dateien/skripte/Skript_Supra.pdf?lang=en`.

[179] M. Tinkham. *Introduction to Superconductivity*. Dover Books on Physics Series. Dover Publications, 2004. URL `https://books.google.it/books?id=VpUk3NfwDIkC`.

[180] G. Tkachov, P. Burset, B. Trauzettel, and E. M. Hankiewicz. Quantum interference of edge supercurrents in a two-dimensional topological insulator. *Phys. Rev. B*, 92:045408, 2015. doi:10.1103/PhysRevB.92.045408.

[181] T. Tokuyasu, J. A. Sauls, and D. Rainer. Proximity effect of a ferromagnetic insulator in contact with a superconductor. *Phys. Rev. B*, 38:8823–8833, 1988. doi:10.1103/PhysRevB.38.8823.

[182] N. Traverso Ziani, C. Fleckenstein, L. Vigliotti, B. Trauzettel, and M. Sassetti. From fractional solitons to Majorana fermions in a paradigmatic model of topological superconductivity. *Phys. Rev. B*, 101:195303, 2020. doi:10.1103/PhysRevB.101.195303.

[183] D. C. Tsui. Nobel Lecture: Interplay of disorder and interaction in two-dimensional electron gas in intense magnetic fields. *Rev. Mod. Phys.*, 71:891–895, 1999. doi:10.1103/RevModPhys.71.891.

[184] A. V. Ustinov and V. K. Kaplunenko. Rapid single-flux quantum logic using π-shifters. *Journal of Applied Physics*, 94(8):5405–5407, 2003. doi:10.1063/1.1604964.

[185] J. A. van Dam, Y. V. Nazarov, E. P. A. M. Bakkers, S. De Franceschi, and L. P. Kouwenhoven. Supercurrent reversal in quantum dots. *Nature*, 442(7103):667–670, 2006. doi:10.1038/nature05018.

[186] D. J. Van Harlingen. Phase-sensitive tests of the symmetry of the pairing state in the high-temperature superconductors—Evidence for $d_{x^2-y^2}$ symmetry. *Rev. Mod. Phys.*, 67:515–535, 1995. doi:10.1103/RevModPhys.67.515.

[187] L. Vigliotti. 4π-periodic AC Josephson current through a reconstructed quantum spin Hall constriction. *Il nuovo cimento C*, 45:1–11, 2022. doi:10.1393/ncc/i2022-22071-2.

[188] L. Vigliotti, A. Calzona, B. Trauzettel, M. Sassetti, and N. Traverso Ziani. Anomalous flux periodicity in proximitised quantum spin Hall constrictions. *New Journal of Physics*, 24(5):053017, 2022. doi:10.1088/1367-2630/ac643b.

[189] L. Vigliotti, A. Calzona, N. Traverso Ziani, F. S. Bergeret, M. Sassetti, and B. Trauzettel. Effects of the Spatial Extension of the Edge Channels on the Interference Pattern of a Helical Josephson Junction. *Nanomaterials*, 13(3), 2023. doi:10.3390/nano13030569.

[190] L. Vigliotti, F. Cavaliere, M. Carrega, and N. Traverso Ziani. Assessing Bound States in a One-Dimensional Topological Superconductor: Majorana versus Tamm. *Symmetry*, 13(6), 2021. doi:10.3390/sym13061100.

[191] L. Vigliotti, F. Cavaliere, G. Passetti, M. Sassetti, and N. Traverso Ziani. Reconstruction-Induced φ_0 Josephson Effect in Quantum Spin Hall Constrictions. *Nanomaterials*, 13(9):1497, 2023. doi:10.3390/nano13091497.

[192] Y. Vinkler-Aviv, P. W. Brouwer, and F. von Oppen. $\mathbb{Z}_4$ parafermions in an interacting quantum spin Hall Josephson junction coupled to an impurity spin. *Phys. Rev. B*, 96:195421, 2017. doi:10.1103/PhysRevB.96.195421.

[193] P. Virtanen and P. Recher. Signatures of Rashba spin-orbit interaction in the superconducting proximity effect in helical Luttinger liquids. *Phys. Rev. B*, 85:035310, 2012. doi:10.1103/PhysRevB.85.035310.

[194] A. Volkov, P. Magnée, B. van Wees, and T. Klapwijk. Proximity and Josephson effects in superconductor-two-dimensional electron gas planar junctions. *Physica C: Superconductivity*, 242(3):261–266, 1995. doi:https://doi.org/10.1016/0921-4534(94)02429-4.

[195] K. von Klitzing, G. Dorda, and M. Pepper. New Method for High-Accuracy Determination of the Fine-Structure Constant Based on Quantized Hall Resistance. *Phys. Rev. Lett.*, 45:494–497, 1980. doi:10.1103/PhysRevLett.45.494.

[196] G. Wang, T. Dvir, G. P. Mazur, C.-X. Liu, N. van Loo, S. L. D. ten Haaf, A. Bordin, S. Gazibegovic, G. Badawy, E. P. A. M. Bakkers, M. Wimmer, and L. P. Kouwenhoven. Singlet and triplet Cooper pair splitting in hybrid superconducting nanowires. *Nature*, 612(7940):448–453, 2022. doi:10.1038/s41586-022-05352-2.

[197] J. Wang, Y. Meir, and Y. Gefen. Spontaneous Breakdown of Topological Protection in Two Dimensions. *Phys. Rev. Lett.*, 118:046801, 2017. doi:10.1103/PhysRevLett.118.046801.

[198] J. Wiedenmann, E. Bocquillon, R. S. Deacon, S. Hartinger, O. Herrmann, T. M. Klapwijk, L. Maier, C. Ames, C. Brüne, C. Gould, A. Oiwa, K. Ishibashi, S. Tarucha, H. Buhmann, and L. W. Molenkamp. 4π-periodic Josephson supercurrent in HgTe-based topological Josephson junctions. *Nature Communications*, 7(1):10303, 2016. doi:10.1038/ncomms10303.

[199] R. Winkler. *Spin-Orbit Coupling Effects in Two-Dimensional Electron and Hole Systems*. Springer, 2003. doi:10.1007/b13586.

[200] C. Wu, B. A. Bernevig, and S.-C. Zhang. Helical Liquid and the Edge of Quantum Spin Hall Systems. *Phys. Rev. Lett.*, 96:106401, 2006. doi:10.1103/PhysRevLett.96.106401.

[201] T. Yamashita, M. Kunita, and Y. Onodera. Magnetic-Field Dependence of Josephson Current Modified by Self-Field. *Journal of Applied Physics*, 39(12):5396–5400, 2003. doi:10.1063/1.1655988.

[202] T. Yokoyama, M. Eto, and Y. V. Nazarov. Anomalous Josephson effect induced by spin-orbit interaction and Zeeman effect in semiconductor nanowires. *Phys. Rev. B*, 89:195407, 2014. doi:10.1103/PhysRevB.89.195407.

[203] F. Zhang and C. L. Kane. Time-Reversal-Invariant Z_4 Fractional Josephson Effect. *Phys. Rev. Lett.*, 113:036401, 2014. doi:10.1103/PhysRevLett.113.036401.

[204] S.-B. Zhang and B. Trauzettel. Perfect Crossed Andreev Reflection in Dirac Hybrid Junctions in the Quantum Hall Regime. *Phys. Rev. Lett.*, 122:257701, 2019. doi:10.1103/PhysRevLett.122.257701.

[205] S.-B. Zhang, Y.-Y. Zhang, and S.-Q. Shen. Robustness of quantum spin Hall effect in an external magnetic field. *Phys. Rev. B*, 90:115305, 2014. doi:10.1103/PhysRevB.90.115305.

[206] Y. Zhang, Y. Gu, P. Li, J. Hu, and K. Jiang. General Theory of Josephson Diodes. *Phys. Rev. X*, 12:041013, 2022. doi:10.1103/PhysRevX.12.041013.